PHD

The friability of nuclear graphite

Hartley, Mark

Award date:
1996

Awarding institution:
University of Bath

The Friability of Nuclear Graphite

submitted by Mark Hartley
for the degree of PhD
of the University of Bath
1997

Signed ______________________

Mark Hartley

Acknowledgements

This work has been carried out as an EPSRC CASE project between the School of Materials Science, University of Bath and Nuclear Electric Ltd. and I would like to thank both bodies for the laboratory facilities provided. I would like to take this opportunity to express my sincere gratitude to a number of people without who's assistance this work would not have been possible.

Prof. Brian McEnaney and Dr. Jim Reed for their continued advice, support and many invaluable discussions and suggestions throughout this work

Prof. R. Stevens, Dr T. Mays, and Dr G, Neighbour for useful discussions during this work.

The staff at Berkeley Technology Centre, particularly P. Dodd, D. Jones and K. Swallow, for their assistance in the testing of irradiated samples.

M. *Taylor for carrying out some laboratory testing at Berkeley Technology Centre.*

The staff of the school of Materials Science for their technical and scientific assistance during my time at Bath.

Heather for always being there for me no matter how things were going.

My family and friends for their support during my time at university.

Abstract

The graphite core of an advanced gas cooled reactor is not only the moderator but also a structural component. Thus, it is paramount that its integrity is ensured throughout the reactor's life. Towards the end of a reactor's life it is possible, because of the oxidation of the graphite, that contact stresses will begin to damage the reactor core and hence, the friability of the graphite is likely to become important. The work reported in this thesis defines friability in relation to the processes occurring within a reactor core and develops test methodologies to investigate how oxidation will affect these processes. A blunt indentation test which utilised small test pieces has been developed to examine the effect of static contact stresses, while a novel test rig based on a small instrumented lathe was used to investigate dynamic contact stresses. It has been demonstrated that the microstructure of the graphite indented has a marked effect on the nature of the damage produced. Very fine textured graphites, such as Poco ZXF, exhibit a classical Hertzian fracture, whereas in coarser graphites, including nuclear graphites, a shear damage zone develops beneath the indenter before long range cracking occurs. For the coarser textured graphites, porosity has been shown to be the dominant factor controlling the degree of damage beneath the indenter. The effect of thermal and radiolytic oxidation on blunt indentation strength of IM1-24 nuclear graphite was investigated. At high levels of oxidation the initial fracture mode changes from shear cracking to a more progressive failure where the indenting sphere begins to crush through the graphite, similar to the blunt indentation of a carbon foam. An adaptation of the Archard wear equation was used to describe the wear of graphite in the dynamic friability tests and the marked increase in wear rate as a result of oxidation. The proportion of large scale debris and the quantity of debris produced during the dynamic wear tests increased with increasing levels of burn off. The value of hardness deduced from the Archard equation decreased in an exponential manner as the percentage burn off was increased.

1. Introduction

This thesis contains the results of a study of the friability of nuclear graphites. Friability (the concept is explained in Section 1.2) of graphite is of increasing concern to the civil nuclear community in the UK as the reactors approach the end of their serviceable lives. Some reasons for these concerns are set out in Section 1.1. The project's aims and objectives and the layout of the thesis are then out-lined in Section 1.3.

1.1 Technical Background

All the nuclear reactors in the United Kingdom with the exception of Sizewell B, are gas cooled (carbon dioxide) and graphite moderated. The graphite serves two purposes, it slows down fast neutrons produced during fission to thermal energies in order to maximise the efficiency of the reaction with the uranium nuclei, as well as providing the channels necessary for both fuel and control rods. The first reactors were built at Calder Hall and Chapel Cross in the 1950s, each one having 1700 fuel channels fuelled with natural uranium clad with a magnesium alloy (Magnox) [1], although later reactors had as many as 6100 channels in order to deliver more power. Early work demonstrated that dimensional changes in the graphite caused by irradiation (discussed in more detail in section 2.3) would be likely to cause distortion in the core. Consequently all but the earliest Magnox reactor cores were designed using a radial keying system (see Figure 1-1) which allowed for dimensional changes without affecting the overall core geometry.

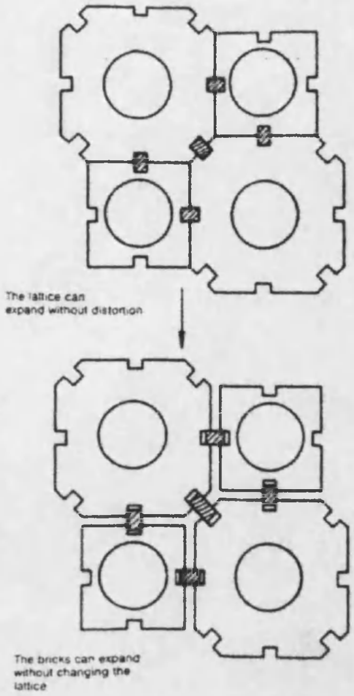

Figure 1-1 : Schematic of a Magnox core showing keys and keyways [1].

By the late 1950s the design of the advanced gas cooled reactor (AGR) was underway, in order to achieve greater power densities and hence improved efficiency. The essential difference between the AGR and the Magnox reactor is that the AGR uses enriched uranium oxide fuel in stainless steel cans, enabling higher temperatures to be achieved and thus greater thermodynamic efficiency [2].

The core of a British AGR is constructed of graphite bricks, Figure 1-2, which are stacked in columns and located on a steel restraint (the Diagrid), (Figure 1-3). The columns are linked with a radial keying system similar to the Magnox reactors and interstitial bricks, which provide channels for the control rods. In the core there are approximately 300 tonnes of graphite bricks which act as both moderator and structural components, whose integrity must be assured throughout the life of the reactor. However, with time, degradation of the mechanical properties of the bricks will occur because of weight loss and development of porosity caused by radiolytic oxidation (see section 2.3). Hence, ultimately it is likely that the condition of the core will limit the life of the reactor as it cannot be replaced.

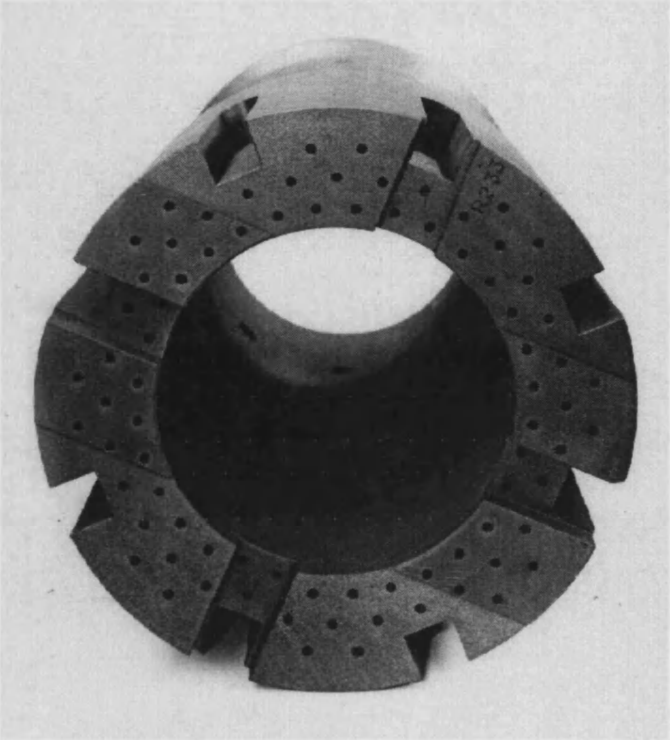

Figure 1-2 : Fuel channel brick (courtesy of Nuclear Electric Ltd.).

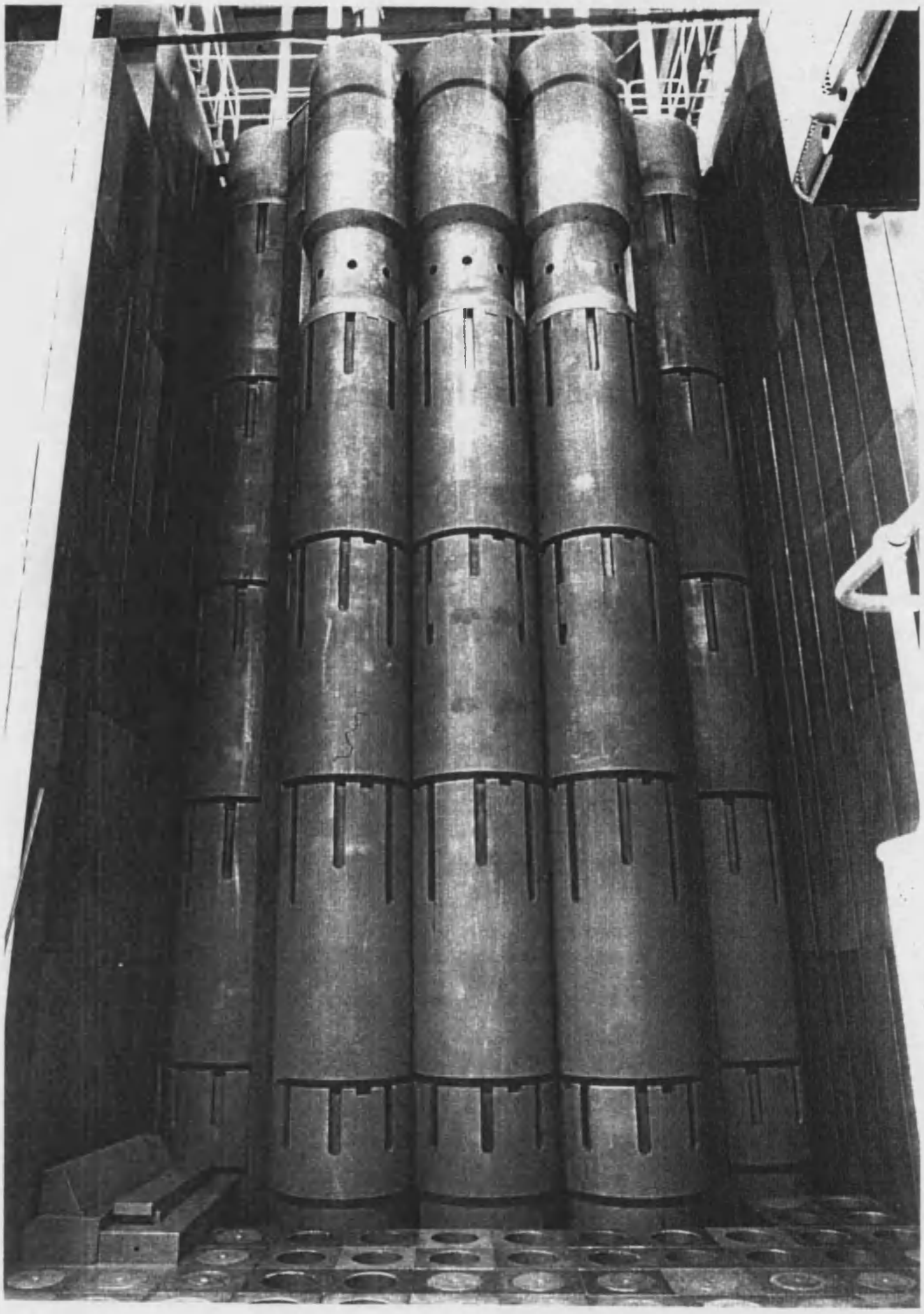

Figure 1-3 : A typical AGR core (courtesy of Nuclear Electric Ltd.).

There has been extensive work carried out on the effects of radiolytic oxidation on the mechanical properties of the core graphite, measured in conventional tests, e.g., in flexural and compressive modes (see Chapter 2). However, relatively little work has been carried out to assess the effects of radiolytic oxidation upon various types of local stress states that are encountered by the moderator graphite in service. Three types of local stresses may be envisaged: "rocking", "dishing" and "abrasion/impact". These stress states are considered in more detail below.

"Rocking" The fuel channel bricks are stacked to provide channels for fuel and control rods. The bottom layer of bricks is located on a steel plate (Diagrid) and the side columns are held in place by steel side restraints, Figure 1-4. As the thermal expansion of steel is considerably larger than that of graphite, in service, differential thermal expansion causes the bricks to rock slightly producing a "zig zag" pattern, Figure 1-4. Point contacts at brick corners and relative movement of the bricks as a result of "rocking" may lead to damage of the graphite, particularly if it is highly oxidised.

"Dishing" Radiation induced end shrinkage within core bricks results in "dishing", i.e., the development of concavities in the top and bottom surfaces of the bricks. The development of "dishing" has the effect of increasing stresses at brick corners, as they carry an increasing proportion of the load transferred through the brick. "Dishing" increases the risk of damage to bricks during "rocking", particularly where relative movement occurs due to power transients in the reactor.

Abrasion/Impact Another potential source of damage to the core bricks occurs during refuelling of the reactor. Material may be removed from the moderator bricks by abrasion from the fuel rod guiding brush or microfracture may occur due to point contacts. Impacts may also occur from the insertion of control rods, possibly removing small quantities of graphite.

Processes such as those described above raise questions about the friability of core graphite bricks that have been radiolytically oxidised to the high weight losses anticipated towards the end of life.

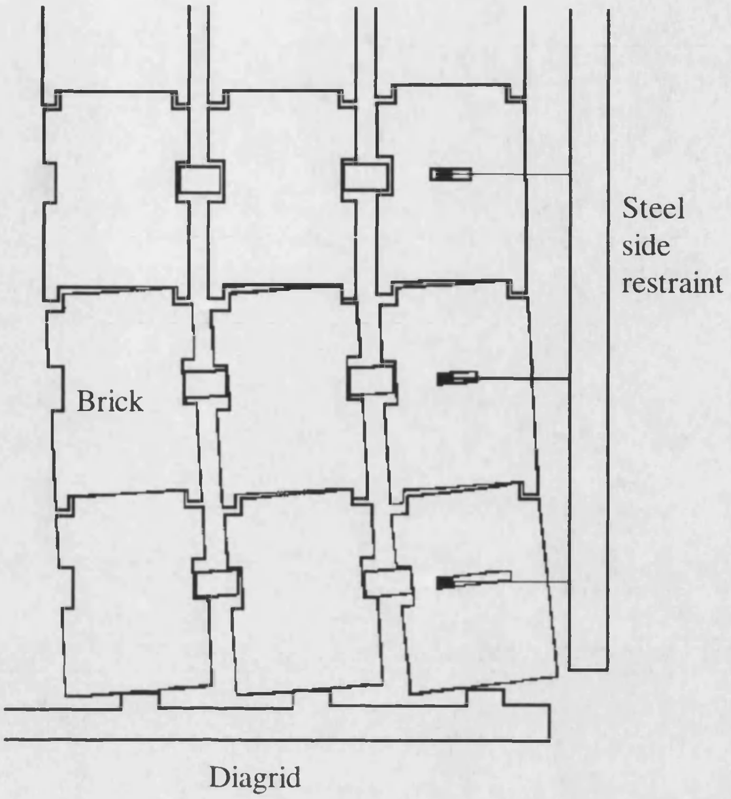

Figure 1-4 : Schematic of a reactor core illustrating the rocking of the bricks.

1.2 The Concept of Friability

A friable material is one that will crumble easily, so that, if a graphite is highly friable, it will be partially reduced to powder under stress. The effects of the local stress states described in the previous section, may be exacerbated by increased friability and are likely ultimately to reduce the integrity of the core. The graphite particles removed from the core bricks, as a result of friability combined with these processes, will be transferred to and increase the activity of the coolant which is also undesirable.

However friability is not a property that is easily quantifiable. There are a number of simple tests that produce a basic friability index which will be briefly discussed in this section, but the information obtained is often limited and relates poorly to a real situation. There are three main classes of test that have been used in the past to try and quantify friability, tumbling and sieving being the most common, with variations on wear tests also being used.

1.2.1 Tumbling tests

The majority of tests use a rotating drum for tumbling the samples, and the percentage weight loss as a function of time is reported [3,4] as a friability index in the manner shown below.

$$F = \frac{\Delta W}{W_0} \qquad 1.1$$

Where F = friability index, ΔW = change in mass, W_0 = original mass.

The apparatus for the Micum index test [5], includes a series of different sized sieves that collect the debris from a rotating drum. This allows the percentage weight loss for a particular particle size range to be calculated.

De Jong [6] related the friability of pharmaceutical tablets to the strength and porosity of a material using a tumbling method. Three tablets are loaded into a drum with an insert to ensure as the drum rotates the tablets always fall from a known height. The relative weight loss is defined as the friability, F, as in equation 1.1, and the assumptions are made that the same quantity of material is removed for every impact and that all the energy is used in fracture. Hence the potential energy, $PE = W_0 gD$, where D = Diameter of the drum. So the potential energy is equal to the breaking energy which is proportional to the breaking force and the deformation. If the pieces removed are said to be approximately equal in size and shape, we can consider the breaking energy proportional to the strength and the volume of the pieces removed, so $PE = \sigma_{crush}\Delta V$ where σ_{crush} = crushing strength $= \frac{K}{HD}$ (where K = diametric crushing force, H = height and D = diameter), ΔV = change in volume.

As $\Delta V = \frac{\Delta W}{\rho_c(1-e)}$ where ρ_c = crystal density and e = fractional porosity, equation 1.2 is obtained.

$$F = \frac{gD\rho_c(1-e)}{\sigma_{crush}} \qquad 1.2$$

This approach is supported by the results shown in Figure 1-5. Equation 1.2 can also be written as

$$F = \frac{gD\rho}{\sigma_{crush}} \qquad 1.3$$

where the bulk density, ρ, $= \rho_c(1-e)$.

It is clear that according to equation 1.3 friability decreases with increasing crushing strength as might be expected. However friability also increases with increasing bulk density which is counter-intuitive, since one might expect friability to decrease with increasing bulk density (or decreasing porosity). It is possible that the crushing strength, σ_{crush}, is the dominating factor which could give rise to the apparently good fit shown in Figure 1-5.

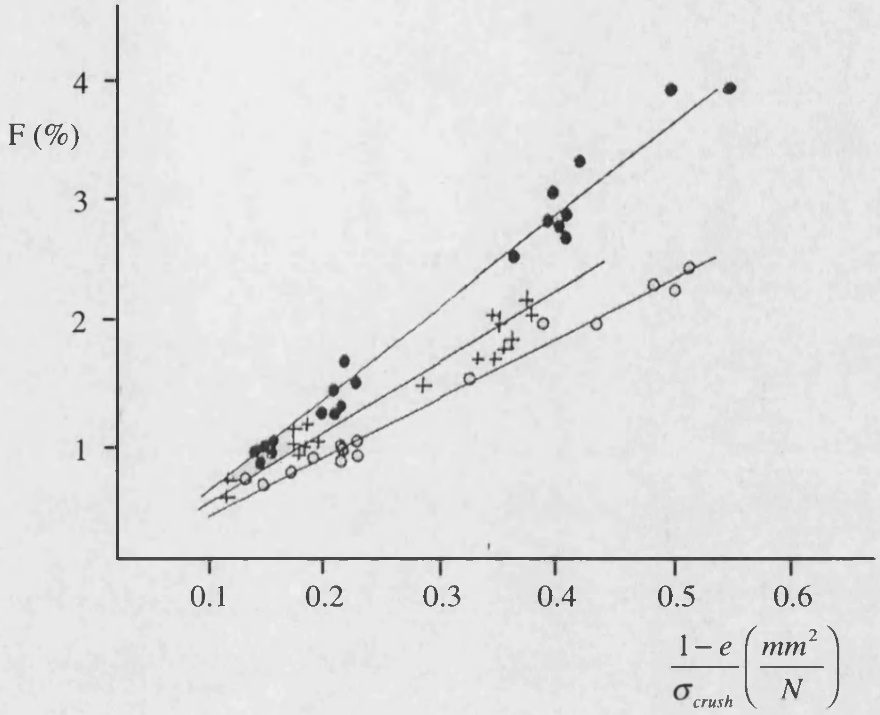

Figure 1-5 : The friability, *F*, as a function of the strength and porosity of tablets, for three binder types [6].

1.2.2 Sieving tests

These [7],[8] tests generally rely on using a vibrating sieve to break up the material, and collect the debris beneath. The friability is then reported as a percentage weight loss per unit time as in equation 1.1. A sieving [9] technique has also been used to provide a size distribution for synthetic diamonds before and after impact loading, giving potentially more useful information than the straight forward friability index.

1.2.3 Wear tests

The only previous attempt at a friability [10] test for nuclear graphite was undertaken nearly thirty years ago and is essentially a sliding wear test. The apparatus (see Figure 1-6) allowed the calculation of a friction coefficient for various porosities of radiolytically oxidised graphite, using readings of force from the strain gauged ring.

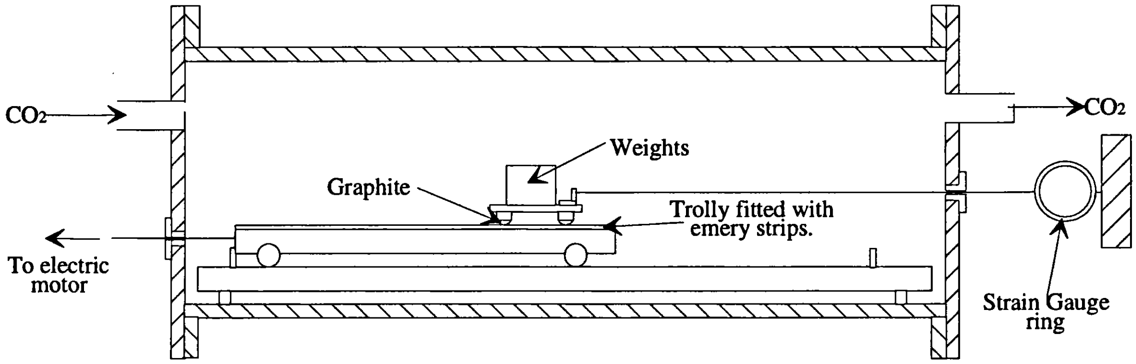

Figure 1-6 : Sliding friability test rig [10].

The results were reported as weight loss of specimen against weight loss due to radiolytic oxidation (Figure 1-7) and volume of graphite removed against weight loss due to radiolytic oxidation (Figure 1-8). These results demonstrate qualitatively that the friability of graphite increases with weight loss due to oxidation, although friability was not formally defined in this work.

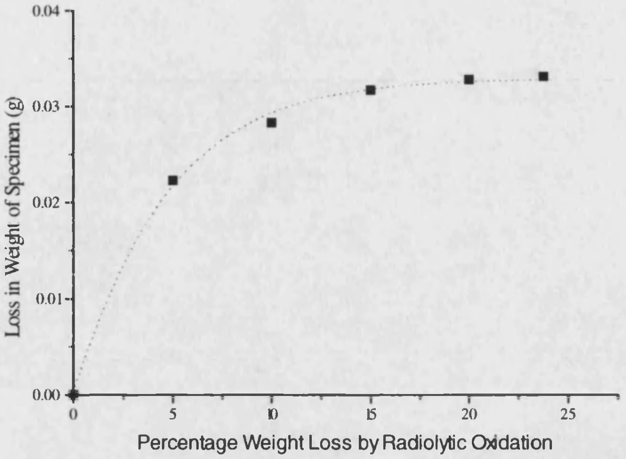

Figure 1-7 : Weight loss due to sliding wear as a function of weight loss by radiolytic oxidation of PGA graphite in CO_2 [10].

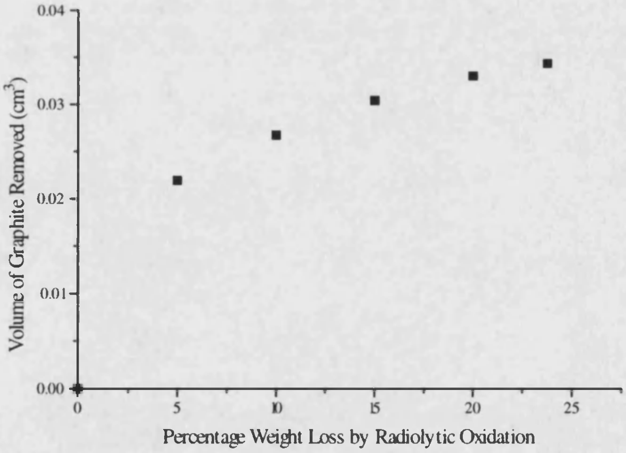

Figure 1-8 : Volume of graphite removed during to sliding wear as a function of weight loss by radiolytic oxidation of PGA graphite in CO_2 [10].

1.3 Project Aims, Objectives and Thesis Layout

1.3.1 Aims

The aim of the project is to investigate the friability of nuclear graphites with particular reference to the processes that may occur in the core of an AGR. In particular it is intended to explore how friability might be affected by the high levels of oxidation likely to occur as the reactors approach the end of their designed lives.

1.3.2 Objectives

1. Devise static and dynamic friability tests which relate to the processes occurring in the reactor core.
2. The tests should be capable of utilising graphite samples trepanned from a reactor core.
3. Develop a blunt indentation technique as the static friability test which can be used on irradiated graphite.
4. Develop the dynamic friability test in the form of a small instrumented lathe.
5. Investigate the effects of thermal and radiolytic oxidation.
6. Investigate the effects of graphite microstructure.

1.3.3 Thesis Layout

Chapters 2 and 3 present the literature review covering the relevant mechanical properties of graphite and blunt indentation. In Chapters 4 and 5 experimental details are presented together with general mechanical properties of the graphites studied. In Chapters 6 - 9 blunt indentation results presented and discussed. Chapters 10 and 11 present dynamic friability results and discussion. The thesis concludes with a summary and conclusions in Chapter 12.

2. The Manufacture and Mechanical Properties of Graphite

In this chapter a general production method for graphite is given in Section 2.1, and the methods of achieving specific properties required for nuclear applications are discussed. The deformation behaviour of graphite and how it is affected by temperature and pre-stressing are reviewed in Section 2.2. Section 2.3 reviews the effects of oxidation on the graphite microstructure and mechanical properties covering both thermal and radiolytic oxidation. The fracture mechanisms that occur in nuclear graphite and methods of modelling them are briefly reviewed in section 2.4, while Section 2.5 reports the effects of fast neutron irradiation on the mechanical properties of nuclear graphite.

2.1 Graphite Manufacture

All synthetic industrial carbons are produced by the pyrolysis of a precursor, which can take many forms and often consists of a number of constituents. The most common precursor for the fabrication of synthetic graphite is a form of pitch although some polymers will also degrade to a tar like liquid [11]. As the temperature of the feedstock is raised the lower molecular weight molecules evaporate raising the average molecular weight of the liquid. The size of the remaining molecules then increases by polymerisation until it is energetically favourable for the homogeneous nucleation of nematic liquid crystals (mesophase). Once formed the mesophase particles continue to grow, consuming the remaining liquid until they come into contact, and assuming the mesophase is fluid enough coalesce [12]. The existence of the mesophase may be only transient before hardening occurs, however the precursor to the graphite structure may be established in a very short time [13]. The formation of the mesophase, coalescence of particles into bulk mesophase and the plastic flow before hardening act to establish the lamellar structure of a graphitizable carbon. Although processes such as gas percolation while the mesophase is liquid will have a marked effect on the final structure by deforming the layered molecules.

2.1.1 *Production of conventional graphites*

The most common method of producing a synthetic graphite is by mixing a precursor with a binder, both of which are then graphitised. The majority of graphites are made using petroleum coke filler and a coal tar pitch binder, although suitable polymers have also been used as binders. The general process to produce graphite in this manner is outlined in Figure 2-1.

This process has been considered in some detail by a number of researchers [14,15,16], hence the major parts of the process will only be briefly discussed here. The coke filler is initially calcined at up to 1400°C to remove any volatile hydrocarbons which would give rise to porosity development during graphitisation. The coke also shrinks significantly which would cause cracking during the graphitisation process [6]. Calcination also has the effect of increasing the order of the structure to a certain extent and will affect the particle size and shape depending on the conditions during the process. Coke fillers are generally calcined before mixing as shown in Figure 2.1 to avoid shrinkage and gas evolution taking place in the finished artefact, although there are exceptions to this [5]. After thorough mixing with a melted pitch, or in some cases a polymer, the carbon artefact is formed usually by either extrusion or moulding. Although, more recently hot isostatic pressing has been utilised for speciality carbons in order to improve consolidation and obtain good control over the microstructure [17].

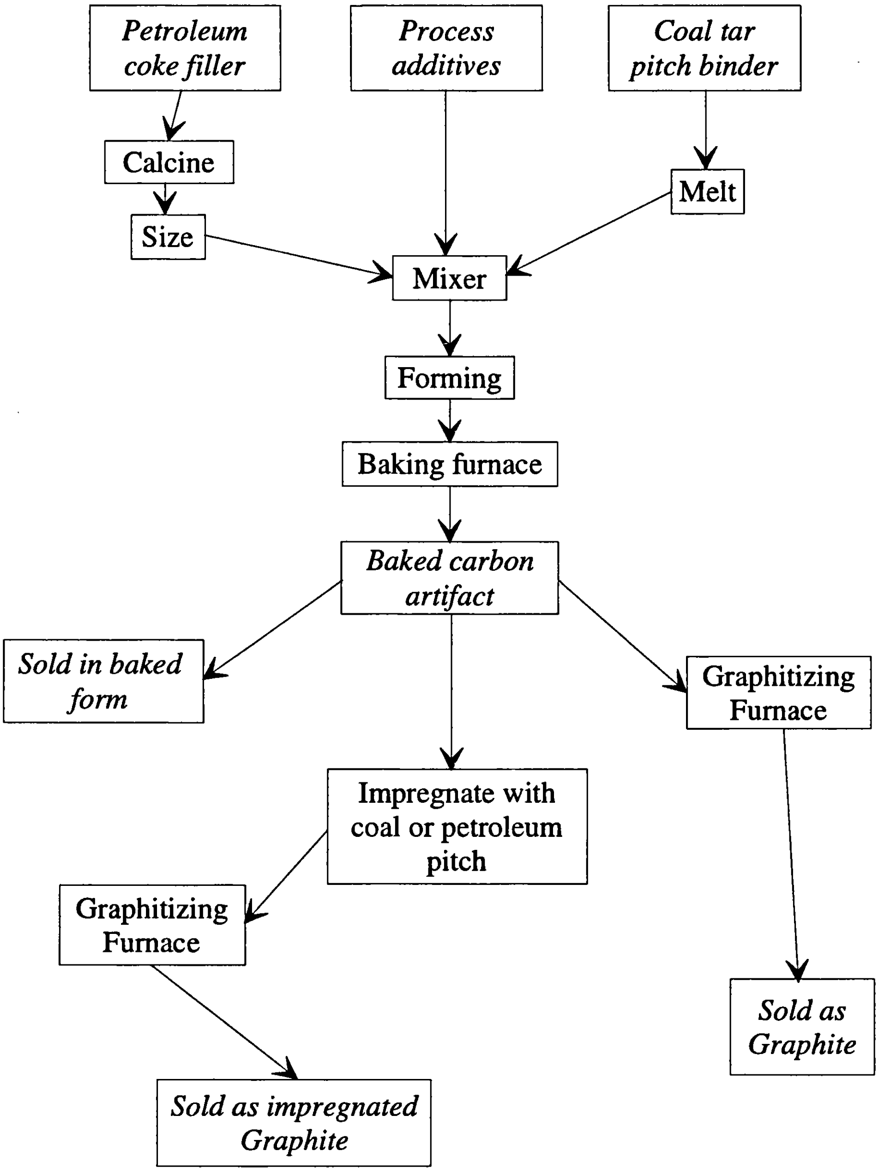

Figure 2-1 : General manufacturing route for graphite (adapted from [15]).

Baking is then carried out to drive off volatiles and facilitate cross linking, giving rise to the production of an ordered structure via the existence of a mesophase. As pitch melts at about 100°C the carbon will lose most of its mechanical strength by 200-300°C so all artefacts must be carefully supported to prevent sagging. Baked carbon is often impregnated with pitch to increase its density, hence improving the mechanical properties. The artefacts are placed in an autoclave which is partially evacuated, molten pitch is then introduced and the pressure raised and held for several hours. This process is often repeated to fill more of the porosity and may be carried out before or after graphitisation. Finally the baked carbon is graphitized, the temperature is raised slowly as baked carbons generally have a high modulus and a high coefficient of thermal expansion making them very susceptible to thermal shock. By the time the temperature reaches 1500°C all the remaining hydrogen has been evolved, crystal growth then takes place up to approximately 2500°C after which the main effects are diffusion and annealing out of crystallite imperfections.

For nuclear graphite used as a moderator very high purity is essential as impurities will absorb neutrons or reduce the effectiveness of the moderator. One possible solution is to use very pure materials, or to purify them before mixing, however there are two methods of purifying formed graphite [6]; thermal and chemical. For thermal purification a very high graphitisation temperature is used (2800-3000°C), which either volatilises impurities or allows them to diffuse to the outside of the artefact. In order to chemically purify graphite, halogens are used, as they will react with the impurities to form volatile compounds. Chlorine gas is admitted when the temperature reaches about 1000°C and the gas is then changed to Freon at approximately 2000°C. Finally the whole furnace is purged with an inert gas during the cooling cycle.

In the early Magnox type reactors an extruded graphite (PGA) containing fairly large needle coke filler particles was used to form the moderator. The combination of the relatively high aspect ratio of the filler particles (Figure 2-2) and the fact that the graphite bricks were formed by an extrusion process produced a highly anisotropic graphite. The anisotropy gives rise to very uneven dimensional changes on irradiation. The dimensional change rates exhibited by PGA are unacceptable at the higher irradiation doses occurring in an AGR. Consequently a new graphite (IM1-24) was developed for use in the AGR's, which utilised Gilsonite pitch coke as a filler. After crushing, the remaining Gilsonite particles (generally referred to as Gilsocarbon particles in the finished graphite) are spherical in shape (Figure 2-3) which in conjunction with the use of a moulding process to form the graphite produced a near isotropic material. Thus the IM1-24 exhibited the required dimensional stability for the greater power ratings in an AGR.

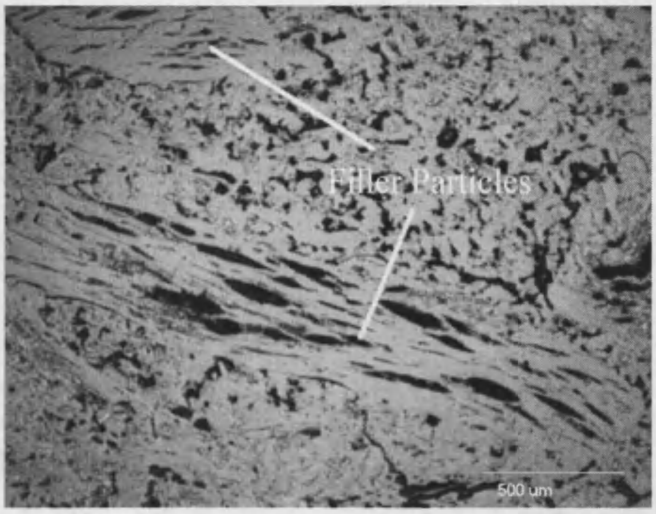

Figure 2-2 : Optical micrograph of PGA graphite.

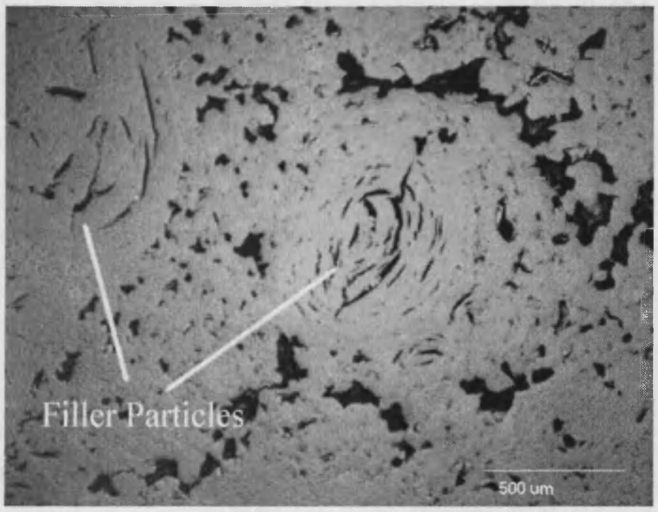

Figure 2-3 : Optical micrograph of IM1-24 graphite.

2.2 The Mechanical Properties of Polycrystalline Graphite

As the graphite core of a reactor not only serves as a moderator, but is also a structural component the mechanical properties relevant to this work are reviewed here. The general deformation behaviour is considered as well the effect of elevated temperatures within the range that the core is exposed to in service. The effect of pre-stressing on the deformation of graphite is also considered. When samples are trepanned from the core and tested they have effectively been pre-stressed because of irradiation shrinkage (see Section 2.5). Thus it may be necessary to take this into account.

The mechanical properties of polycrystalline graphite (graphite is not polycrystalline in the same way as a metal, but the term is commonly used to describe engineering graphites so I will continue to use it here) vary greatly depending on the microstructure and the density of the material. The flexural and compressive strengths vary from ~ 5-120MPa and 30-200MPa respectively while the modulus falls within the range of 5-25GPa (see Chapter 4). In many ways graphite could be considered an engineering ceramic, although when compared to a material such as silicon nitride which has a modulus of approximately 150GPa and a bend strength of around 300MPa [18] the mechanical properties seem rather poor. Polycrystalline graphite is perhaps mechanically nearer to concrete which is also essentially composed of a filler (aggregate) and a binder (cement). The compressive strength of a standard concrete can be up to 100MPa [19] although with new aluminous cements compressive strengths up to 300MPa can be achieved. The strain to failure of concrete increases as the strength is increased so the modulus is in the range 15-50GPa.

2.2.1 Deformation of Polycrystalline Graphite.

The loading response of a polycrystalline graphite is markedly non-linear for both tension and compression, with a large permanent set also being apparent. A typical stress-strain plot for tensile loading is shown in Figure 2-4. The initial loading curve is not linear,[20] but if the load is removed and reapplied the loading curve is linear and can be used to define modulus. However, if the load is cycled in compression (Figure 2-5) the reloading curves exhibit marked hysteresis and their slopes decrease with increasing stress. Thus in compression the modulus decreases as the maximum stress increases. This is broadly similar to the behaviour of concrete [21] shown in Figure 2-6a. Figure 2-6b shows there is also a marked level of hysteresis on unloading.

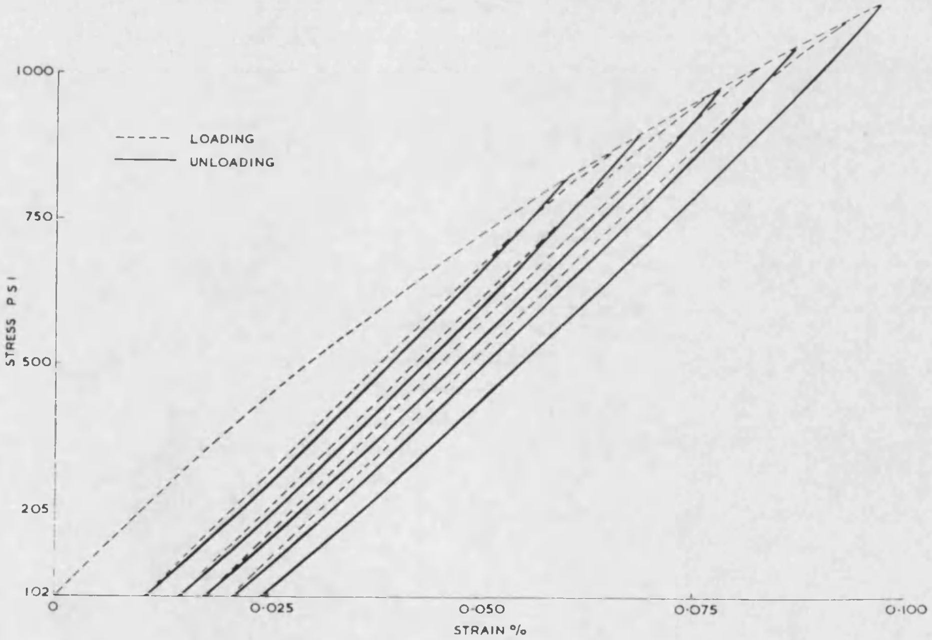

Figure 2-4 : Typical tensile stress-strain diagram for reactor graphite [20].

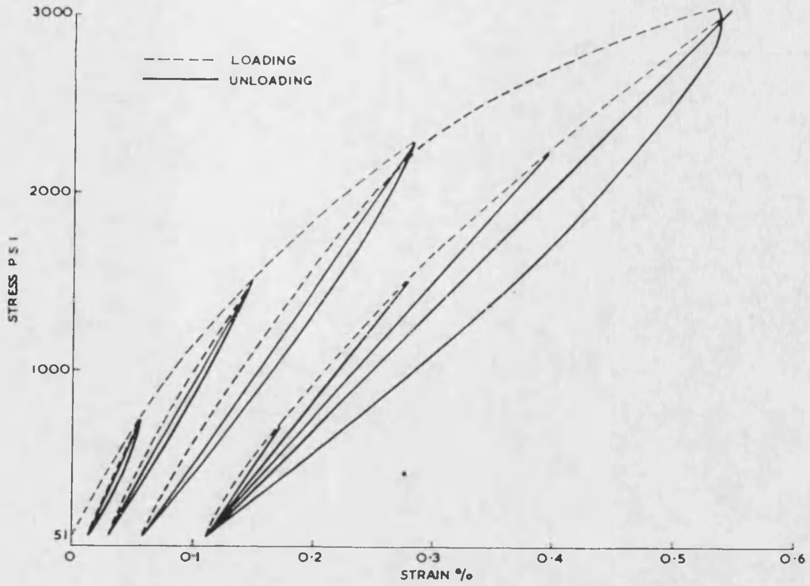

Figure 2-5 : Compressive stress-strain diagram for reactor graphite [20].

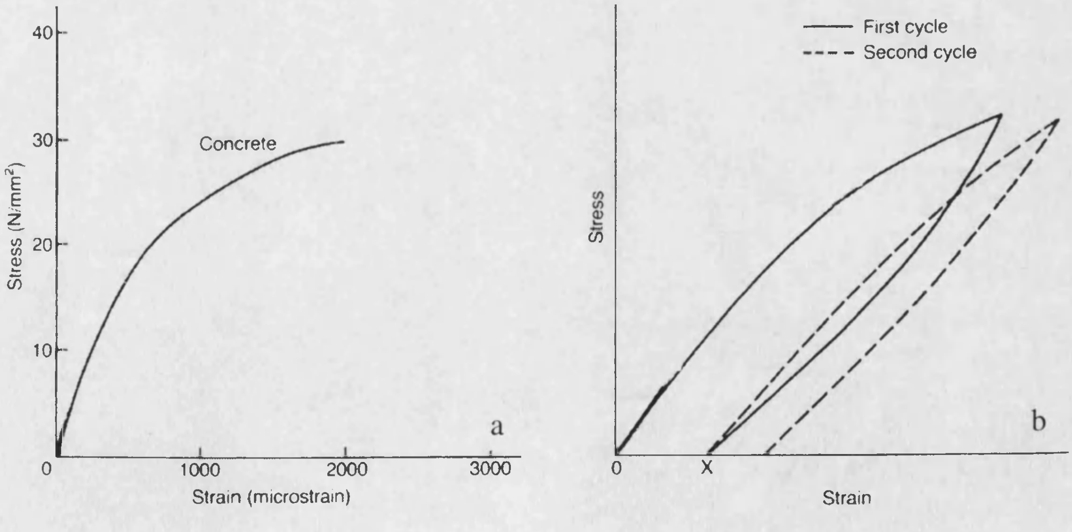

Figure 2-6 : Stress-strain relationship for concrete (adapted from [19]).

Losty and Orchard [20] carried out an experiment to vary the modulus by impregnating graphite with sugar solution and calcining. They found that the increase in strength was proportional to the increase in modulus, hence the graphite failed at a constant strain over a range of densities. Assuming that the calcined sugar solution behaved in the same way as the binder phase they concluded that the failure of graphite was likely to be strain controlled. Jenkins [22] suggested a simple model based on a Voigt element linked to a Hookean one in series. It was assumed that the applied compressive stress is only large enough to produce plastic deformation in some isolated parts of the structure, which are restrained by an elastic network in which they are embedded. The suggested microstructural mode of plastic deformation was by slip of the well orientated graphite planes which are restrained by the binder phase. Seldin [23] demonstrated that Jenkins model was a good first approximation to experimental data, particularly at low strains. However the model predicts the stress-strain curves to be the same in tension and compression which is not the case. It was suggested [23] that the difference in behaviour can be accounted for by the distribution of internal stresses that were frozen in on cooling from the graphitisation temperature, and how they interact with the external stresses. The discovery that the permanent set can be annealed out by heating to high temperatures raised the question of how internal stresses might interact with external stresses while still allowing any deformation to be reversible. Microstructural examination performed by Slagle [24] indicated that inelastic behaviour was associated with interlayer cracking in crystallites, which means the micro-cracks must heal on annealing.

The elastic moduli of the graphite single crystal are all notably higher than those for a polycrystalline graphite with the exception of that for shear parallel to the basal plane. This led Simmons to suggest that the deformation of polycrystalline graphite under an applied stress was controlled by basal plane shear of the single crystal [25]. He also proposed that the plastic effects were associated with basal plane slip, as dislocations had been demonstrated to move on the basal plane by Amelinckx and Delavignette [26]. The idea of the properties of polycrystalline graphite being controlled by the shear of the graphite crystals was developed in detail by Kelly who produced a model explaining many of the properties of graphite [27], particularly when irradiated, in terms of the single crystal. Kelly also suggested [28] that the interplaner shear could be treated with the idea of Coulomb friction. Thus the shear component on the plane can be expressed as $\tau = \tau_0 + \mu\sigma$ where τ_0 = shear stress, μ = friction coefficient and σ = compressive stress. This idea explains the observed hysteresis, as the shear stress must exceed a critical value depending on the friction coefficient for slip to occur.

2.2.2 The effect of Pre-stressing on the mechanical properties of graphite

Hart [29] observed a decrease in Youngs modulus after both tensile and compressive pre-stressing of ATJ and AXF graphite. He attributed this to the formation of microcracks and the increase in dislocation density, although a earlier work by Slagle [30] suggested crack closure would occur during compressive loading. Crack closure would give rise to an increase in Youngs modulus as the size and number of flaws would be reduced. Consequently, Hart suggested that crack closure took place but the effect was masked by the increased formation of microcracks and greater dislocation density. Later work by Ioka and Yoda [31] broadly agreed with these findings showing that Youngs modulus decreases with increasing levels of compressive pre-stress. However, the flexural strength increased to a limit before decreasing abruptly. Using resistivity measurements the authors demonstrated that the main mechanisms that occur during deformation are microcrack formation and closure as well as basal plane slip. Figure 2-7 shows schematics of the graphite microstructure and how pre-stress affects it. As a compressive stress is applied microcracks orientated perpendicular to the loading begin to close, while microcracks parallel to the loading axis are opened by the resolved tensile stress. Grains at 45° to the loading axis start to deform plastically by basal plane slip while the rest of the structure only deforms elastically. As the stress increases shear fracture begins to occur producing new microcracks.

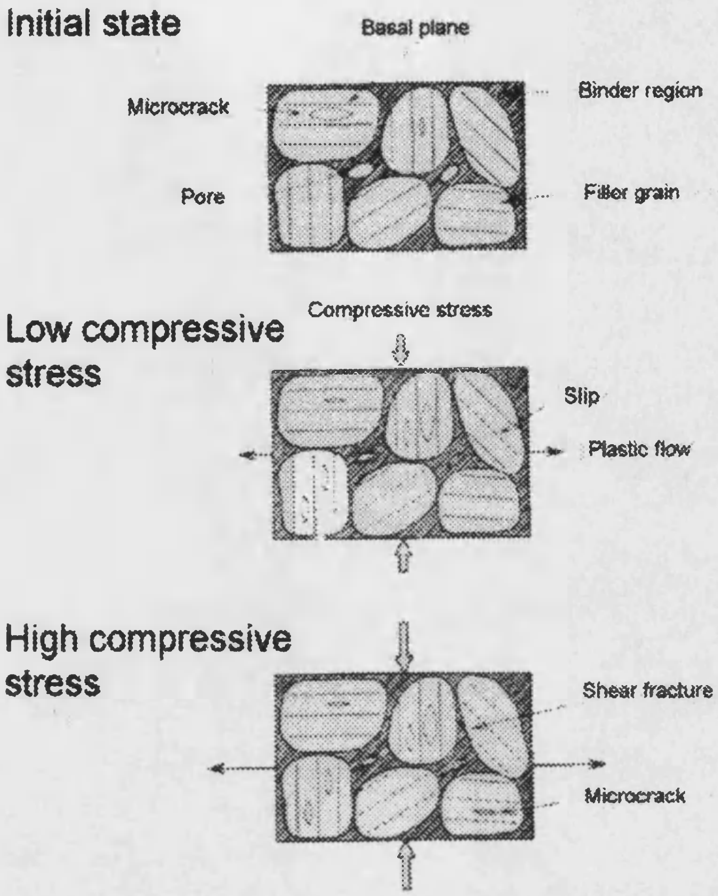

Figure 2-7 : Schematic showing the effect of prestress on graphite [31] .

2.2.3 *The effect of temperature on the mechanical properties of graphite*

Andrew and Sato [32] investigated the effect of temperature on the deformation behaviour of polycrystalline graphite by carrying out load cycles in flexure as the temperature was slowly raised. They noted that Youngs modulus stayed roughly constant until approximately 600°C then increased with increasing temperature. Mason and Knibbs [33] reported a very similar trend using a resonant frequency method to measure Youngs modulus. Maruyama *et al* [34] used sound velocity measurements to obtain the elastic modulus, as well as measuring the bend strength at various temperatures. They found that the modulus and strength rose with increasing temperature in the same manner, starting to increase at approximately 500°C. It is worth noting that all these tests were carried out in a vacuum which means that any changes in mechanical properties are due solely to the change in temperature, rather that the effect of any adsorbed gases. The change in Youngs modulus is due to a combination of closure of microporosity and the unpinning of dislocations. The closure of microporosity raising Youngs modulus while the unpinning of dislocations would reduce it. As the modulus increases Maruyama *et al* [34] assumed that the dominant mechanism was the closure of microporosity, however it seems unlikely that micropores could begin to close at a temperature as low as 500°C [35]. Maruyama *et al* [34] also imply that the fact that strength and modulus vary in the same way adds weight to this theory. Assuming that closure of microporosity is indeed occurring it still seems unlikely that the larger strength controlling flaws would decrease in size significantly. Hence it is unlikely that the strength would be effected by the closure of microporosity.

Although there are a number of unresolved questions about the mechanism by which a rise in temperature could cause an increase in Youngs modulus, the effect in an AGR would be extremely small as the gas outlet temperature is only ~650°C.

2.3 Oxidation of Nuclear Graphite

As all the commercial reactors in the UK but one are CO_2 cooled and graphite moderated, the oxidation of graphite, particularly in CO_2, has been the subject of a large number of studies. There has been extensive work on thermal oxidation in air and CO_2 which has often been used as a model for the effect on the mechanical properties caused by the more complex radiolytic oxidation.

In general, the rate of oxidation increases with increasing temperature. Initially, at low temperatures (zone 1 in Figure 2-8) the concentration of the gas in the pores is the same as the bulk concentration, [36] so the reaction rate is under chemical control giving uniform oxidation. As the temperature is increased the concentration of the reactant gas within the pores decreases, so the diffusion of the reactant gas in the pores plays a part in controlling the reaction rate (zone *a* in Figure 2-8). Within zone a the concentration of the reactant gas at the centre of the sample will decrease progressively as the temperature rises until it falls to zero. This represents the transition to zone 2 where the reaction rate is controlled exclusively by in pore diffusion. So if an oxidation reaction took place in zone 2 a weight loss profile across the sample would be produced, with zero weight loss in the centre and a maximum at the surface. Further increases in temperature give rise to a reduction in gas concentration at the sample surface (zone *b* in Figure 2-8). Thus gaseous diffusion through the boundary layer now contributes to the overall reaction rate. The surface concentration of the reactant gas falls progressively with increasing temperature until zone 3 is reached where the surface concentration approaches zero. In zone 3 the reaction rate is controlled by the diffusion of the reactant gas to the surface, hence if oxidation takes place in this zone surface burn off will occur.

For experimental purposes uniform oxidation is usually preferable as the analysis is simplified, so ideally the oxidation should take place in the chemical control regime (zone 1). However, practically the best we can hope to achieve is oxidation in zone *a*, as close to zone 1 as is possible.

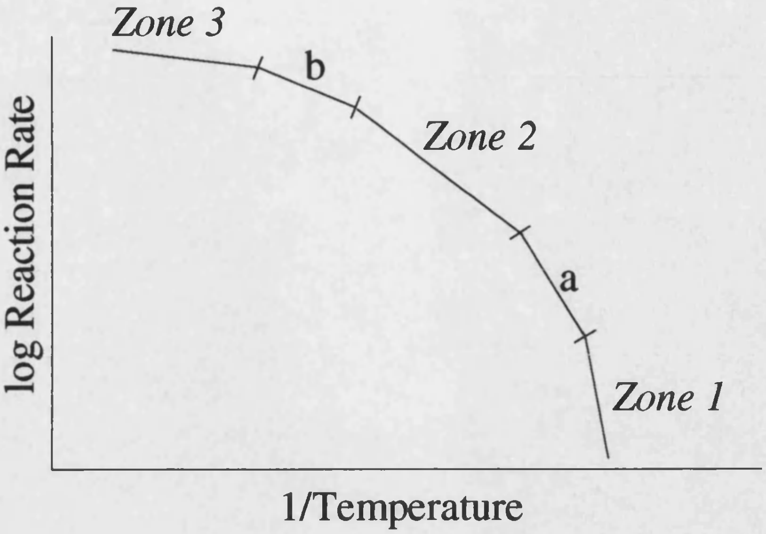

Figure 2-8 : Schematic Arrhenius plot for carbon gasification.

The thermal oxidation of carbon by carbon dioxide is generally accepted to be a two stage process as proposed by Ergun [37] in order to explain experimental observations. Initially the oxygen exchange reaction $C + CO_2 \leftrightarrow C(O) + CO$ takes place extremely quickly producing a bound oxide C(O) at the surface, and gaseous carbon monoxide [15]. The gasification reaction $C(O) \rightarrow CO$ then transfers carbon from the solid phase to the gaseous one [15]. Assuming oxidation occurs in the chemical control regime (zone 1 is dominant), which is likely to be the case below ~950°C [15], the gasification reaction is the rate controlling step.

The situation becomes more complex in the presence of fast neutron irradiation, when the oxidation reaction becomes significant at much lower temperatures. Radiolytic oxidation of graphite occurs when more energetic chemical species are generated in the open pore structure of the graphite [38] by the absorption of mainly gamma radiation energy. These species then drift to the pore wall where they attack the graphite. There have been considerable problems in trying to determine experimentally the active species, and severe conditions in an AGR reactor (gas pressure ~4.1 MPa and maximum gas temperature ~650°C) give added complications. There have been a number of experiments using ion chambers with radioactively labelled carbon electrodes to try and identify the charge on the oxidising species, but the results have been inconclusive [39]. However, it is believed that the principal chemical species formed from irradiated CO_2 that is capable of chemical attack on carbon is CO_3^-, as it has the correct kinetic characteristics.

If inhibitors, such as the reaction product carbon monoxide, are present (as they will always be in practice) there is a possibility of any chemical species capable of attacking carbon recombining. For instance, assuming that CO_3^- is the principal active species, then it will combine with carbon monoxide in the following manner $CO_3^- + CO \rightarrow 2CO_2 + e^-$ [38]. The carbon monoxide present is sufficient to inhibit the oxidation reaction in the Magnox reactors, but owing to the higher gas temperatures and pressures in an AGR methane is added to improve inhibition. Methane has long been assumed to create a sacrificial soot like deposit on the surface of the graphite that oxidises preferentially to the graphite [39]. If this was the mechanism, then one would expect to find a greater quantity of soot deposited in an AGR than in a Magnox reactor, which is often not the case. Although the mechanism by which methane inhibits the oxidation reaction is not well understood, there is no doubt that its presence in relatively small quantities does reduce the rate of oxidation.

2.3.1 *Effect of oxidation on graphite microstructure*

IM1-24 graphite contains mostly large open pores in the binder phase while the spherical Gilsocarbon filler particles contain closed porosity arranged in an "onion skin" morphology (see Figure 2-3). In the early stages of radiolytic oxidation of IM1-24 (up to 5% burn off) with both carbon monoxide and methane present as inhibitors, small pores <100μm wide are developed from the existing open porosity [40] [41]. As the oxidation proceeds, closed porosity is gradually opened up so that by 13% weight loss all the filler particles contain some open porosity [41]. This is demonstrated in Figure 2.9 where thermally oxidised IM1-24 graphite has been impregnated with a fluorescent dye and sectioned so that only the open porosity filled with resin shows up as being white. This opening of previously closed porosity increases the surface area that the oxidising species can attack. Consequently, the rate of oxidation will increase assuming we are close to zone 1 oxidation.

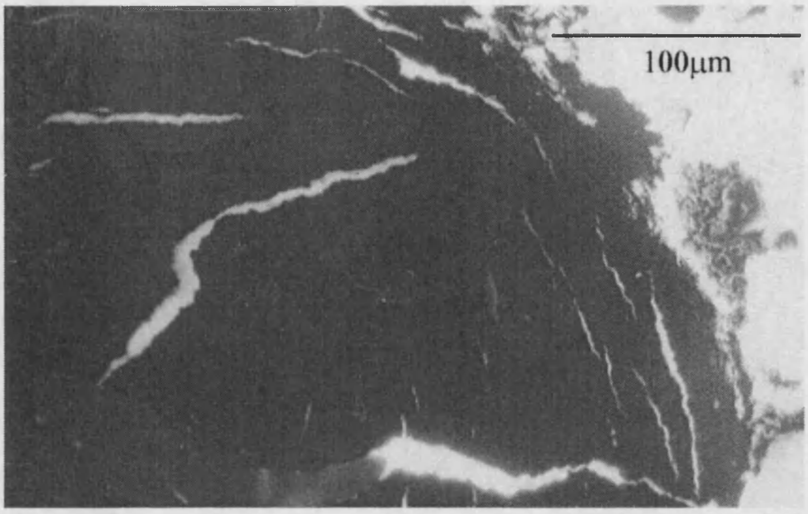

Figure 2-9 : Florescence enhanced micrograph of lenticular porosity within a Gilsocarbon particle which has been opened due to oxidation [52].

By 17% weight loss, pores in the size range 20-100μm are interconnected and further porosity develops [40]. It is apparent that small pores grow while the large ones remain a similar size. This is due to the greater probability of gas phase deactivation of the oxidising species by the inhibitors in a larger volume [41].

If we compare the effect of radiolytic oxidation on the microstructure with that of thermal oxidation, a difference in the type of porosity developed is apparent. Figure 2-10b shows small filament-like pores in the binder of PGA 1-5μm in width, which have been developed in the early stages of thermal oxidation [42]; for comparison the unoxidised microstructure is shown in Figure 2-10a. Both micrographs have been produced by impregnating with a fluorescent resin so, as with the previous figure, only open porosity is shown, thus providing a good insight into the development of porosity during thermal oxidation. Figure 2-11 compares normal optical micrographs, the first (a) of unoxidised PGA and the second (b) of radiolytically oxidised PGA. The porosity produced by radiolytic oxidation is larger than that due to thermal oxidation, and almost spherical in nature. The whole process also appears to be far less selective than thermal oxidation, attacking all parts of the microstructure, as might be expected for a more energetic oxidising species. The effects of these differences upon the strength and modulus of oxidised graphites will be discussed in the context of mechanical properties in the next section.

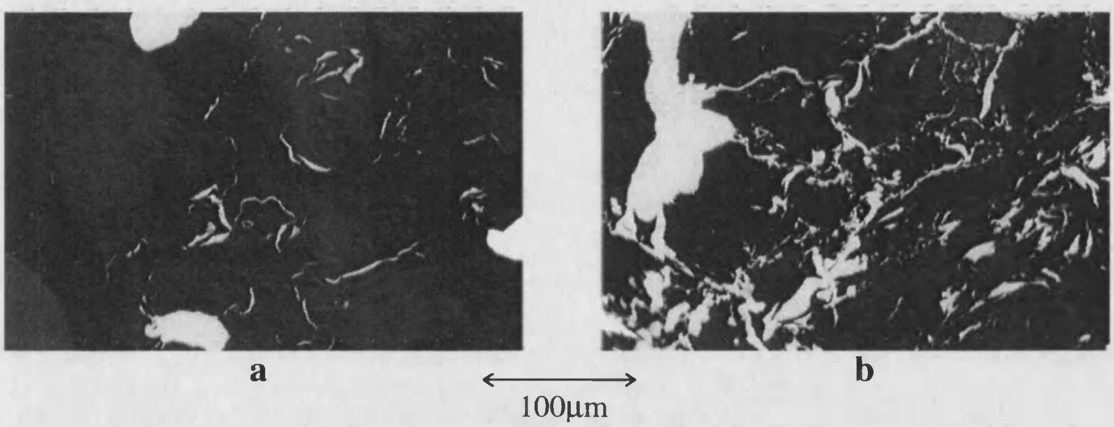

Figure 2-10 : Fluorescence enhanced micrographs (pores in bright contrast) of needle coke graphite (PGA) , a, unoxidised. b, thermally oxidised to 2.4% weight loss [52].

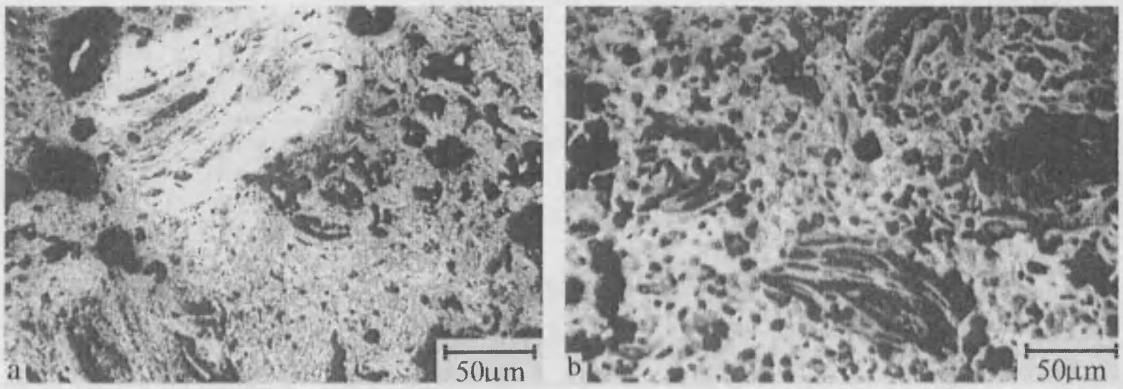

Figure 2-11 : Needle coke graphite (PGA), a, unoxidised. b, radiolytically oxidised to 4.2% weight loss [43].

2.3.2 The Effect of Oxidation on the Mechanical Properties of Graphite

Board and Squires [44] thermally oxidised PGA graphite in CO_2 at temperatures ranging between 750°C and 950°C and found that the rate of oxidation varied depending on the size of the sample, suggesting that some of their samples were oxidising in the diffusion controlled regime. The strength and modulus both decreased in a similar linear manner up to 7% burn off, indicating that graphite thermally oxidised in CO_2 fails at constant strain regardless of the level of oxidation. These results compare well with Losty and Orchards results [20] from their experiments increasing the density of graphite by sugar impregnation. The mechanism of fracture in the unoxidised graphite occurred by the linking of porosity often through large grains. However, after oxidation, the crack tended to propagate through the binder at the filler/binder interface. A number of researchers [45] [46] [47] found that they could relate the measured degradation in strength with increasing oxidation to a decrease in bulk density, ρ, using an empirical power law of the form. $\frac{\sigma_f}{\sigma_0} = \left(\frac{\rho_{ox}}{\rho_0}\right)^n$ where σ_f = fracture strength of oxidised graphite, σ_0 = fracture strength of as received graphite, ρ_{ox} = density of oxidised graphite, ρ_0 = Density of as received graphite and n = constant.

This relationship is demonstrated in Figure 2-12 where the reductions in compressive strength and bulk density produced by oxidation in air are shown (n = 4.5). Yoda et al. [46] also found that the compressive strain to failure for a fine grained nuclear graphite decreased with increasing burn off in air (Figure 2-13) contrary to the results for the coarser PGA graphite [44]. However, Thrower and Bognet [48] reported that the strain to failure remained constant up to 30% weight loss obtained by thermal oxidation of Stackpole 2020 grade graphite in air; after which the failure strain increased considerably. Radiolytic oxidation of Gilsocarbon graphite in CO_2 was reported to have no effect on the strain to failure by Kelly *et al* [49]. This raises the question of whether there is a fundamental difference between the effect of oxidation in air and oxidation in CO_2 on the mechanical properties of graphite. This however seems unlikely. I propose that the most likely cause of these differences is variations in the uniformity of the oxidation. It is generally quite difficult to obtain uniform oxidation of graphite in a CO_2

atmosphere and even more so when oxidising in air. If a density gradient was introduced across the sample by oxidation then the strain at failure may change considerably. Knibbs and Morris [47] found that the severity of the effect of oxidation varied depending on the atmosphere used, decreasing in the order thermal-air>thermal-carbon dioxide>radiolytic-carbon dioxide.

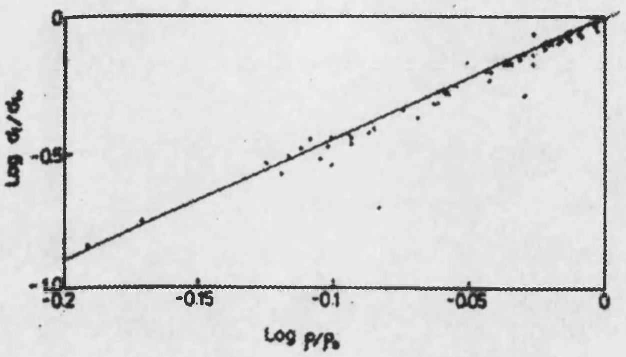

Figure 2-12 : Logarithmic plot of compressive fracture strength against density for oxidation in air of IG11 graphite [46].

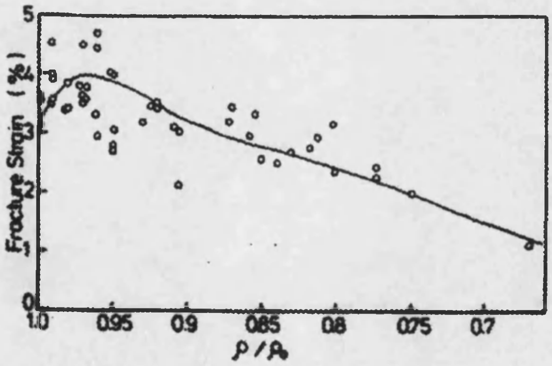

Figure 2-13 : Change of compressive strain to failure as a function of density for oxidation in air of IG11 graphite [46].

Thrower and Bognet [48] thermally oxidised graphite in air up to 40% weight loss and reported an exponential decrease in the compressive strength with increasing weight loss. Other researchers [49] [50] [51] [52] have obtained similar results for thermal and radiolytic oxidation in CO_2 and have commonly used an empirical exponential equation $\sigma_f = A.exp\text{-}(b.e)$ to describe their results, where A = empirical constant, b = empirical constant and e = fractional porosity.

The exponential decrease in strength with increasing porosity seems to have been first noted by Ryshkewitch [53] for polycrystalline ceramics and was formally expressed by Duckworth [54] in a discussion of Ryshkewitch's paper. Knudsen [55] later tested the relationship for a wider range of porous ceramics and extended the equation to include the effects of grain size. Although the equation is empirical, it has long been known that the term b corresponds in some way to the shape of the pores. More recently Buch [56] developed a theoretical derivation of the exponential relationship for the reduction in elastic modulus and increased porosity based on far field displacements. The derivation shows that the pores contributing the most to the reduction in modulus are those which have the greatest projected area per unit volume i.e. those of high aspect ratio. So filamentary pores have a greater effect than spherical ones. This demonstrates why thermal oxidation has a more detrimental effect on the mechanical properties than radiolytic oxidation (see Figure 2-14).

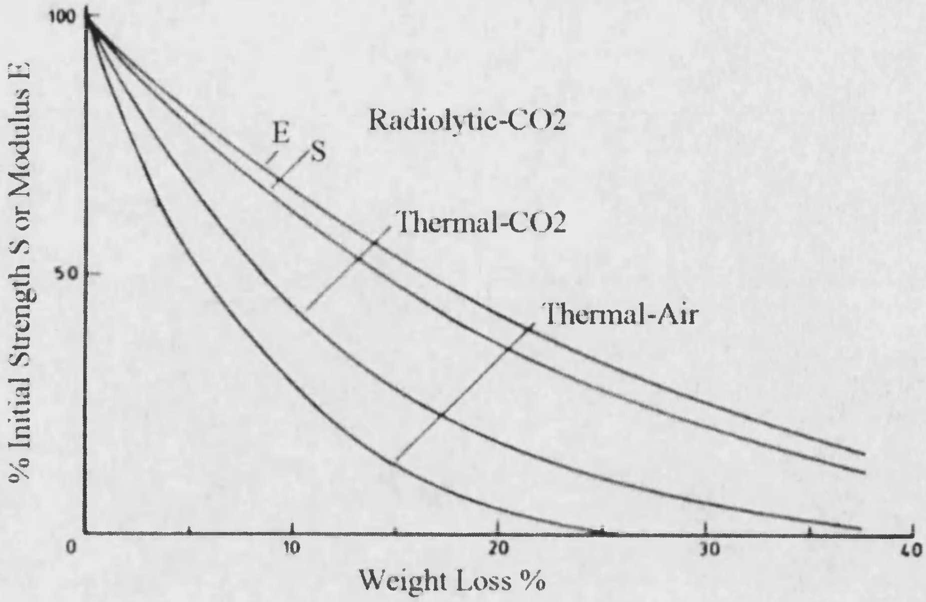

Figure 2-14 : The effect of oxidation in different atmospheres on the mechanical properties of graphite [57].

2.4 Fracture of Graphite

Since Brocklehurst's [57] exhaustive review on fracture in polycrystalline graphite, a number of researchers have continued to investigate the microstructural fracture processes of graphite. Much of this has been utilised to create predictive fracture models with a microstructural basis, which generally stem from basic fracture mechanics.

The study of fracture mechanics began with Griffith [58] who proposed that the difference between the theoretical and actual strength of glass could be accounted for by the presence of microcracks. He went on to postulate that for a stable propagating crack the strain energy released was equal to the energy required to create the new surface as the crack propagates. He expressed this in the form $\sigma_f = \sqrt{\frac{2\gamma_s E}{\pi c}}$ where γ_s = surface energy, E = Youngs modulus and c = crack length. Later, both Orowan [59] and Irwin [60] working independently extended Griffiths relationship to take account of a small quantity of plastic flow at the crack tip. Suggesting that the extra energy required to plastically deform a material could be accounted for using another term, γ_p. From this idea they defined a critical strain energy release rate, G_c, as $2(\gamma_s+\gamma_p)$, hence the Griffith relationship becomes $\sigma_f = \sqrt{\frac{EG_c}{\pi c}}$. This equation states that "the critical combination of stress and crack length at which fast fracture commences is a materials constant" [61] and has become one of the cornerstones of fracture analysis. Another approach to the same problem is to calculate the stress distribution just ahead of the crack tip [62], from which the much quoted stress intensity factor, K, is obtained. $K = \sigma\sqrt{\pi c}$ for plane stress, and is referred to at the point of failure as the critical stress intensity factor, K_c, which describes part of the Griffith equation and is often referred to as the fracture toughness.

Rodig *et al* [63] investigated the fracture mechanics properties of a number of graphites with different textures. They observed that, in graphite with a fine microstructure, once a crack is initiated it will only arrest on removal of the stress. With a coarser microstructure, the crack often arrests because of the tortuous path it is forced to follow by filler particles and porosity. Also, using a fine grained graphite, Wood *et al* [64] demonstrated the marked effect of orientation of filler particles on toughness. The graphite was significantly tougher perpendicular to the direction of extrusion than parallel to it, because of the orientation of the basal planes within the filler particles. When a moulded graphite was tested, no difference in toughness with orientation was found. They also noted that the fracture path was generally through the binder phase or across the favourably orientated filler particles.

Burchell [65] *et al* studied the effect of the different microstructures of nuclear graphite on the fracture, and how filler and binder phases interact with a propagating crack. Figure 2-15 a-d illustrates how the orientation of well graphitised filler particles will affect the propagation of a crack. Preferred crack paths include filler/binder interfaces, cleavage of needle coke particles and the linking of porosity. Parts e to f of Figure 1 shows the interaction of a crack with a Gilsocarbon filler particle, demonstrating how a sub-critical crack might propagate through a particle. A crack is more likely to propagate through a Gilsocarbon particle than through the filler/binder interface, because of the internal stresses frozen in on cooling from the graphitisation temperature. The internal stresses are tensile in the radial direction, causing the particle to split into the characteristic onion skin morphology, and compressive in the tangential direction. The consequent stress relief means that the filler/binder interface is under compression, hence a crack is more likely to join with internal porosity. These fracture mechanisms are initiated by microcrack formation at low stress, typically in regions of well arranged binder or at a pore acting as a suitable stress concentrator [66].

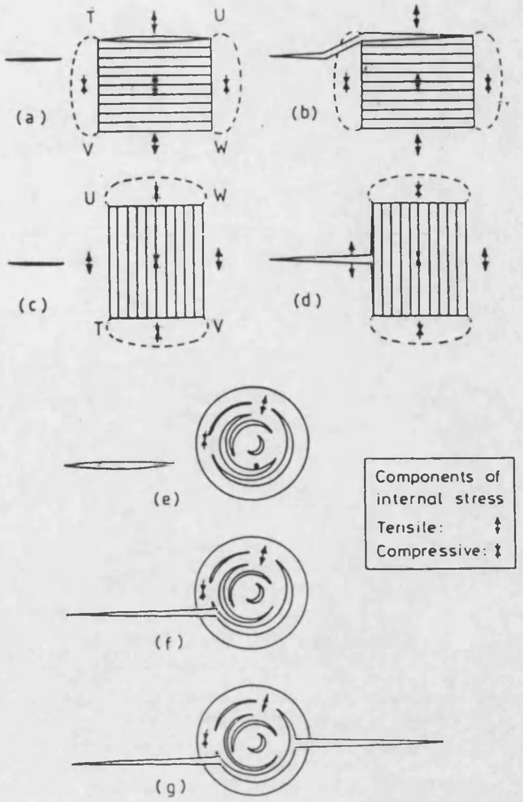

Figure 2-15 : Schematic illustration of the interactions of subcritical cracks with needle coke filler particles (a-d), and gilsocarbon filler particles (e-f) [66].

On oxidation, the reported decrease in strength with increasing porosity (see section 2.3.1) could be accounted for by a combination of an increase in critical flaw size and a decrease in fracture toughness, or subcritical crack growth. However, the decrease in strength is reported to be [51] matched by a very similar decrease in K_{IC}, therefore there need not be any increase in flaw size. Pickup *et al* [67] determined the effective surface energy required for crack propagation, γ_s, for thermally oxidised IM1-24 graphite and found that it did not change significantly with weight loss. From linear elastic fracture mechanics, strength, $\sigma_f = \frac{1}{Y}\left(\frac{K_{1C}}{c^{\frac{1}{2}}}\right)$ where Y is a geometrical factor. The Griffith equation gives $\sigma_f = \frac{1}{Y}\left(\frac{2E\gamma_s}{c}\right)^{\frac{1}{2}}$, hence $K_{1C} = 2E\gamma_s$. Consequently the change in modulus is the dominant factor controlling strength, which is consistent with the observation that strength and modulus vary in the same way (section 2.32). During the study it was apparent that there was no change in fracture mechanism caused by oxidation.

2.4.1 Fracture models

Rose and Tucker [68] considered the approach of Buch [56] assuming graphite to consist of discrete particles each with an easy cleavage direction. If the stress on any particle is sufficient it fails, so under appropriate loading, cracks link up to form a critical flaw which then propagates according to linear elastic fracture mechanics. The input parameters to their model are fracture toughness, particle size, particle cleavage stress and percentage porosity which is represented by particles of zero cleavage stress. The model extends the approach of Buch to the non uniform loading situations of three and four point bend, obtaining reasonable correlation with experimental results. However the model tends to under predict the failure probability at low stresses [69] which is largely due to the limited microstructural information required by the model. Predictions were improved for bend tests by including a measured particle size distribution in the model. The Rose-Tucker model was also assessed against a variety of criteria (shown in Figure 2-16) along with a number of other models [70]. The critical strain criterion and critical stress criterion were found in general to be rather poor (see Figure 2-16). The Weibull model provided good predictions for effects relating to the geometry of the system rather than those relating to the microstructure, but was on the whole inferior to the Rose-Tucker model (see Figure 2-16).

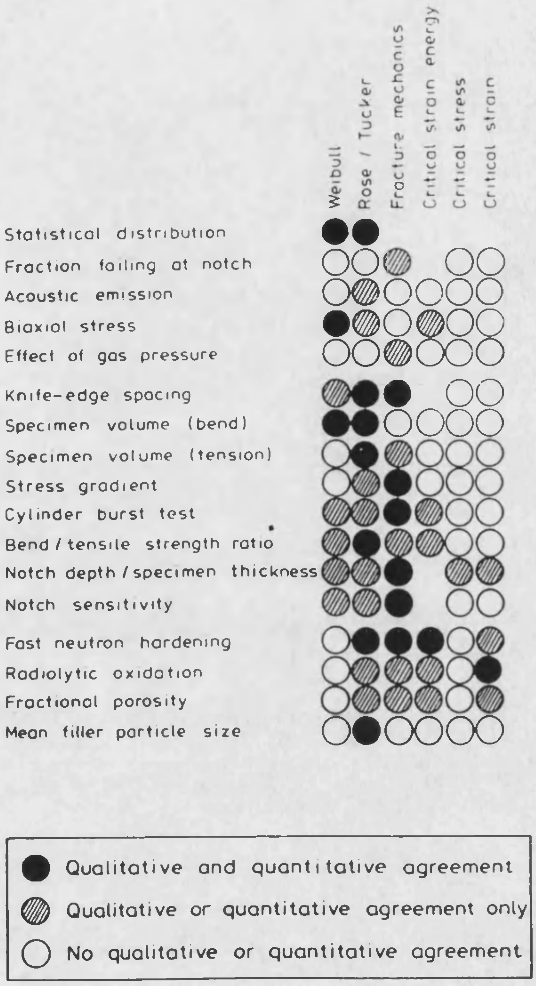

	Weibull	Rose / Tucker	Fracture mechanics	Critical strain energy	Critical stress	Critical strain
Statistical distribution	●	●				
Fraction failing at notch	○	○	▨		○	○
Acoustic emission	○	▨	○	○	○	○
Biaxial stress	●	▨	○	▨	○	○
Effect of gas pressure	○	○	▨	○	○	○
Knife-edge spacing	▨	●	●		○	○
Specimen volume (bend)	●	●	○	○	○	○
Specimen volume (tension)	○	●	▨	○	○	○
Stress gradient	○	▨	●	○	○	○
Cylinder burst test	▨	▨	●	▨	○	○
Bend / tensile strength ratio	▨	●	▨	▨	○	○
Notch depth / specimen thickness	▨	▨	●		▨	▨
Notch sensitivity	▨	▨	●		○	○
Fast neutron hardening	○	●	●	●	○	▨
Radiolytic oxidation	○	▨	▨	▨	○	●
Fractional porosity	○	▨	▨	▨	○	▨
Mean filler particle size	○	●	○	○	○	○

● Qualitative and quantitative agreement
▨ Qualitative or quantitative agreement only
○ No qualitative or quantitative agreement

Figure 2-16 : The effectiveness of six fracture models [70].

The model was further extended by Tucker and McLachlan [71] to describe stress related physical properties other than fracture, such as strain hysteresis and acoustic emission. The fracture predictions did not improve significantly, however predictions of notch sensitivity and acoustic emission were improved. Burchell [72] developed the model further based on the same principles, but incorporating more microstructural information in the form of filler particle size distribution, pore size distribution, average pore area and the pore density. The model was then validated with experimentation on a range of graphites from a very fine textured Poco graphite to an extremely coarse electrode graphite.

2.5 Fast neutron irradiation of graphite.

Fission of uranium isotopes produces neutrons in a range of energies from less than 1MeV to greater than 10MeV, with an average of 2MeV [73]. The role of a graphite moderator is to slow fast neutrons down to the thermal energies by a series of collisions with carbon nuclei. In a collision, a substantial amount of energy is transferred to the carbon nucleus which is generally displaced within the lattice as the binding energy is only about 5eV. The energy required to permanently displace a carbon atom has been measured at 25 - 60eV so many atoms are displaced [2], not just by neutron collisions, but also by secondary collisions with recoiling carbon atoms.

In a peak rated AGR reactor, each carbon atom is displaced on average 20 times during the reactor's life [73]. A large quantity of vacancies and interstitials are created, many of which quickly recombine, annihilating each other. A balance is reached between the rate at which atoms are displaced (neutron flux) and the mobility of the defects (temperature). Below about 300°C interstitials are sufficiently mobile to allow them to form groups of around four atoms which expand the lattice perpendicular to the basal plane [2] causing large strains locally (see Figure 2-17). The accompanying vacancies are far less mobile, but when several are formed adjacent to each other the lattice collapses, contracting the basal plane. The energy stored around these defects at low temperatures is known as Wigner energy, and is released as heat when the defects are annealed out. Above 300°C, which is the temperature range relevant to an AGR, the interstitials are so mobile that they aggregate into new areas of graphitic sheet (see Figure 2-17). So in effect the irradiation redistributes the carbon atoms shrinking the basal planes and inserting new ones, giving expansion in the c-axis and contraction in the a-axis.

These single crystal effects manifest themselves in the polycrystalline graphite (IM1-24) in an AGR, by first causing the graphite to shrink in both directions even though the single crystals are deforming with no significant volume change [73]. The reason for this is that the expansion is taken up by porosity. So, once the porosity has closed, the expansion is observed as the crystallites gradually jack the structure apart creating new porosity. The point at which this occurs is known as shrinkage turnaround and will occur towards the end of a reactor's life (Figure 2-18).

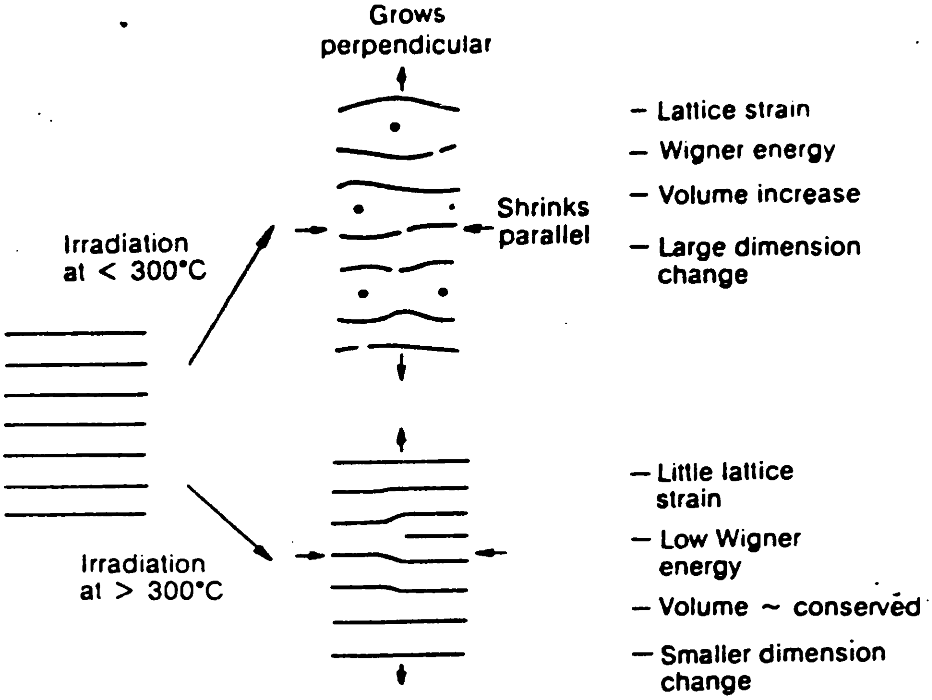

Figure 2-17 : Effect of Irradiation temperature on graphite lattice damage [2].

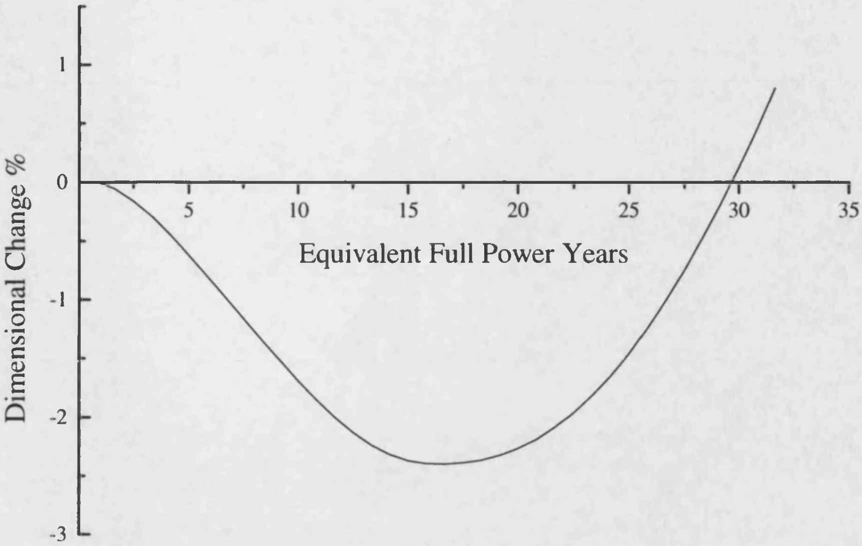

Figure 2-18 : Diagram showing shrinkage turnaround for an AGR (plotted using data for 550°C).

The distortion in the lattice markedly effects the deformation behaviour of polycrystalline graphite. The stress-strain curve becomes more linear, the strength and modulus are greatly increased and the strain to failure is significantly reduced [74]. This was confirmed in later research [75] and is illustrated well in Figure 2-19. On annealing the Young's modulus returned almost to its original value and the hysteresis losses increased again. However at very high doses the elastic constants will fall to a very low value, but this is associated with turnaround and enormous amounts of pore generation. There are two distinct mechanisms involved in these changes [76]; firstly the pinning of dislocations and secondly the change in the elastic constants of the crystals because of the large deformation of the lattice below 300°C. Work on highly oriented pyrolytic graphite demonstrated the rapid increase in elastic constants due to pinning of dislocations, while at lower temperatures the elastic constants determined by the interlayer spacing declined dramatically due to the lattice distortion.

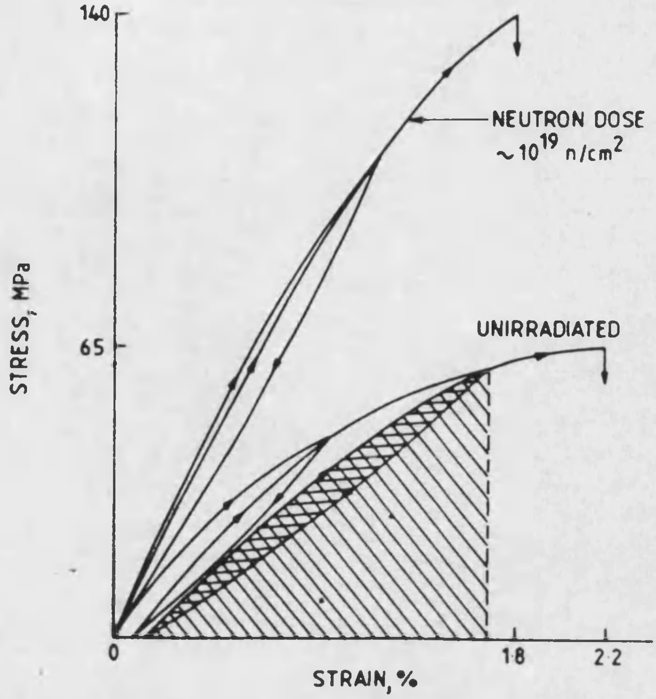

Figure 2-19 : The effect of neutron irradiation on the compressive stress-strain curve for graphite [75].

In reality the mechanical properties of a graphite moderator are determined by a combination of irradiation effects that initially increase the strength and modulus, and radiolytic oxidation that reduce them.

2.6 Chapter Summary

The general manufacturing route in which a pitch binder is combined with a coke filler is common to all the graphites studied here. However, there are specific requirements for the nuclear industry that must be addressed, particularly the purity and isotropy of the graphite.

The mechanical properties of polycrystalline graphite vary greatly; the compressive strength lies between 30 and 200MPa, while the modulus will vary from 5-25GPa. The stress-strain curve is also markedly non-linear and on unloading, a large degree of hysteresis and permanent set are evident. These characteristics are perhaps nearer to those of concrete than those of engineering ceramics.

The severe environment within the core of a nuclear reactor will affect the mechanical properties of the graphite in a number of ways. The temperatures experienced are unlikely to be high enough to have any significant effect on the mechanical properties of graphite. Pre-stressing has been found to reduce the Young's modulus of graphite, which may be of interest to this work, as any samples removed from the core of an AGR are effectively pre-stressed in one axis due to irradiation induced shrinkage. The aspects of reactor environment that have the greatest effect on the mechanical properties of graphite are oxidation by the CO_2 coolant and the effects of fast neutron irradiation on the graphite lattice. Carbon monoxide and methane inhibit oxidation when added to the CO_2 coolant, but some oxidation will always occur. Oxidation causes a severe reduction in strength, σ, which can be described by the equation, $\sigma = A\exp(-be)$, where A and b are constants and e is the fractional porosity. The strain at failure remains approximately constant regardless of the level of oxidation, providing that it is uniform throughout the sample. Thus the modulus will decrease with increasing oxidation in the same manner as the strength. The irradiation of graphite causes substantial damage to the lattice giving rise to dimensional changes and an increase in the mechanical properties in the early part of reactor life.

3. Blunt Indentation

In the past blunt indentation of homogeneous brittle solids such as glass, has been extensively studied. The fracture mode has been well characterised and methods of obtaining fracture toughness values have been established. However it is only relatively recently that the technique has been used on polycrystalline ceramics like alumina, silicon nitride and silicon carbide. The mode of fracture changes markedly when the microstructure is varied so the stress field must be considered in detail. Only then do the reasons for the change in fracture morphology become apparent. In this work the principles of blunt indentation have been used to test polycrystalline graphite for the first time.

3.1 The Stress Field Beneath a Spherical Indenter.

The first successful analysis of an elastic contact problem was by Hertz in 1882, and originated from his work on the optical interference fringes between two glass lenses. This work was concerned with the possible influence of elastic deformation caused by the contact pressure between the lenses on the observed pattern of interference fringes. Hertz hypothesised that in general the contact was elliptical and went on to make the simplification, that the two solids could be treated as an elastic half space loaded on a small region of its surface. In order for this simplification to be justified the contact area must be small compared to the dimensions of the body and the relative radii of curvature of the surfaces. This means that the body must be considered to be semi-infinite so that the stress field is contained within it and not perturbed by any edges. The second condition ensures that the surface outside the contact approximates to the surface of the half space and that the strains are within the elastic range of the material. Lastly, the surfaces are considered to be smooth, i.e. frictionless so only a normal pressure is transmitted between them. Hence normal displacements are taken to act parallel to the Z

- axis and tangential displacements act in the X - Y plane (see Figure 3-1). If the problem is now considered as the contact of two spheres the Hertz equations can be obtained [77].

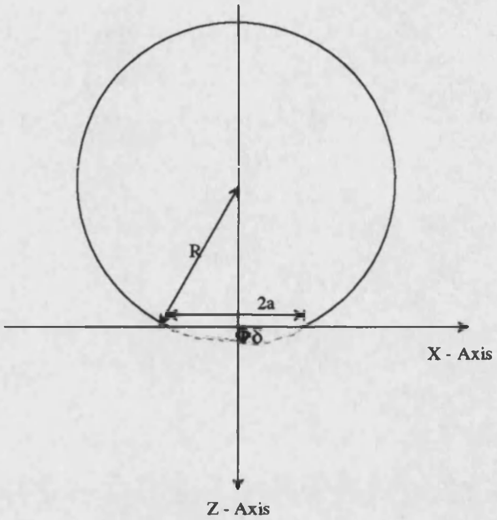

Figure 3-1: An elastic sphere pressing on a semi-infinite elastic slab.

Hertz Equations

Radius of the contact circle, $a = \left(\dfrac{3PR}{4E^*}\right)^{1/3}$ 3.1

Maximum distance compressed, $\delta = \dfrac{a^2}{R} = \left(\dfrac{9P^2}{16RE^{*2}}\right)^{1/3}$ 3.2

Maximum pressure, $P_0 = \dfrac{3P}{2\pi a^2} = \left(\dfrac{6PE^{*2}}{\pi^3 R^2}\right)^{1/3}$ 3.3

where P = load, R = radius and $\frac{1}{E^*}=\frac{1-\nu_1^2}{E_1}+\frac{1-\nu_2^2}{E_2}$, where E_1 and ν_1 are the Youngs modulus and the Poissons ratio of the substrate respectively, while E_2 and ν_2 refer to the sphere.

However calculating a complete stress distribution is no trivial matter. Hertz's original attempt was partly conjectural and was later found to be erroneous in some of its features. Huber (1904) managed to obtain closed solutions for the contact of two spherical surfaces, but the mathematics is still far from simple to evaluate. Morton and Close [78] also evaluated the stress distribution in two dimensions using a different method, although the authors note that their solution is no simpler than that of Huber. Figure 3-2 shows the variation of the stresses in the surface of an elastic half space indented with an elastic sphere, plotted using equations given by Johnson [77]. As would be expected the Z-axis stress is always compressive and is at a maximum directly beneath the indenter decaying to zero at the edge of the contact. A more important feature is that the radial stress in the surface becomes tensile reaching a maximum at the edge of the contact (the implications of this will be discussed in more detail in a Chapters 7 and 8).

More recently a number of researchers have presented three dimensional solutions to the Hertzian problem. Sackfield and Hills [79] have put forward a general solution allowing for elliptical contacts, which is of interest since, if there is any lateral movement as in a bearing, an elliptical contact is created. They then present a solution in closed form for the special case of a vertical plane of symmetry, i.e. when the contact is circular. However, although the problem is now formulated so as to be two dimensional, the solution still involves evaluating elliptic integrals. Zeng *et al* [80] presented a solution in closed form to the problem in cylindrical co-ordinates for a spherical contact. As the problem is axially symmetric, it reduces to what is essentially a two dimensional problem. Using the given solutions the principal stresses at any point within the solid can be readily calculated. However, when the relevant limits are applied to obtain the stresses in the surface, the solutions do not give the expected values, which casts doubt on the validity of their approach. Similar problems are evident in work by other researchers [81] researchers [81] where the stresses within the contact area appear reasonable, but outside the contact the solutions seem inadequate. Explicit solutions for the stress beneath a sliding spherical contact are given by Hamilton [82], which can be used to calculate full stress distributions at any point beneath the surface. When limits are applied to obtain stresses in the surface, the distribution shown in Figure 3-2 is obtained.

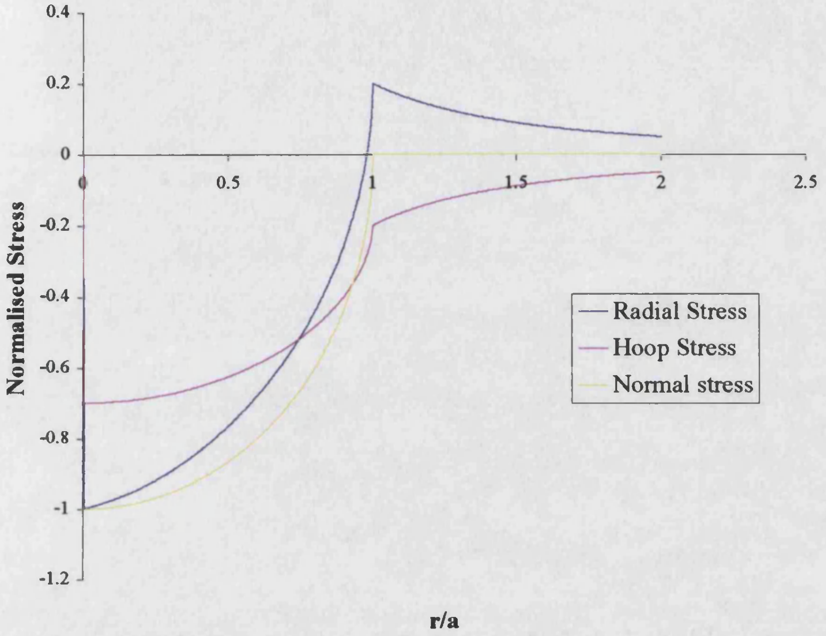

Figure 3-2 : The variation of the surface stresses beneath a Hertzian contact, calculated from equations given by Johnson [77]. The stresses are normalised by dividing them by the maximum stress P_0, r is the radial distance from the centre and a is the contact radius.

There are a number of limitations to the Hertz theory which have been mentioned earlier, one of which being that the radius of the contact should be small compared to the radius of the indenting sphere. However the solutions are commonly applied to a sphere indenting a flat plate for which this limitation does not necessarily hold. Errors in the Hertz solution have been considered by Yoffe [83] for a rigid indenter pressed against a flat surface of an elastic half space. Near the Z-axis the Hertzian displacements give a good fit of the deformed surface to the radius of the sphere.

However as the Hertzian displacements define a parabola, the fit diverges from a sphere as the radial distance from the centre of the contact increases. This error has been accounted for by combining the solution with a second elastic field, and hence extending the ability to use the Hertz equations beyond the original range.

A series of rigid indenters with different profiles pressed on to an elastic half space were considered by Sneddon [84]. For the case of indentation by a sphere, expressions relating indentation depth and load to the radius of contact are given, however they produce apparently unrealistic results. Bunzai [85] also analysed the elasticity problem for a rigid sphere pressed on to the plane surface of a semi-infinite elastic solid, for both smooth and rough indenters. The solutions are considerably more complex than those given by Sneddon and expressions are given for the stresses along the surface in polar co-ordinates. However the radial stress component seems not to predict any tensile forces at the edge of the contact which is unlikely.

Despite all of this work with these models, all of the analytical solutions mentioned are based on the solid being purely elastic and homogeneous, which produces considerable problems when trying to use them in many real systems. A potential solution is to use finite element analysis to predict the contact stresses beneath the indenter. Elastic analysis is relatively straight forward although there are a number of non linear models capable of dealing with porous media [86], which have been incorporated into many finite element packages. There are however limitations to finite element analysis; great care must be taken to achieve a correct representation of the test geometry, and good quality experimental data is required.

3.2 Hertzian Fracture

Indentation techniques have historically been used to measure hardness, but have more recently found use as a method of measuring fracture toughness [87]. Fracture under a blunt indenter is particularly sensitive to surface finish for reasons that will be discussed below, but it is often very difficult to determine the critical load. This means that it is often difficult to use blunt indentation in the measurement of fracture toughness, although a number of researchers have worked in this area [88] [89] [90]. Other limitations are, that for the Hertzian solution to apply, the material must behave elastically up to the point of fracture, and the indentation depth must be small in comparison to the sphere radius in order for the assumption of a planar contact to be valid. For these reasons glass has been the subject of many experimental studies on blunt indentation, and being transparent, it allows the cone crack to be easily seen as in Figure 3-3.

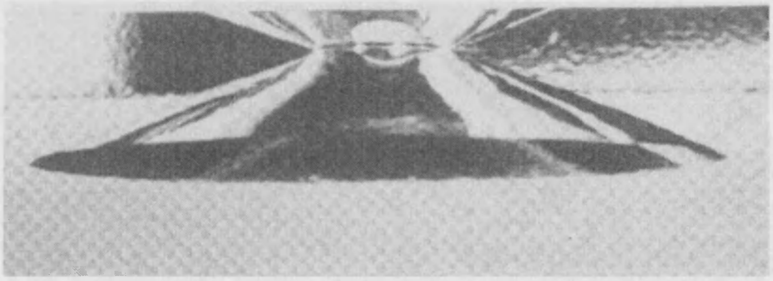

Figure 3-3 : Blunt indentation of glass showing a cone crack [91].

As a spherical indenter is pressed onto the surface of a homogeneous elastic material, for example glass, the stress field develops in the manner discussed in the previous section. Hence pre-existing surface flaws are subjected to tensile stresses outside the contact zone Figure 3-4(i) [92]. When a critical stress is reached fracture is initiated from a surface flaw and propagates around the contact circle to form a shallow ring crack which is shown in cross section in Figure 3-4(ii). On further loading the crack propagates incrementally downwards orthogonally to the maximum tensile stress Figure 3-4(iii);

at another critical stress the crack becomes unstable and rapidly propagates into the full Hertzian cone Figure 3-4(iv). On further loading the cone continues to increase in size in a stable manner until the contact expands to cover the ring crack Figure 3-4(v). The cone will then close on unloading Figure 3-4(vi).

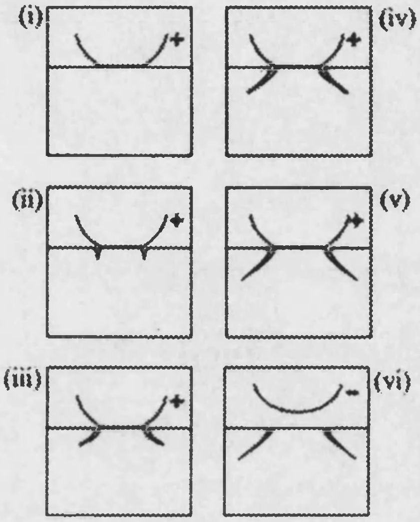

Figure 3-4 : Evolution of the radial crack system during a blunt indentation load cycle [92].

3.2.1 *Auerbach's Law*

In 1891 Auerbach [93] demonstrated experimentally that for small indenters the failure load is is directly proportional to the indenter radius (Auerbach's law). Over the years Auerbach's law has been shown to apply to a wide range of materials. However, assuming that a cone crack is initiated from a pre-existing surface flaw somewhere close to the region of maximum tensile stress, the Griffith equation (see page 35) can be used to calculate the critical stress at which the surface flaw spontaneously propagates. Using Hertzian mechanics the maximum tensile stress, σ_m, can be calculated from

$\sigma_m = \frac{1}{2}(1-2\nu)P_{av}$, where P_{av} is the average Hertz pressure, $\frac{P}{\pi a^2}$. At the point of fracture the maximum tensile stress is equal to the critical fracture stress [94], thus $\frac{1}{2}(1-2\nu)P_{av} = \sqrt{\frac{2E\gamma}{\pi c}}$. P_{av} can be expressed by the more easily measurable parameters P and R by eliminating a from equation 3.1 and the equation for the average Hertz pressure. By rearranging the equation $\frac{P}{R^2} = Qc^{-3/2}$ is obtained where Q represents the materials properties. Thus Hertzian mechanics predict the failure load to be proportional to the indenter radius squared [94], contrary to Auerbach's law.

Some very detailed experimental work has been performed using glass [95] to try and reconcile Auerbach's law with the results predicted by Hertzian mechanics. It was found that while Auerbach's law applied to small indenters, the Hertzian prediction applied to large ones. It was suggested that this might be a consequence of the statistical nature of brittle strength, although no experimental data has been presented in support of this [95]. Roesler [96] disagreed with this hypothesis on the grounds that, as a small indenter samples a smaller area than a large indenter there is less chance of finding a critical flaw. Thus the scatter in results should be greater for a small indenter, which is not the case. It is also hard to believe that the statistics of the flaw distribution on different materials could always lead to such a simple law.

Frank and Lawn [97] explained Auerbach's law in terms of four crack lengths, c_0, c_1, c_2, c_3, corresponding to stationary values in energy; c_0 and c_2 represent critical unstable crack lengths which decrease with increasing load while c_1 and c_3 represent critical stable crack lengths which increase with increasing load. So with small indenters c_0 soon becomes less than pre-existing flaws and a shallow ring crack of depth c_1 is produced, then as the load is increased c_1 increases until it reaches c_2 which allows fast propagation into a full cone crack, c_3. This fits with Auerbach's law and observed behaviour. For large indenters c_1 and c_2 merge and disappear before c_0 exceeds the pre-existing flaws, hence the Hertzian condition is realised. Lawn [98] later used these principles to obtain information on the fracture surface energy of single crystals.

3.2.2 The Effect of Elastic Mismatch

The effect of the elastic constraints of the indenter and substrate can be readily explained in qualitative terms. When a sphere is pressed into the surface of a plate both surfaces will move tangentially in a radially inward direction by amounts (excluding the effects of friction) that are proportional to the value of $(1-2\nu)/G$, where G is the shear modulus [99]. So a hard indenter will move inwards by a small amount compared to the more compliant substrate, hence the net effect is that the substrate moves radially inwards (see Figure 3-5). Thus in a real situation friction acts radially outwards on the more compliant surface and inwards on the more rigid one. This modifies the radial tensile stress outside the contact, reducing it in the more compliant solid and increasing it in the rigid one. Hence the values for the tensile stress are over estimated by the Hertz equations for a solid indented with a hard sphere. More importantly, the position of the maximum tensile stress occurs further out than predicted by Hertzian analysis, which explains the observation that ring cracking occurs outside the predicted region of maximum stress. This explanation is supported experimentally and is consistent with the suggestion that fracture initiates from pre-existing flaws, although in all cases the fracture was concentric as opposed to Frank and Lawn's [97] suggestion that the fracture is eccentric. Warren and Hills [100] follow a very similar line of reasoning to Johnson *et al* and their work centres on trying to maximise the tensile stresses in the surface in order to initiate cracking. With the aim of enabling the indentation test to be used to measure fracture toughness on a wider range of ceramics. The work demonstrates that an indenter more compliant than the substrate will give rise to greater tensile stresses because of the perturbation of the stress field by shear tractions within the substrate.

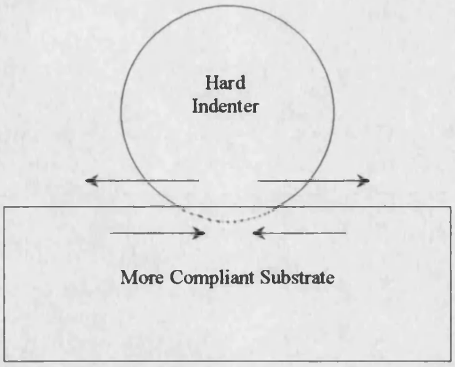

Figure 3-5 : Shear tractions caused by the elastic mismatch between sphere and indenter.

3.3 Blunt Indentation of Polycrystalline Ceramics

The blunt indentation of homogeneous brittle materials such as glasses has been extensively researched over the years (some of which has been reported in the previous sections), but more recently there has been considerable interest in the indentation of structural ceramics. Increasingly, these ceramics are being used in bearings and valves as well as in many other applications where they are likely to be subjected to highly concentrated contact stresses. Individual cracks may be initiated from either pre-existing surface flaws, as with classic Hertzian fracture, or from precursor plastic deformation [101]; furthermore, the nature of the fracture is controlled by events at a microstructural level.

Several researchers [101,102,103] have investigated the effect of microstructure on the blunt indentation fracture of various polycrystalline ceramics. In most cases it was found that subsurface damage preceded any Hertzian cracking. However, as the microstructure becomes finer (sub-micron) Hertzian cracking becomes more evident and the propensity to sub-surface damage is reduced. Figure 3-6 shows the increasing damage zone in silicon nitride as greater loads are applied. Two immediately apparent features are the shape of the damage zone, and the fact there is little or no damage near to the surface (indentations were made at the top of each micrograph, so the view is of a cross section through the damage zone). In a similar study on alumina [98] evidence of shear faulting within the alumina grains was found within the damage zone on all the materials tested, which ultimately causes the development of microcracks. If the net shear stress, acting on the fault plane is defined as $S = |\tau_F| - \mu|\sigma_F|$ where τ_F = local shear stress and σ_F = local compressive stress, the distribution of S can be plotted for varying friction coefficients, μ, [102] (Figure 3-7). So it seems likely that the drop shaped region of damage is caused by shear stresses giving rise to microcracking. As compression is constantly acting on the shear faults there must be some element of friction, hence an area of hydrostatic compression will be present. It is therefore likely that the region of limited damage near the surface corresponds to an area of hydrostatic compression, effectively holding the material together, which will vary in size and shape depending on internal friction.

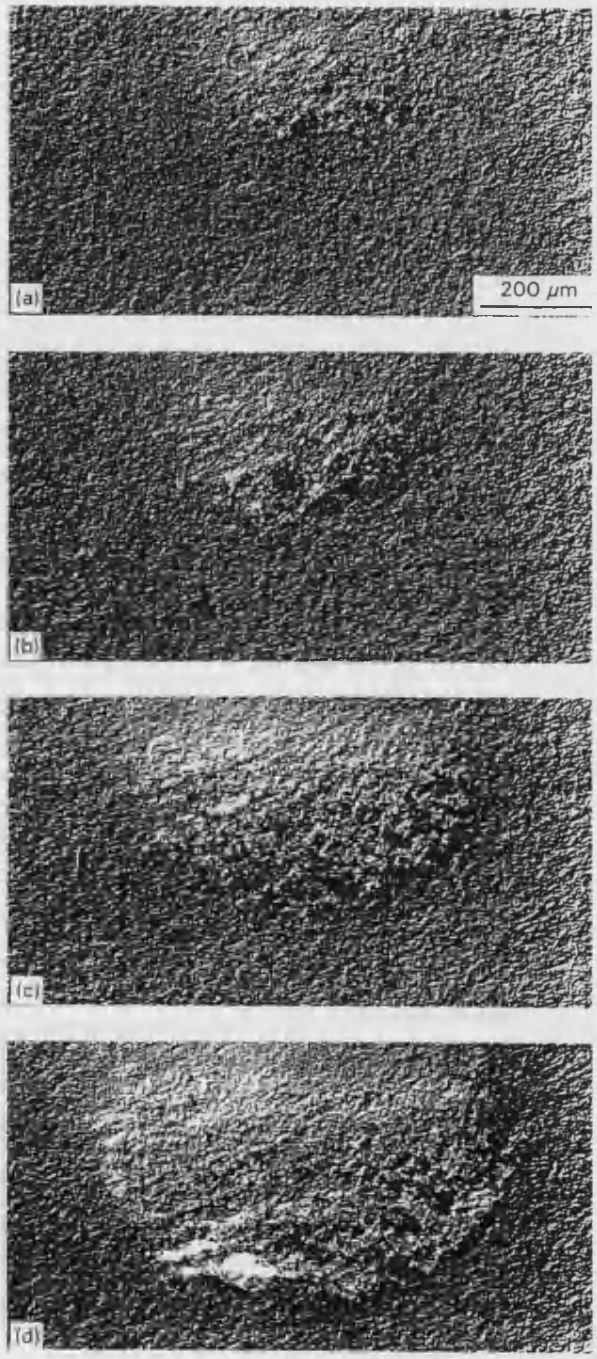

Figure 3-6 : Optical micrographs in Normaski interference illumination showing cross sections of single cycle Hertzian contact damage in coarse grained silicon nitride, for indentation loads: (a), 1500 N, (b) 2000N, (c) 3000N and (d) 4000N [102].

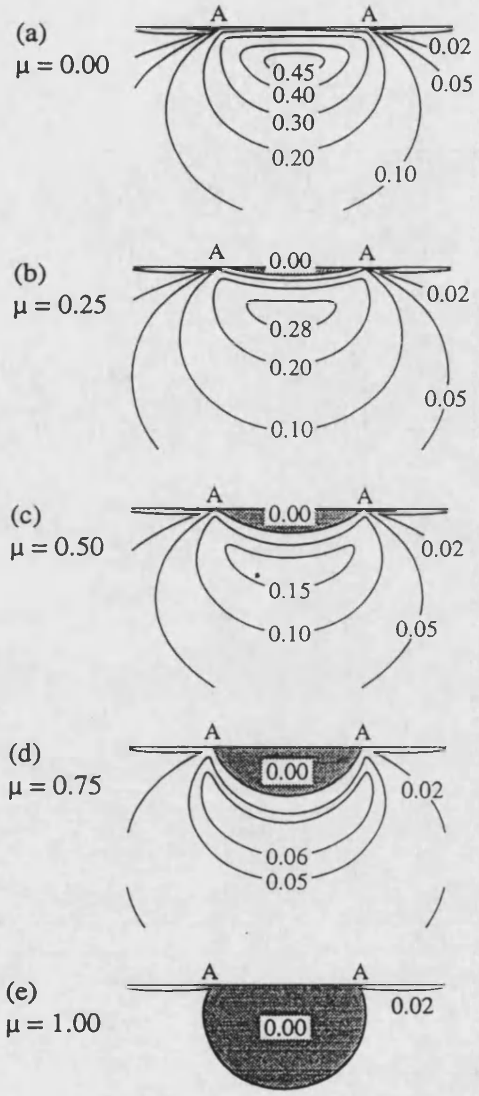

Figure 3-7 : Contours of net shear stress S for different coefficients of friction and a Poisson's ratio of 0.29 [103].

Researchers [101], [102] noted that as the grain size of a ceramic was increased, the tendency for a shear damage zone to form rather than a Hertzian cone crack was greatly increased. There are essentially two factors controlling what is effectively a brittle ductile transition [102]. Larger grain sizes will suppress Hertzian fracture by increasing the deflection of the downward propagating crack from the maximum local tensile stress.

Larger grain sizes also enhance the likelihood of subsurface microfracture as the stress concentration at the edge of the shear fault will be increased.

Guiberteau *et al* [104] and Cai *et al* [105] demonstrated the existence of cyclic fatigue in polycrystalline ceramics beneath a blunt indenter. In both cases marked hysteresis on load cycling showed that the fatigue has a strong mechanical component, which is due primarily to the formation of a subsurface damage zone as previously discussed. With increasing numbers of load cycles an increase in both quantity and intensity of surface and subsurface damage was clearly visible.

Models for both micro-crack initiation and the brittle-ductile transition have been developed in order to account for some observed trends. Lawn *et al* [106] developed a model for microcrack initiation based on experimental work carried out on alumina. The model assumes the existence of a shear fault and then considers it in terms of a detailed stress intensity analysis, which continues to explain the observed effects of microstructure. It is possible that the model may be applicable to a more complex multiphase system, although, in general, slip occurs at some weak interface rather than a shear fault across a grain.

Mouginot [107] calculated a critical indenter size below which shear deformation would preceed Hertzian cracking, which is effectively a measure of the brittle to ductile transition. This was achieved by equating the critical load for cone crack initiation with the critical load for permanent deformation in an elastic plastic material, defined as J_2 by Hamilton [82]. Again this proposal has limitations as the model is based on equations for elastic solids and the Von Mises criterion, and the deformation clearly shows the materials are not elastic.

3.4 Chapter Summary

The stress field produced in an elastic solid when indented with a hard sphere can be calculated using Hertzian mechanics. This demonstrates the existence of a hemispherical shear zone beneath the indenter, and tensile stresses which reach a maximum in the surface of the substrate just outside the edge of the contact area.

When glass is indented with a hard sphere fracture is initiated from a pre-existing flaw by the tensile stresses in the surface at the edge of the contact area. The crack propagates around the contact area forming a ring, but only penetrates a short distance into the surface of the substrate owing to the rapidly diminishing tensile stress field. As the load is increased the crack continues to propagate orthogonally to the maximum tensile stress forming a classical Hertzian cone crack.

When a polycrystalline ceramic is indented with a sphere the damage produced is very different to the classical Hertzian cone crack. A hemispherical damage zone, that is attributed to shear, is produced beneath the indenter before there is any evidence of long range cracking. Both the type and degree of damage are markedly effected by the microstructural scale. For very small grain sizes there is little shear damage evident, and cone cracking is more likely to occur than in a coarser ceramic. As the grain size is increased the size and intensity of the shear damage zone increases.

4. Materials

A number of graphites produced by various manufacturers were used in order to investigate a range of different microstructures. All the graphites, except those produced by Poco Graphite Inc. were manufactured from a filler and a binder using processes similar to the standard method outlined in section 2.1. The Poco graphites are still produced using a filler and binder, but because of their extremely fine microstructure (see Figure 4-1and Figure 4-2) the processing route is likely to differ from that outlined in section 2.1.

This chapter presents brief mechanical data for the graphites used, taken from manufacturers data sheets in all cases except IM1-24 where the sources are referenced. These data illustrate the range of mechanical properties of the graphites used in this work.

Figure 4-1 to 4-8 show polarised light micrographs of the graphite microstructures which vary greatly depending on the size of the raw materials used, as well as the processing methods. However, it becomes increasingly difficult to discern the components of the microstructure as the texture becomes finer. For Poco ZXF graphite only one solid phase can be detected. In general the mechanical properties improve as the scale of the microstructural features is reduced. This is particularly so in the case of the strength which increases markedly on the reduction of pore size, as would be expected.

4.1 Mechanical Properties of Graphites

Graphite : ZXF-5Q
Manufacturer : Poco Graphite Inc.
Forming process : Isostatic moulding

Density (g/cc)	1.80
Average Particle Size (μm)	1
Average Pore Size (μm)	0.2
Total Porosity (%)	20
Flexural Strength (MPa)	115
Tensile Strength (MPa)	90
Compressive Strength (MPa)	195
Modulus (GPa)	14.5

Manufacturers data.

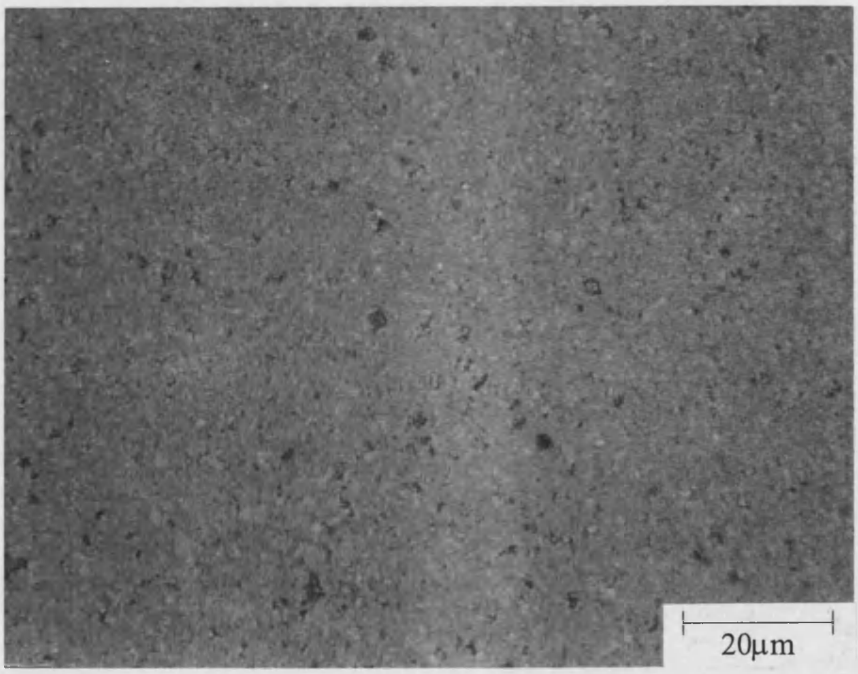

Figure 4-1 : Polarised light optical micrograph of Poco ZXF-5Q graphite.

Graphite : AXF-5Q
Manufacturer : Poco Graphite Inc.
Forming process : Isostatic moulding

Density (g/cc)	1.80
Average Particle Size (μm)	5
Average Pore Size (μm)	0.8
Total Porosity (%)	20
Flexural Strength (MPa)	90
Tensile Strength (MPa)	65
Compressive Strength (MPa)	145
Modulus (GPa)	11

Manufacturers data.

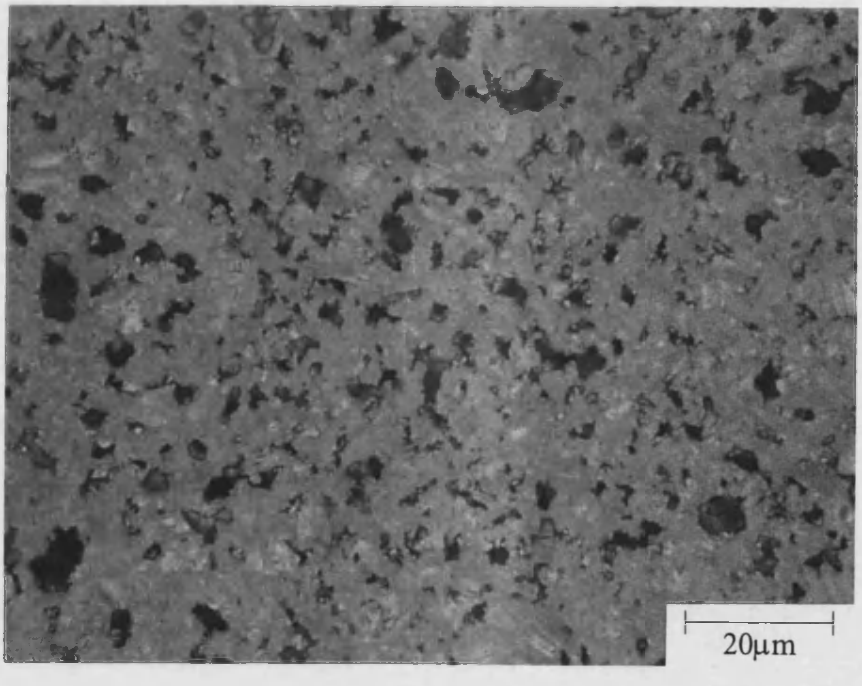

Figure 4-2 : Polarised light optical micrograph of Poco AXF-5Q graphite.

Graphite : EY306
Manufacturer : Morganite Special Carbons
Forming process : Moulded

Density (g/cc)	1.80
Average Particle Size (µm)	10
Helium Porosity (%)	14
Flexural Strength (MPa)	60
Tensile Strength (MPa)	34
Compressive Strength (MPa)	110
Modulus (GPa)	13.5

Manufacturers data.

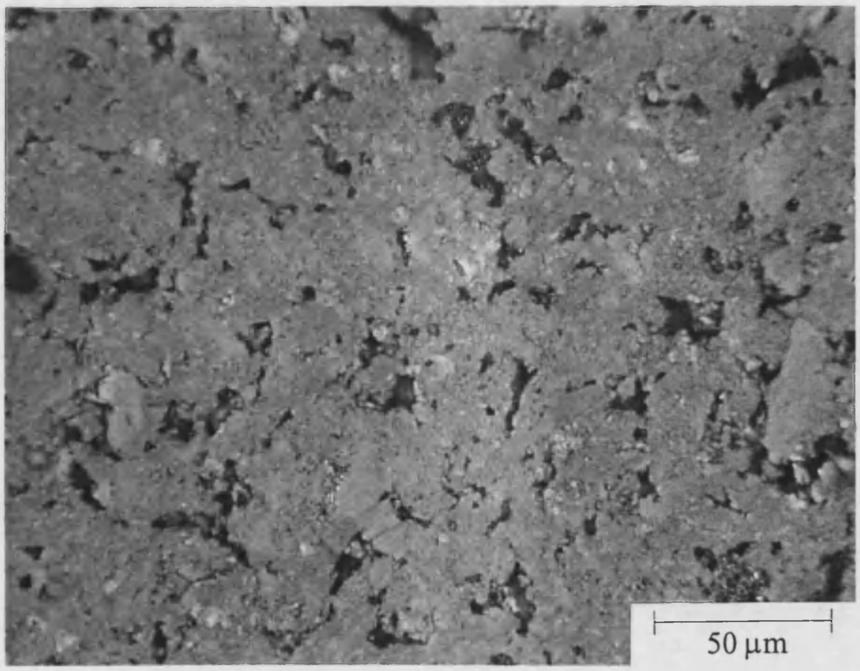

Figure 4-3 : Polarised light optical micrograph of EY306 graphite.

Graphite : ATJ
Manufacturer : UCAR
Forming process : Iso-moulded

Density (g/cc)	1.76
Average Particle Size (μm)	25
Helium Porosity (%)	14
Flexural Strength (MPa)	29.5
Tensile Strength (MPa)	25.5
Compressive Strength (MPa)	67
Modulus (GPa)	9.6

Manufacturers data.

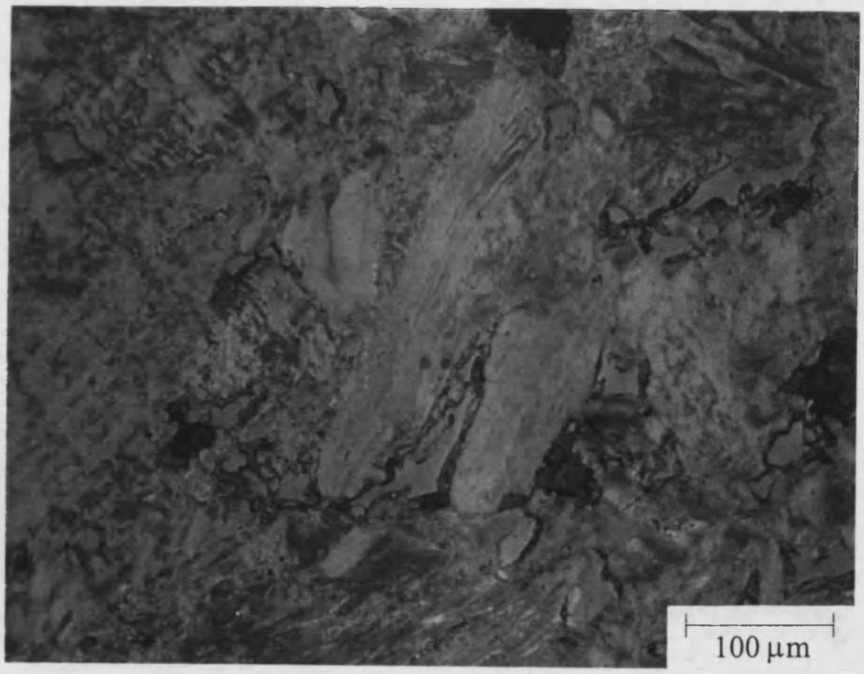

Figure 4-4 : Polarised light optical micrograph of ATJ graphite.

Graphite : SF53

Manufacturer : UCAR

Forming process : Extrusion

Orientation	Parallel to extrusion axis	Perpendicular to extrusion axis
Number of Impregnations	0	
Density (g/cc)	1.59	
Average Particle Size (µm)	150	70
Helium Porosity (%)	25	
Flexural Strength (MPa)	18	8
Tensile Strength (MPa)	13	5
Compressive Strength (MPa)	31	-

Manufacturers data.

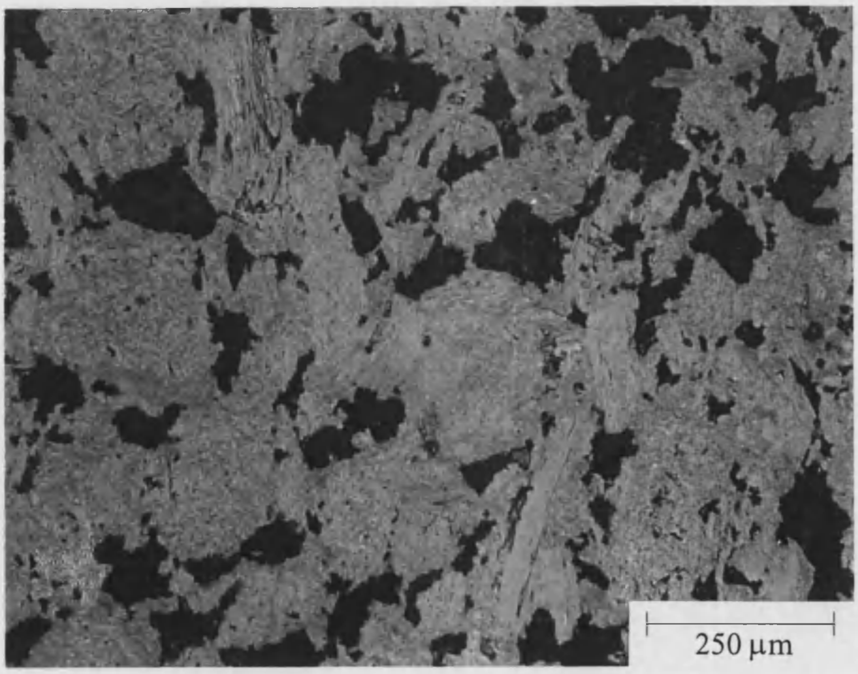

Figure 4-5 : Polarised light optical micrograph of SF53 graphite.

Graphite : FGE

Manufacturer : UCAR

Forming process : Extrusion

Orientation	Parallel to extrusion axis	Perpendicular to extrusion axis
Number of Impregnations	1	
Density (g/cc)	1.7	
Average Particle Size (μm)	150	70
Helium Porosity (%)	20	
Flexural Strength (MPa)	22	13.5
Tensile Strength (MPa)	17.5	8
Compressive Strength (MPa)	45	-

Manufacturers data.

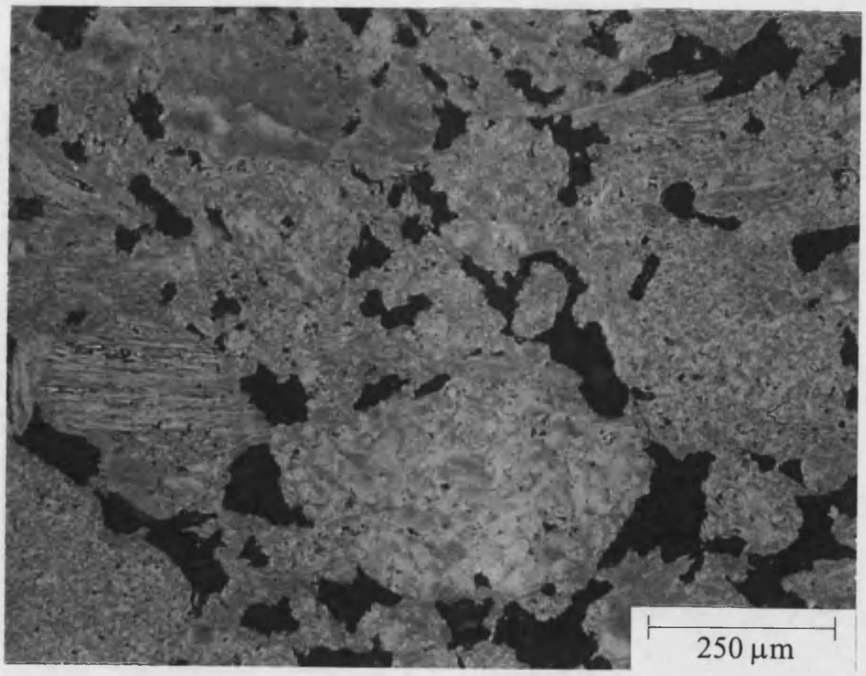

Figure 4-6 : Polarised light optical micrograph of FGE graphite.

Graphite : FGEX

Manufacturer : UCAR

Forming process : Extrusion

Orientation	Parallel to extrusion axis	Perpendicular to extrusion axis
Number of Impregnations	2	
Density (g/cc)	1.76	
Average Particle Size (µm)	150	70
Helium Porosity (%)	14	
Flexural Strength (MPa)	28	13
Tensile Strength (MPa)	23	10
Compressive Strength (MPa)	53	-

Manufacturers data.

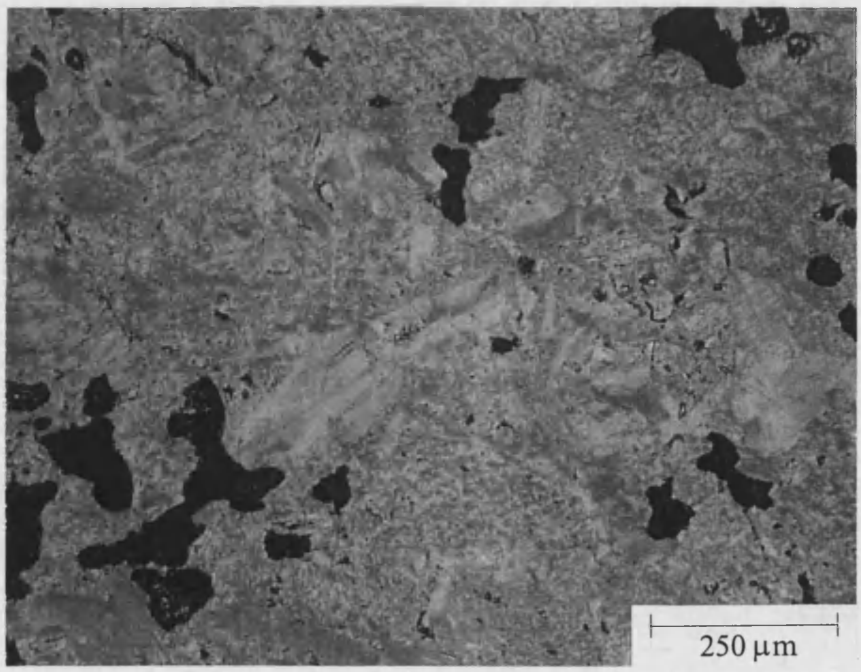

Figure 4-7 : Polarised light optical micrograph of FGEX graphite.

Graphite :	IM1-24
Manufacturer :	BAEL
Forming process :	Moulding

Density (g/cc)	1.82 [109]
Average Particle Size (µm)	500 [52]
Total Porosity (%)	19 [109]
Flexural Strength (MPa)	27.2 [108]
Tensile Strength (MPa)	19.5 [108]
Compressive Strength (MPa)	72 [109]- 85 [57]
Modulus (GPa)	11.6 [108]

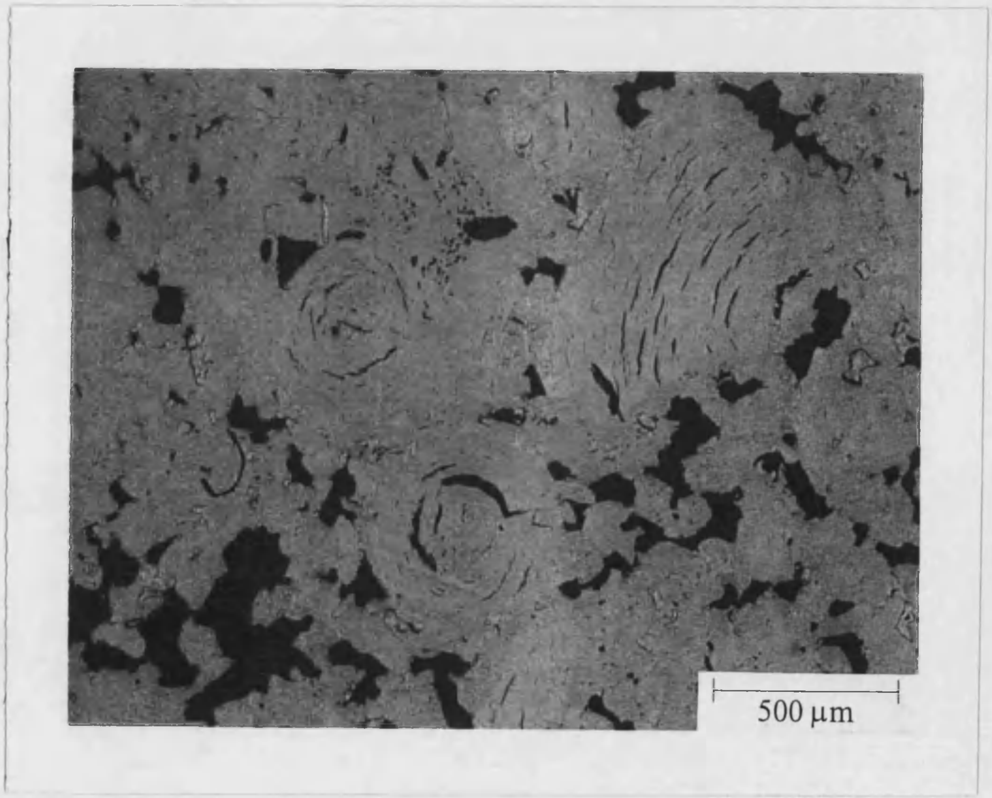

Figure 4-8 : Polarised light optical micrograph of IM1-24 graphite.

5. Experimental Methods

The experiments on friability of nuclear graphite have been divided into two areas, static and dynamic, which relate to the reactor processes mentioned in Chapter 1. A blunt indentation test was designed as a means of investigating the high localised stresses likely to be caused by distortions in the core such as rocking and dishing. For the dynamic friability studies a novel apparatus was designed and constructed to simulate a high localised wear situation. In all cases the effect of high weight loss due to oxidation was then examined.

5.1 Sample Dimensions

The blunt indentation test was designed to use samples of the size routinely trepanned from AGR cores so that the test could potentially be used as part of the core monitoring program. Consequently, the samples were in the form of 19mm diameter discs, with a thickness of 10mm (see Figure 5-1a). These dimensions were chosen after considering the samples geometric factors, which are presented in Chapter 6. For the dynamic testing, cylinders 19mm in diameter and approximately 50mm in length were chosen for convenience of machining and ease of oxidation (see Figure 5-1b).

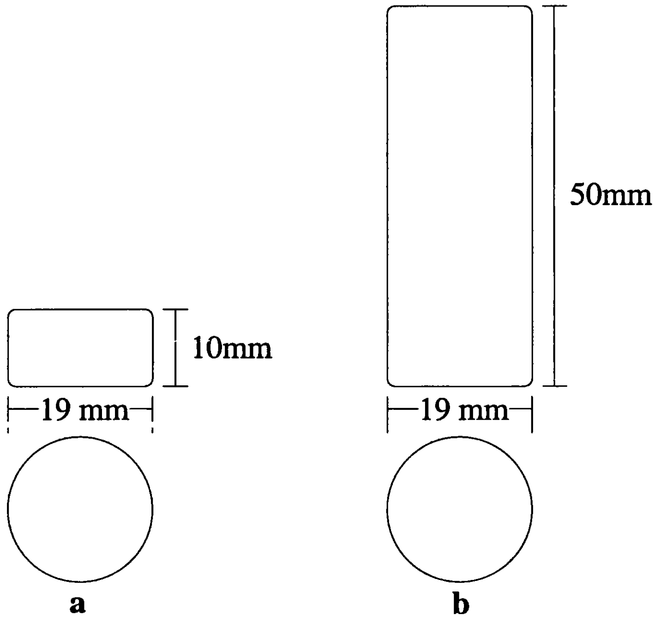

Figure 5-1 : Sample geometry.

5.2 Thermal Oxidation

The graphite sample was weighed, it's dimensions measured, and then oxidised in a horizontal tube furnace (see Figure 5-2) at 900°C in pure carbon dioxide with a flow rate of 10ml/min. A higher flow rate of 50ml/min was used for the first three hours to ensure all air was purged from the system. The tube furnace had ~20cm hot zone at 900°C ± 10°C allowing twelve of the small samples or four of the large ones to be oxidised at a time. The gas is heated in the quartz tube so it enters the main tube at the desired temperature, where the flow is broken up by a baffle. The temperature was raised at 120°C per hour in order to prevent thermal shock of the main tube, and to allow time to purge all air from the system. The weight loss of the samples was then monitored regularly until the required level was reached, when the samples were measured again to check for external burn off.

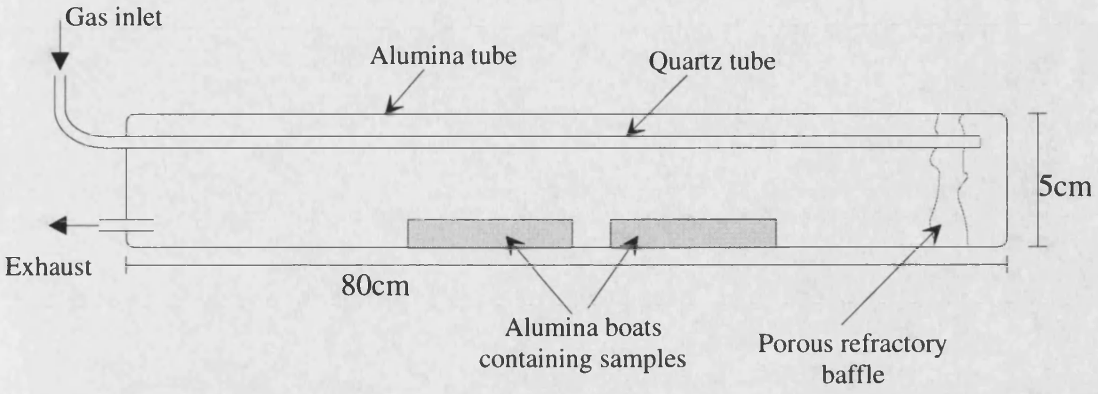

Figure 5-2 : Schematic of tube furnace used for oxidation.

5.3 Blunt Indentation

The apparatus shown in Figure 5-3 was constructed from mild steel and was designed to fit onto a standard Instron testing machine. The load was measured using a 0-5kN range load cell, while the displacement was recorded using a Penny and Giles displacement transducer (LVDT) with a 10mm range. The voltage outputs from the LVDT and the Instron load cell were logged by computer allowing the data to be processed using a spreadsheet package. A constant crosshead speed of 0.5mm/min was used for both tests to failure and load cycling. Tests to failure and load cycles were then performed on a number of graphites, as well as unoxidised and thermally oxidised IM1-24 graphite.

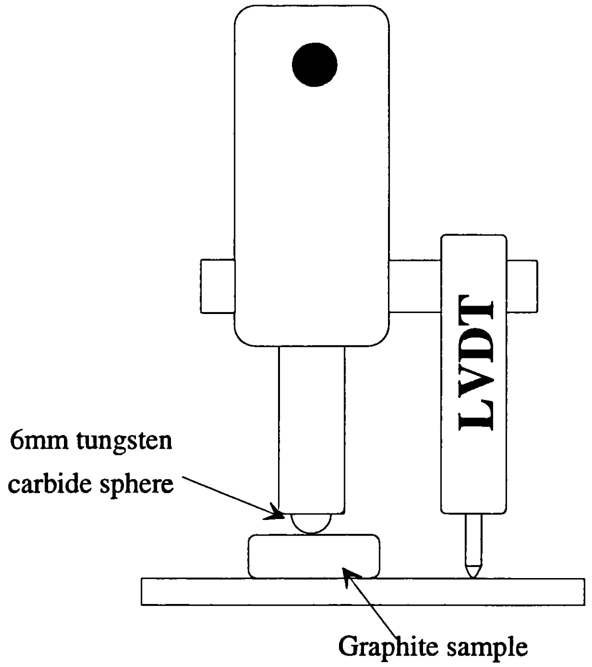

Figure 5-3 : Blunt indentation test rig.

Indentation tests using very similar apparatus were also undertaken on radiolytically oxidised IM1-24 graphite, in a shielded facility at Berkeley Technology Centre. The test rig was similar in design, using a tungsten carbide sphere, but the body was constructed from stainless steel rather than mild steel to prevent rapid degradation when irradiated. The LVDT was a model AG-5 produced by Solartron Schlumberger known to perform well under irradiation conditions.

5.4 Optical Microscopy

Samples were prepared for polishing by vacuum impregnating with a low viscosity epoxy resin (epothin), then sectioning and remounting in a phenolic resin. The graphite was then polished using the routine in Table 5-1, and viewed under normal illumination at a range of magnifications.

Step	**Mat**	**Polishing Medium**	**Time (mins)**	**Pressure (1b/sample)**
1	400 grit	silicon carbide	1	5
2	Perftex	9μm diamond in oil	4	5
3	Texmet	0.05μm α-alumina	5	10

Table 5-1 : Polishing route for graphite.

5.5 Bonded Interface Technique

A major problem with studying indentation of any kind is characterising the damage introduced by a load cycle. A method often employed is to take a section through the centre of the indentation, then polish it and view under an optical microscope. However, it is difficult to be certain that features have neither been introduced or removed by the polishing process. The fact that the whole surface is ground flat often makes small microstructural deformation invisible. One solution to this problem is the bonded interface technique, which allows viewing of the damage zone with no aggressive post indentation preparation. The technique has been used in the past on fully dense engineering ceramics [101, 102] but, this is the first time it has been used on materials with an appreciable degree of porosity. The underlying assumption that is made is that the adhesive bond serves only to transfer stress from one piece of graphite to another, playing no part in defining the deformation mechanisms.

Graphite was machined to the approximate dimensions of 50x50x15mm and bonded to an aluminium disc using a double sided tape produced by Advanced Tapes International Ltd. The aluminium disc could then be attached to the head of a polishing machine, and the routine in Table 5-1 followed with the exception of an increase in time for step 1. This allowed four pieces of graphite to be ground flat and polished at a time. Acetone was then used to remove the graphite from the aluminium disc.

To produce the bonded interface test pieces the polished surfaces were bonded together with a cyanoacrylate gel adhesive (Prism 454, Loctite UK). A razor blade was used to apply the adhesive very thinly and pressure was applied using a vice in order to minimise the thickness of the glue line. After curing for at least 24 hours the bonded graphite was cut into four samples sized approximately 25x25x30mm.

Indentation load cycles were then carried out on the join (see Figure 5-4) of each sample using the apparatus described in section 5.3. The two halves of the sample were then separated by refluxing in acetone for approximately three hours, allowing the damage zone to be viewed under an optical microscope with no further preparation.

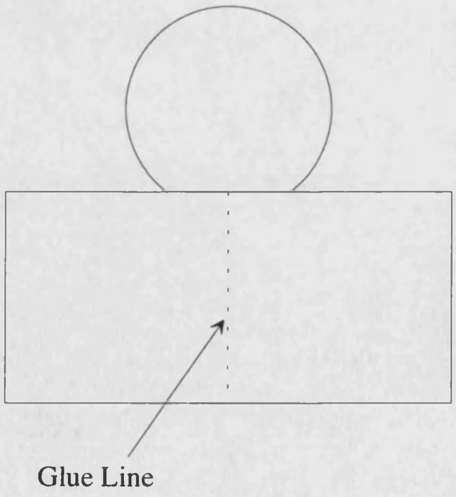

Figure 5-4 : Indentation of a bonded interface sample.

5.6 Electron Microscopy

Fracture surfaces were examined using a Jeol T330 scanning electron microscope with no extra preparation. Magnifications ranging from x15 to x1000 were used.

5.7 Surface Profiling

Surface profiling was used to investigate how oxidation affects the deformation behaviour of graphite. Samples were oxidised to different levels then indented up to a load of 1kN and finally surface profiled. This was carried out using a Taylor-Hobson Form Talysurf 50 with a long arm pickup and a spherical sapphire tip stylus, radius 500μm. The measurable range was 28mm with a resolution of 850nm. The size of the spherical tip does not allow the measurement of narrow features if they are more than a few microns deep, thus the main features of the surface are recorded rather than very fine details. The spherical tip also helps to prevent the stylus snagging and damaging the sample. Care was taken to make the measurements as close to the centre of the indentation as possible.

5.8 Particle Size Measurement

The particle sizes of debris from a range of friability tests were recorded using a Malvern Instruments Ltd. Mastersizer laser particle sizer with a long bed to allow measurement over a large range of sizes (1μm-3mm). When covering a size range as large as this, the smallest measurable particle is likely to be approximately 10μm. Normally particles are dispersed in either air or a liquid and cycled through a cell in front of the laser, where they are measured. However, these methods of dispersion were too aggressive and caused the particles to disintegrate. Hence the tests were carried out by allowing the debris to fall a few centimetres in air through the laser beam, after which the debris was caught in a tray. A special feeder designed for handling fragile particles was used to give a controlled feed rate of the debris. The debris was placed into a vibrating hopper, and the frequency of vibration was adjusted to give a slow but steady feed of particles into the laser.

5.9 The Dynamic Friability Test

The apparatus was designed to investigate a severe wear situation with high contact stresses present. This test was intended to relate to not only movement of core bricks, but also abrasion by sliding fuel stringer and control rods although at a greatly accelerated rate.

Figure 5-5 shows schematics of the test rig which was designed to fit onto an Instron testing machine in case a varying load be required in later tests. Accurate rates of rotation in the range 0-50 rpm were attained using a computer controlled stepper motor, which was geared down by 25:1 in order to obtain a smooth action. The whole motor and gear box assembly was mounted on bearings so that it would rotate freely until the strain gauged beam was in contact with the support pillar. Hence, when the tool is brought into contact with the rotating sample a torque is applied which will cause the motor and gearbox to move bending the beam, producing a voltage output that is proportional to the torque. The strain gauged beam was purchased from Graham and White Instruments, but had to be modified to increase the sensitivity. This was achieved by reducing the thickness of the beam slightly in the area of the strain gauges. The strain gauged beam was calibrated for torque by connecting a small torque driver to the chuck and taking measurements of voltage for each torque (see Figure 5-6), then obtaining the equation of the line. So during a test the torque was logged against time while the rate of rotation was kept constant.

The cutting tool was mounted on a sliding bed and a constant load applied by connecting weights to it (see Figure 5-7). Initially, a steel tool was used, but the wear rate was so high that it had to be sharpened every two or three cuts, which introduced far too much variability. So, a 3mm wide tungsten carbide grooving tool produced by Sandvik was used, which greatly reduced the wear rate to an acceptable level. As the tool used easily replaceable tungsten carbide inserts, sharpening was not necessary. Instead, the insert was replaced, although this was a very infrequent occurrence.

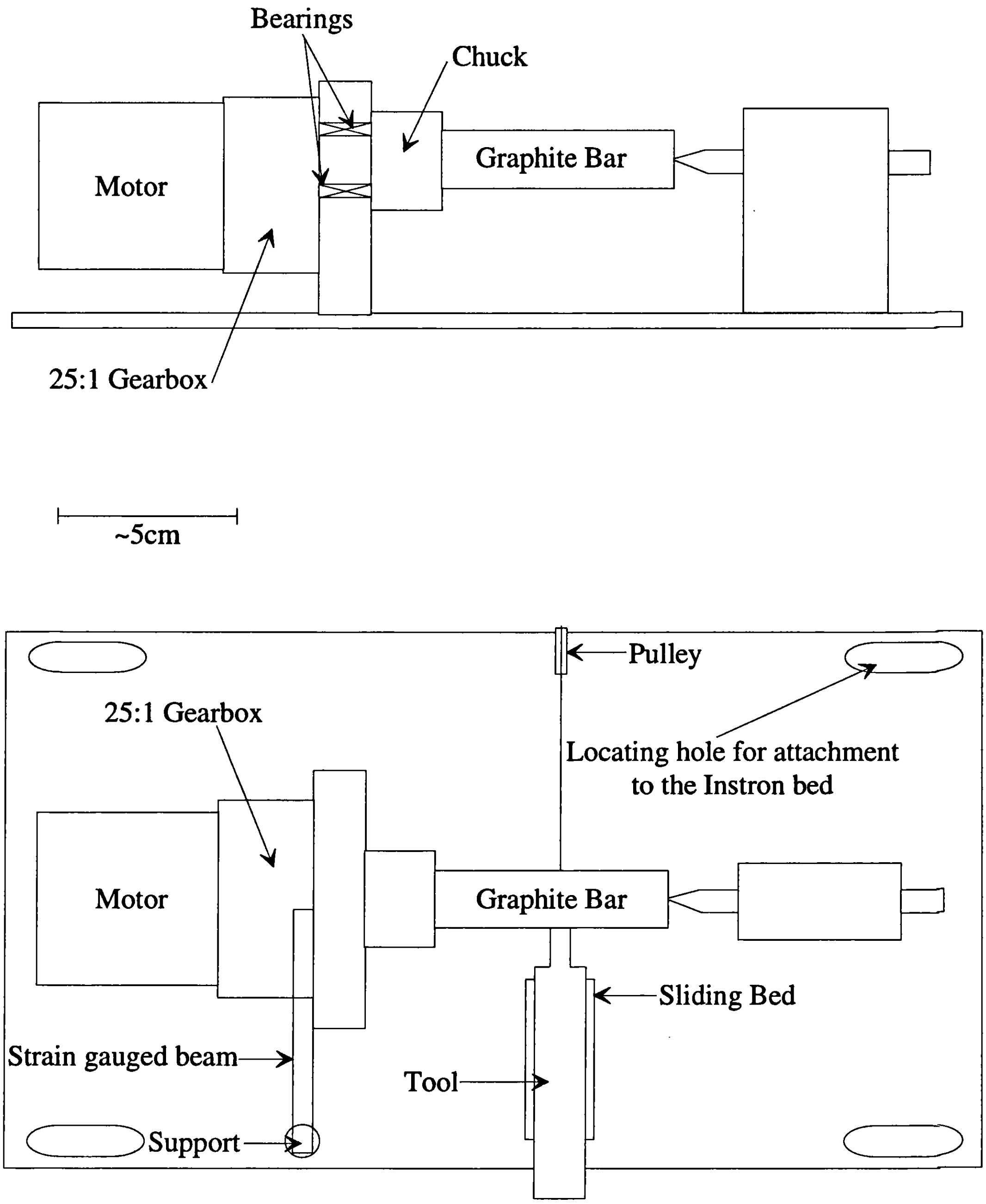

Figure 5-5 : Schematics showing plan and side view of the test rig.

All the debris was collected for each run and examined under a scanning electron microscope; then the particle size distribution was measured. As the grooving tool took a very uniform cut, the volume of material removed was easily calculated from measurements taken before and after each test.

The variables the test rig was designed to cope with were rate of rotation, tool load and different test materials i.e. varying degrees of oxidation. The quantities recorded were the torque logged against time and the volume of material removed.

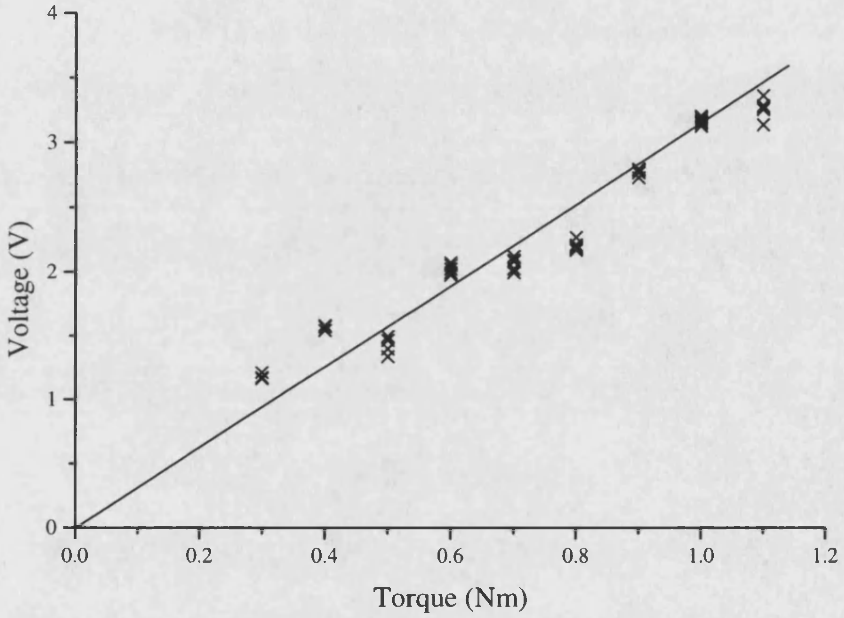

Figure 5-6 : Load cell calibration for torque.

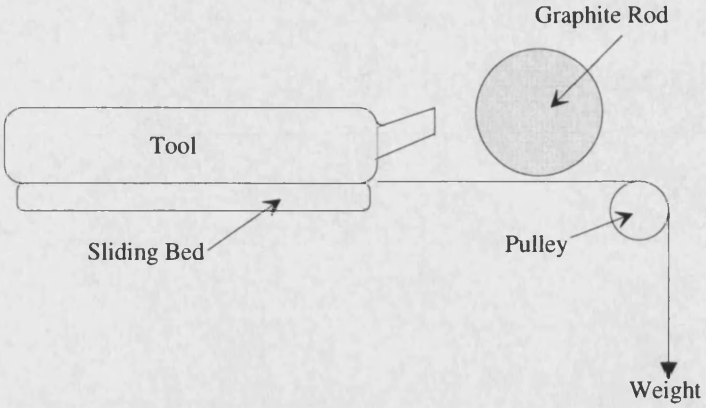

Figure 5-7 : Schematic of a method for applying constant load to the tool.

6. Assessment of the Blunt Indentation Test Method

One of the main attractions of the blunt indentation method used in this work is its ability to test small samples. In this chapter some typical results for the blunt indentation of IM1-24 graphite are presented, and compared with the response predicted by Hertzian mechanics. The greater part of this chapter is then devoted to the analysis of how sample geometry and sphere size affect the mode of fracture.

6.1 Stress Strain behaviour

Figure 6-1 shows a typical load-displacement curve for IM1-24 graphite. There is an initial change in slope visible up to 0.2mm indentation depth, the curve is then almost linear until fracture occurs at a load of ~3.5kN and a displacement of ~1.27mm.

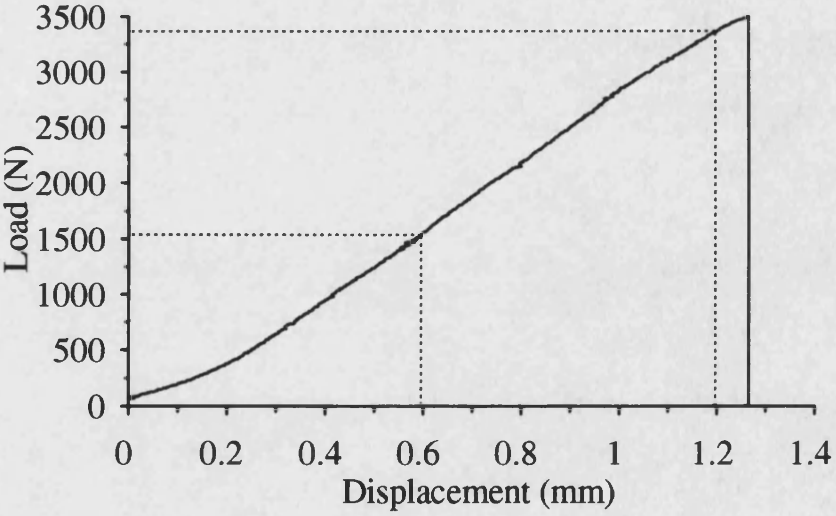

Figure 6-1 : Load displacement plot for the blunt indentation of unoxidised IM1-24 graphite.

Figure 6-2 shows the load-displacement curve calculated from the Hertzian equation 3.2 in Chapter 3. There are two main assumptions that are implicit in Hertzian mechanics. Firstly both the indenter and the substrate are assumed to be elastic and homogeneous. Secondly the contact between the indenter and the substrate is assumed to be planar, which is a reasonable approximation for materials such as glass providing that the indenter is very much larger than the contact area. The shape of the calculated load-displacement curve in Figure 6-2 is similar to the experimental curve in Figure 6-1, but the calculated load at a displacement of ~0.6mm or ~1.2mm is about one order of magnitude higher than the experimental value (see dotted lines in Figure 6-1 and Figure 6-2). This illustrates the limitations of applying the Hertz equations to graphites which are neither elastic nor homogeneous. It will be shown in Chapter 7 that the lower stresses found for IM1-24 are associated with stress relief mechanisms, such as shear and microcracking of the graphite.

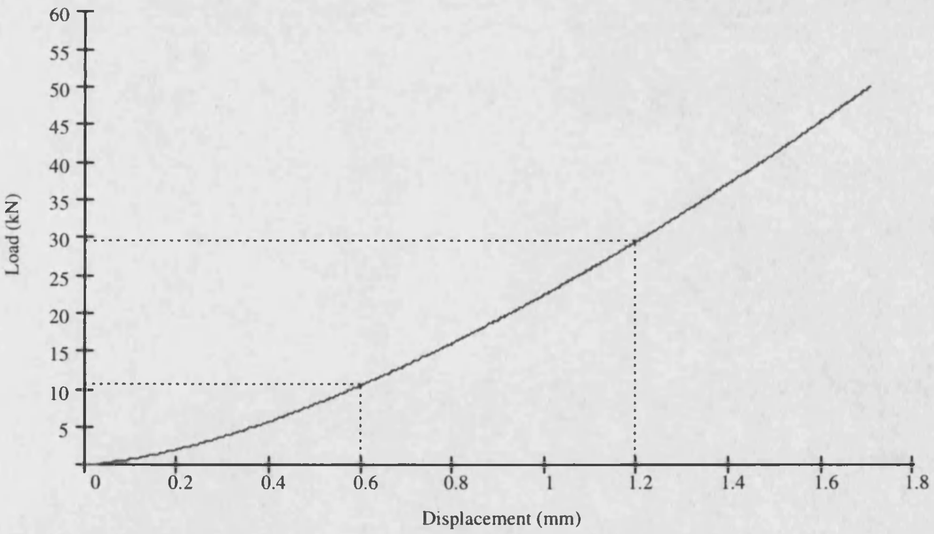

Figure 6-2 : Load-displacement plot calculated from Hertzian equations.

Defining the blunt indentation failure stress is not a trivial problem as it is not clear how failure is initiated. An average pressure can be defined, as with the Hertzian equations, by assuming the contact is planar. Thus, the stress averaged in this way will be the load divided by the projected area of contact. However, as graphite is very much more compliant than the indenter, it is certain that the contact is not planar. It is more reasonable to assume that the tungsten carbide sphere is effectively incompressible giving the contact area $A = 2\pi R\delta$. Thus, the average stress is simply the load divided by this area.

Figure 6-3 shows average stress calculated in this way using the load-displacement data shown in Figure 6-1. As the sphere is assumed to be incompressible the contact is initially a point giving rise to very high stresses. The graphite deforms under the initial high stress allowing the indenter to “bed in” which is visible as the initial non-linearity in the load displacement curve (Figure 6-1). As the contact area expands the stress decreases to ~95MPa at a displacement of 0.15mm. In the middle range of the test the load increases more rapidly than the displacement does. For example, from Figure 6-1 as the displacement increases from 0.4 to 0.8mm, the load increases from ~900N to ~2200N. This produces the increase in average stress shown in Figure 6-3.

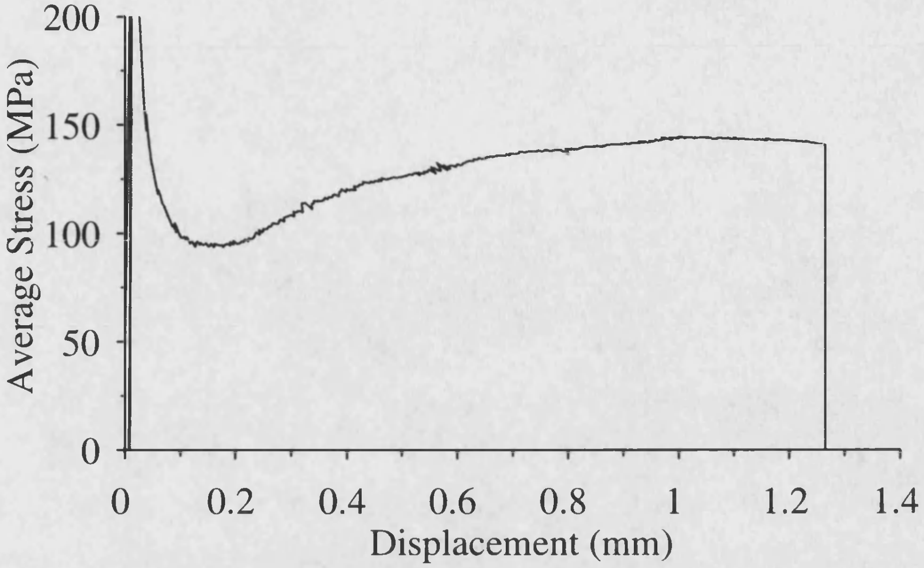

Figure 6-3 : A typical average stress-displacement plot for IM1-24 graphite.

6.2 Hertzian calculations of the stress distribution

The size of sphere used is largely determined by two criteria;

1. It should be small enough that the stress field is contained within the sample, avoiding back face or edge effects.
2. It should adequately sample the microstructure of the graphite.

Utilising some information obtained from initial tests, stress calculations were performed using Hertzian equations given by Johnson [77], in order to obtain an idea of the sample size required to avoid perturbations to the stress field by the samples edges.

To investigate whether a diameter of 19mm is likely to be sufficiently large to encompass the stress field thus avoiding edge effects, the magnitude of stress at the edge must be calculated. The problem can be simplified by considering which stress components will act outside the contact area, and at what point in the solid they will attain a maximum. The only stresses acting outside the contact area are the radial stress, σ_r, and the hoop stress, σ_θ, (see Figure 3.2) and these will be at a maximum in the surface. The distribution of these stresses in the sample surface outside the contact area, can be calculated using equation 6.1, where r is the radial distance from the centre of the contact.

$$\frac{\sigma_r}{P_0} = \frac{\sigma_\theta}{P_0} = \frac{(1-2v)a^2}{3r^2} \qquad 6.1$$

From Figure 6-1 the indentation depth at failure was ~1.3mm, allowing the calculation of a = 2.504mm. The sphere is assumed to be incompressible (see Figure 3.1), which is reasonable bearing in mind the large difference in modulus between IM1-24 graphite (11GPa) and tungsten carbide (600GPa). The Poisson's ratio of IM1-24 is 0.2 and, assuming the indentation is made in the centre of the disc the radial distance to the edge will be 9.5mm.

Figure 6-4 shows the decrease in stress as the distance from the indentation increases. Initially the stress decreases rapidly, declining to 1% of the maximum Hertzian pressure, P_0, at a 11.2mm from the centre of the indentation. At the edge of the sample (r = 9.5mm) the stress is approximately 1.5% of P_0 and hence can be neglected.

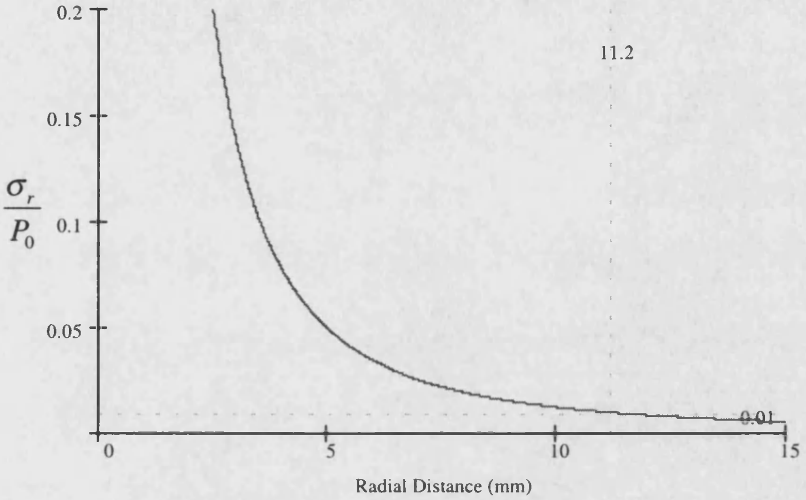

Figure 6-4 : The variation in surface stress outside the contact area for a blunt indentation.

The remaining question is how thick the sample must be to prevent significant distortion of the stress field at the back face? This can be treated using a simple Hertzian expression given by Johnson[77] $\frac{\sigma_z}{p_0} = -\left(1+\frac{z^2}{a^2}\right)^{-1}$ where σ_z = stress on the z-axis and z = z-axis distance from the contact. Using this equation, expressions for the stress in the surface of the sample (equation 6.2), and in the back face of the sample (equation 6.3) are obtained.

$$\frac{\sigma_{z(Front)}}{P_0} = -\left(\frac{1}{1+\frac{0}{a^2}}\right) = -1 \qquad 6.2$$

where $\sigma_{z\,(Front)}$ = z-axis stress at the surface.

$$\frac{\sigma_{z(Back)}}{P_0} = -\left(\frac{1}{1+\frac{t^2}{a^2}}\right) \qquad 6.3$$

where $\sigma_{z\,(Back)}$ = z-axis stress at the back face, t = sample thickness.

Figure 6-5 shows the variation in back face stress as a fraction of the surface stress, $\frac{\sigma_{z(Back)}}{\sigma_{z(Front)}}$, with increasing sample thickness. Calculated using the same value of a as Figure 6-4. The stress at the back face initially decays rapidly as the sample thickness is increased, but does not decrease to 1% of the applied stress until a thickness of ~25mm.

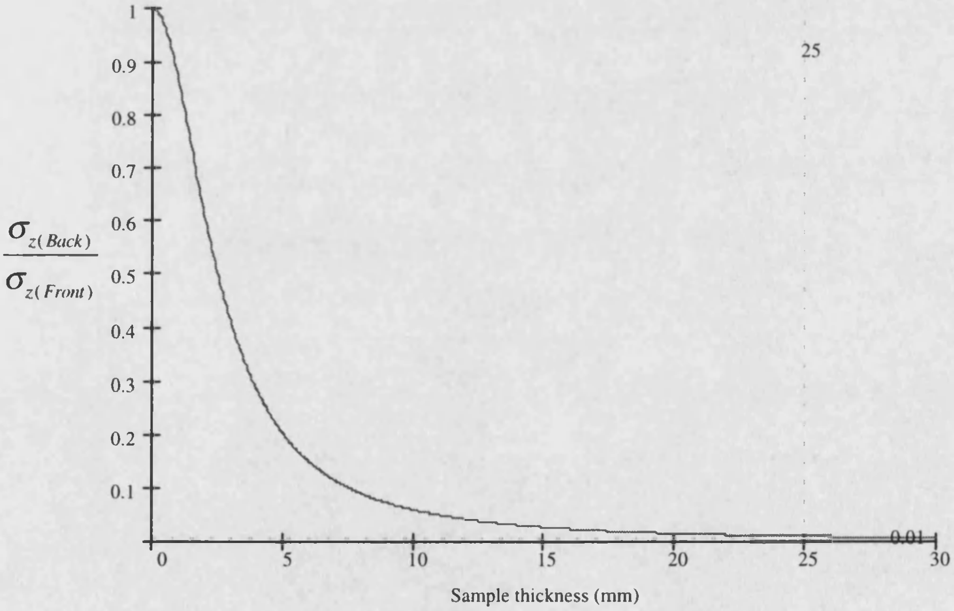

Figure 6-5 : The decay of back face stress as a fraction of the surface stress, with increasing sample thickness.

At a thickness of 10mm the stress at the back face is ~6% of the applied stress, suggesting it may not be a negligible effect. This brings into question the use of a 10mm thick sample suggesting perhaps it should be thicker. However, it demonstrated in the previous section that Hertzian mechanics over predict the load for any given indentation depth. Thus it is quite feasible that the stress is considerably lower than calculated for an elastic solid, as it is likely that some microcracking will occur relieving stress.

6.3 Effect of sample thickness

Owing to the limitations of the Hertzian approach when calculating the stress distribution, a series of tests on samples of different thickness were undertaken to determine experimentally the minimum sample size suitable for indentation tests to failure. Indentations were made on standard diameter samples with a range of thicknesses using a 6mm sphere.

6.3.1 Mechanical Testing

Figure 6-6 and Figure 6-7 show the failure load and displacement at failure for IM1-24 and SF53 graphites for a range of sample thicknesses. Both load and indentation depth at failure appear to reach a constant value at a thickness less than 10mm, suggesting that a sample 10mm thick would be adequate to ensure that the test is valid. IM1-24 and SF53 have very different strengths (see Chapter 4) which is clearly indicated by the different maximum loads obtained in Figure 6-6. However the displacement at failure shown in Figure 6-7 does not vary greatly for the different materials, lying in the range of 1.3-1.7mm. This demonstrates, as might be expected that there is a considerable difference in elastic modulus. If the data are normalised for the different strength and indentation depth to failure by dividing by the constant value achieved at a thickness greater than ~7mm (~3750N load and ~1.65mm displacement for IM1-24, and ~1800N load and ~1.45mm displacement for SF53), Figure 6-8 and Figure 6-9 are obtained. The data for the two graphites in Figure 6-8 and Figure 6-9 lie on similar curves. These results show that the shapes of the curves are not a function of the mechanical properties of the graphites, but are governed by the dimensions of the test piece. Both the failure load and the indentation depth at failure become independent of sample thickness when the thickness exceeds ~7mm.

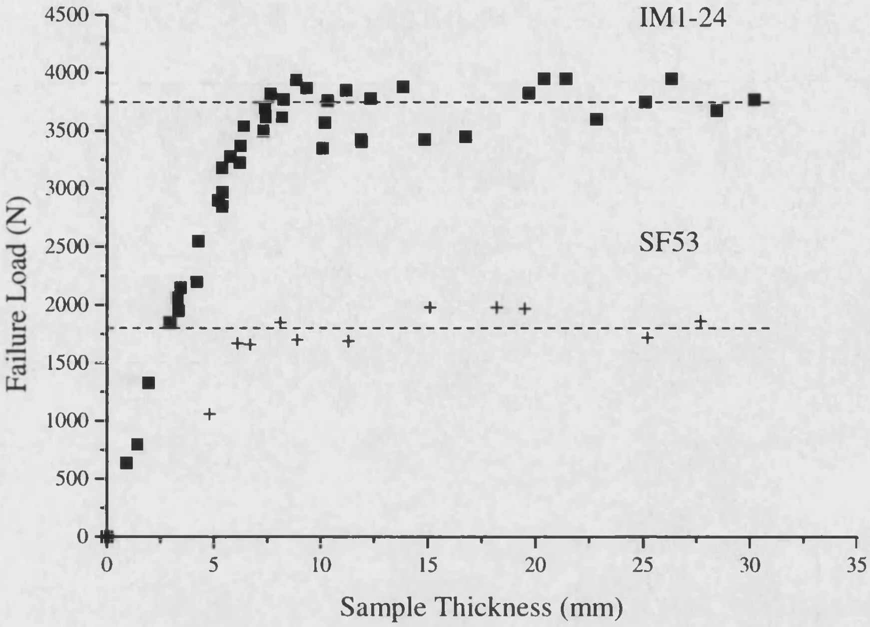

Figure 6-6 : The effect of sample thickness on failure load for IM1-24 and SF53 graphite.

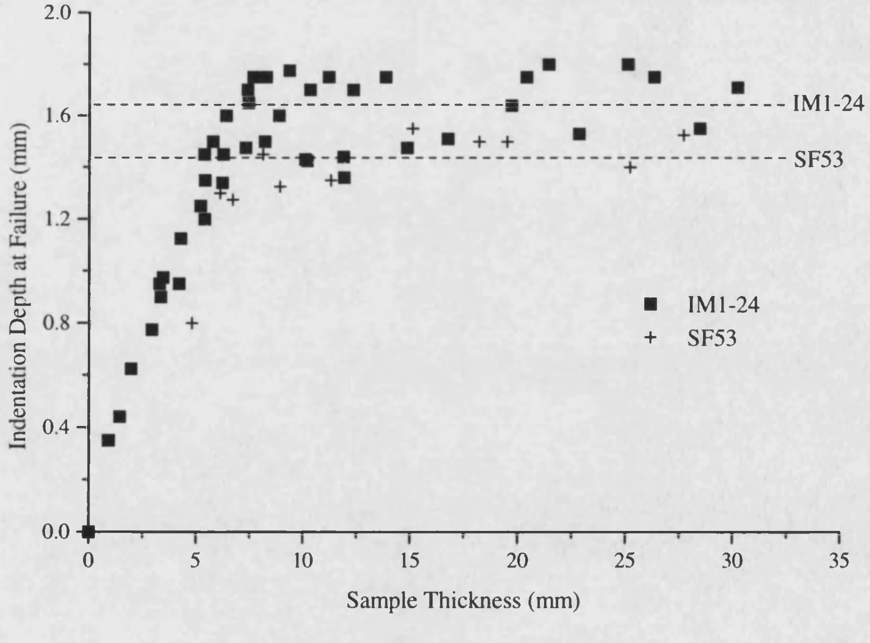

Figure 6-7 : The effect of sample thickness on indentation depth at failure for IM1-24 and SF53 graphite.

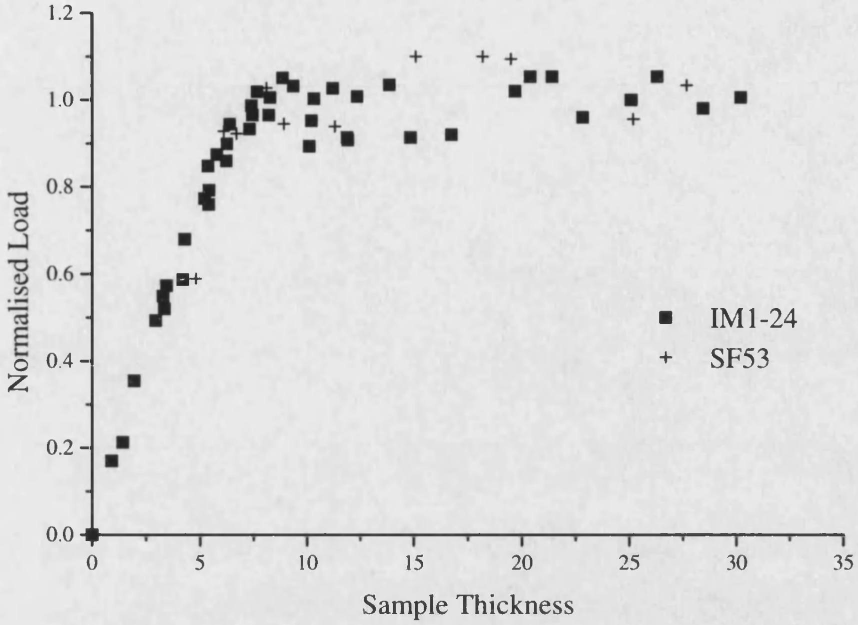

Figure 6-8 : Effect of sample thickness on normalised failure load for IM1-24 and SF53 graphite.

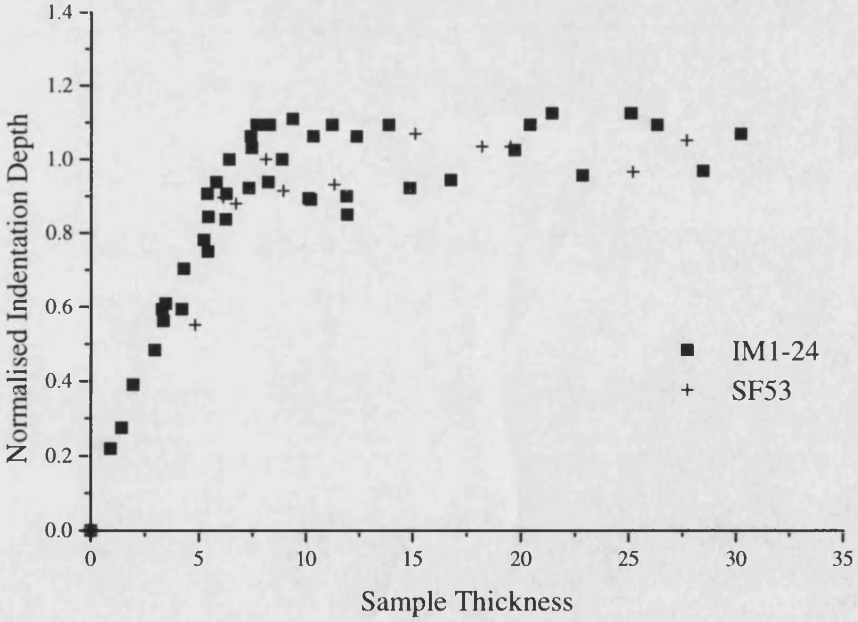

Figure 6-9 : Effect of sample thickness on normalised indentation depth to failure for IM1-24 and SF53 graphite.

Another factor worth noting, is that a constant value for the blunt indentation failure stress is likely to be reached at a lower sample thickness (see Figure 6-10) than for either failure load or the displacement at failure. The reason for this is that the contact area (defined in section 6.1) is a function of the indentation depth which varies in a manner similar to the failure load (see Figure 6-6 and Figure 6-7). Consequently when an average blunt indentation stress is calculated, (load / contact area) a constant failure stress is reached at a lower sample thickness of ~3mm.

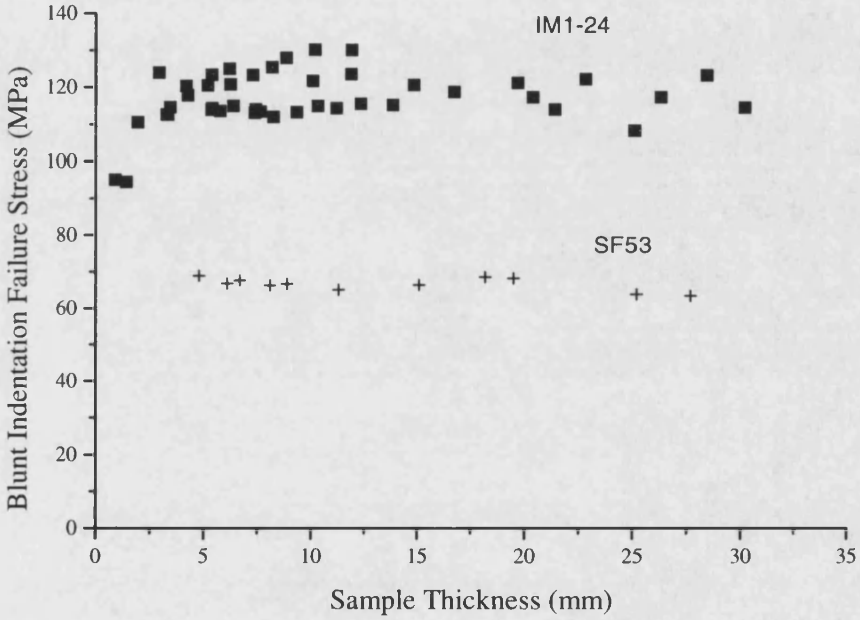

Figure 6-10 : Effect of sample thickness on blunt indentation failure stress for IM1-24 and SF53 graphite.

6.3.2 *Fracture Morphology*

The fracture morphology also varies with sample thickness (see Figure 6-11). The thin samples (≤~8mm) break into three roughly equal pieces, while samples 10mm thick or greater fracture approximately in half. Thus there is a change in fracture mode as the sample thickness is increased that occurs between 8 and 10mm thickness. A possible explanation that encompasses the observed change in fracture morphology, is that there are two competing fracture mechanisms operating. When a nominally flat graphite sample is indented on a nominally flat steel plate the initial contact is made by the asperities. For the sample to be stable it is probable that it will rest on the three largest asperities spaced at approximately 120° intervals, which provide stress concentrations and a bending moment. Consequently, if the stress produced by this bending moment is high enough, fracture will be initiated in the centre and will follow the maximum tensile stresses where the asperities are in contact, producing three pieces. This fracture morphology is indicative of a ball on ring biaxial flexure test [110]. The failure stress, $\sigma_{\mathrm{Biaxial}}$, can be calculated using equation 6.4 [111, 112], where s is the radius of the support circle (6mm), u is the radius of the region of uniform loading in the centre, and d is the radius of the disk (9.5mm).

$$\sigma_{Biaxial} = \left(\frac{3P(1+\nu)}{4\pi t^2}\right) \times \left(1 + 2\left(\ln\frac{s}{u}\right) + \left(\frac{(1-\nu)s^2}{(1+\nu)d^2}\right) \times \left(1 - \frac{u^2}{2s^2}\right)\right) \qquad 6.4$$

The problem is determining the correct value of u. Westergaard [113] produced a solution using a combination of analytical and numerical methods. This states that $u = t$ *for* $a > 1.724t$, $u = \left(1.6a^2 + t^2\right)^{\frac{1}{2}} - 0.675t$ *for* $a < 1.724t$, *and* $u = 0.325t$ *for* $a \rightarrow 0$, where a is the radius of the contact area of the sphere with the disk.

The other possibility is that fracture is initiated by the tensile stresses due to the indentation in the surface, which would be likely to produce only a single crack. These stresses can be estimated using equation 6.1.

Figure 6-12 and Figure 6-13 show plots of the Hertzian stresses and the biaxial bend stresses, calculated using equations 6.1 and 6.4 respectively. The failure load is taken from the data for IM1-24 in Figure 6-6 and used directly in both approaches, while the indentation depth from the IM1-24 data shown in Figure 6-7 was used to calculate a value for a. Figure 6-12 and Figure 6-13 show that the Hertzian stresses are relatively insensitive to sample thickness, but the biaxial bend stresses at failure are inversely proportional to the sample thickness squared causing a rapid decrease in the biaxial bend stress as the sample thickness is increased. Figure 6-13 shows that the calculated Hertzian and biaxial stresses intersect at ~10mm.

This suggests that, at thicknesses smaller than ~10mm fracture is initiated at the back face by a bending mechanism. At larger thicknesses the tensile stress produced at the edge of the contact reaches the strength of the graphite before the bend stress at the back face does. Thus fracture is initiated at the surface by Hertzian contact stresses for samples thicker than ~10mm, which ties in reasonably well with the observations shown in Figure 6-11. In these calculations an arbitary support circle radius of 6mm was used. If we assume that the disk is supported on its edges so the radius of the support circle is equal to the disk radius the transition between the two fracture mechanisms is at a thickness of ~13mm. Hence the model is fairly insensitive to the position of the support circle.

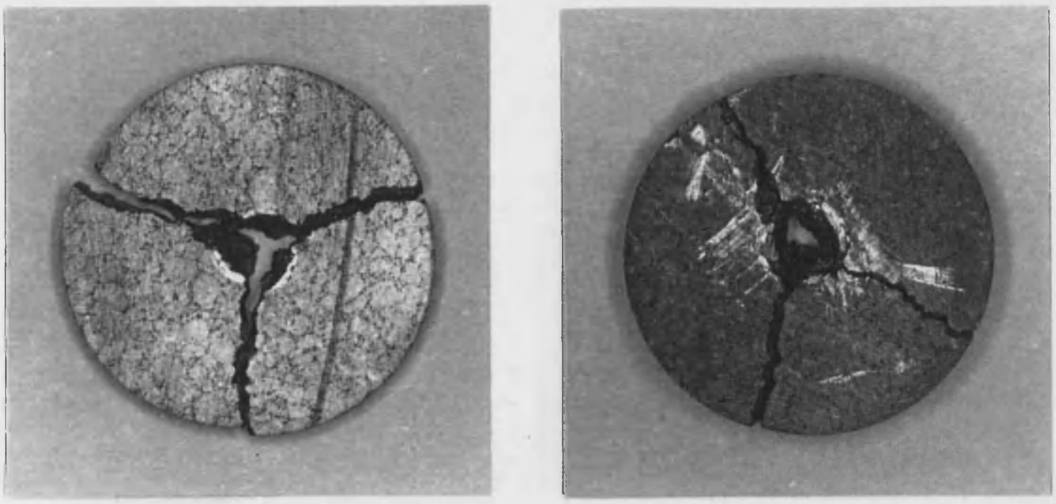

(a) 4.2mm thick (b) 7.3mm thick

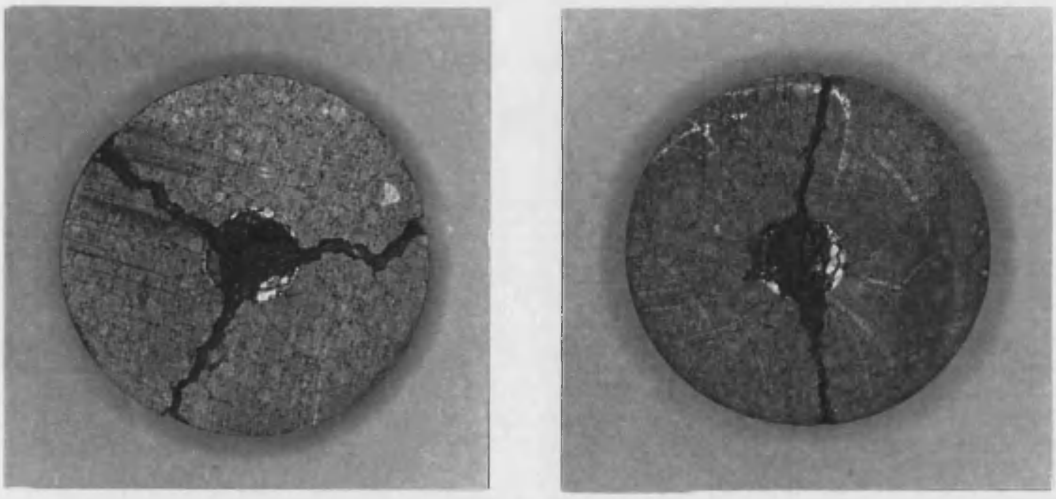

(c) 8.2mm thick (d) 10.1mm thick

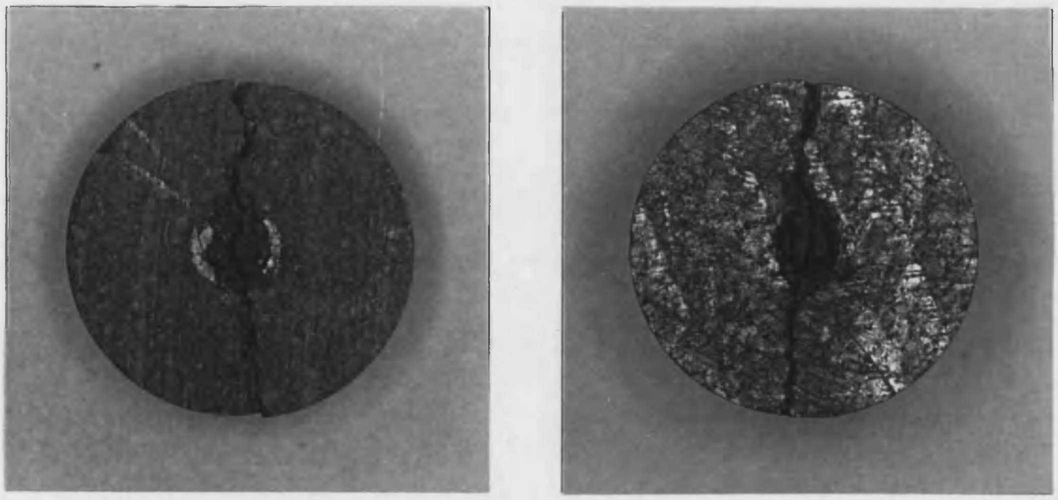

(e) 11.9mm thick (f) 22.8mm thick

Figure 6-11 : Effect of sample thickness on fracture morphology.

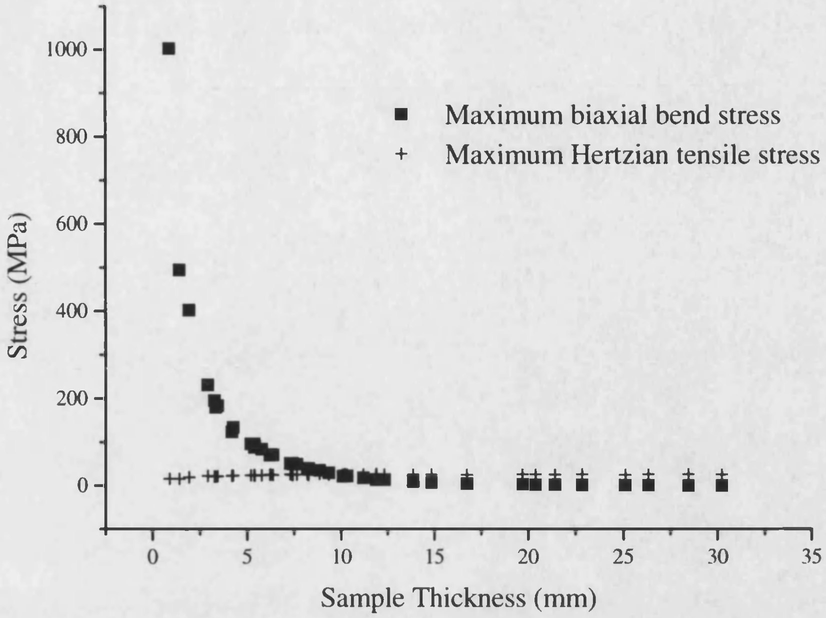

Figure 6-12 : The variation of Hertzian tensile stresses and biaxial bend stresses with thickness for IM1-24 graphite.

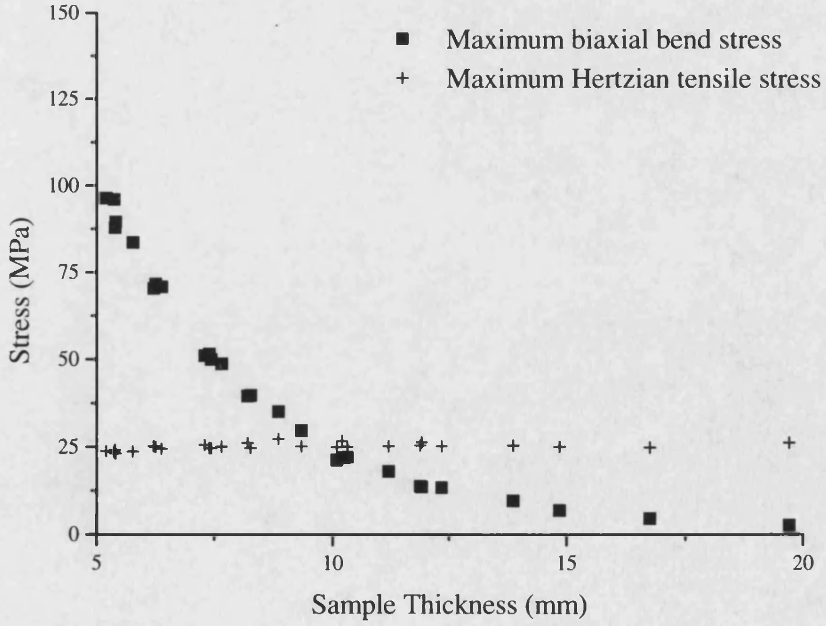

Figure 6-13 : As Figure 6-12 with expanded scales.

6.4 The effect of sphere size [*]

To investigate the effect of sphere size, IM1-24 graphite samples of the standard trepanned size (19mm diameter x 10mm) were indented to failure with 3, 6, 10 and 15mm diameter spheres. No results could be obtained for the 3mm sphere, as it penetrated the surface of the graphite without causing a catastrophic failure allowing the body of the test rig to come into contact with the sample.

6.4.1 Mechanical Testing

Figure 6-14 shows the fracture load for the three different sphere sizes, with error bars marking plus or minus two standard deviations. A straight line can be fitted to the data demonstrating that Auerbach's law (see chapter 3) is a reasonable description of the effect of sphere size on the fracture load. Auerbach's law states that the critical load for ring crack formation is proportional to the radius of the sphere. However in this case no ring crack is produced until just before catastrophic fracture and the fracture pattern is very different from a Hertzian cone crack. Details of the blunt indentation fracture morphology in IM1-24 graphite will be discussed in the next chapter.

As the sphere size is increased the average blunt indentation failure stress, which is defined as in the section 6.1, decreases as shown in Figure 6-15. It is interesting to note that for a 15mm diameter sphere the failure stress has decreased almost to the same magnitude as the uniaxial compressive strength for IM1-24 graphite (72-85MPa see Chapter 4). As considered in the previous section, the sample size is likely to be just large enough to encompass the stress field produced by the indentation of IM1-24 graphite with a 6mm diameter sphere. Thus it is possible that a 10mm thick sample is too small to encompass the stress field entirely when the indenting sphere is 10 or 15mm in diameter. So, the decline in fracture stress could well be a function of back face and edge effects. It is also quite likely that with a 15mm diameter sphere, the contact area is sufficiently large that the test approaches a uniaxial compression test.

---

[*] The experimental work in this section was carried out by M.Taylor at Berkeley Technology Centre.

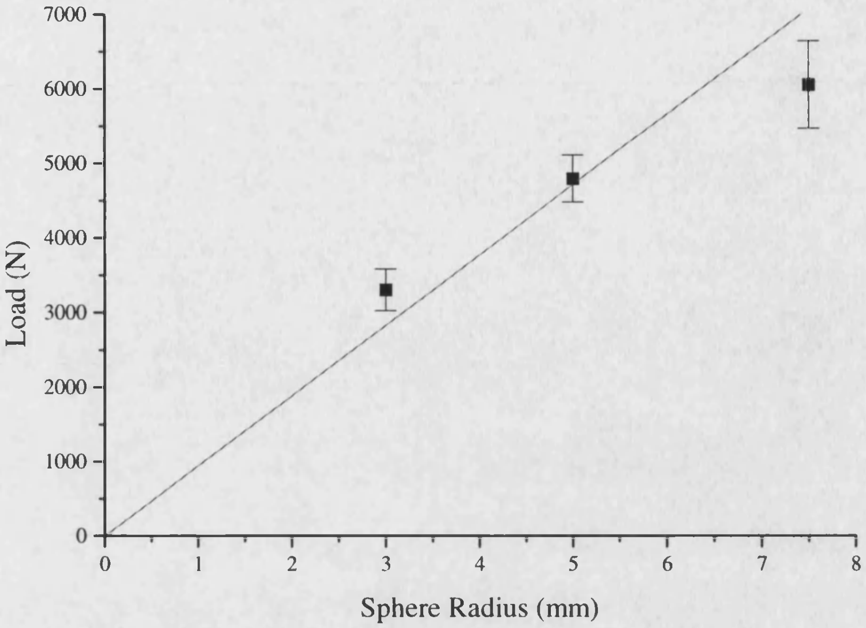

Figure 6-14 : The effect of sphere size on the failure load for IM1-24 graphite.

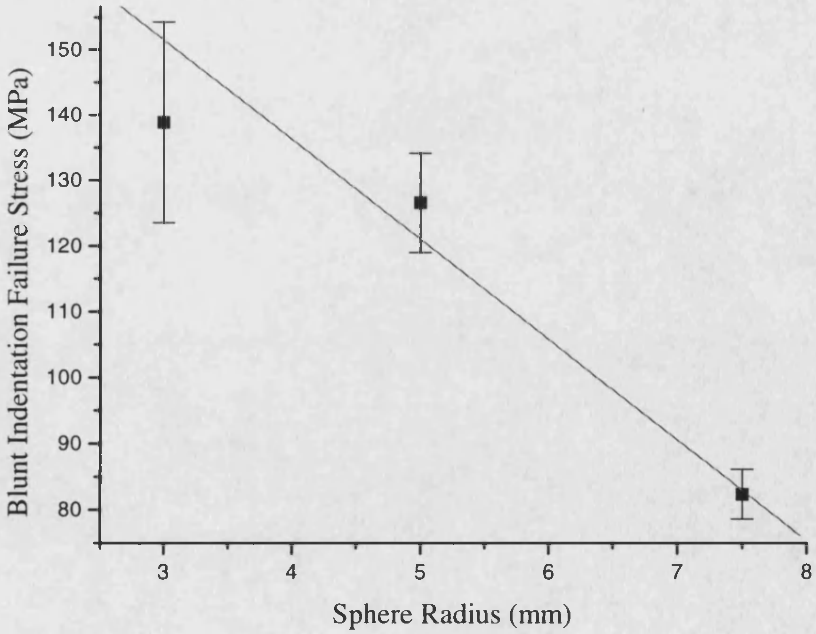

Figure 6-15 : The effect of sphere size on the compressive failure stress for IM1-24 graphite.

6.4.2 Fracture morphology

For the standard test, indenting a 10mm thick sample with a 6mm diameter sphere, fracture occurs approximately through the centre of the sample (see Figure 6-11d). A small cone directly beneath the indenter (see Figure 6-16) is reduced to powder. The same fracture morphology is observed for a 10mm diameter indenter. Figure 6-17a shows the fracture morphology produced by an indentation to failure with a 15mm sphere. Fracture has occurred roughly through the middle of the sample leaving the two halves (Figure 6-17b), and an ejected cone (Figure 6-17c).

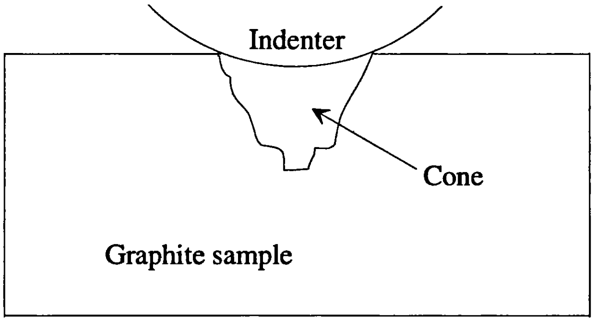

Figure 6-16 : Schematic showing the cone produced in IM1-24 by a spherical indenter.

The mechanics of the indentation do not change with increasing sphere size, but an intact cone is only visible for the 15mm diameter sphere. This may be because of the coarse structure of IM1-24 and the nature of the damage produced by the indentation within this conical region. If the cone is small (produced by indentation with a 6mm diameter sphere) the flaws cause it to disintegrate, whereas a larger area is not spanned by the flaws produced during indentation. The flaws may be pre-existing cracks or microcracks generated during the indentation. The nature of blunt indentation damage will be dealt with in more detail in Chapter 7.

However, this raises the question of whether a 6mm diameter sphere is large enough to sample the microstructure adequately. Figure 6-18 shows the projected area of contact for approximately one third the indentation depth at failure of an unoxidised IM1-24 graphite sample when indented with a 6mm sphere. Although the contact is initially very small it rapidly expands as the sphere is pushed into the surface, covering a reasonable number of microstructural features.

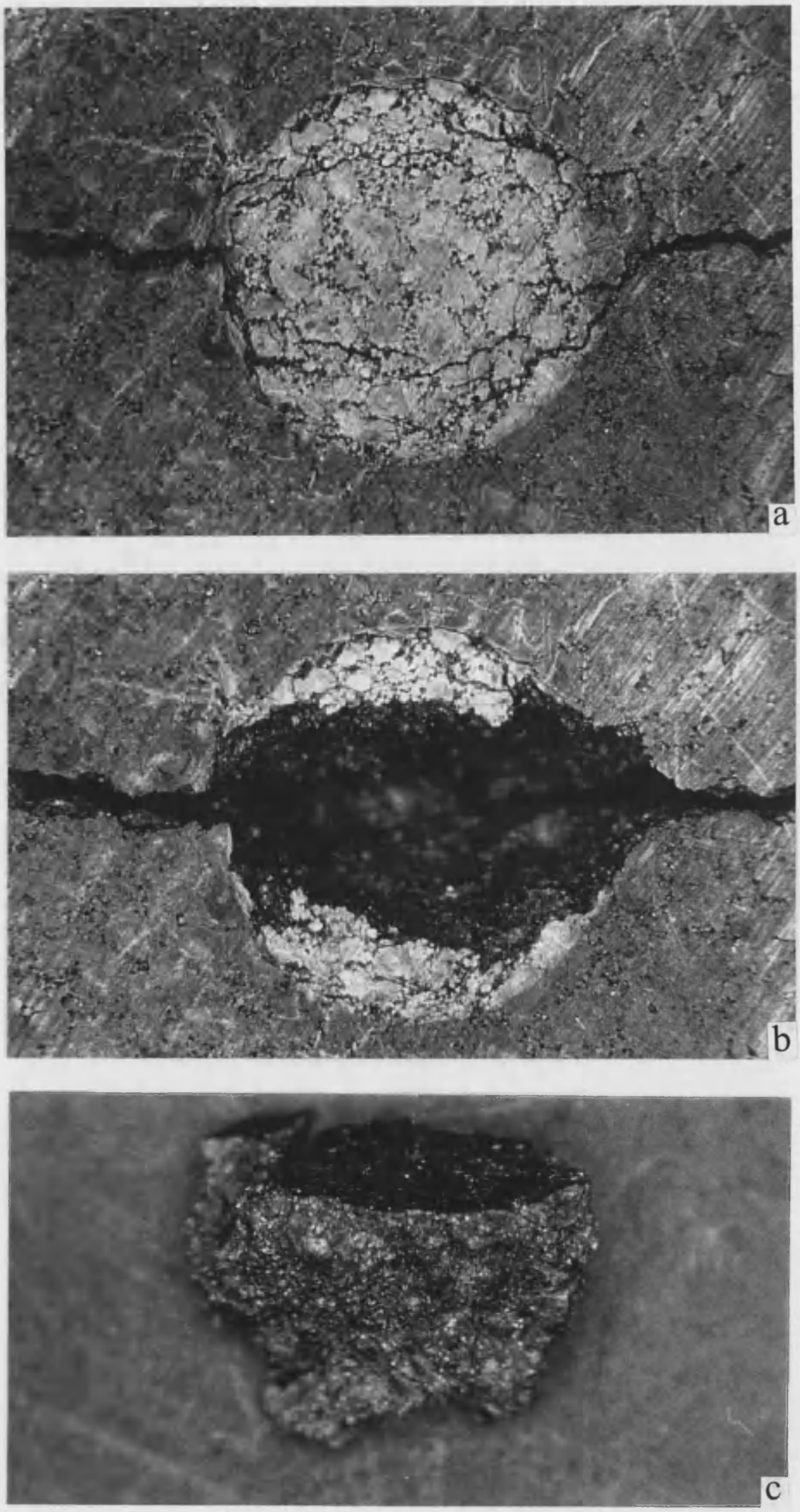

Figure 6-17 : Fracture caused by indentation with a 15mm sphere, a, whole sample after fracture, b, two halves of the sample, c, the ejected cone.

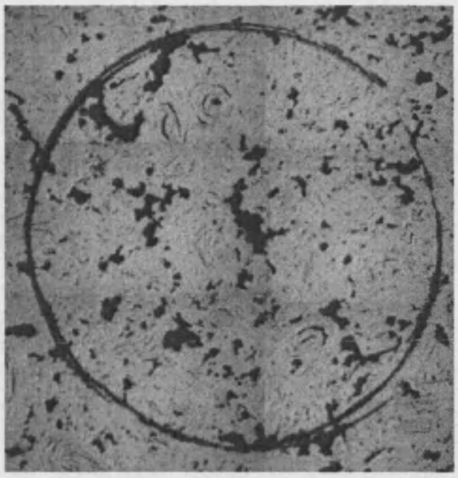

Figure 6-18 : Micrograph showing the projected area of contact for an indentation depth of 0.5mm on unoxidised IM1-24 graphite.

6.5 Chapter Summary

It has been demonstrated that Hertzian mechanics over predicts the load at any given displacement by approximately one order of magnitude, for the indentation of IM1-24 graphite with a 6mm diameter sphere. The difference between the predicted and observed load at a given displacement is likely to be because sub-critical cracking is relieving stress in the graphite, whereas the Hertzian equations are based on a purely elastic solid.

The sample size of 19mm diameter x 10mm thick is likely to be sufficient to prevent back face and edge effects occurring, and although the Hertzian equations have been shown to over predict the stress they are adequate as a first approximation. The failure load and displacement become independant of sample thickness for thicknesses greater than ~8mm. There is also a transition between fracture mechanisms at approximately this thickness. Thin samples, ≤ 8mm, fracture into three roughly equal pieces, which is indicative of biaxial flexure, whereas samples thicker than ~8mm fracture roughly in half. It has been demonstrated that a possible explanation for this transition is the change in the relative magnitudes of biaxial bending stresses and Hertzian tensile stresses. For thinner samples the biaxial bending stress is greater than the Hertzian one, so fracture is initiated from the back face of the sample. Then, as the initial contact between the sample and the supporting plate is by the asperities there will be stress concentrations running radially outwards. For the sample to be stable it will rest on the three largest asperities spaced at approximately 120° from each other. Thus when fracture is initiated it follows the stress concentrations created by these asperities, breaking the sample into three pieces. However, for thicker samples the Hertzian tensile stresses at the edge of the contact between the indenter and the sample are greater than the stress due to biaxial bending, hence fracture is initiated at the edge of the contact.

Sphere size over the range of 6-15mm diameter has little effect on the fracture morphology of IM1-24 graphite. The only difference is that the cone removed on fracture is reduced to dust for the 6 and 10mm diameter indenters, but the cone remains intact for the 15mm diameter indenter. This may be due to the different size of the cones removed compared to the scale of the microstructural flaws. It is also possible that the fracture stress is greater for a smaller sphere, thus the localised damage is likely to be greater.

7. Blunt Indentation of IM1-24 Graphite

The results discussed in this section were all produced using the standard 6mm diameter tungsten carbide sphere, either loading a sample to failure or performing a load cycle. Characteristic load-displacement curves for the blunt indentation of IM1-24 have been presented in the previous chapter. Hence this chapter will concentrate mainly on the nature of the damage produced by a blunt indentation and how cyclic loading affects it.

7.1 Indentation Damage

A damage zone beneath the indenter precedes any visible cracking on the surface of the sample. Figure 7-1a shows the sample surface after a 2kN load has been applied, while Figure 7-1b shows the damage zone created beneath the contact as a concentration of white crazing in a hemispherical shape. When compared to an indentation from a 3kN load shown in Figure 7-2 it is immediately apparent that the damage zone produced by the higher load is substantially larger. As well as being greater in extent the damage caused by the greater load also appears more intense. Similar results were found [102] for a very fine grained silicon nitride shown in Figure 3-6.

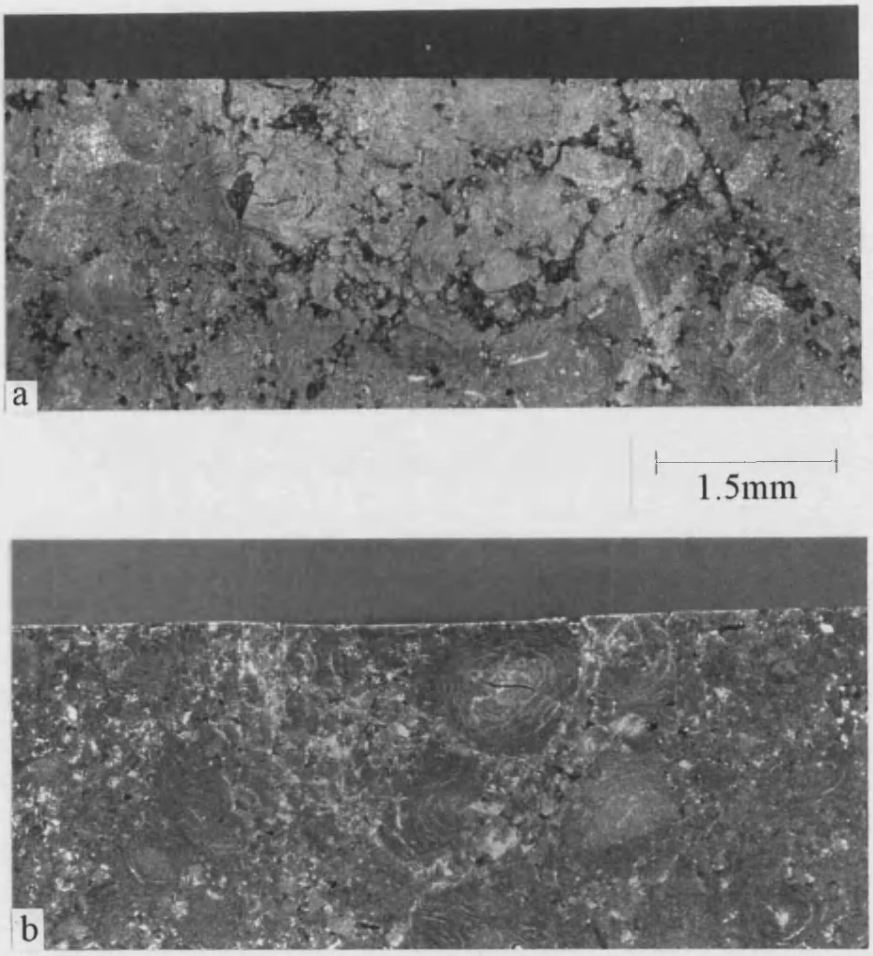

Figure 7-1 : Bonded interface micrograph of IM1-24 graphite after 2kN indentation load cycle taken using incident illumination, a, surface, b, cross section.

The indentation surface appears brighter in Figure 7-2 as though it has been polished in some way. A possible explanation is that the greater stress has allowed more shearing to take place at the surface during slip between the indenter and the graphite. Relative motion will occur between the two surfaces because of the elastic mismatch of the two materials (see Chapter 3).

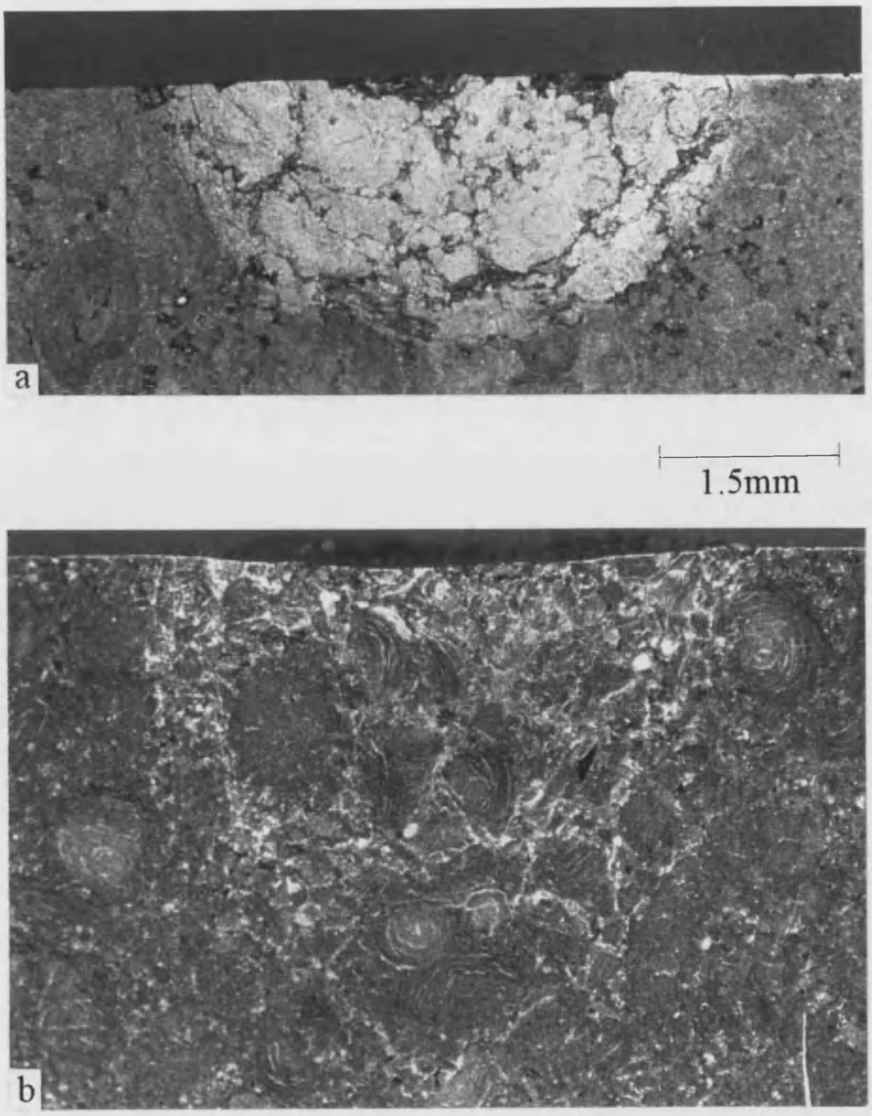

Figure 7-2 : Bonded interface micrograph of IM1-24 graphite after 3kN indentation load cycle taken using incident illumination, a, surface, b, cross section.

The stress distribution beneath a spherical indenter is illustrated well in Figure 7-3, which shows the indentation of Perspex with a 6mm diameter tungsten carbide sphere viewed under polarised light. The different coloured regions represent areas of equal stress magnitude, showing the hemispherical shape of the stress distribution. As the modulus of Perspex is only 3GPa [115] the sphere is effectively incompressible thus the loading geometry closer to that for graphite than that defined in the Hertzian assumptions. Despite this the distribution of stresses appear very similar to that predicted by Hertz so it is reasonable to use Hertzian mechanics to determine the shape of the stress distribution if not the magnitude. So it is not surprising that the damage zone is roughly hemispherical.

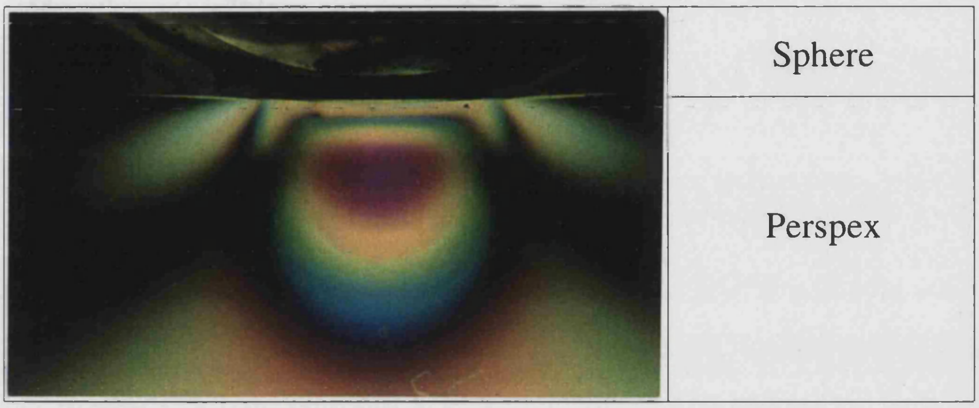

Figure 7-3 : Stress distribution in Perspex beneath a blunt indenter [115].

The damage can be seen more clearly in Figure 7-4 demonstrating the vast difference between this kind of damage zone and the classical Hertzian fracture seen in glass (Figure 3-3). The fracture appears to have occurred primarily by linking porosity, although in places the Gilsocarbon filler particles have also been fractured. Despite the severity of the microstructural damage it is confined to a fairly small region roughly as deep as the contact diameter. Whereas with Hertzian fracture the crack propagates orthogonally to the maximum tensile stress, the damage to IM1-24 graphite is most likely due to the shear stresses produced on the faulting planes beneath the indenter (see Chapter 3 page 55). Figure 3-7 shows the contours of net shear stress for a spherical contact using a poissons ratio of 0.29. The shape of the damage correlates quite well with the predicted shear stress envelope despite the inaccuracies introduced by treating graphite as an elastic solid, although the damage zone is more elongated than might be expected. This is very likely due to the coarse microstructure of IM1-24 graphite. When a crack propagates through a filler particle or a region of binder, the distance it is displaced from the region of maximum stress may be quite large producing a far less uniformly shaped damage zone. Figure 3-6 shows that the minimum damage occurs in the region just below the surface, corresponding to a region of hydrostatic compression in Figure 3-7. However, the damage is, if anything, more intense at the surface in IM1-24, which may be accounted for by the large scale of the microstructure allowing crack propagation away from the maximum stress trajectories.

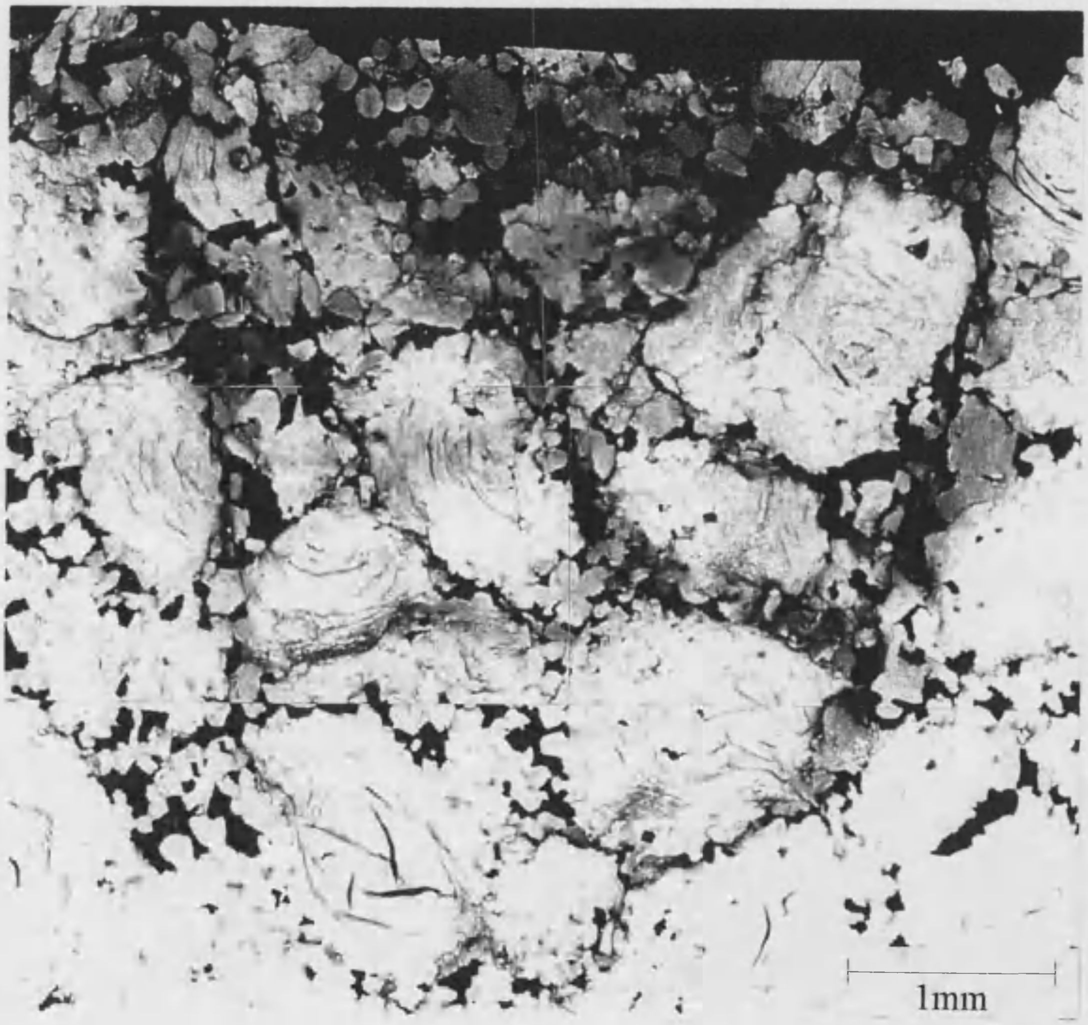

Figure 7-4 : Damage produced in IM1-24 graphite by a 3kN blunt indentation shown here using the bonded interface technique.

If the graphite is loaded to failure and the microstructure within the damage zone compared with that outside, a clear difference is evident. Figure 7-5 shows the fracture surface outside the indentation region. The fracture morphology is very similar to that for fast fracture as one would expect if a crack were initiated by tensile stresses, for example in a bend test. However, roughly in the centre of the damage zone the microstructure appears flattened into large flakes (see Figure 7-6) as though the graphite has been sheared. Similar fracture surfaces were observed by Neighbour [109] in compressive fracture of IM1-24 graphite and attributed to shear stresses.

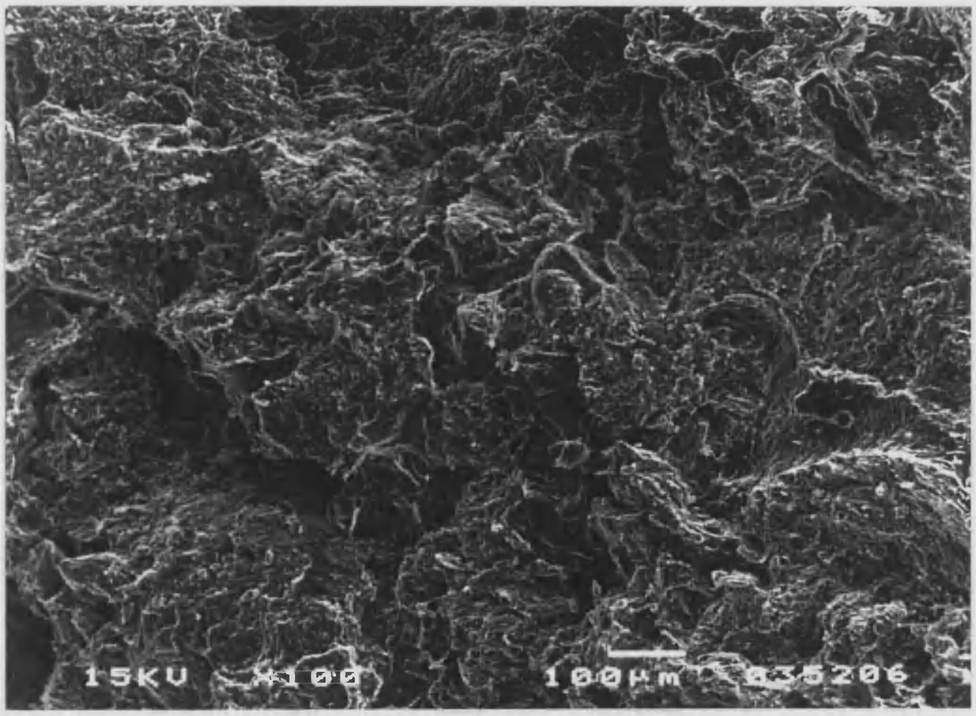

Figure 7-5 : Fracture surface of IM1-24 graphite away from the indentation region.

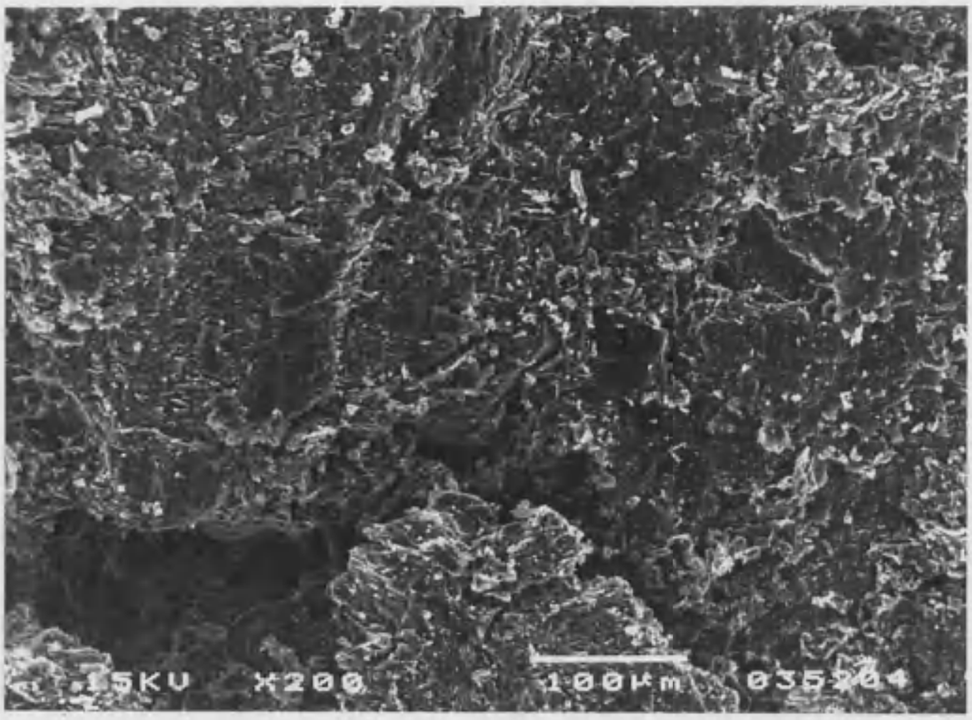

Figure 7-6 : Fracture surface of IM1-24 graphite roughly in the centre of the indentation damage zone.

It seems likely that catastrophic failure is initiated by the tensile stresses produced at the edge of the contact propagating downwards around the damage zone as shown schematically in Figure 7-7. The difference between the microstructures inside and outside the damage zone lends some support to this argument as there is strong evidence of shear inside the damage zone whereas outside the microstructure strongly resembles that of a fracture initiated by tensile stresses.

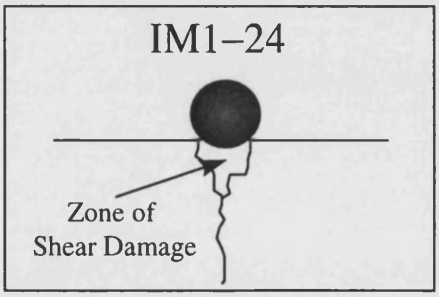

Figure 7-7 : Schematic of damage zone showing crack patterns.

7.2 Cyclic Loading

From Figure 7-1 and Figure 7-2 it is apparent that the damage caused by blunt indentation increases with increasing load, as would be expected. This effect is clearly seen in the series of load indentation depth traces in Figure 7-8. A notable feature of these traces is the hysteresis on unloading which increases greatly as the load is increased. It is also worth noting that, although each test was carried out on a different sample the loading part of the cycles lie practically on the same curve.

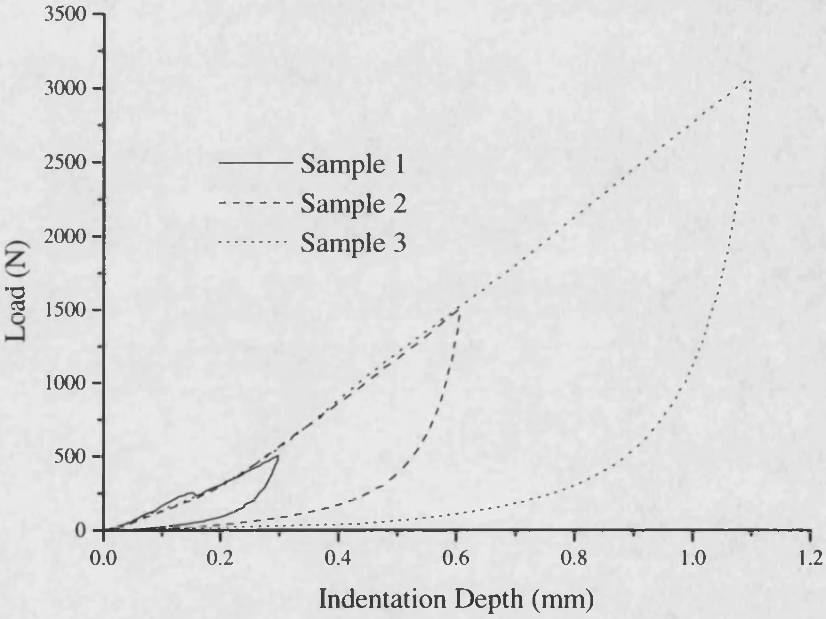

Figure 7-8 : Cyclic Loading of IM1-24 graphite.

The area of a hysteresis loop represents the amount of energy dissipated during the loading cycle. Evidently, the hysteresis is associated with the damage occurring during cyclic loading and the area under the hysteresis can be used as a quantitative measure for the damage taking place. Figure 7-9 shows hysteresis loop area as a function of load for a series of cyclic loading tests. The results indicate that the damage induced increases with increasing load in a non linear manner, as might be expected for graphite.

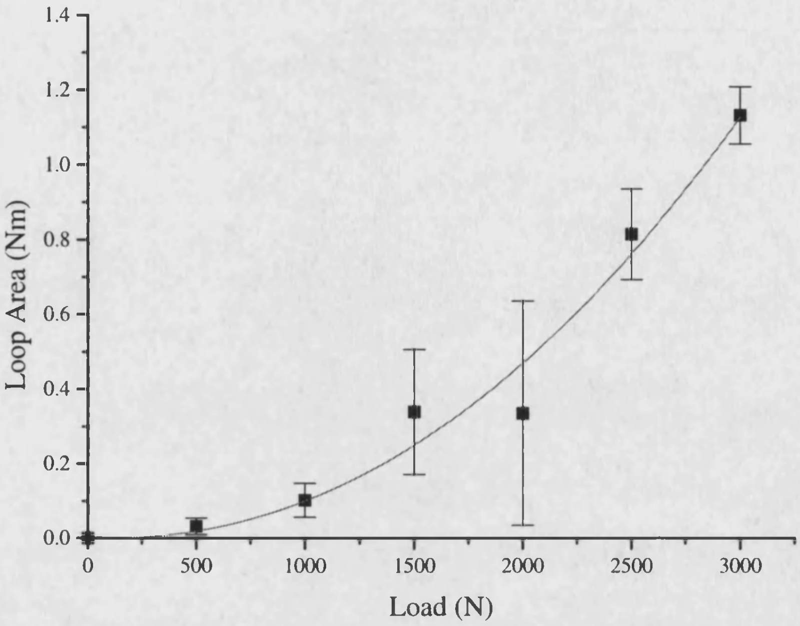

Figure 7-9 : The effect of indentation load on hysteresis loop area, error bars show ± two standard deviations.

Figure 7-10 shows the hysteresis loops for ten load cycles between 0 and 2kN and Figure 7-11 shows the hysteresis loop area as a function of the number of cycles. It is immediately apparent from Figure 7-10 that there is a large permanent set after the first cycle similar to that reported for more conventional mechanical tests [15, 20]. The permanent set increases progressively with the number of load cycles while, the hysteresis loops are fairly uniform in size and shape. Hysteresis loop areas decrease rapidly after the first cycle and the decrease more gradually tending towards a limiting value, Figure 7-11. This suggests that the initial cycles do more damage to the graphite than the later ones.

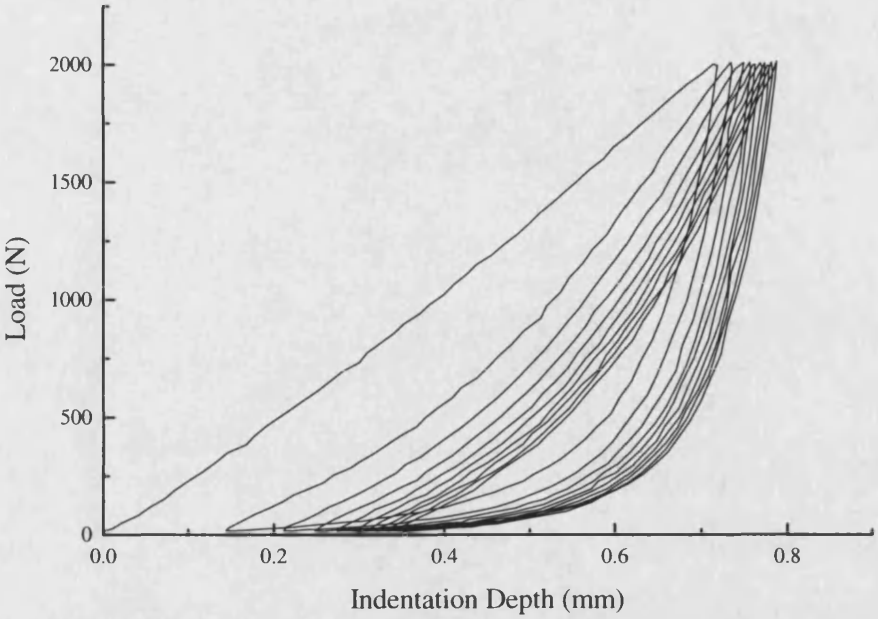

Figure 7-10 : Indentation load cycling for IM1-24.

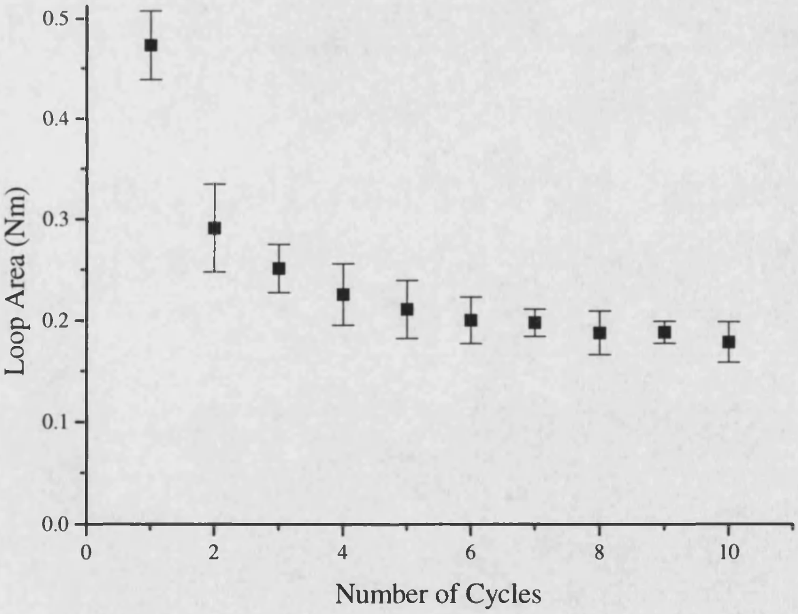

Figure 7-11 : Change in hysteresis loop areas for repeated load cycles.

There appears to be a low cycle mechanical fatigue effect which is caused by damage accumulation in the graphite. It is possible that much of the shear damage occurs in the first few load cycles giving rise to the larger hysteresis loops (see Figure 7-11), then as the size of the loops decrease to a limit, crack propagation is occurring with each cycle. So as the load cycles are repeated longer range cracks are driven through and around the already present shear damage zone. Thus it is possible that there are three stages to the mechanical fatigue exhibited here, which are similar to those seen under more conventional loading. Figure 7-12 shows the variation of crack growth rate with cyclic stress intensity, ΔK, for a conventional fatigue test, where ΔK is defined as the stress intensity at the maximum load minus the stress intensity at the minimum load [116].When the crack is initiated there is a rapid increase in the crack growth rate, which could correspond to the initial blunt indentation load cycle in Figure 7-11. At intermediate stress intensities there is a steady state regime that may correspond to the limit that is reached by approximately five cycles in Figure 7-11.

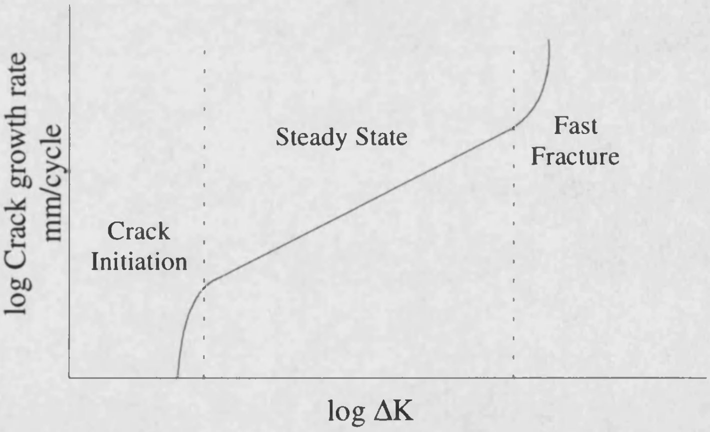

Figure 7-12 : Graph showing the relationship between fatigue crack growth and cyclic stress intensity.

The idea of low cycle mechanical fatigue can be supported with microstructural evidence. Figure 7-1 shows that damage occurs during a single 2kN load cycle although when sectioned and polished in the conventional manner rather than using the bonded interface method there is no evidence of any damage zone. However after ten 2kN loading cycles cracking around the damage zone is clearly visible (see Figure 7-13), and is marked as a-b and c-d. Substantial cracking is also visible at the centre of the indentation linking pores following the path of least resistance. This supports the idea that there is an element of mechanical fatigue. Hence it is plausible that during the steady state of crack growth rate long range cracks are being driven around the shear damage zone, which forms largely during the initial few cycles.

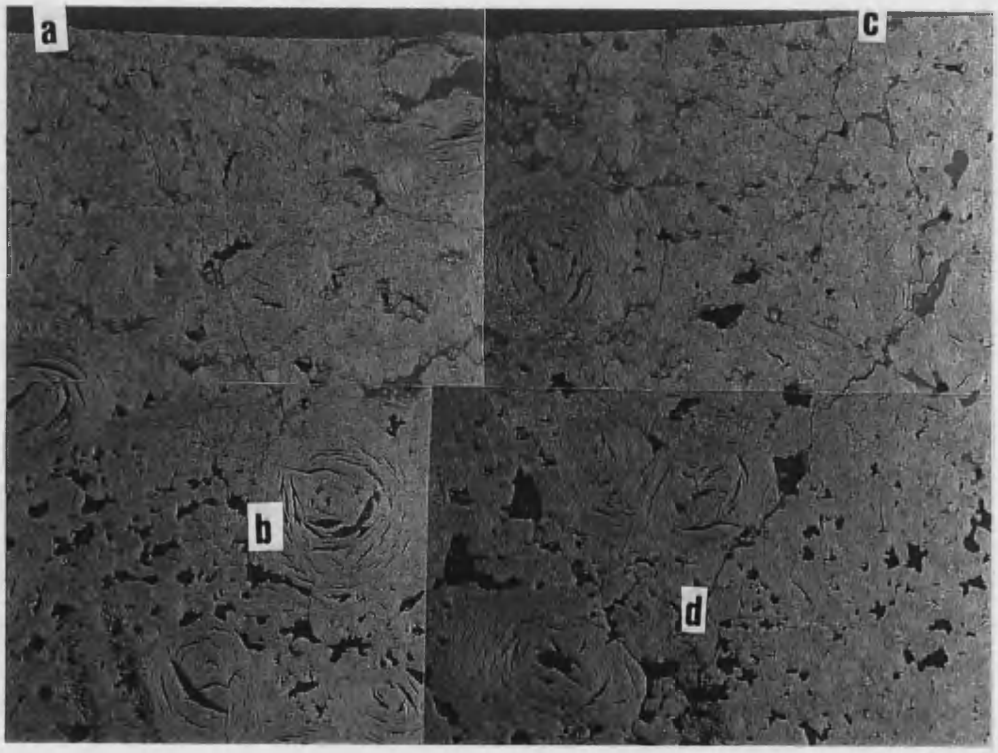

Figure 7-13 : Cross section of IM1-24 after 10 load cycles to 2kN, a-c shows the diameter of the contact, a-b and c-d mark crack paths.

7.3 Chapter Summary

After a blunt indentation test has been performed on IM1-24 graphite a hemispherical damage zone is evident directly beneath the indenter. Both the size and the intensity of the damage are increased by increasing the applied load. Microstructural evidence suggests that the damage zone is due largely to shear faulting. This is supported by similar findings for engineering ceramics [101, 102] and correlates well with the shape of the calculated stress distribution. When the tensile stresses at the edge of the indentation reach a critical level catastrophic fracture occurs, by crack propagation around the damage zone.

If a load cycle is performed, on unloading there is considerable hysteresis that increases as the load is increased. When a cyclic load is applied the degree of damage done by a single cycle rapidly decreases towards a limit, after which the damage per cycle remains approximately constant. This could be considered to be a form of low cycle mechanical fatigue. So, the regime of constant damage evolution could be considered to be the steady state regime of crack growth rate. There is some microstructural evidence to support the idea of a fatigue process. A well defined cone shaped crack pattern is not visible until approximately ten 2kN load cycles have been performed, suggesting that the repeated loading produces long range cracking.

8. The Effect of Microstructure on Blunt Indentation Damage

The bonded interface technique was used to view the damage produced by an indentation with a 6mm tungsten carbide sphere on a variety of different graphites, selected in order to cover a range of microstructures. The hysteresis loops produced on cyclic loading were then examined to provide quantitative information about the degree of damage in each graphite.

8.1 The effect of microstructural scale

The graphites used here are listed in Table 8-1 along with their average particle sizes to give an idea of the scale of the microstructure (see Chapter 4).

Graphite	**Average Particle Size (μm)**
IM1-24	500
ATJ	25
EY306	10
Poco AXF	5
Poco ZXF	1

Table 8-1 : Average particle size of graphites.

8.1.1 Mechanical Testing

Load cycles to 3kN for the first four graphites in Table 8-1 are plotted in Figure 8-1. As the particle size is increased (AXF to IM1-24) the load for a given indentation depth decreases, which is due to the reduction in mechanical properties. The loading curves are similar in form, having an initial non-linear region then becoming close to linear until the point of unloading is reached. The indentation depths when the loading curves become close to linear are, AXF = ~0.1mm, EY306 = ~0.21mm, ATJ = ~0.27 and IM1-24 = ~0.33. Hence, the non-linear region becomes larger as the particle size is increased. On unloading there is considerable hysteresis evident in all cases, that increases as the particle size is increased.

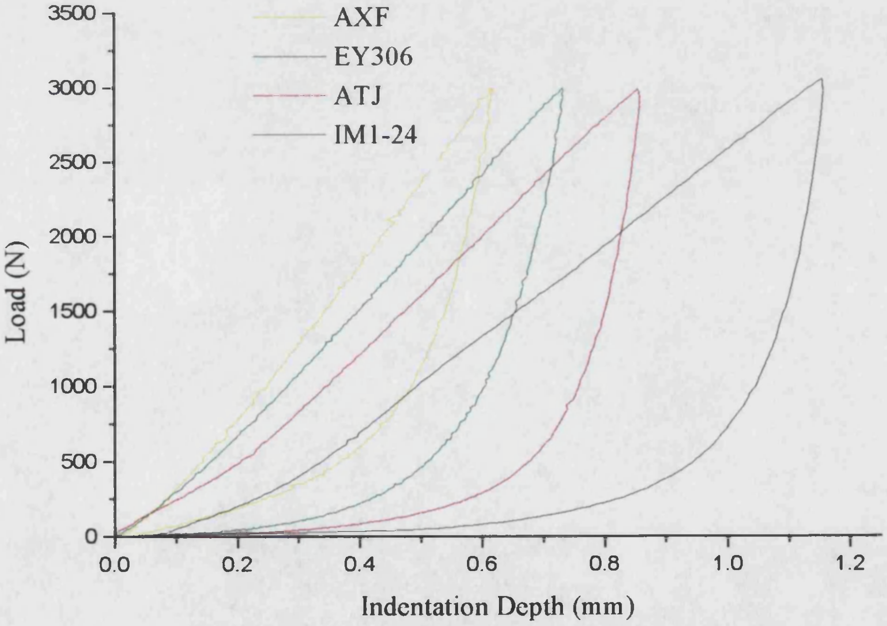

Figure 8-1 : 3kN load cycles for AXF, EY306, ATJ and IM1-24 graphites.

Figure 8-2 shows the effect of increasing load on the degree of hysteresis for the first four graphites in Table 8-1. As the load is increased the difference between the graphites becomes greater so that by 2kN load a clear trend is visible. Suggesting that the larger the microstructure, the greater the hysteresis and hence the degree of damage for a given load.

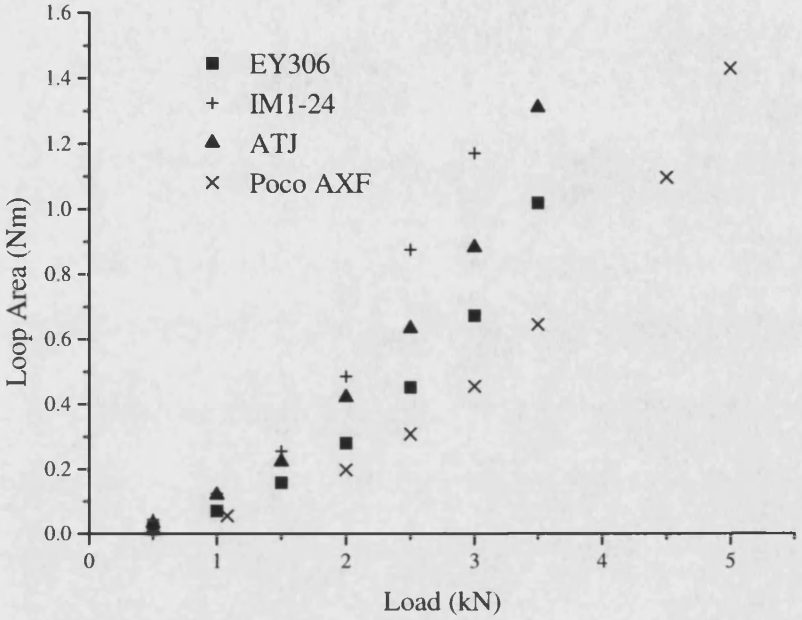

Figure 8-2 : The effect of load on hysteresis loop area for IM1-24, ATJ, EY306 and Poco AXF graphites.

However these differences could be due at least in part to the different strengths and moduli of the various graphites (see Chapter 4) rather than simply to the effects of microstructure. One way of normalising for the mechanical properties is to calculate the fraction of permanent deformation in each material by considering the load displacement trace. A schematic of a load cycle on graphite is shown in Figure 8-3 where line AB is the loading curve, the loop area is marked as C and the area under the loading curve, (triangle ABE) is marked as D. So, if a material exhibited total elastic recovery on unloading, the curve would return down AB, and conversely, if the deformation were entirely permanent, the curve would fall to point E on unloading.

Thus, the fractional permanent deformation can be represented by $\frac{C}{D}$, providing that there is always some hysteresis, and the fractional elastic recovery will be $1-\frac{C}{D}$.

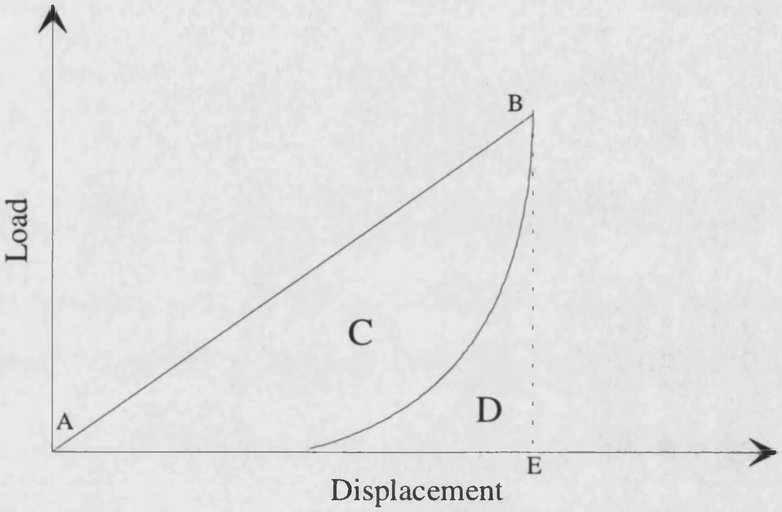

Figure 8-3 : Schematic of a load cycle on graphite.

The percentage permanent deformation for AXF, EY306, ATJ and IM1-24 graphites is shown as a function of indentation load in Figure 8-4. In general, for any given load the damage induced is greater in coarser graphites. However, the results for ATJ and IM1-24 lie very close the same line, which is surprising when the large difference between the sizes of the microstructure are considered. The curves are close to being linear and in general there is a slight difference in the gradients of the lines. This suggests that for a given increase in load, the increase in the quantity of the damage is greater for the graphites with a coarser microstructure, until a particle size of ~25μm (corresponding to ATJ graphite) is reached. At this point there is no further increase in the permanent deformation with increasing microstructural scale. When the percentage permanent deformation is plotted against percentage of the blunt indentation failure load (see Figure 8-5), the lines become almost parallel, demonstrating that the differences in slope in Figure 8-4 is caused by the disparity in indentation failure strength between the graphites. So the effect of increasing load on the degree of damage is the same for all the graphites. Figure 8-4 and Figure 8-5 show that for AXF, EY306, ATJ and IM1-24 graphites, the extent of deformation increases as the scale of the microstructure is increased.

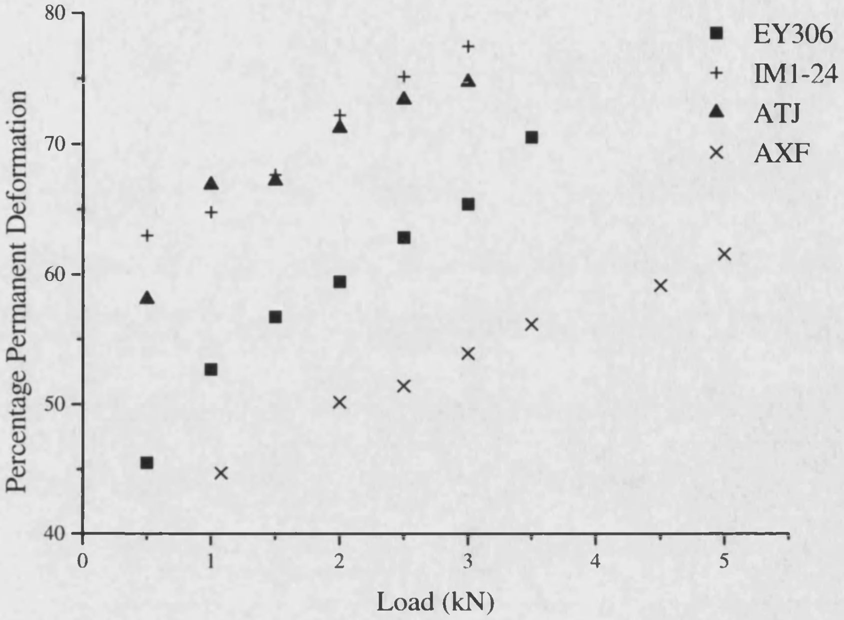

Figure 8-4 : The effect of indentation load on permanent deformation.

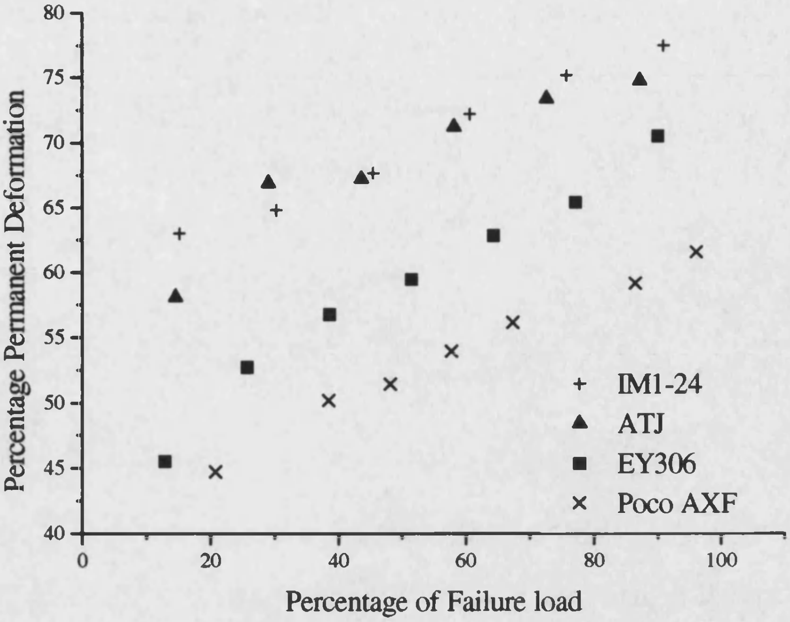

Figure 8-5: The effect of indentation load shown as a percentage of the indentation failure load on permanent deformation.

8.1.2 Bonded Interface Testing

The bonded interface technique is an extremely useful technique for elucidating the nature of subsurface damage resulting from a blunt indentation. Results for IM1-24 graphite were presented in Chapter 7, and show that a hemispherical damage zone evolves beneath the indenter before there is any evidence of cracking due to the Hertzian stresses. The technique has been utilised here to investigate the effect of microstructural scale on the nature of the damage produced by a blunt indentation.

Bonded interface test pieces were produced for the graphites listed in Table 8-1 and indented with 1, 2 and 3kN loads. Figure 8-6 shows the damage zone for the ATJ graphite which, although the depth of damage is slightly less, is similar in size and shape to the damage produced in IM1-24 graphite. The shape of the damage zone is the same as that seen elsewhere in polycrystalline ceramics, Lawn *et al* [102, 103], suggesting that it can be attributed to the shear forces present. A region of low damage intensity is discernible directly beneath the indenter contact which may have resulted from a region of hydrostatic compression (see Figure 3-7) limiting the degree of microcracking. As the mode of damage is essentially the same in both IM1-24 and ATJ graphites, it is not surprising that the degree of damage indicated by the mechanical testing (Figure 8-4 and Figure 8-6) is so similar.

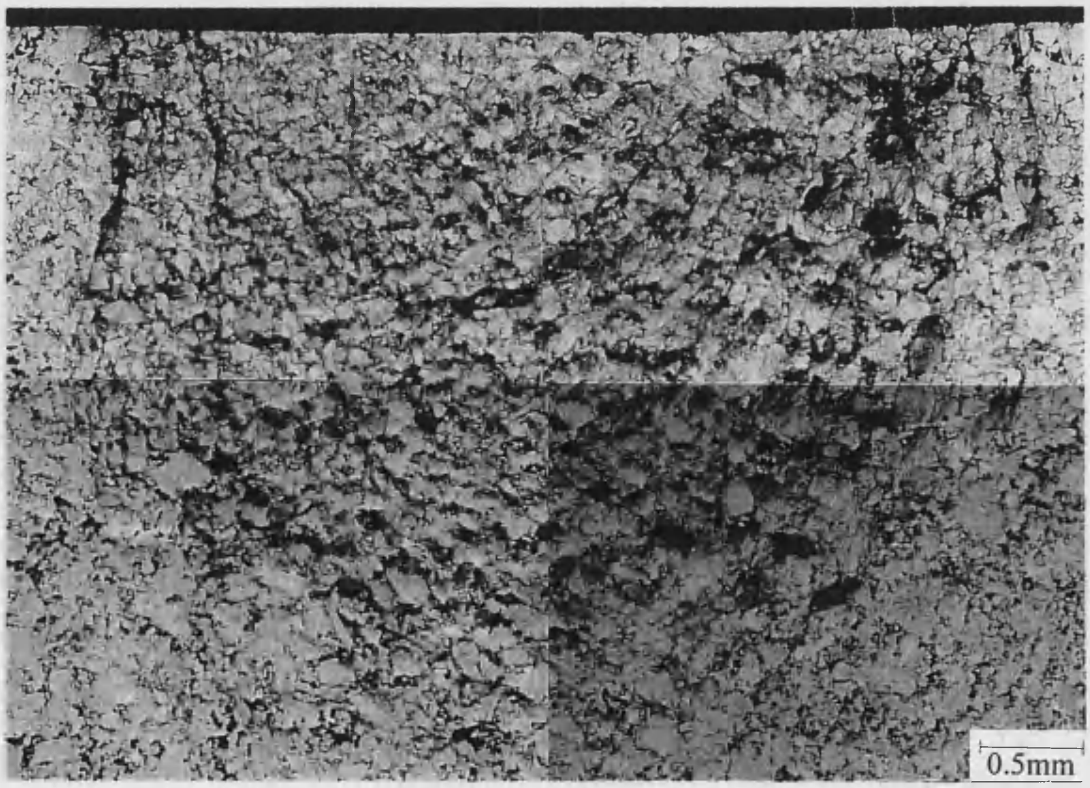

Figure 8-6 : Cross section of the damage zone in ATJ graphite produced by a 3kN load on a 6mm diameter sphere, (elucidated using the bonded interface technique).

When the size of the microstructure is reduced further as in EY306 graphite (see Figure 8-7) there is still an extensive shear damage zone after indentation, but with large cracks AB and CD running from the edge of the contact into the material. On fracture, the central cone (Figure 8-8) is ejected and remains intact, suggesting that the long range cracks AB and CD in Figure 8-7 cause failure by propagating around the damage zone. This is very similar to the fracture morphology for the indentation of IM1-24 with a 15mm diameter sphere (see Chapter 6). On examination of the fracture surfaces of the cone and the indentation region, shear damage is evident (Figure 8-9), whereas outside the indentation region (Figure 8-10) the fracture surface is quite different and very similar to a fracture initiated by a tensile stress (Figure 8-11). Figure 8-12 shows the damage zone produced in EY306 graphite by a 2kN load (as opposed to the 3kN load used in Figure 8-7) demonstrating that the shear zone forms before the large cracks are initiated. So it seems likely that there are two fracture mechanisms taking place in IM1-24, ATJ and EY306graphites.

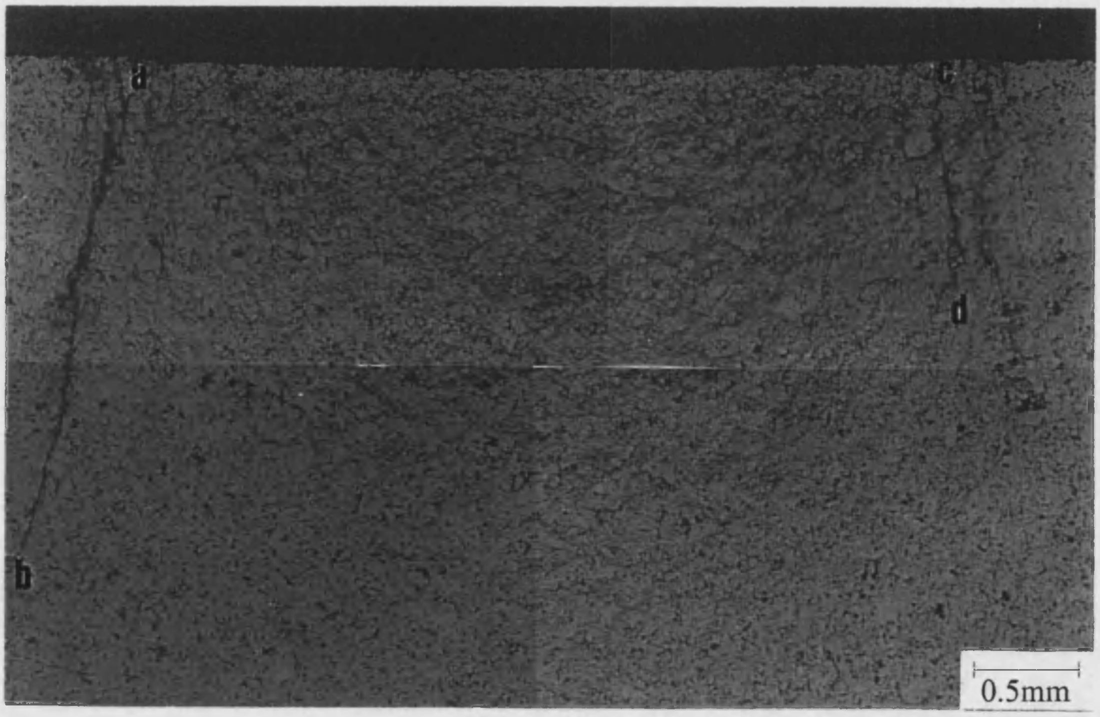

Figure 8-7 : Damage zone in EY306 graphite produced by a 3kN load on a 6mm diameter sphere, (elucidated using the bonded interface technique).

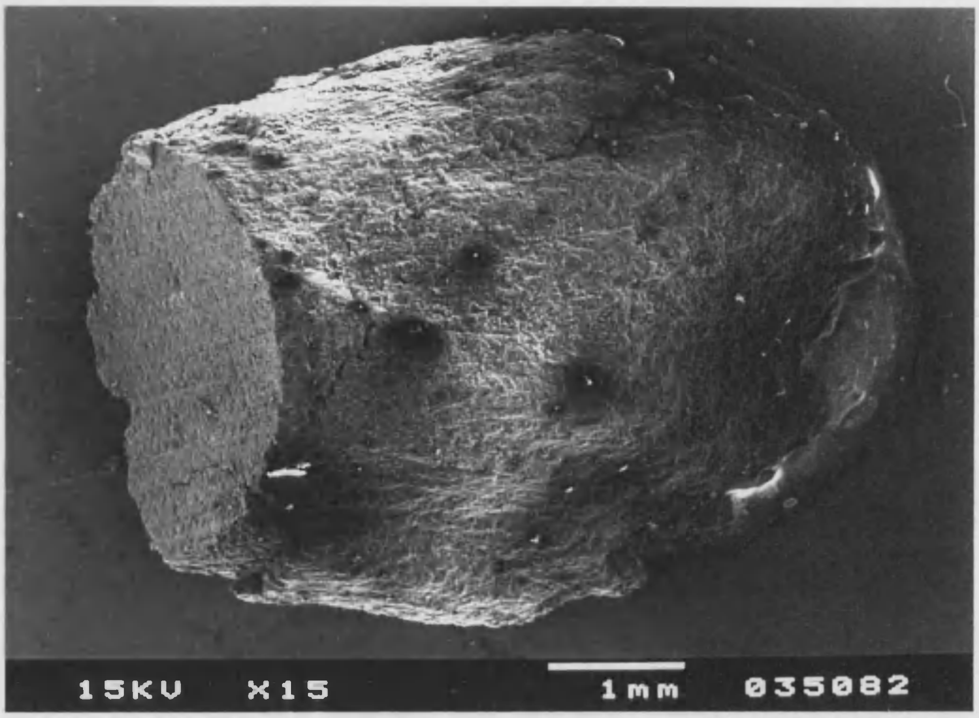

Figure 8-8 : Cone ejected from EY306 graphite when loaded to failure with a 6mm diameter sphere.

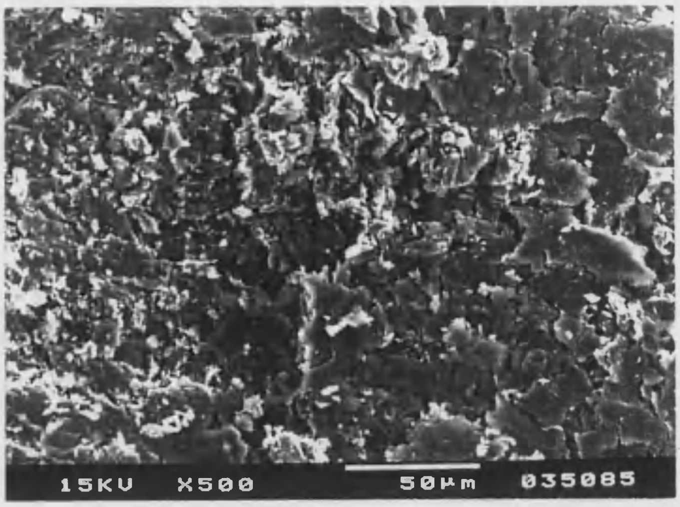

Figure 8-9 : EY306 fracture morphology in the centre of the indentation region.

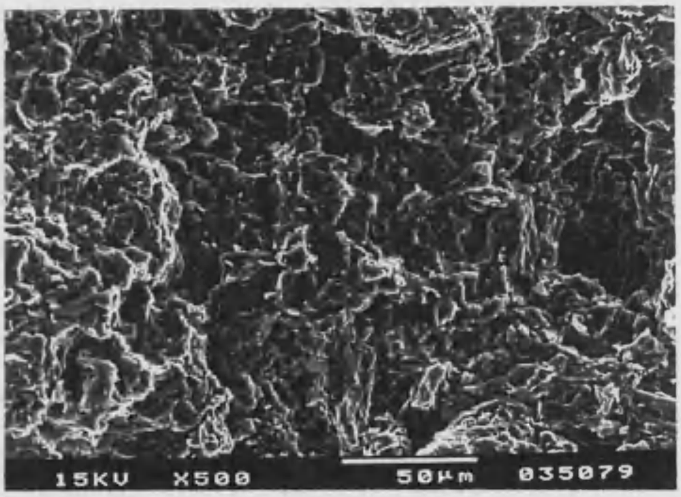

Figure 8-10 : EY306 fracture morphology outside the indentation region.

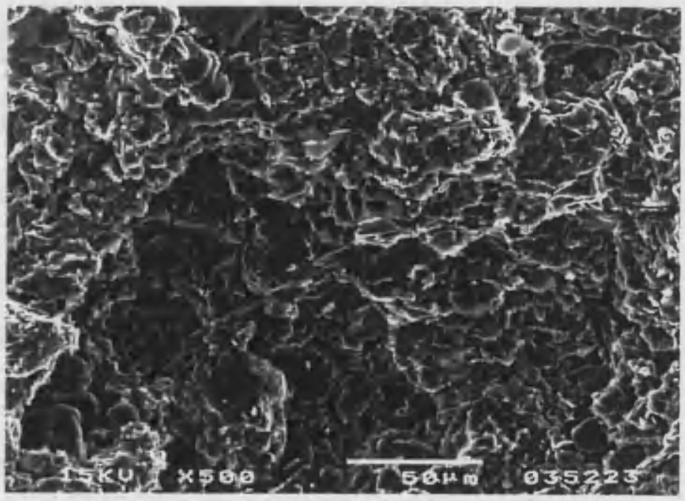

Figure 8-11 : EY306 fracture morphology for 3 point bend.

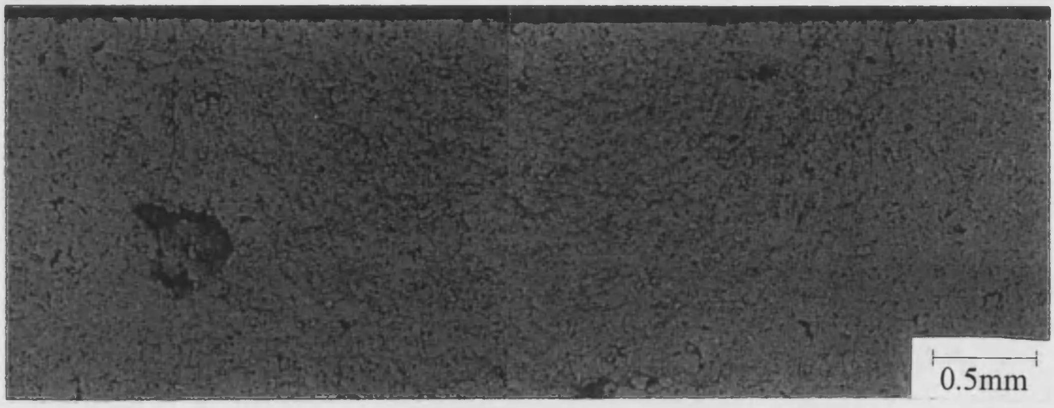

Figure 8-12 : Damage zone in EY306 graphite produced by a 2kN load on a 6mm diameter sphere, (elucidated using the bonded interface technique).

Initially, at low loads the shear stresses developed beneath the indenter cause shear deformation and microcracking in the shear stress zone (see Figure 8-13A) . As the load is increased the tensile stresses produced at the edge of the contact reach a critical value and initiate cracks that ultimately cause failure (see Figure 8-13B). However instead of the tensile cracks forming a classical diverging Hertzian cone crack, they interact with the damage zone created by the shear stresses to form a converging cone crack (see Figure 8-13C). On fracture the cone of material formed by this crack can sometimes remain intact when ejected from the graphite sample (see Figure 8-8). The idea of this process leading to catastrophic fracture is supported by Figure 8-14 which shows the fully developed crack pattern just before failure occurs in FGEX graphite (this graphite will be discussed in more detail in the next section).

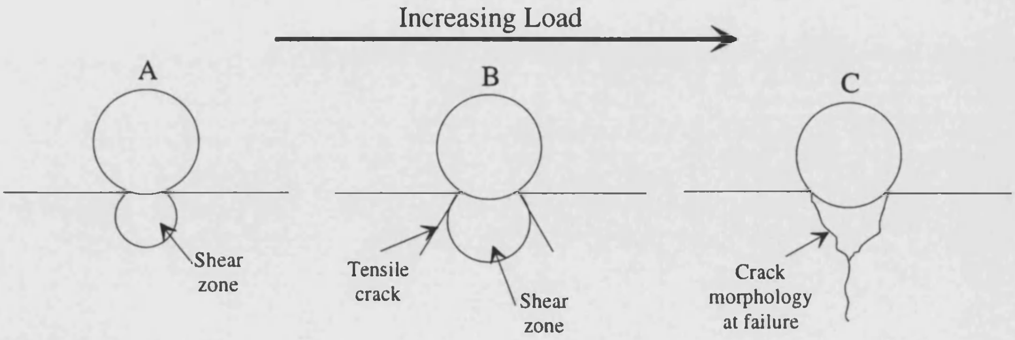

Figure 8-13 : Schematic showing the fracture of IM1-24, ATJ and EY306 graphites.

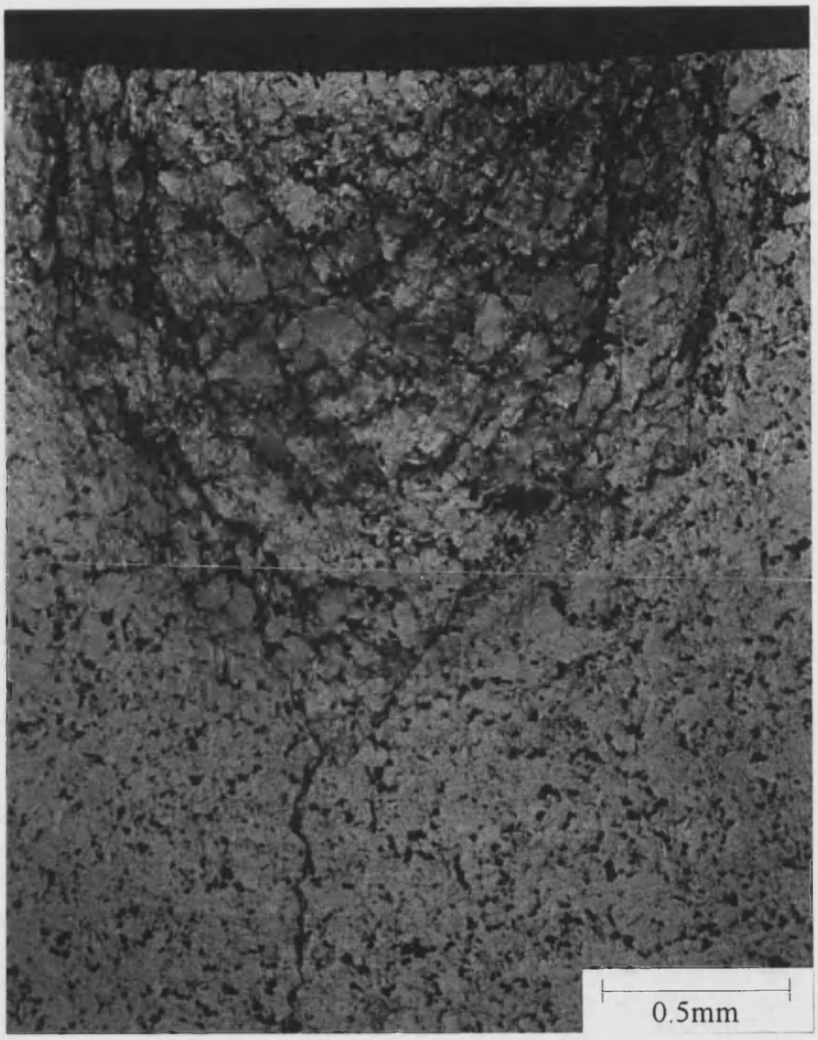

Figure 8-14 : Damage zone in FGEX graphite just before failure after approximately a 2.5kN load indentation.

When the fine textured Poco AXF is examined optically after indentation to 3kN load (Figure 8-15) only cracks at the edge of the contact zone are evident and there is no evidence of a shear damage zone. The fracture mode is very similar to the formation of a classical Hertzian cone crack. The cracks propagating outwards orthogonal to the maximum tensile stress (Figure 8-16), leaving a fracture surface that is level in the centre with no material ejected as was found for IM1-24, ATJ and EY306 graphites. On the right hand side of Figure 8-16 pieces have chipped away from the surface, but there is no evidence of the cracking following a pre-existing damage zone. However, when the fracture surface is examined in the centre of the indentation region (Figure 8-17) and compared to the fracture morphology outside the indentation region (Figure 8-18), there is evidence of shear deformation in places.

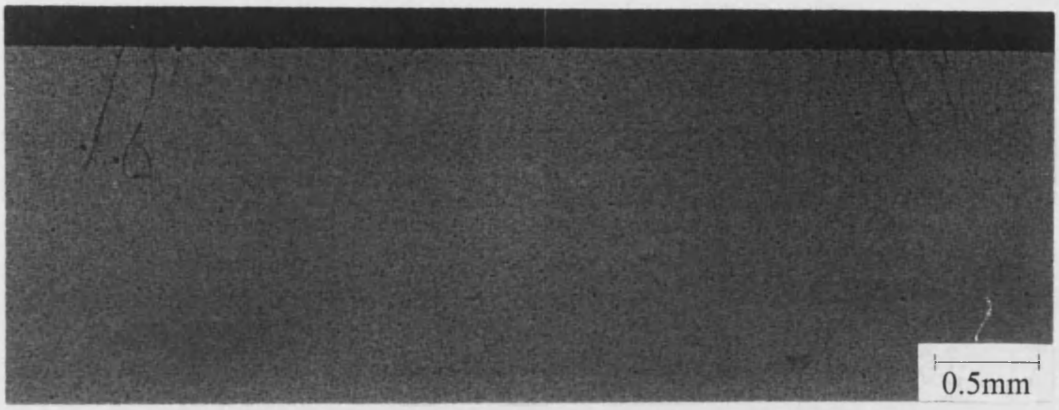

Figure 8-15 : Fracture in Poco AXF graphite produced by a 3kN load on a 6mm diameter sphere, (elucidated using the bonded interface technique).

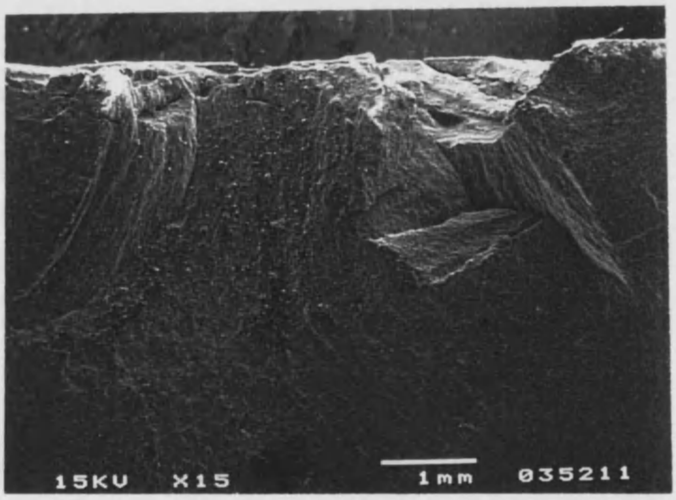

Figure 8-16 : Fracture morphology in Poco AXF beneath a 6mm diameter sphere.

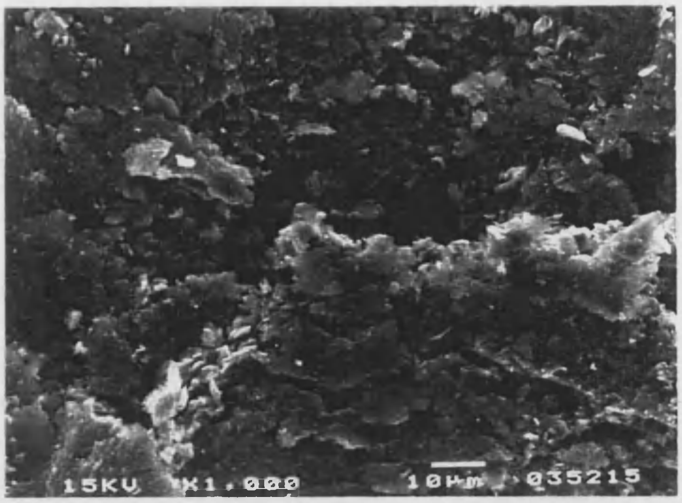

Figure 8-17 : Poco AXF fracture morphology in the centre of the indentation region.

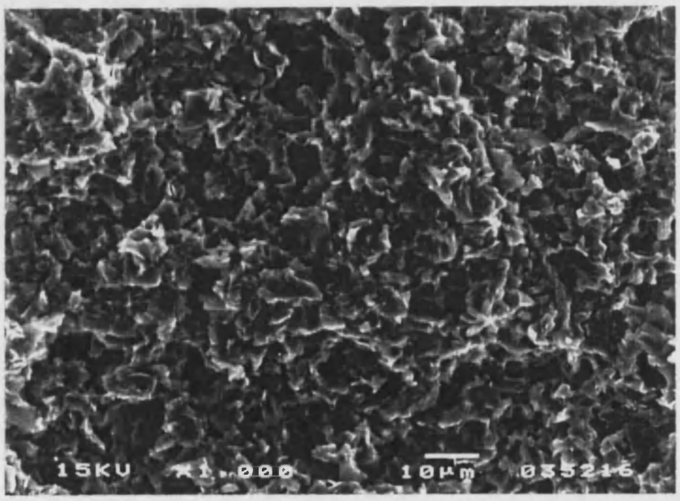

Figure 8-18 : Poco AXF fracture morphology outside the indentation region.

Figure 8-19 shows a classical Hertzian cone crack in the very fine textured Poco ZXF graphite, similar to that seen in glass (Figure 3-3). The higher magnification in Figure 8-20 shows the initial downward propagation of the crack which occurs when a critical tensile stress is reached, followed by the formation of a cone as the stress is increased. On examination of the fracture surfaces there is no evidence of the shear deformation found for the previous graphites. Hence, it is likely that the Hertzian equations could be used to calculate the mechanical properties of Poco ZXF graphite from a similar test, providing a method of accurately determining the load at which the ring crack is formed could be found.

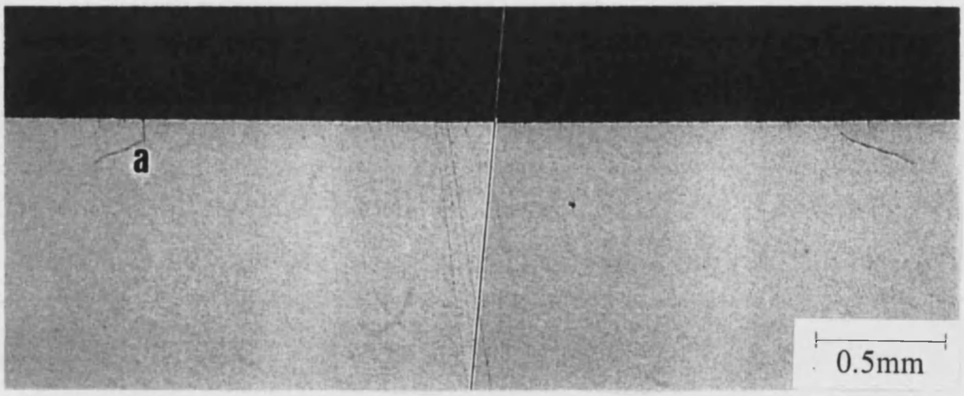

Figure 8-19 : Cracking in Poco ZXF produced by a 3kN load indentation with a 6mm diameter sphere (elucidated using the bonded interface technique).

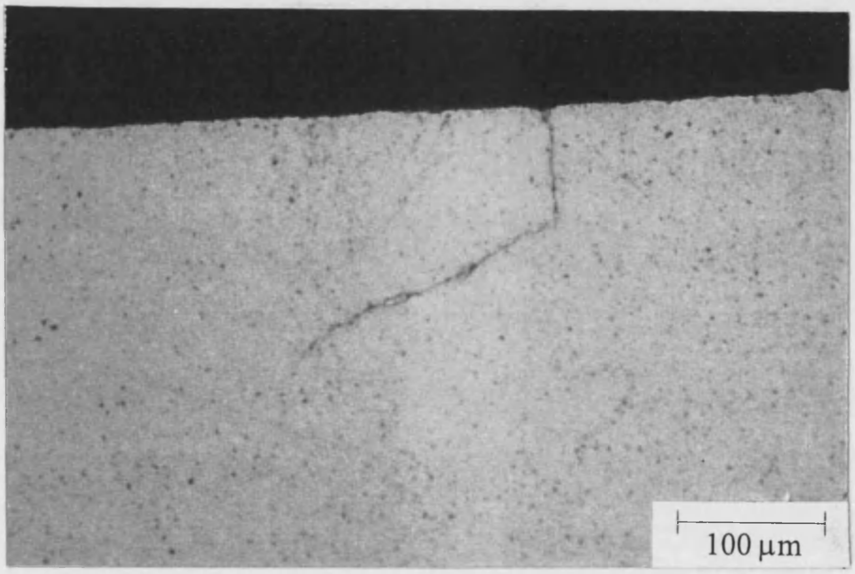

Figure 8-20 : Increased magnification of crack a in Figure 8-19.

A transition in behaviour as the size of the microstructure is increased is clearly visible when Figure 8-6, Figure 8-7, Figure 8-15 and Figure 8-19 are compared. This is summarised schematically in Figure 8-21. The very fine textured Poco ZXF graphite behaves as an isotropic elastic solid, and fractures in a classical Hertzian manner (Figure 8-21a). As the size of the microstructure is increased, a transition in behaviour is visible (Figure 8-21b) where fracture in the Hertzian direction is still evident, but a shear damage zone is also visible beneath the sphere. When the size of the microstructure is increased further, there ceases to be any evidence of Hertzian type cracking (Figure 8-21c) and only shear damage is visible.

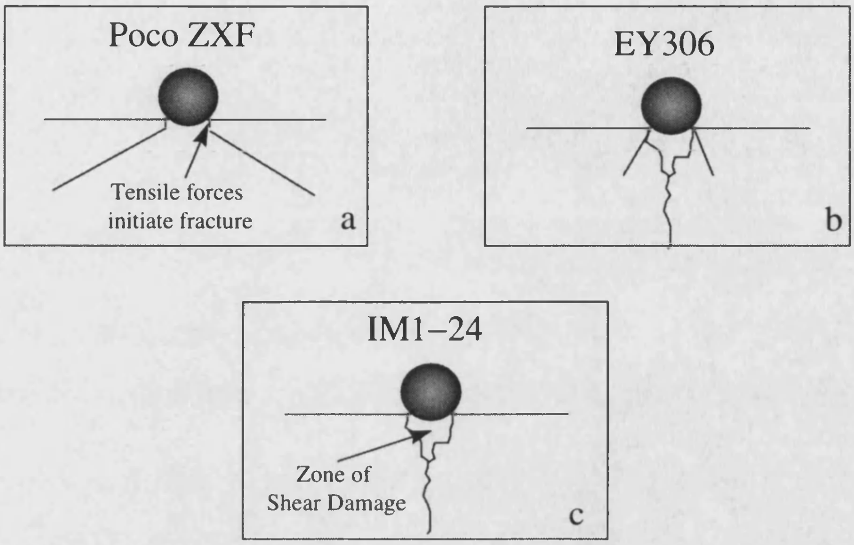

Figure 8-21 : Summary of the effect of microstructure in the indentation damage in graphite.

Other researchers [101, 102] have found that a shear damage zone is produced in polycrystalline ceramics by blunt indentation. The mechanism identified was the development of a shear fault across the grain ultimately leading to microcracking, often along the grain boundaries. For work on the indentation of pyrolitic graphite [117] the suggested explanation for the non-linearity exhibited, was frictional sliding of the graphite planes constrained by the indentation pressure. So, again, the deformation seen on this very fine scale in pyrolitic graphite appears to be a shear zone, as found for polcrystaline ceramics. The explanation for the transition in behaviour from Hertzian cracking to shear deformation given by Lawn et al. [106] would seem to apply here. The two reasons suggested were.

1. Cone fracture is suppressed at larger grain sizes by increasing deflection of the downward propagating crack away from the principal stress trajectories that

otherwise drive the crack into a cone. So as these deflections are greater there is an increased tendency for the crack to arrest.

2. The subsurface microfracture in the shear zone is enhanced at larger grain sizes, because of an increased stress concentration at the shear fault edges. Lawn et al. [106] found that the stress intensity scaled with $d^{1/2}$ when they treated the fault as a simple shear crack extending across a grain of diameter d.

8.2 The effect of porosity

In order to try and separate the effects of porosity on the evolution of blunt indentation damage from the effects of microstructure, three graphites (see Table 8-1) with nominally identical microstructures, but with different quantities of porosity were used. The porosity in the graphite was varied by impregnation with pitch followed by graphitisation (see Chapter 2). Also, the graphite was formed by extrusion, so providing the opportunity to investigate the effect of microstructural orientation.

Graphite	Average Particle Size (μm)	Total Porosity (%)	Number of Impregnations
SF53	70 x 150	30	0
FGE	70 x 150	25	1
FGEX	70 x 150	22	2

Table 8-2 : Porosity of UCAR graphites.

Figure 8-22, Figure 8-23 and Figure 8-24 show the damage created by an indentation with a 6mm diameter sphere to a load of 1kN perpendicular to the extrusion direction. A comparison of the figures immediately shows that, as the quantity of porosity is decreased, the size and intensity of the damage zone is reduced. This can be explained by considering the increase in elastic modulus that will accompany a decrease in porosity. At any given load the stress field produced in SF53 will be larger than that in FGE, which is larger than the stress field in FGEX, because of the respective increase in modulus (see Chapter 4).

Figure 8-22 : Damage produced in SF53 by a 1kN indentation on a bonded interface sample with a 6mm diameter sphere perpendicular to the extrusion direction, (25% porosity).

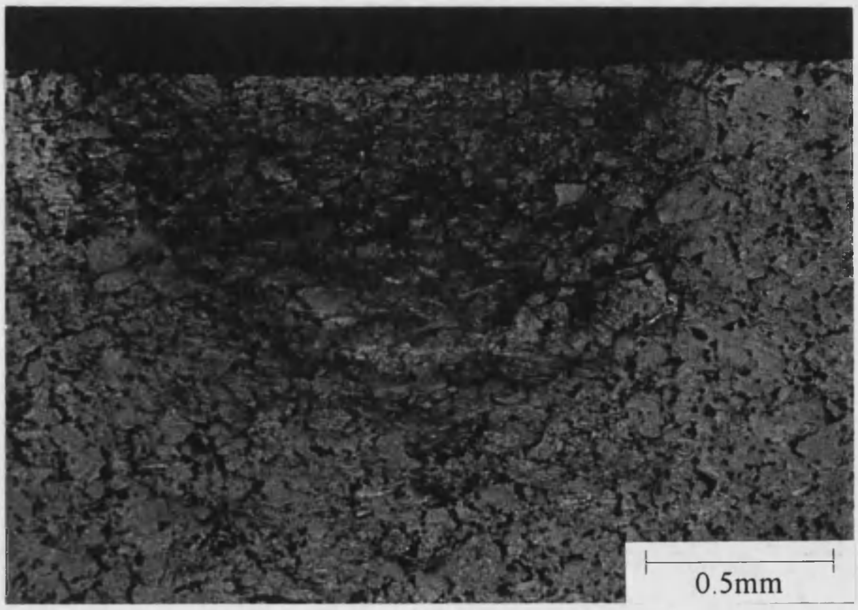

Figure 8-23 : Damage produced in FGE by a 1kN indentation on a bonded interface sample with a 6mm diameter sphere perpendicular to the extrusion direction, (20% porosity).

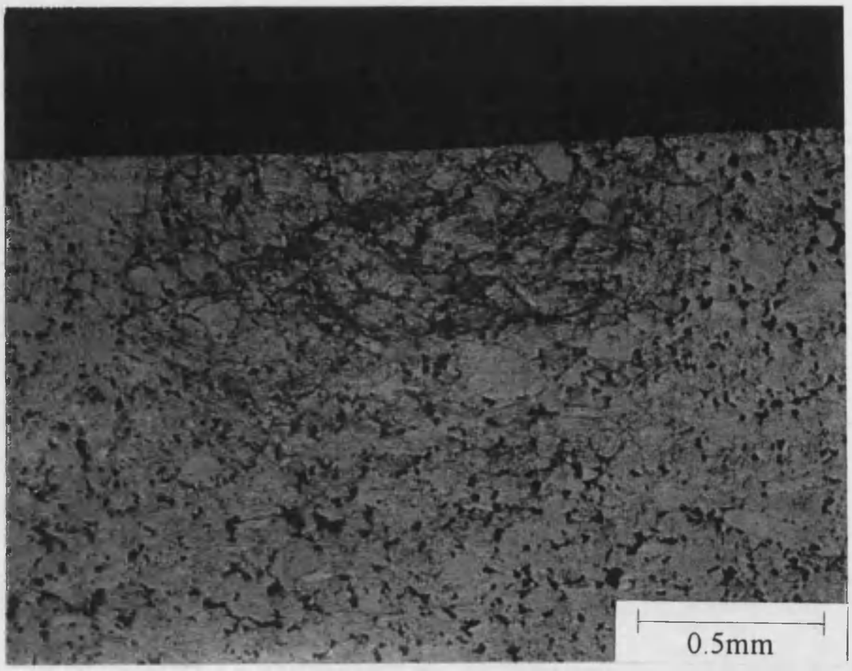

Figure 8-24 : Damage produced in FGEX by a 1kN indentation on a bonded interface sample with a 6mm diameter sphere perpendicular to the extrusion direction, (14% porosity).

The permanent deformation was calculated in the same way as in the previous section, which will normalise for the mechanical properties. The effect of porosity on the permanent deformation produced by a 1kN indentation is shown in Figure 8-25, and a general increase in the permanent deformation with increasing porosity is evident. This can be viewed with a probabilistic approach. As more pores are introduced into the graphite, there is a greater probability of flaws above the critical size for microcrack initiation existing within the stress field. Thus, it is more likely that cracking will proceed at any given stress. As the pore density increases it also becomes more likely that a crack will propagate between pores at any given stress.

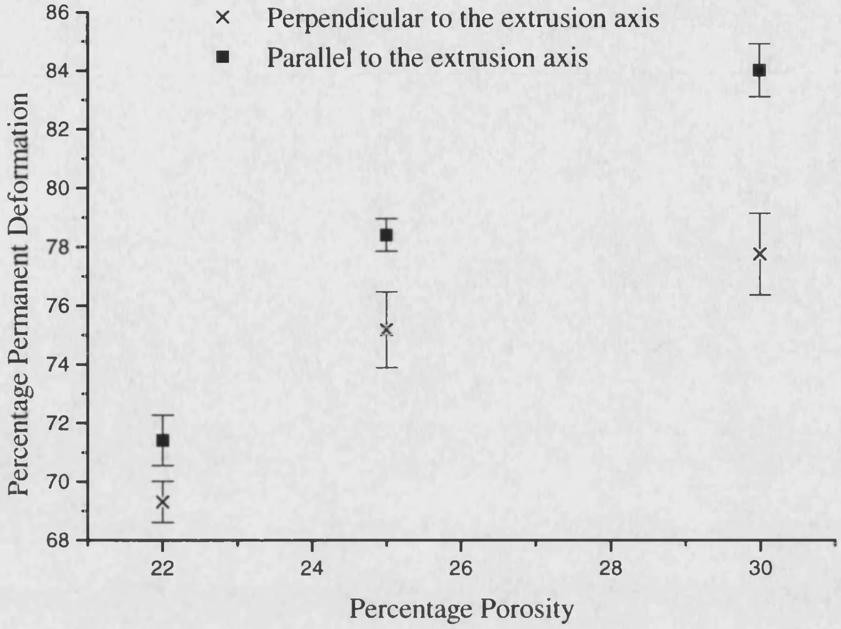

Figure 8-25 : The effect of total porosity on permanent deformation in graphite for a 1kN load.

The effect of microstructural orientation on the extent of permanent deformation can be seen in Figure 8-25. There is consistently more damage for a given load when the indentation is made parallel to the extrusion axis. Figure 8-26 and Figure 8-27 provide microstructural evidence of this showing visually that the damage is considerably more severe when the indentation is made parallel to the extrusion axis. The effect of microstructural orientation is likely to be due to the orientation of the filler particles. Burchell *et al* [42] reported that in nuclear graphite a crack will propagate through well graphitised filler particles if they are oriented with the graphitic planes approximately parallel to the crack. Whereas if the crack is perpendicular to the graphitic planes it will tend to propagate around the filler particle (Figure 2-15). Extruding graphite will tend to orient the filler particles so that the graphitic planes are approximately parallel to the extrusion axis. Thus, a crack propagating perpendicular to the extrusion axis is likely to have a more tortuous path than if it were parallel to the extrusion axis (see Figure 8-28) and consequently require more energy to propagate a set distance. Figure 8-25 also suggests that the effect of microstructural orientation increases with increasing porosity.

Hence, the difference between the damage in the two orientations is greater for the 30% porous graphite than for the 22% porous one.

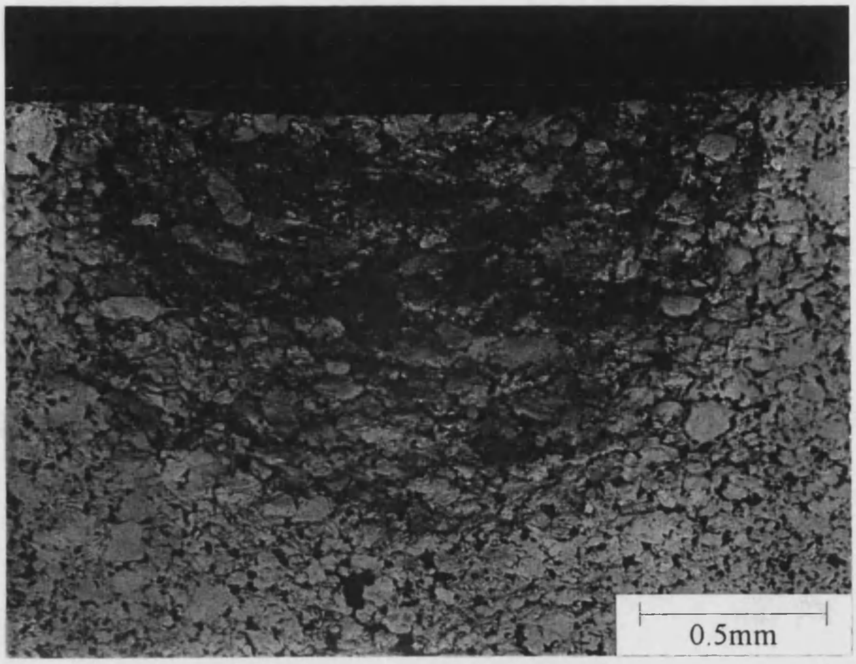

Figure 8-26 : Blunt indentation damage in SF53 produced by a 1kN load indentation perpendicular to the extrusion direction.

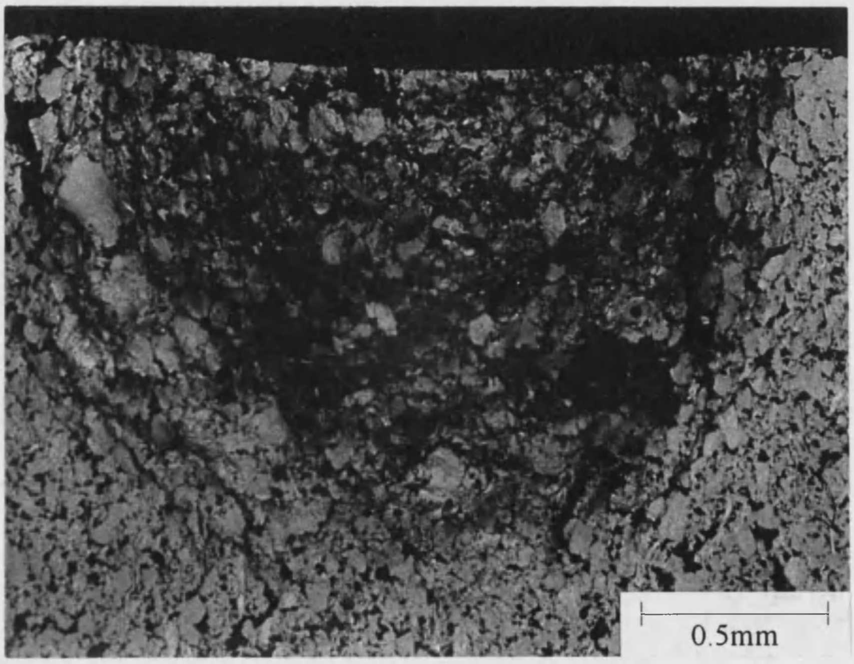

Figure 8-27 : Blunt indentation damage in SF53 produced by a 1kN load indentation parallel to the extrusion direction.

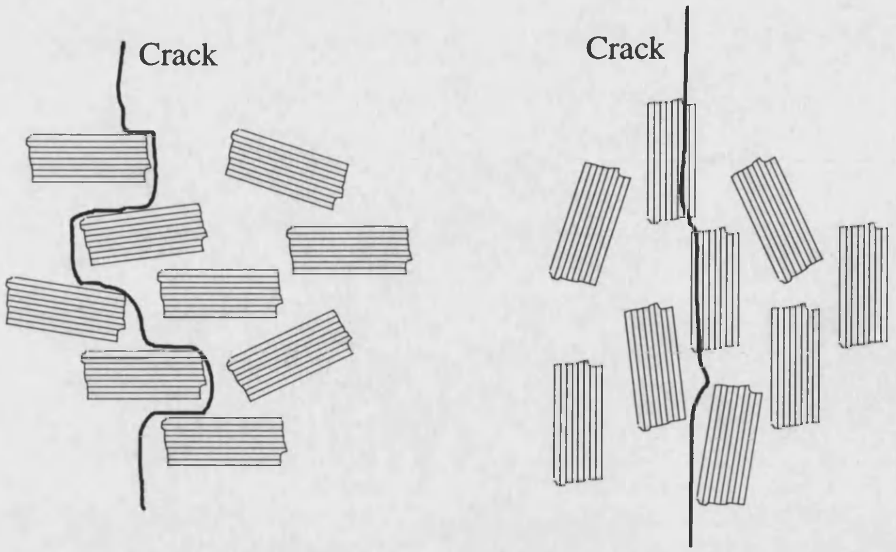

Crack propagation perpendicular to the axis of extrusion.

Crack propagation parallel to the axis of extrusion.

Figure 8-28 : Schematic showing crack propagation parallel and perpendicular to the extrusion direction.

Figure 8-29 shows the calculated permanent deformation caused by a 1kN indentation for all the graphites tested. The UCAR graphites exhibit an approximately linear increase in percentage deformation with increasing porosity, and despite the fact that the structure in IM1-24 (filler particle size is ~500μm) is approximately five times the size of that in the UCAR graphite (filler particle size is ~70 x 150μm), it lies close to the same line. ATJ has a filler size of ~25μm which is substantially smaller than that of the UCAR graphites, but also has a similar percentage permanent deformation putting it on approximately the same line as the UCAR graphite. However, the percentage permanent deformation for EY306 is approximately 15% lower than that for ATJ, although there is very little difference in percentage porosity. The percentage permanent deformation for Poco AXF is lower still despite percentage porosity being nominally the same as that for EY306. Hence, the quantity of porosity seems to be the dominant factor controlling the degree of permanent deformation for a wide range of microstructural scales. This observation remains valid until the scale of the microstructure becomes small, ~10μm, when the structure imposes itself more strongly on the nature of the deformation. This correlates well with microstructural evidence of a change in fracture mechanism. IM1-24, ATJ and the UCAR graphites show a similar fracture mechanism, with the development of a hemispherical shear damage zone beneath the indenter. However, EY306 shows evidence of long range cracking in the Hertzian direction as well as a shear damage zone, and for Poco AXF only Hertzian cracking is visible under an optical microscope. So, it may be concluded that porosity is the dominant factor controlling deformation, providing that the fracture mechanism does not change.

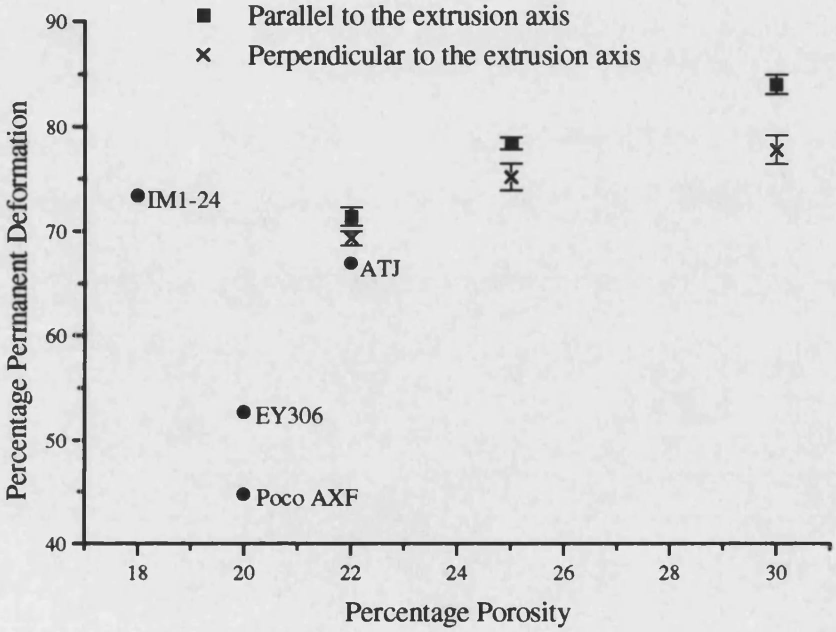

Figure 8-29 : The effect of porosity and microstructural scale on the permanent deformation produced by a 1kN indentation for a range of graphites. The error bars represent a ± two standard deviations for the UCAR data.

8.3 Chapter Summary

As the size of the microstructure is decreased there is a transition in blunt indentation fracture behaviour. IM1-24 (filler particle size ~500μm) and ATJ (filler particle size ~25μm) graphites both develop a hemispherical shear damage zone beneath the indenter, with no evidence of Hertzian cracking. EY306 graphite (filler particle size ~10μm) exhibits a shear damage zone and long range cracking in the Hertzian directions. Hertzian cracking is evident in Poco AXF graphite (filler particle size ~5μm), but there is no evidence of a shear damage zone before failure. In this case, shear is only evident on the fracture surface when examined using an SEM. In Poco ZXF (filler particle size ~1μm) there is no evidence of shear at all, although a Hertzian cone crack is clearly visible. Thus, classical Hertzian fracture is suppressed by coarser textured microstructures.

UCAR graphites with nominally the same microstructure, but different quantities of porosity, were used to investigate the effect of porosity on the nature of blunt indentation damage. The size and intensity of the damage zone was found to increase with increasing porosity. When compared with IM1-24, ATJ, EY306 and AXF graphites, it was apparent that porosity was the dominant factor in controlling the degree of damage, providing the damage was produced by shear. As the texture of the graphite structure becomes very fine (~10μm) it imposes itself strongly on the process of damage evolution. Thus the structure of the graphite becomes the dominant factor in determining the degree of damage produced by a blunt indentation.

9. The Effect of Oxidation on Blunt Indentation

IM1-24 graphite was thermally oxidised producing graphites with a range of weight losses. These graphites were subjected to indentation tests to failure, and indentation load cycles. Samples trepanned from a number of reactors were also tested in a shielded facility to investigate the effect of reactor environment.

9.1 Thermal Oxidation

9.1.1 The effect of thermal oxidation on deformation behaviour

Load displacement curves for unoxidised, 27% weight loss and 45% weight loss IM1-24 are shown in Figure 9-1. It is immediately apparent that there is a large decrease in failure load as the burn off increases, while the indentation depth at failure increases slightly with burn off. All the curves are approximately linear at this scale apart from during the early stages of loading where the sphere beds in. More detailed examination of the load-indentation curve for graphite oxidised to 45% weight loss, Figure 9-2, shows that the slope of the curve increases gradually with loading and the fracture is more progressive.

If the average stress is defined as before, in Chapter 6, i.e., as the load divided by the area of contact, Figure 9-3 is obtained. Figure 9-3 also shows that the strength of the graphite decreases dramatically with increasing burn off. It is also apparent that the stress-indentation depth curve becomes flatter with increasing weight loss.

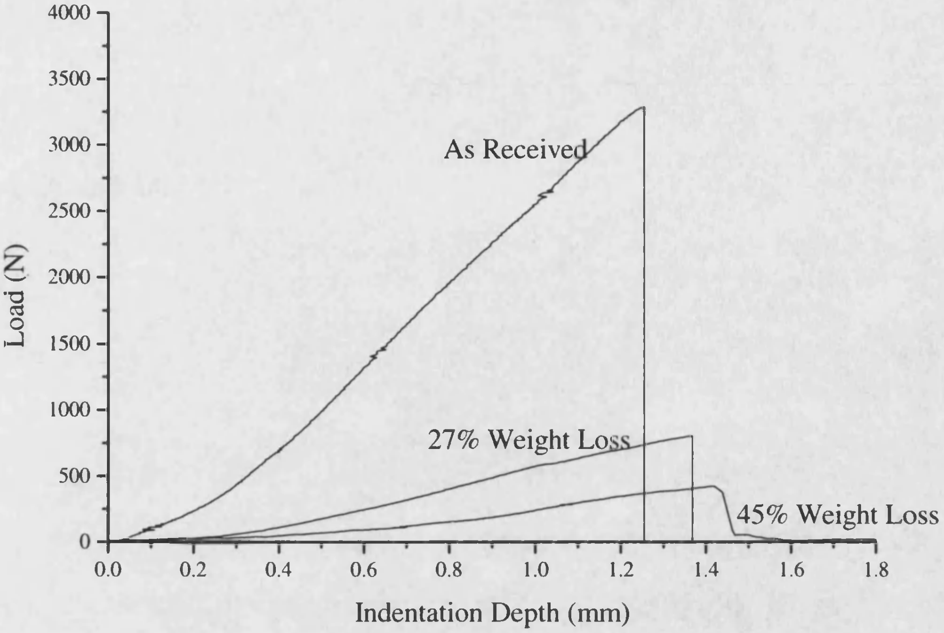

Figure 9-1 : Blunt indentation load deflection curves for unoxidised IM1-24 and when oxidised to intermediate and high weight losses.

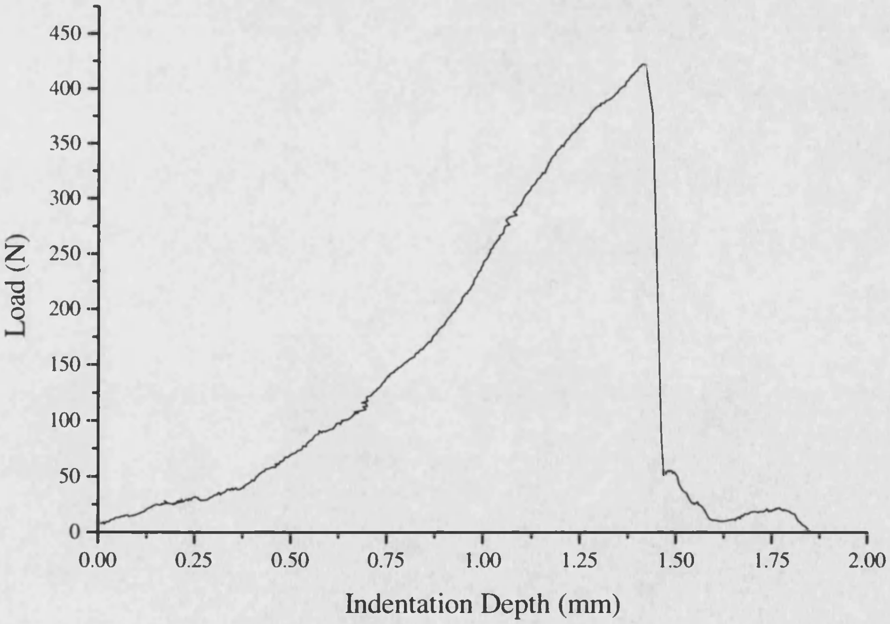

Figure 9-2 : Blunt indentation load deflection curve for IM1-24 graphite oxidised to 45% weight loss.

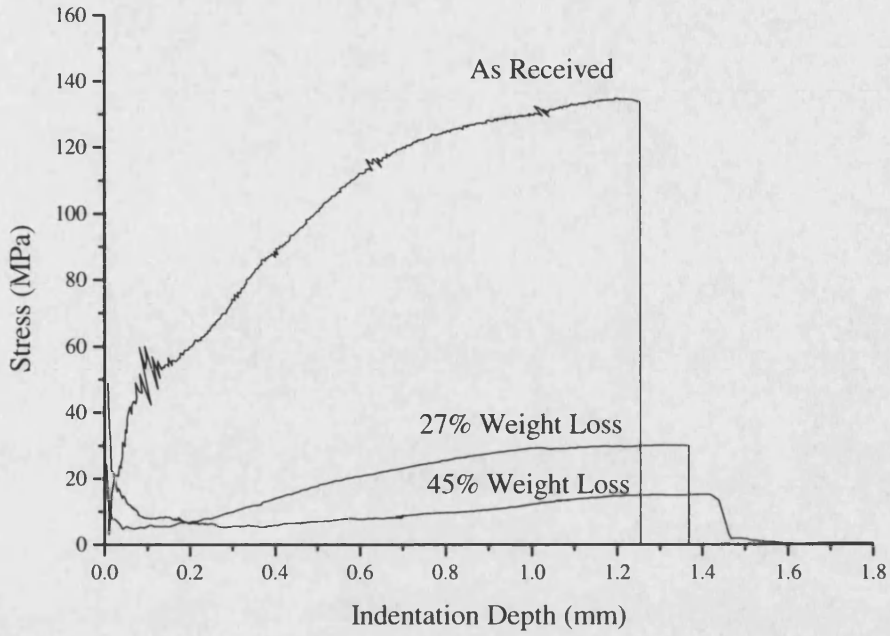

Figure 9-3 : Average blunt indentation stress versus indentation depth for unoxidised and oxidised IM1-24 graphite.

Figure 9-4 shows stress displacement curve for a carbon foam whose microstructure is shown in Figure 9-5. The bright regions are the carbon and the remaining grey colour is pores filled by resin, it can be seen that there is very much more porosity than solid material, in fact the foam is approximately 98% porous. The perturbations in the stress curve in Figure 9-4 are indicative of crushing, there is a rise in stress as ligaments are stressed followed by a sudden reduction as they fail. The material below the indenter is then stressed to a higher degree. By an indentation depth of about 1.5mm the critical stress has been reached at which the indenter will continue to crush through the foam so there is no further increase in stress. Thus failure is now by compression causing shearing of individual ligaments rather than the initiation of a crack by tensile stresses at the surface which was found to be the case for unoxidised graphite.

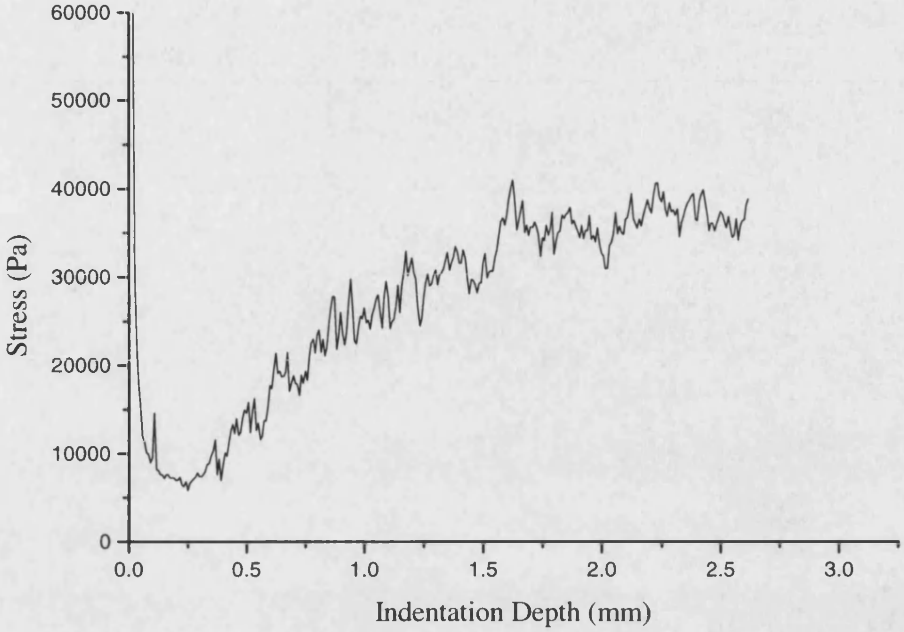

Figure 9-4 : Stress displacement trace for the blunt indentation of a carbon foam.

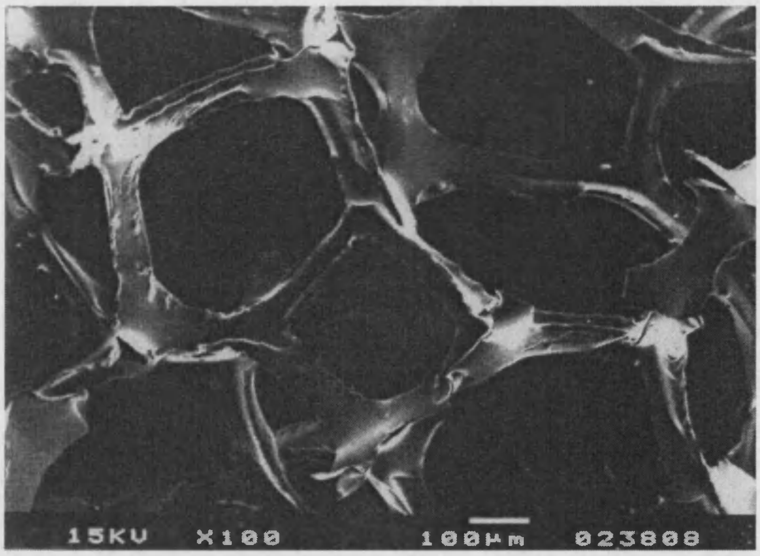

Figure 9-5 : Microstructure of carbon foam [118].

When the foam is compared to the behaviour of highly oxidised IM1-24 graphite (Figure 9-6) there are some similarities. There is some evidence of crushing taking place between 0 and 0.75mm indentation depth and the subsequent rise in stress is quite small compared to that occurring for unoxidised IM1-24 graphite. However there is still a sudden failure at an indentation depth of around 1.5mm, but the sample is still intact and capable of bearing a small load although presumably with large cracks running through it.

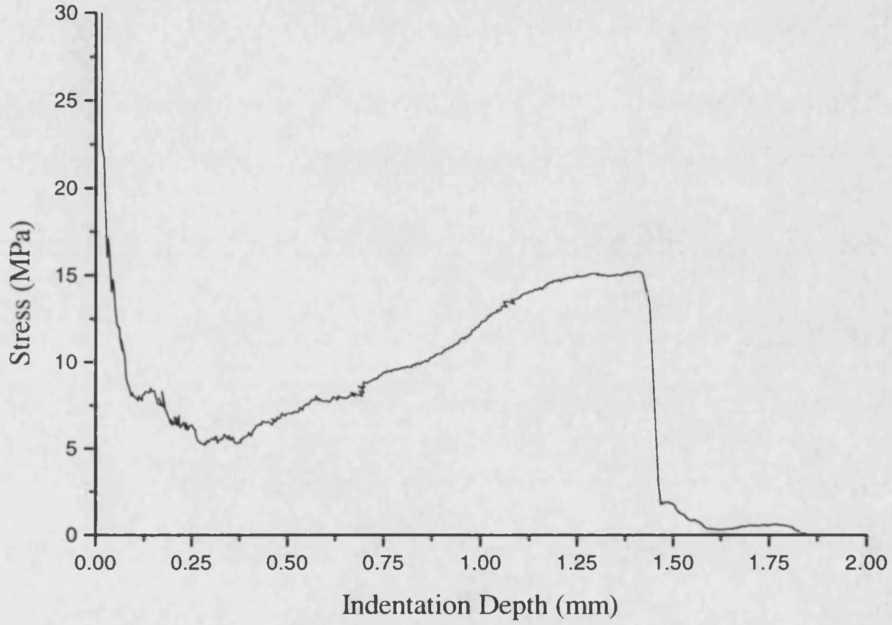

Figure 9-6 : Stress indentation depth plot for IM1-24 graphite with 45% burn off.

The damage in highly oxidised IM1-24 graphite after an indentation cycle is shown in Figure 9-7. The indentation is large and there is evidence of debris produced by crushing in the base of the indentation. There is no clearly defined crack path on failure, and the structure is so porous that it is not easy to separate indentation damage from pre-existing flaws created by oxidation. When the indentation of highly oxidised IM1-24 graphite (Figure 9-7) is compared with the indentation in unoxidised IM1-24 (Figure 7-4) a substantial difference in the size of the impression is evident. This may be largely due to the difference in elastic modulus caused by the introduction of porosity, although there is also a change in fracture behaviour. There is also evidence of large deformation at the edge of the contact area (top right corner of Figure 9-7) possibly due to cracking in that region, which is not seen in the unoxidised graphite (Figure 7-4).

Figure 9-7 : Cross section of an indentation in IM1-24 oxidised to approximately 45% burn off, (indentation load 0.5kN).

The effect of increasing oxidation on the indentation size and nature of the deformation can be better seen by surface profiling a series of 1kN load indentations for a range of weight losses (See Figure 9-8-Figure 9-12). Figure 9-8 shows a neat uniform depression in unoxidised IM1-24 graphite with a depth of about 20μm. Samples with 5 and 10% burn off (Figure 9-9 and Figure 9-10) show an increase in surface roughness where the surface has been attacked. The size of the indentation has also increased markedly as the percentage burn off increases. By 16% weight loss (Figure 9-11) areas of raised material at the edge of the indentation are evident as well as an increase the size of the indentation. For 25% weight loss (Figure 9-12), there is a substantial increase in the size of the indentation, but the regions of raised material also increase substantially in size. This indicates that, as the weight loss is increased, more crushing takes place and some material is pushed up at the edges of the indentation.

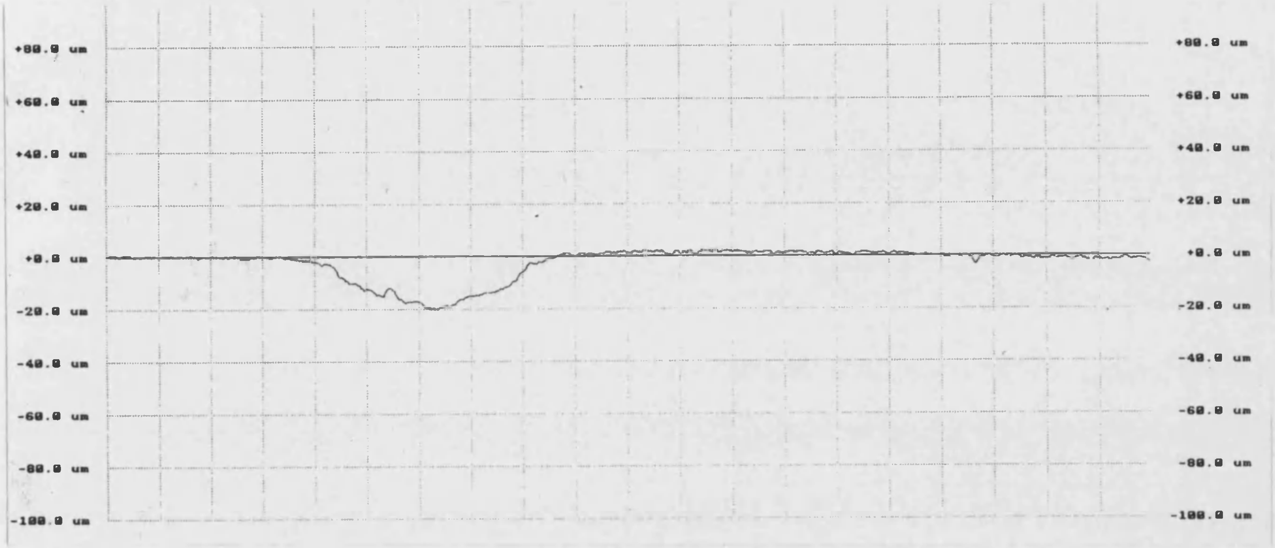

Figure 9-8 : Surface profile of a 1kN load indentation in unoxidised IM1-24, (horizontally each square represents 0.5mm).

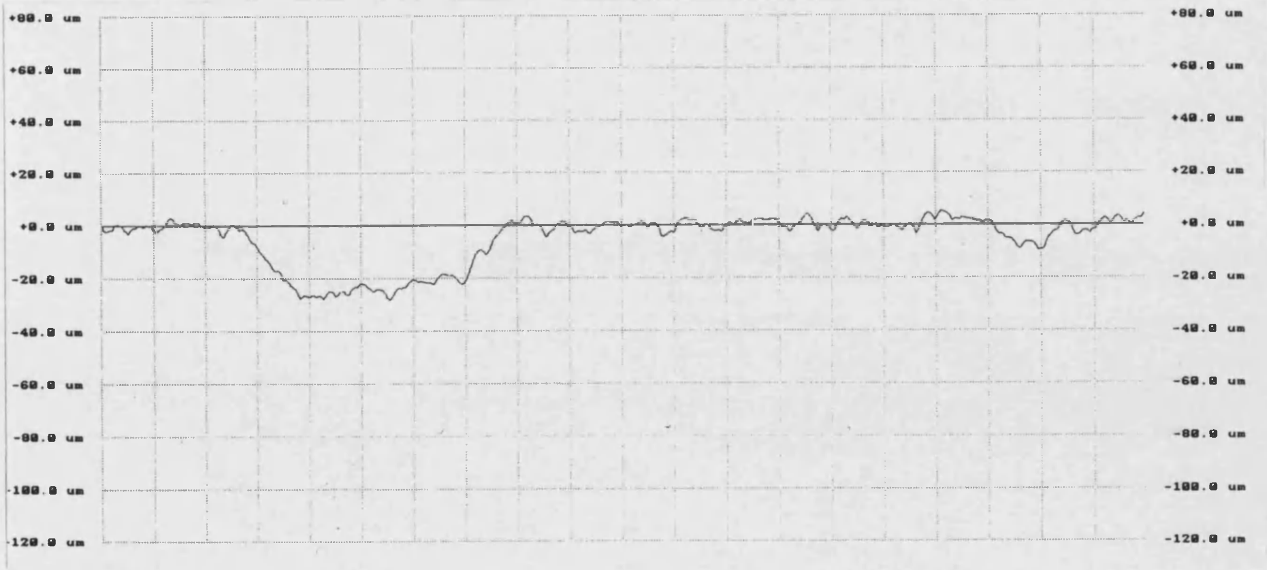

Figure 9-9 : Surface profile of a 1kN load indentation in oxidised IM1-24 with 5% weight loss, (horizontally each square represents 0.5mm).

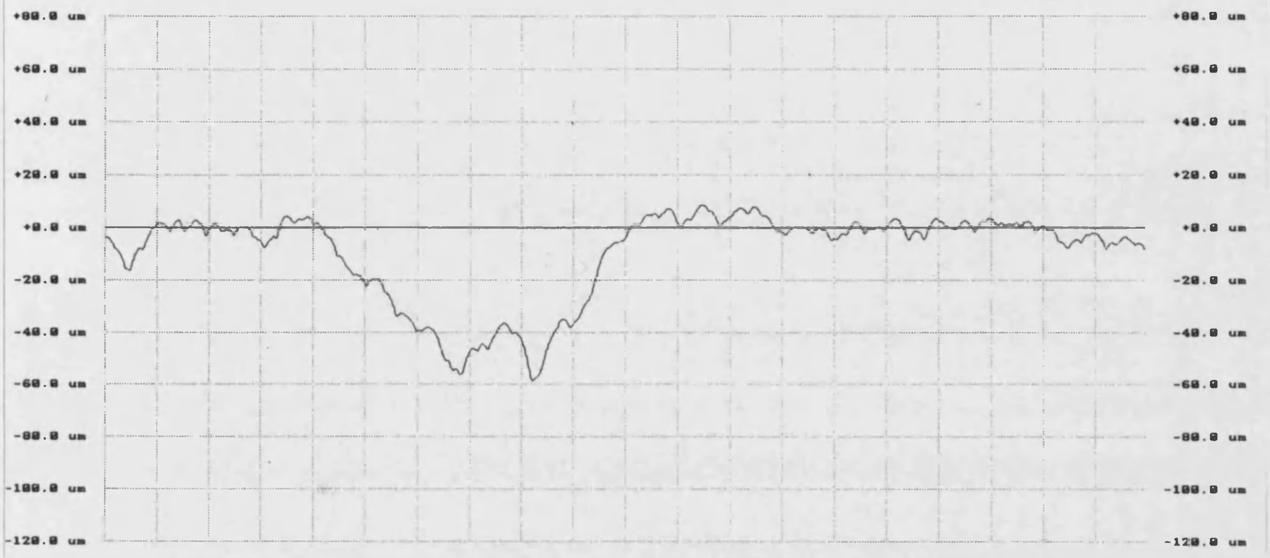

Figure 9-10 : Surface profile of a 1kN load indentation in oxidised IM1-24 with 10% weight loss, (horizontally each square represents 0.5mm).

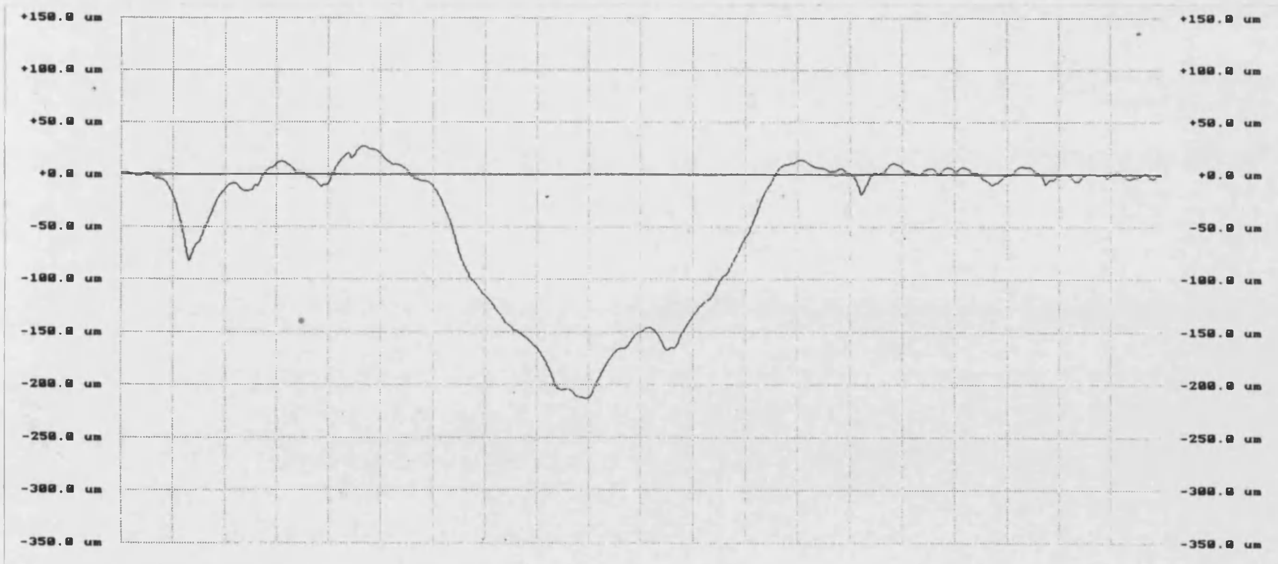

Figure 9-11 : Surface profile of a 1kN load indentation in oxidised IM1-24 with 16% weight loss, (horizontally each square represents 0.5mm).

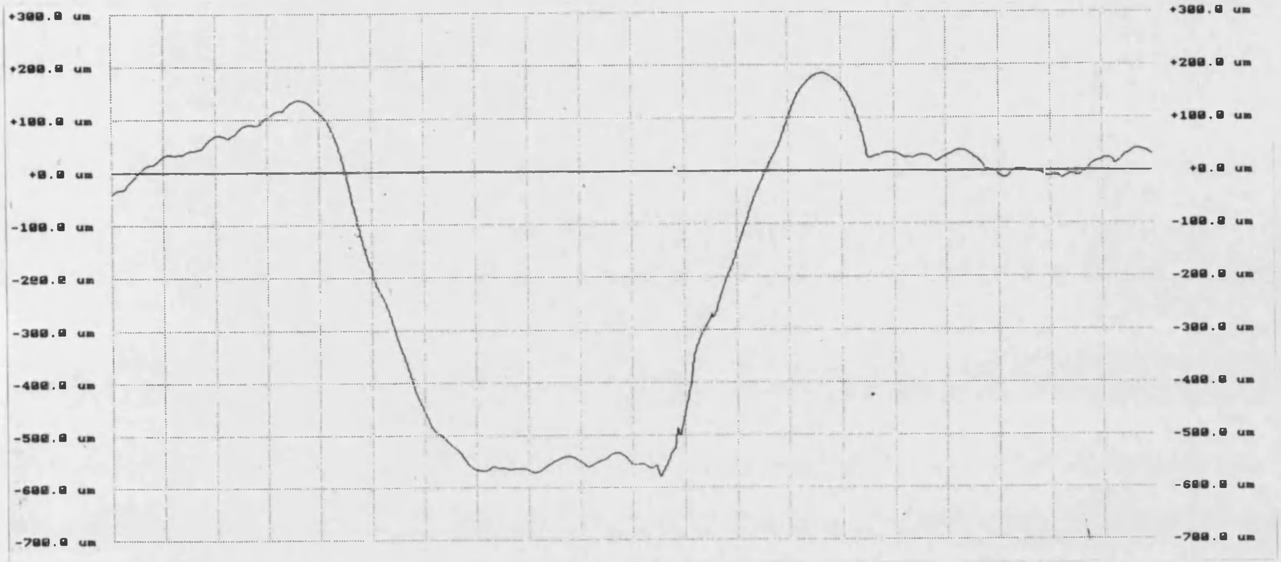

Figure 9-12 : Surface profile of a 1kN load indentation in oxidised IM1-24 with 25% weight loss, (horizontally each square represents 0.5mm).

The load deflection traces for the IM1-24 graphite samples that were surface profiled are shown in Figure 9-13. As might be expected the hysteresis loops increase in size as the weight loss increases, indicating that more damage is occurring. The permanent set increases markedly from less than 0.1mm for unoxidised IM1-24 to ~1mm for IM1-24 oxidised to 25% weight loss, which correlates reasonably well with the surface profile results shown in Figure 9-8 to Figure 9-12.

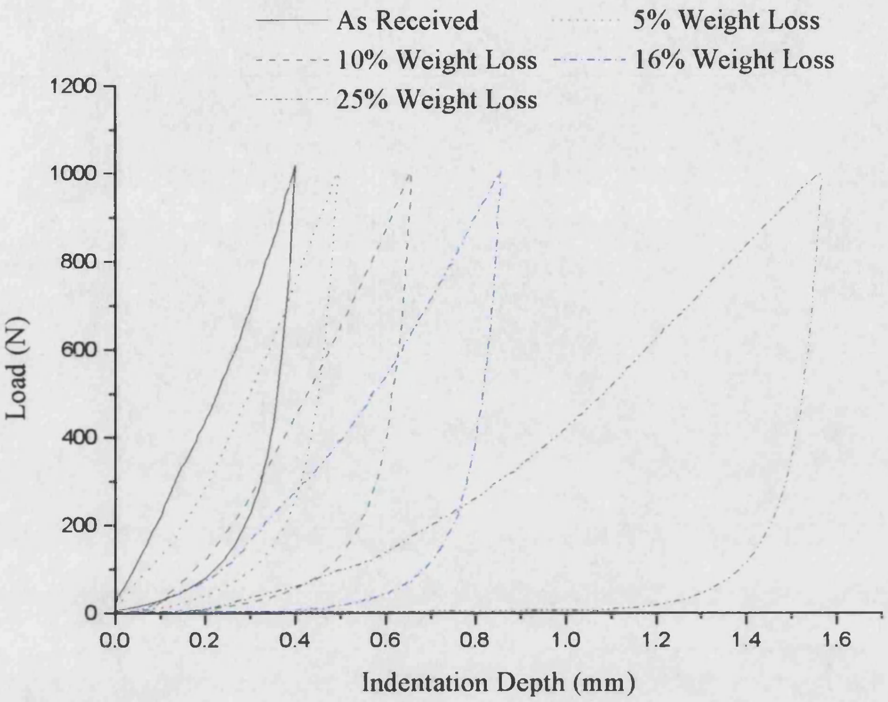

Figure 9-13 : Load cycles for oxidised and unoxidised IM1-24 graphite.

The fractional recoverable deformation was calculated as defined in Chapter 8 and will be referred to as the percentage elastic recovery here. Figure 9-14 shows that the elastic recovery decreases towards some low limit with increasing weight loss due to oxidation. Hence, at high levels of weight loss (40%), there is likely to be almost no elastic recovery, which is similar to the behaviour of a foam. The point at which this low limit is reached corresponds approximately with the change in fracture behaviour. So, at ~40% weight loss, there is not enough stored strain energy to cause the sample to fast fracture, hence the failure is more progressive.

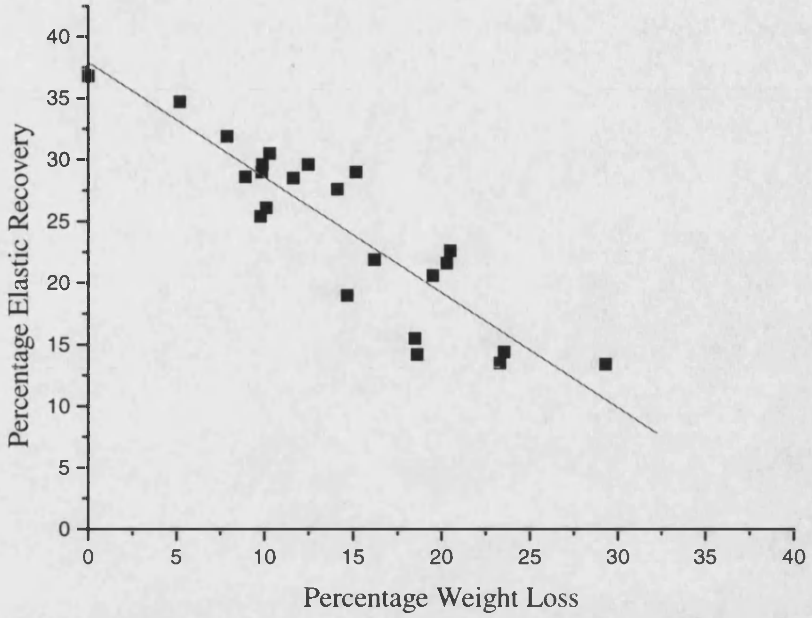

Figure 9-14 : The effect of oxidation on the degree of elastic recovery.

Figure 9-15 shows the fractional permanent deformation for the oxidised IM1-24 plotted in conjunction with the data for the graphites examined in the previous chapter (see Figure 8-29). The dotted lines represent ± two standard deviations. Thus, despite the different methods of introducing porosity and the large difference in microstructural scale between IM1-24 and the UCAR graphites, on the whole they show a similar increase in permanent deformation with increasing porosity. This reinforces the suggestion that the nature of the deformation is dominated by the quantity of porosity, for graphites deforming predominantly by shear rather than Hertzian cracking.

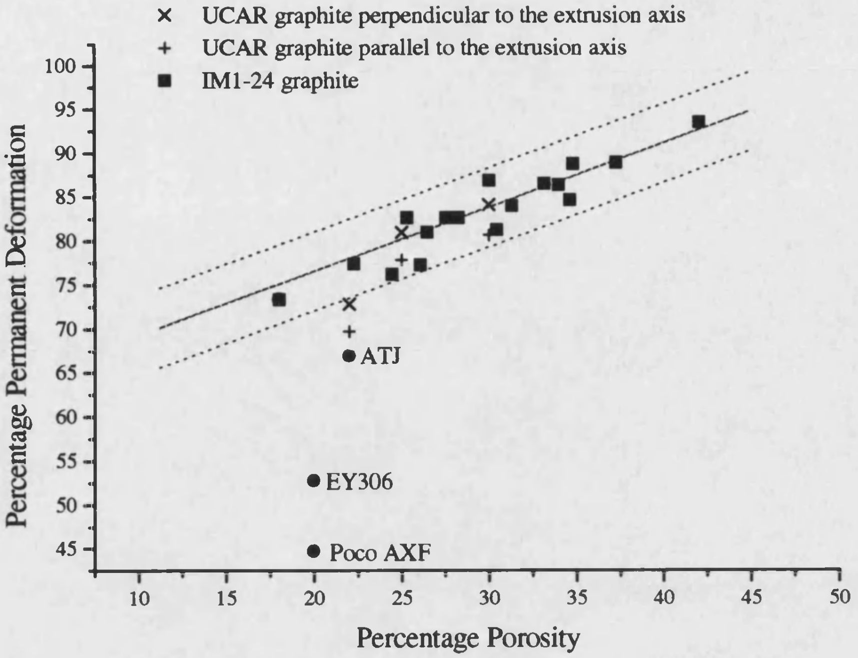

Figure 9-15 : The effect of porosity and microstructural scale on the permanent deformation produced by a 1kN indentation for a range of graphites. The dotted lines represent a ± two standard deviations for the linear regression of the IM1-24 data.

9.1.2 The effect of thermal oxidation on blunt indentation strength

IM1-24 samples with up to 50% weight loss were indented to failure, the maximum average compressive stress at failure being shown in Figure 9-16.

As other researchers [46, 50, 49, 52, 108] have found for a variety of more conventional strength tests there is a sharp decline in the strength with increasing burn off. An exponential fit using equation 9.1 and linear regression line are shown in Figure 9-16. Although the exponential appears to give a better fit there is very little difference in the correlation coefficients. However there is some theoretical justification due to Buch [56] for fitting an exponential to the data (see Chapter 2).

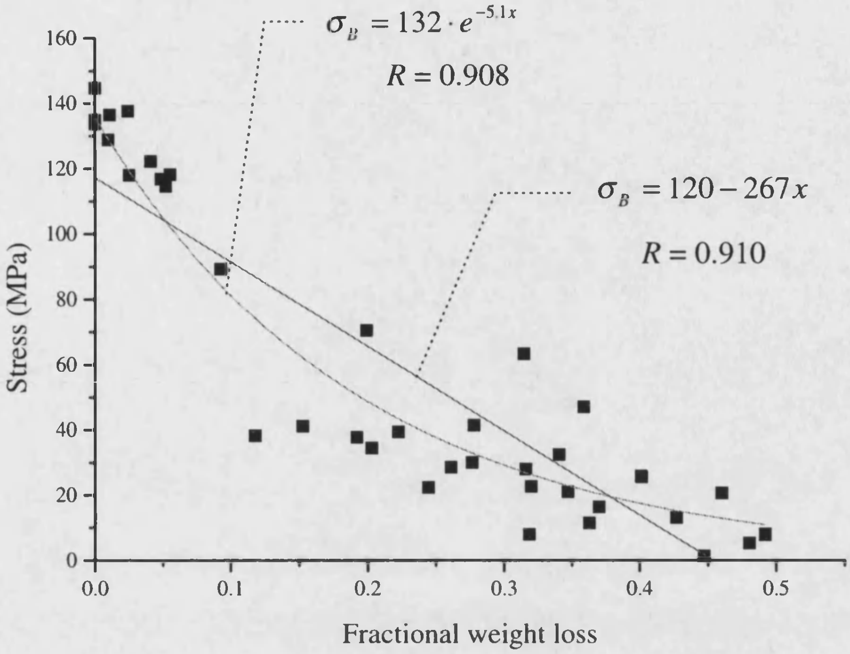

Figure 9-16 : The effect of weight loss by thermal oxidation on blunt indentation strength.

$$\sigma = \sigma_0 \times e^{-b.x} \qquad 9.1$$

Where σ = failure stress, σ_0 = failure stress of unoxidised graphite, x = fractional weight loss, and b = constant.

Equation 9.1 has also commonly been used by other researchers to describe their data and consequently will be used here for comparison. For example Pickup [52] studied the effect of thermal oxidation in CO_2 on three point bend strength and found b~10, whereas here b~5. However, weight losses were limited to 10% in Pickups work.

Figure 9-17 shows the effect of oxidation on the indentation depth at failure, which is effectively proportional to the failure strain. There is considerable spread in the results, but there is little effect of oxidation on the blunt indentation strain to failure, which has found to be the case in studies of the effects of thermal oxidation on conventional mechanical properties [44].

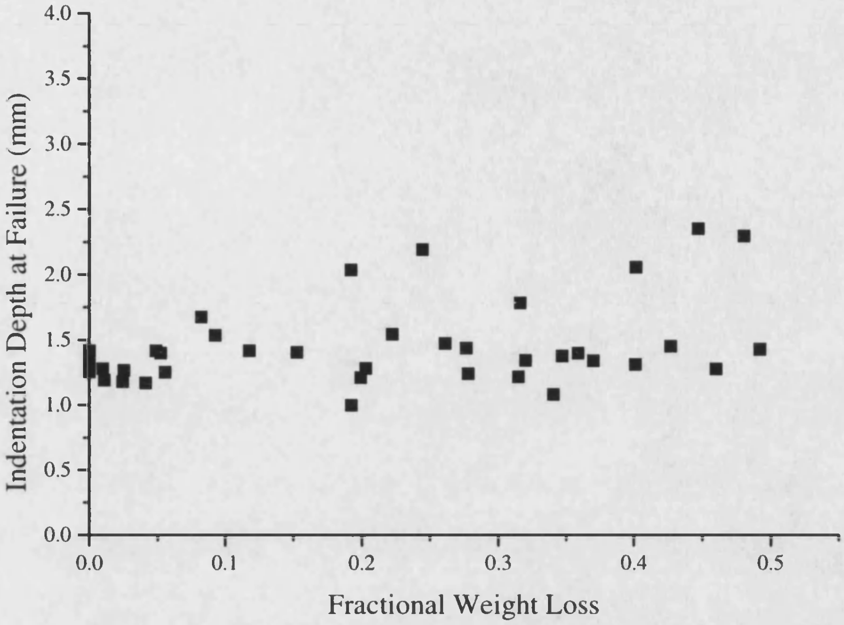

Figure 9-17 : The effect of oxidation on the indentation depth at failure of IM1-24 graphite.

9.2 Radiolytic Oxidation

Blunt indentation tests to failure were carried out on IM1-24 graphite samples trepanned from the cores of a number of advanced gas cooled reactors. The tests were carried out in a shielded facility at Berkeley Technology Centre using a 6mm diameter indenter and a sample size of 19mm diameter x 6mm thick.

Figure 9-18 shows the effect of weight loss on the normalised blunt indentation strength (strength divided by the strength of unoxidised IM1-24). There is a large scatter on the results which occurs for a number of reasons. Firstly, the experiment can not be as well controlled as it is in the laboratory. Weight loss can not be measured directly so is calculated by subtracting the measured sample density from the average density of IM1-24 graphite. However, there are small variations in density across a core brick which will result in an inherent error in the weight loss for these small samples. Secondly, the irradiation of the cables, load cell and displacement transducer will eventually cause degradation and they will cease to function correctly. Finally, the process occurring within the graphite is far more complicated than for thermal oxidation. The oxidation takes place by a different chemical species and there are inhibitors that complicate the process further (see section 2.3). There is also irradiation hardening that initially increases the modulus (see section 2.5). Figure 9-18 shows that there is an initial increase in the strength, up to ~30%, due to an increase in modulus caused by neutron irradiation hardening. At ~10% weight loss there is a decrease in strength due to the introduction of porosity by radiolytic oxidation.

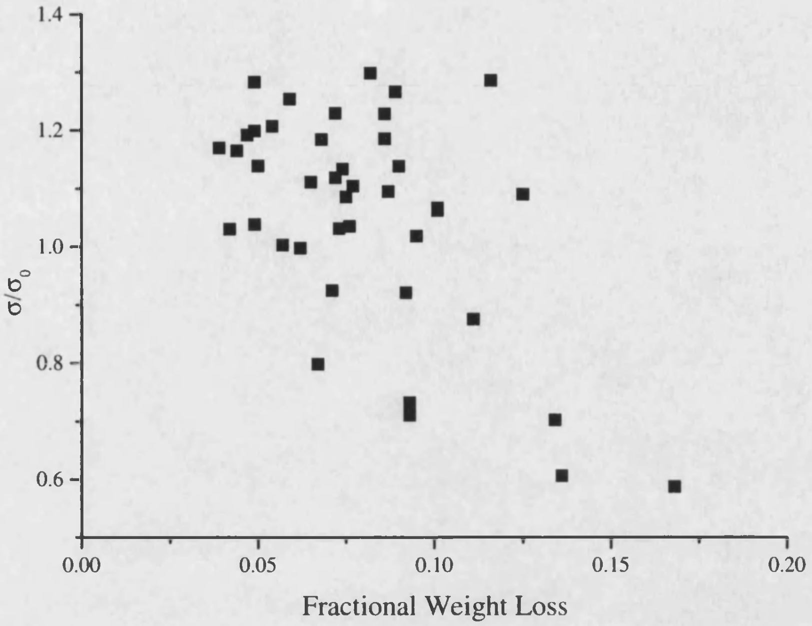

Figure 9-18 : The effect of radiolytic oxidation and reactor environment on the blunt indentation strength of strength of IM1-24 graphite.

The change in strength with radiolytic oxidation has been described by equation 9.2 [48] in the past.

$$\sigma_f = \sigma_0 . \sqrt{I.S} . x \qquad 9.2$$

Where I = pinning term to allow for pinning of mobile dislocations and S = modified structure term to allow for structural changes due to irradiation damage. Equation 9.2 allows the effects of irradiation to be calculated and removed to show the effects of radiolytic oxidation on blunt indentation strength, Figure 9-19. The scatter in the results is also large but Figure 9-19 shows a general decrease in strength with increasing weight loss.

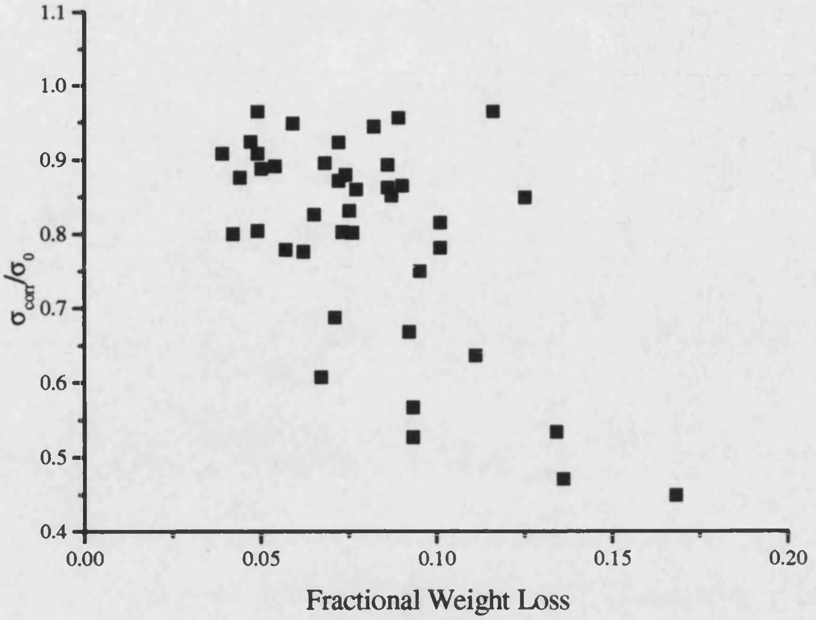

Figure 9-19 : The effect of radiolytic oxidation on the blunt indentation strength of IM1-24 graphite, where σ_{corr} is the failure strength after the irradiation effects been removed using equation 9.2.

However, if the data in Figure 9-18 and Figure 9-19 are split into ranges the standard deviation can be compared over a selected range of weight losses (see Table 9-1). Table 9-1 shows that removing the hardening effect due to neutron irradiation has decreased the standard deviation slightly. This supports the suggestion that the increased scatter of the results is partly due to the increased complexity of the process.

Weight loss	σ/σ_0 from Figure 9-18		σ/σ_0 from Figure 9-19	
%	Mean	Standard deviation	Mean	Standard deviation
2.5 - 5	1.153	0.09223	0.8816	0.06156
5 - 7.5	1.108	0.0327	0.839	0.0228
7.5 - 10	0.957	0.157	0.718	0.123

Table 9-1 : The effect of removing the irradiation hardening using equation 9.1 on the statistics of the blunt indentation failure stress.

There are other problems when comparing these results with those for thermal oxidation apart from the large spread in the data. The sample thickness used here was only 6mm as only irradiated samples of this size were available at the time. The samples were generally observed to fracture into three approximately equal pieces, suggesting that the failure was caused by biaxial bending rather than the Hertzian stresses at the surface (see section 6.3.2).

9.3 Chapter Summary

As high weight losses (~40%) are achieved there is a change in behaviour (see Figure 9-20), the fracture becomes more progressive and the sample no longer fractures into two or three pieces, but is slowly driven apart. There is also evidence of crushing and material is pushed up at the edges of the indentation. The fracture path is no longer definable in the highly oxidised graphite as the structure is so diffuse.

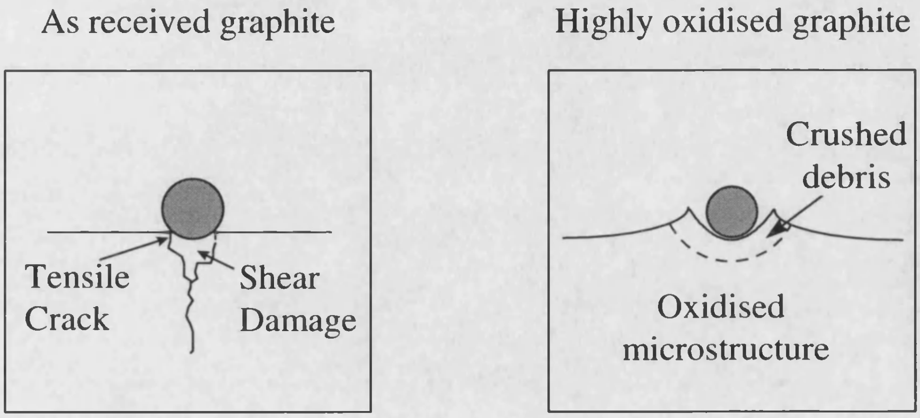

Figure 9-20 : Schematic showing change in behaviour with high levels of oxidation.

The percentage of elastic recovery seems to approach a low limit at about 40% weight loss coinciding with the change in behaviour observed. It is possible that at high levels of oxidation there is not sufficient stored elastic strain energy to cause the explosive fast fracture seen for low levels of oxidation. It also seems likely that the fracture tends to be compressive at high burn off, similar to that observed for a foam, rather than being initiated by tensile stresses at the surface.

The blunt indentation strength has been shown to decrease with increasing oxidation in a manner similar to that reported by other researchers for more conventional test methods. The value of b is found to be ~5 for thermal oxidation which is much closer to the value quoted for radiolytic oxidation of 3.7 [108] determined with more conventional testing, than has been the case in the past. This may be due to the test geometry or the small sample size which indirectly is the most likely reason, since uniform oxidation is much easier to achieve with a small sample.

The indentation test can be used in a shielded area with manipulators, but there are currently problems with the scatter of the data, and it is likely that thicker samples would have to be used to enable comparison with the data for thermal oxidation.

10. Dynamic Friability

The apparatus used to measure dynamic friability was similar to a small instrumented lathe, and is described fully in Chapter 5. A grooving tool was used to take a uniform rectangular cut out of the graphite sample, which allowed easy calculation of the volume of material removed. The motor and gear box were mounted on bearings allowing them to rotate, bending a strain gauged beam. Thus, when a torque was applied by the cutting tool, the beam bent and the force was recorded. Hence, after calibration, torque could be measured continuously during the test. This chapter presents results obtained using this apparatus, concentrating largely on the effect of oxidation and how the wear might be predicted.

10.1 Torque Measurements

A typical torque trace for the cutting of IM1-24 graphite is shown in Figure 10-1, where the measured torque is that resulting from the load applied by the tool. The torque increases rapidly when the tool is put in contact with the surface, point “a” on the trace, large peaks and troughs are then evident. The large oscillations in torque have a periodicity corresponding to the rate of rotation, thus are likely to be caused by the sample being slightly off centre. The average torque can be easily calculated and is approximately 1.75Nm, but it is difficult to obtain any further information pertaining to the fracture events taking place during cutting.

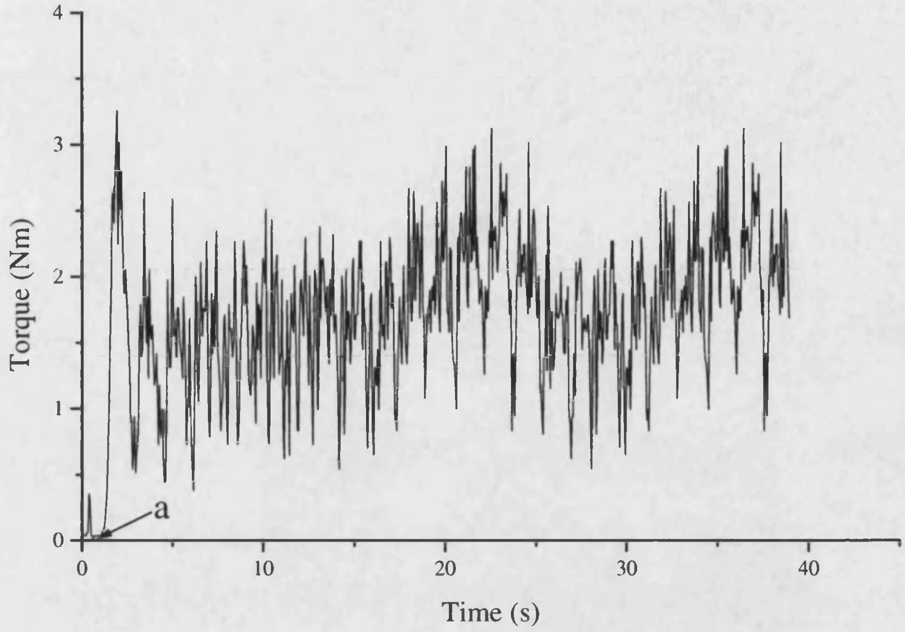

Figure 10-1 : The variation of torque applied by the cutting tool with time for unoxidised IM1-24 graphite (rate of rotation = 40rpm and tool load = 500g).

More information may be obtained by applying a filter to the data in order to reduce the chaotic appearance. Figure 10-2 shows a plot of amplitude versus frequency calculated using a fast Fourier transform (FFT) technique. This method assumes that the trace can be represented by a series of sine waves [119] whose amplitude and frequency are displayed in Figure 10-2. The phase difference between the component sine waves is not shown here as it is unlikely to have any physical meaning for this situation. The first peak is the base line amplitude upon which the sine waves are superimposed to produce the torque trace, thus it is effectively a measure of the average torque being applied. Peak A is equivalent to the frequency of rotation, thus it is likely that peak A is due to the sample Rotating eccentrically producing a slightly higher torque at a particular point in the revolution. Peaks B and C occur at multiples of the frequency of peak A and so it is likely that these peaks are resonant frequencies of the fundamental frequency of peak A, i.e. harmonics.

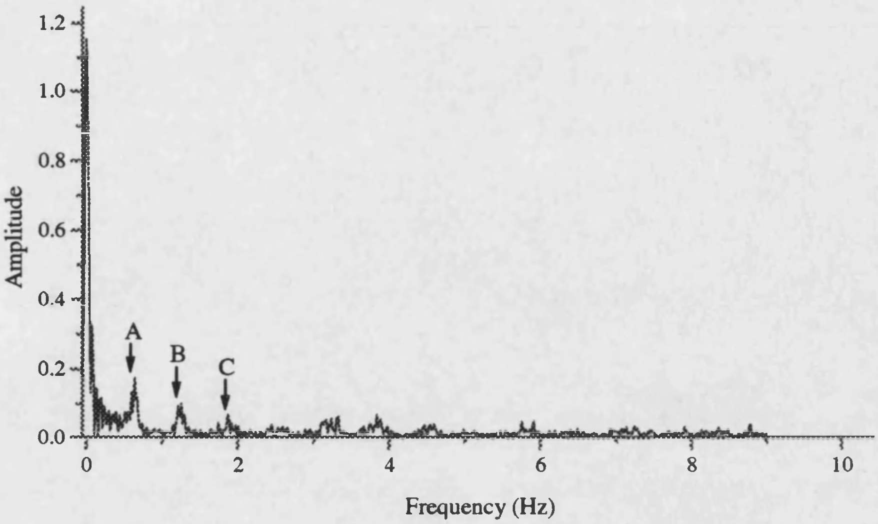

Figure 10-2 : Fast Fourier transform of the data shown in Figure 10.1.

Thus even when a FFT filter is applied the only frequencies evident apart from the average torque are due to the eccentricity of the sample rotation. It was hoped that information relating to the fracture processes occurring during cutting might be revealed in the torque data. However, this is not possible with the sensitivity of the present apparatus. Hence in the rest of this chapter the torque referred to is an average torque, calculated by taking the median value from the trace. This gives an indication of the force required during the cutting process.

10.1.1 The effect of the rate of rotation

Figure 10-3 shows the average torque decreases with increasing rate of rotation of the sample. This may be because the indentation of the surface by the wedge-shaped tool is time dependent, so at low speeds the tool penetrates further into the sample. The torque becomes nearly independent of the rate of rotation for values greater than ~ 20 rpm.

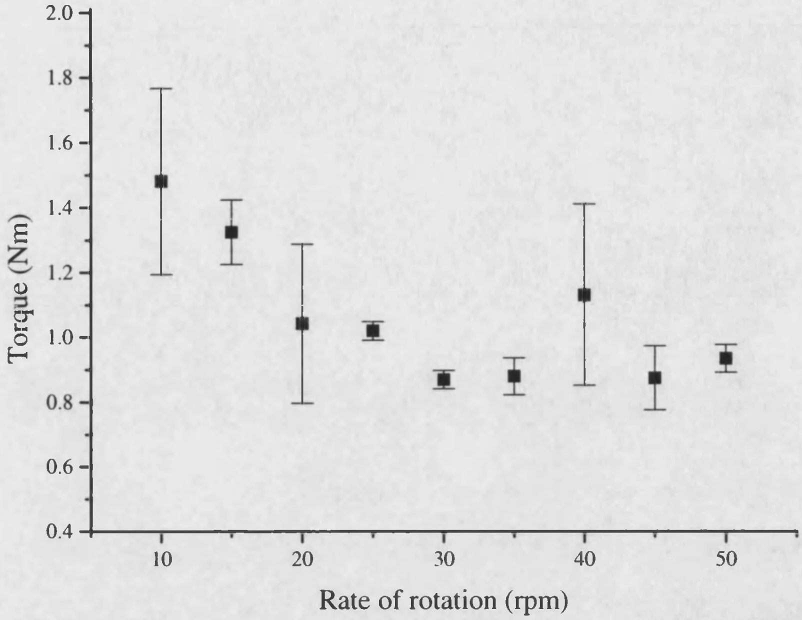

Figure 10-3 : The effect of rate of rotation on the measured torque for unoxidised IM1-24 graphite with a constant tool load of 500g, (error bars show ± 2 standard deviations).

10.1.2 The effect of tool load on the measured torque

Until a tool load of approximately 500g is reached there is no measurable torque (see Figure 10-4), the torque then increases with increasing tool load. The reason for the initial region of extremely low torque is that there is not sufficient force to cause penetration of the surface of the graphite, so the tool slides over the surface. Once enough force is applied to cause penetration of the surface, the tool cuts and fractures off pieces of graphite, producing a far more severe wear regime. The increase in torque suggests that the tool is being driven further into the sample with increasing applied load.

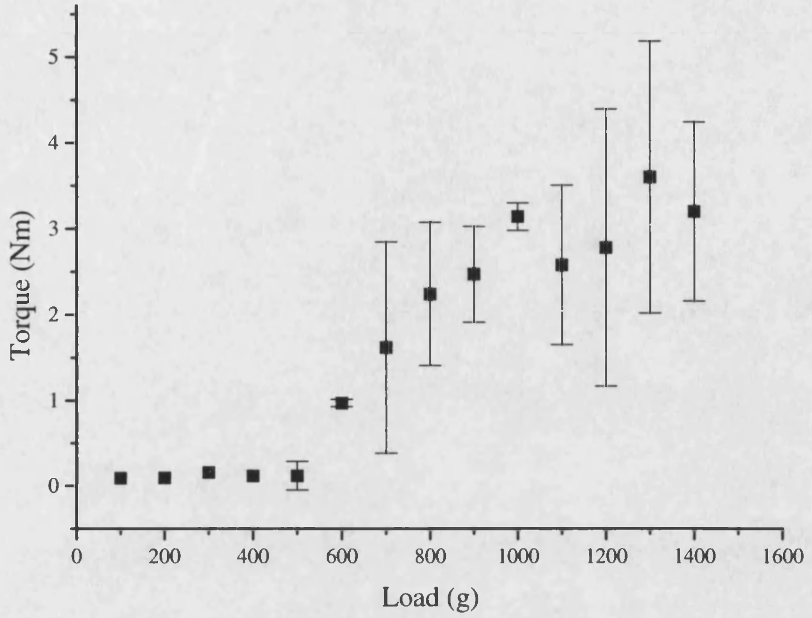

Figure 10-4 : The effect of increasing tool load on the measured torque for unoxidised IM1-24 graphite, (all tests were carried out at 50rpm, and the error bars show ± 2 standard deviations).

10.1.3 The effect of oxidation on the measured torque.

Figure 10-5 shows that generally the torque increases with increasing extent of oxidation of graphite, although there is a substantial scatter of results. This trend is counter intuitive as the modulus and strength of the graphite will decrease substantially upon oxidation as more porosity is introduced. It is possible that as the graphite becomes more compliant the tool penetrates further into the sample taking a larger depth of cut so giving rise to a greater torque. If this is true, it implies that the indentation depth of the tool must be the dominant factor controlling torque rather than the decrease in strength of the graphite. Taken together, the results in Figure 10-1 - Figure 10-5 suggest that the torque developed is dominated by the characteristics of the test rig rather than the nature of fracture processes occurring in the graphite.

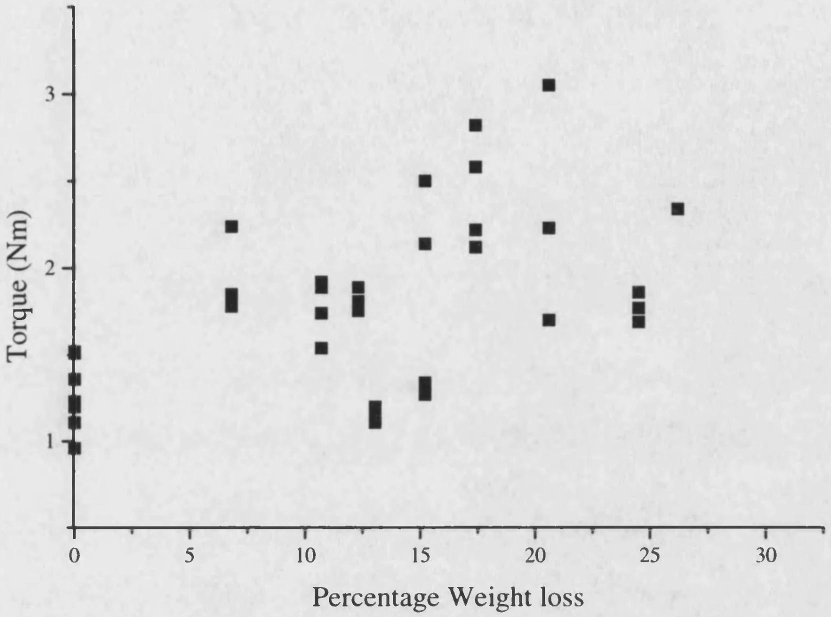

Figure 10-5 : The effect of oxidation of IM1-24 graphite on the recorded torque, (all tests carried out at 50 rpm and a constant load of 500g).

10.2 Measurement of the volume of material removed

The tool used has a profile shown schematically in Figure 10-6 so a straight cut 3mm wide is always made. Thus, in order to calculate the volume of material removed only the initial and final diameters of the cylindrical sample need to be measured.

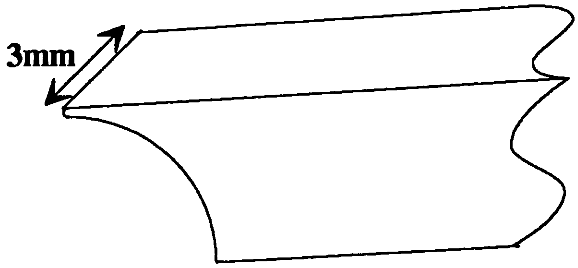

Figure 10-6 : Schematic of the cutting tool tip.

The simplest way to express these results is as a wear rate, i.e. volume removed per unit time, mm^3/min, since the duration of test is known accurately. However it is potentially more useful to express them as volume of material removed per unit sliding distance, mm^3/m. The sliding distance can be simply calculated provided that the rate of material removal is constant during the test. This is the case as the rotation speed is controlled accurately and remains constant throughout a test. Consequently, the sliding distance, S, will be given by equation 10.1 where R_1 = initial sample radius, R_2 = final sample radius and N = number of revolutions.

$$S = \left(\frac{R_1 + R_2}{2}\right) \times 2 \times \pi \times N \qquad 10.1$$

Typical values for R_1 and R_2 are 9.5mm and 7mm respectively.

10.2.1 The effect of rate of rotation on the volume of material removed

Figure 10-7 shows the effect of rate of rotation on the wear per unit sliding distance. The evidence suggests that more material is removed per unit sliding distance at the lower rotational speeds. This supports the hypothesis that the tool is penetrating further into the surface at low speeds, as demonstrated in section 10.1.1. However, as with the measured torque, the wear per unit siding distance becomes almost independent of rotational speed above ~20 rpm.

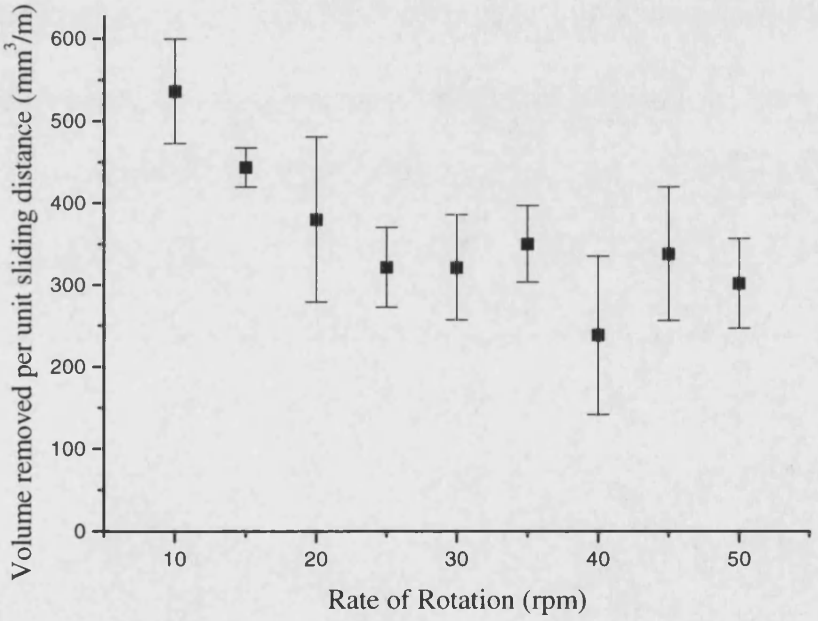

Figure 10-7 : The effect of rotation rate on material removal for unoxidised IM1-24 with a constant tool load of 500g, (error bars show ± 2 standard deviations).

10.2.2 The effect of tool load on the volume of material removed

As might be expected from the torque data presented in section 10.1.2, there is no measurable removal of material until a threshold cutting load is surpassed (see Figure 10-8), that allows the tool to penetrate the surface of the sample rather than just sliding over it. The quantity of material removed per unit sliding distance then rises in an approximately linear manner (Figure 10-8), generally giving a smaller standard deviation than the recorded torque. These results are as expected since when the load is increased the tool can penetrate further into the graphite removing more material.

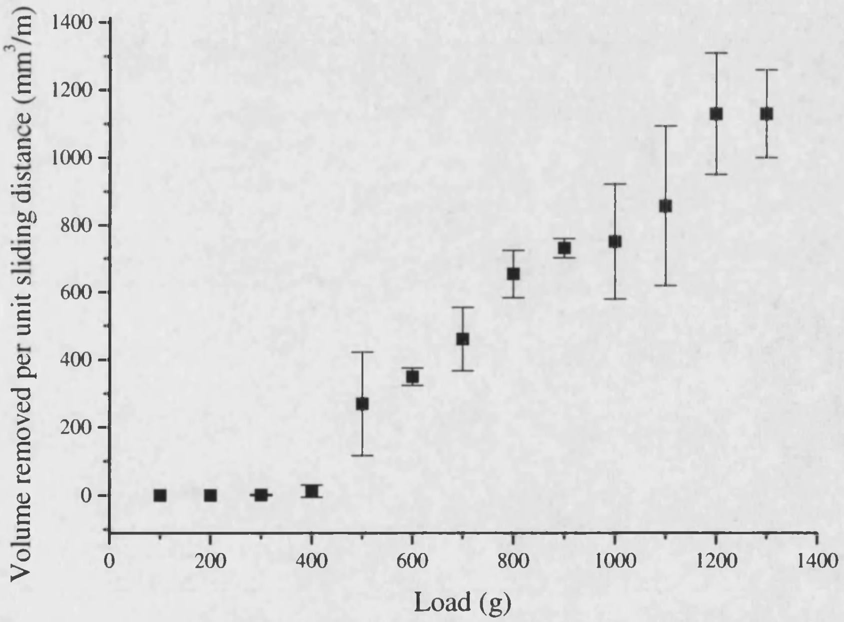

Figure 10-8 : The effect of increasing tool load on the volume of material removed per unit sliding distance for unoxidised IM1-24 graphite, (all tests were carried out at 50rpm, and the error bars show ± 2 standard deviations).

An adaptation of the Archard wear equation, $Q = \frac{ML}{h} + C$, where Q = volume of material removed per unit sliding distance, L = tool load, h = hardness, M = constant and C = scaling constant, can be used to describe the data in Figure 10-8. The standard Archard wear equation [120] has no scaling constant C as it was conceived for a single wear mechanism in non work hardening metals. However for use in this application the constant, C, is added to take account of the threshold cutting load.

Figure 10-9 shows a graphical representation of the adapted Archard relationship, where T is the threshold load for cutting . It is evident from Figure 10-9 that the Archard Slope = $\frac{C}{T}$, hence $T = \frac{C}{M}h$. So, according to the Archard equation the threshold load for cutting is proportional to hardness as would be expected.

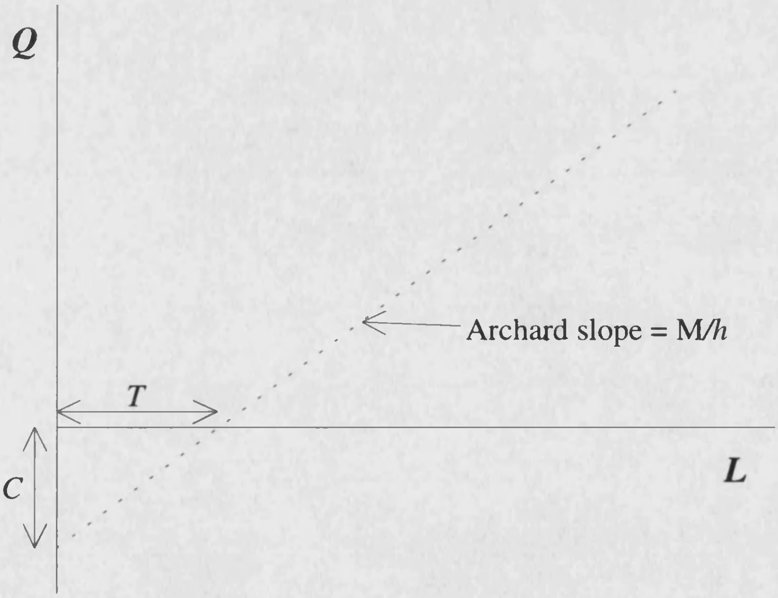

Figure 10-9 : Graphical representation of the adapted Archard relationship.

10.2.3 The effect of oxidation on the quantity of material removed

Figure 10-10 shows examples of the effect of increasing tool load on wear of IM1-24 graphite for a number of samples with different levels of burn off. It is apparent that the adapted Archard relationship can be applied to oxidised IM1-24 graphite, and that there are a number of marked differences that occur with increasing weight loss.

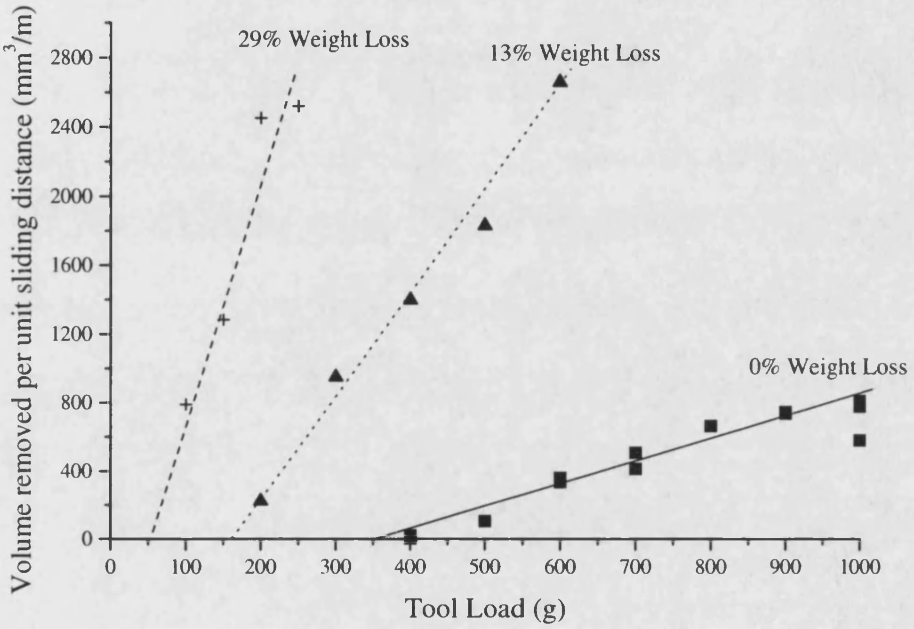

Figure 10-10 : The effect of tool load on the wear of IM1-24 graphite for different levels of burn off (constant rate of rotation of 50rpm).

The Archard equation parameters for oxidised IM1-24 graphite are given in Table 10-1, which shows that generally the slopes of the lines increase and their intercepts with the x-axis decrease as the percentage burn off increases. This trend is expected since the Archard slope is inversely proportional to hardness and the threshold load for cutting is directly proportional to hardness and intuitively we would expect hardness to decrease with increasing burn off. However, there are two data points that have negative values (see Table 10-1), which quite clearly is physically impossible. This occurs because a small error in the slope of the line will produce a large difference when extrapolated to give a threshold value for cutting, *T*. The situation is worse still when the value of the y-axis intersection, *C*, is plotted as a greater extrapolation is involved.

Weight Loss %	Archard slope, *M/h* $mm^3m^{-1}g^{-1}$	Cutting threshold g
0	1.16	336
5	1.67	248
5.2	1.94	211
9.4	2.77	179
9.9	1.52	134
11.2	3.41	-15
12.1	4.46	143
13.3	5.75	154
16.8	6.5	-1
18.2	5.1	80
21.2	12.14	51
22.2	9.67	60
23.7	8.29	30
25.1	15.98	76
25.5	13.56	56
29.1	12.71	36

Table 10-1 : The effect of thermal oxidation of IM1-24 graphite on the measured Archard slope and threshold load for cutting.

The variation of the Archard slope, *M/h*, with increasing oxidation is shown in Figure 10-11. The curve can be fitted to an exponential equation $\frac{M}{h} = 1.2\exp(8.7x)$ where x is fractional weight loss. The error bars show ± two standard deviations and increase in size with increasing burn off, so that by ~25% weight loss there is a large degree of scatter evident. An exponential increase in M/h has also been found to be the case for wear tests on zirconia [121], investigating the influence of porosity. This suggests that porosity and its effect on the mechanical properties of a material is a dominant factor here.

Figure 10-12 shows that the threshold load for cutting decreases exponentially and can be fitted to the equation $T = 336\exp(-8.8x)$. This demonstrates that the threshold cutting load is inversely proportional to the Archard slope which, must be the case if the adapted Archard equation is to be applicable to oxidised IM1-24 (see Figure 10-9).

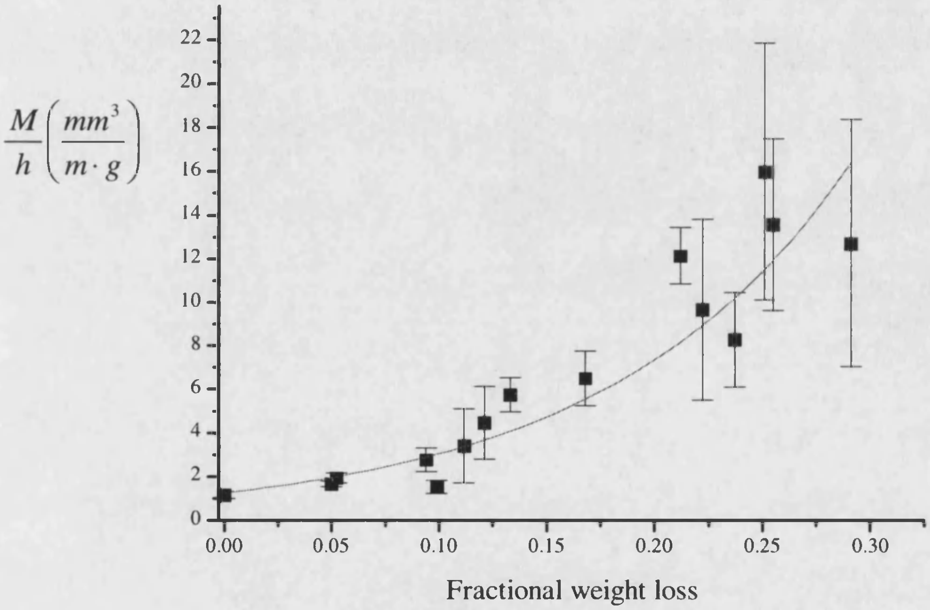

Figure 10-11 : The variation of the Archard slope, *M/h*, with increasing burn off for oxidised IM1-24 graphite (error bars = ±2 standard deviations).

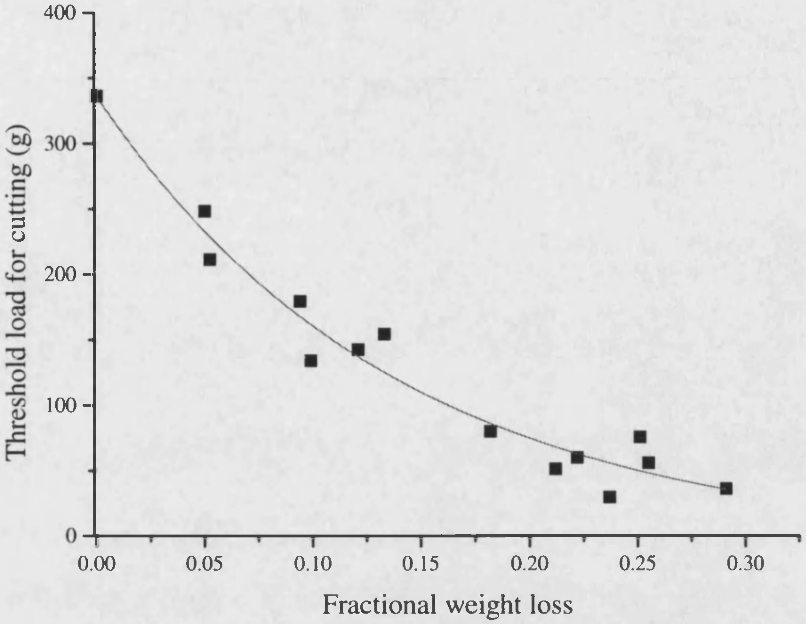

Figure 10-12 : The effect of oxidation on the threshold cutting load for oxidised IM1-24 graphite.

The application of the Archard wear equation to oxidised IM1-24 graphite raises the possibility of using a hardness measurement to predict dynamic wear characteristics. In section 9.1.2 it was shown that blunt indentation strength decreased exponentially with increasing oxidation in a manner described by the equation $\frac{\sigma}{\sigma_0} = \exp(-5.3x)$. Figure 10-13 shows a plot of the changes in indentation strength and the changes in the inverse of the Archard slope, *h/M,* with weight loss, in both cases normalised to the values for unoxidised graphite. It is plausible to argue that the data all lie on the same curve allowing for the scatter in results. This demonstrates a correlation of what could be termed hardness measurements made using a blunt indentation technique, with a hardness term obtained from these dynamic tests. This in turn raises the possibility of using a static indentation technique to predict the dynamic wear characteristics of IM1-24 graphite.

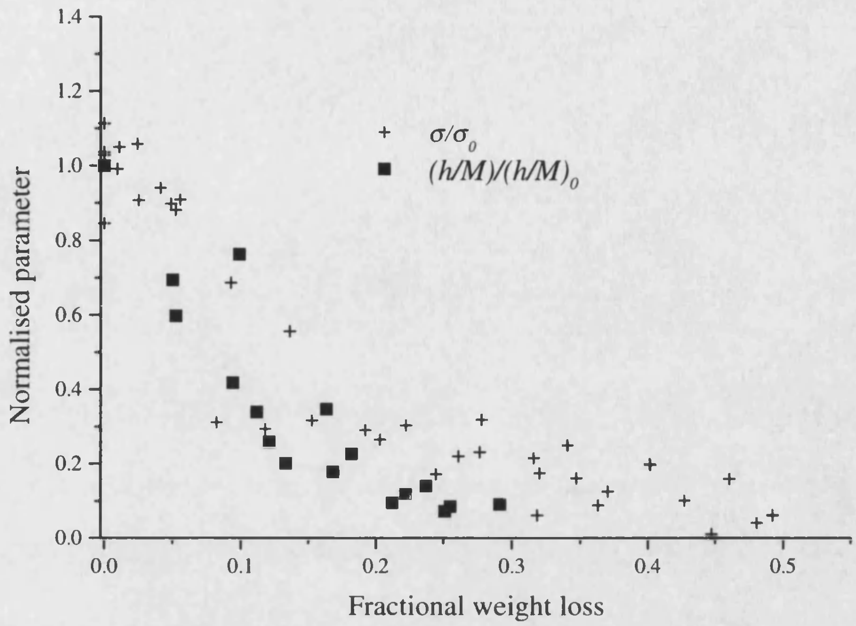

Figure 10-13 : Correlation between blunt indentation strength, σ, and *h/M* for oxidised IM1-24 graphite. Data normalised to values for unoxidised graphite.

The indentation and wear data plotted in Figure 10-13 can be grouped together and fitted to the exponential equation Normalised parameter = exp(-7.2x). Using this relationship and the data for the dynamic wear of unoxidised IM1-24 graphite (Figure 10-10) the wear characteristics can be predicted for any weight loss (see Figure 10-14).

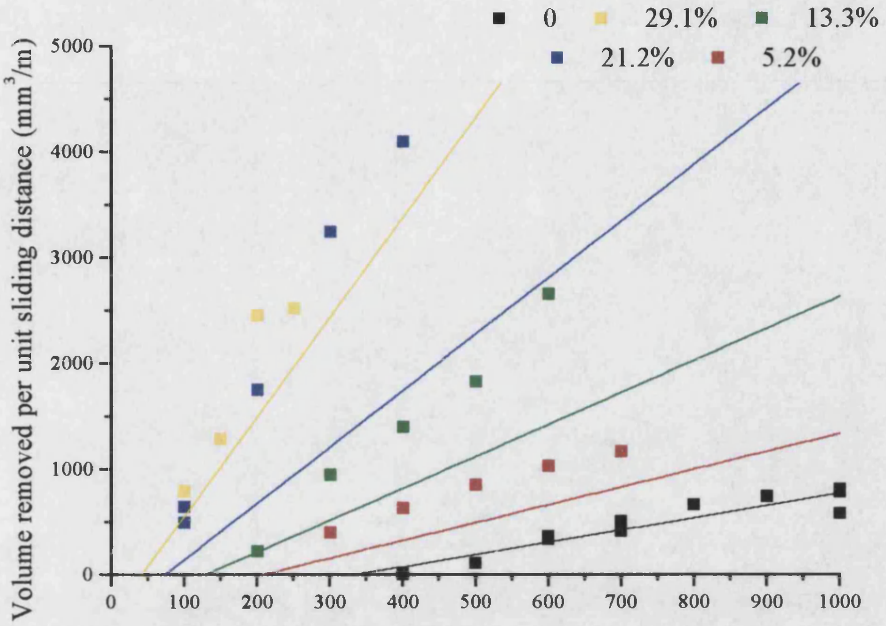

Figure 10-14 : The effect of oxidation on the wear of IM1-24 graphite. Data points are measured values and the lines show the calculated prediction for that weight loss.

It is evident from Figure 10-14 that the prediction seriously underestimates the wear of oxidised IM1-24 graphite improving slightly at high weight losses (~30%). Hence, it is concluded that the scatter in the data in Figure 10-13 does not allow an accurate prediction of wear rates.

10.3 A friability index for oxidised nuclear graphite ?

The concept of friability and some previous attempts to measure friability were considered in Chapter 1. A friable material can be defined as one that is partially reduced to powder when a stress is applied. So, if this definition were to be embodied in a numerical index in the same manner as hardness has been in the past, there are two main variables that must be considered.

1. There should be some measure of the quantity of the sample that is reduced to powder. Hence the debris must be accounted for, perhaps just in terms of the amount or number of particles produced, although the nature of the particles may also be important.
2. The force required for any debris to be produced must also be accounted for, for example, as a maximum stress in a particular loading regime.

Thus in a simple form friability, F, could be described by the equation $F = \frac{N_P}{\sigma}$ where, σ = applied stress and N_P = number of particles produced. If this equation was applied to a blunt indentation test then σ would be the blunt indentation strength defined in Chapter 7. For unoxidised IM1-24 graphite the sample generally breaks into 2, 3 or maybe 4 pieces producing a fairly low value of this index that corresponds to a low friability. However as higher levels of porosity are introduced by oxidation the indentation strength decreases and the sample begins to break into more pieces, until a point is reached where there is significant crushing occurring producing many small pieces. Consequently, as the sample becomes more friable the value of the index will increase.

Another way of treating friability would be as a form of wear, as in the dynamic friability test, which still relies on knowing the force applied and the quantity of debris produced. Wear is commonly expressed as a volume of material removed per unit sliding distance, which could be used to rank materials for a constant load. This has the disadvantage of being a more complex test than blunt indentation, and in general it does not account for the nature of the debris. It is also on the whole more difficult to relate to material properties, but it has the advantage of being a better model than blunt indentation of a friable process. The wear rate and hence the friability have been shown to increase significantly as the graphite is oxidised e.g. Figure 10-10.

These methods are not practical for use by the nuclear industry as collecting and measuring the quantity of debris produced from highly radioactive graphite is extremely difficult, so an indirect measurement of friability is required. It was demonstrated that the volume of material removed during the dynamic friability test is governed by the hardness and the load applied to the contact. This provides a possible link between the simple blunt indentation test and the more complex dynamic friability test. However, the wear rate is substantially under predicted when the decrease in blunt indentation strength with increasing oxidation is assumed to be the same as the decrease in the hardness calculated from the Archard equation (see Figure 10-14).

Thus, it has not proved possible to define a single index that adequately describes the friability of oxidised nuclear graphite that can be measured in a reactor core.

10.4 Summary

The torque measurements recorded here were found to be noisy (see Figure 10-1) so a fast Fourier technique was employed to investigate how the amplitude varies, and to see if fracture information can be extracted from torque measurements. However, the only discrete peaks visible (see Figure 10-2) are the offset which is due to the average torque, the fundamental frequency and harmonics due to the eccentricity of sample rotation. It seems likely that some of the noise is inherent in the test and may be occurring as small fractures take place, but, without greatly increased sensitivity, it is impossible to distinguish fracture events from the background noise. So it seems that the torque can only be used to give an indication of the average force required for cutting under certain conditions, for comparison purposes.

Both the torque and the volume of material removed per unit sliding distance decrease slightly as the rotation speed is increased (see Figure 10-3 and Figure 10-7), quickly reaching an almost constant value. This corresponds to larger depth cuts being taken at low speeds. So at low speeds the tool has more time to indent the surface in a given place allowing greater penetration. This removes more material, requiring a greater force and hence a higher torque is recorded. This also explains the observed increase in wear and recorded torque (see Figure 10-4 and Figure 10-8) as the tool load is increased.

An adaptation of the Archard wear equation (see equation 10.2) can be used to describe the effect of tool load on the volume of material removed, and it provides a useful way of comparing graphites with different degrees of oxidation. The graphite hardness calculated from the equation, and the cutting threshold, exhibit a similar exponential decrease with increasing burn off as the blunt indentation strength. However, the wear characteristics of IM1-24 graphite can not be accurately predicted from blunt indentation measurements. Thus, it has not proved possible to define a simple index encompassing both static an dynamic friability that can be easily used by the nuclear industry.

11. Debris Analysis

The particle size distribution was measured for debris produced during the friability tests under a range of conditions. The measurements were made using a Malvern instruments laser sizer with a ultrasonic feeder to avoid damaging fragile particles, which is described in Chapter 5. The debris was microstructurally examined by mounting and sectioning then viewing under an optical microscope.

11.1 Particle size distributions

11.1.1 The effect of rate of rotation

Figure 11-1 shows a characteristic particle size distribution for unoxidised IM1-24 graphite, which generally has three maxima that vary in size. The distribution can be deconvoluted into three separate peaks, by using a Gaussian fit, (see Figure 11-1) that when combined make up the shape of the distribution. The approximate median particle sizes for the peaks are as follows, peak 1 = 40μm, peak 2 = 200μm, peak 3 = 2000μm. It is possible that these sizes correspond to debris produced by individual microstructural processes. Figure 11-2 shows that the median particle size for each peak remains roughly constant over the range of rotation speeds tested.

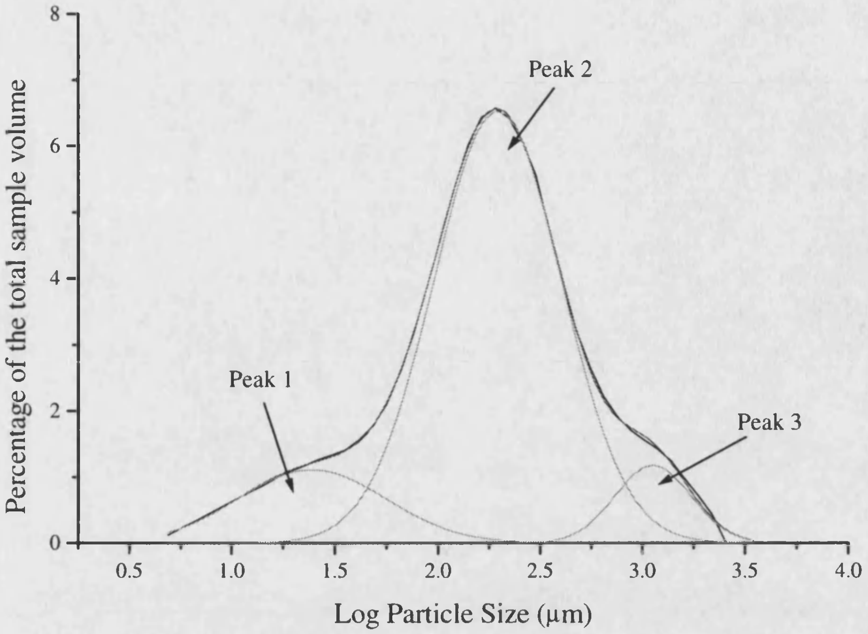

Figure 11-1 : Particle size distribution of debris from unoxidised IM1-24 produced at a rate of rotation of 10 rpm using a tool load of 500g.

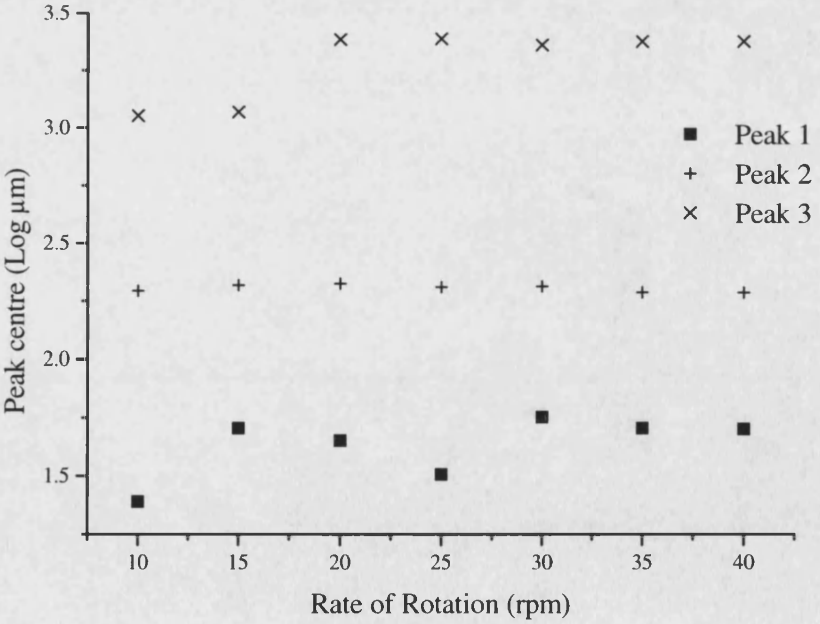

Figure 11-2 : The variation of the median particle size of unoxidised IM1-24 graphite for each peak with increasing rate of rotation, at a constant tool load of 500g.

The relative sizes of these peaks expressed as peak areas in Figure 11-3 also appear to remain roughly constant over the range of rotation rate tested. So, although the volume of material removed is greater at lower rates of rotation (see section 10.2.1), there is no evidence of larger debris being produced. Thus the rate of rotation appears to have no significant effect on the size distribution of the debris.

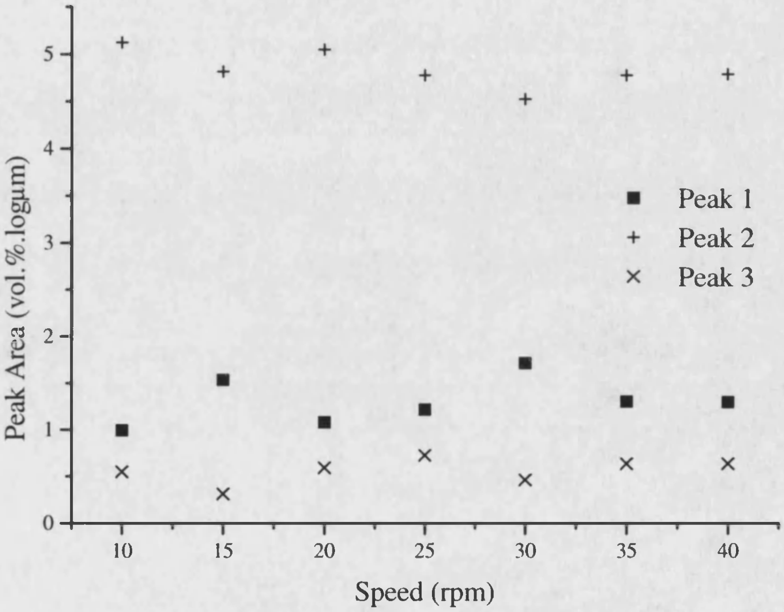

Figure 11-3 : The effect of rotation rate on the peak area for unoxidised IM1-24 graphite debris produced using a 500g tool load.

11.1.2 The effect of tool load

The particle size distribution in Figure 11-4, was deconvoluted into three peaks in the same manner as before. The median particle sizes of the debris in peaks 2 and 3 (see

Figure 11-5) remain approximately constant with increasing load; there is a slight decrease in the size of the debris in peak 3 with increasing load.

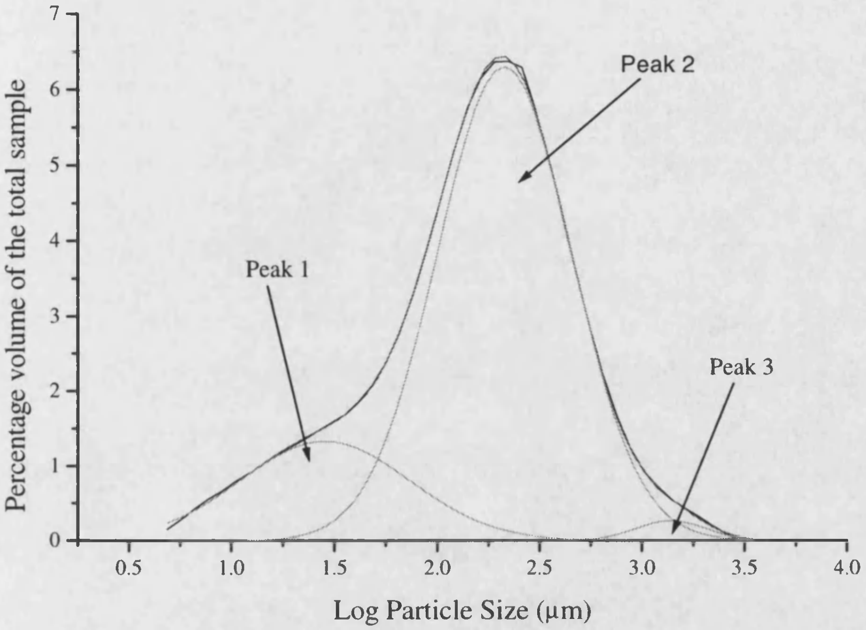

Figure 11-4 : Particle size distribution for unoxidised IM1-24 graphite debris produced at 50 rpm under a 700g load.

Figure 11-6 shows that the area of the first peak (very fine debris) changes very little, but as high loads (~900g) are reached the area of peak 2 (intermediate sized debris) declines slightly while the area of peak 3 (large debris) increases. The volume of material removed per unit sliding distance increases in an approximately linear manner over these tool loads (see section 10.2.2). So one would expect deeper cuts to be taken as the load is increased, which may explain the increase in the quantity of large scale debris. Generally the effect of the tool load on the size of the debris produced is small, but there is the possibility that at high loads there is a tendency towards the formation of larger debris.

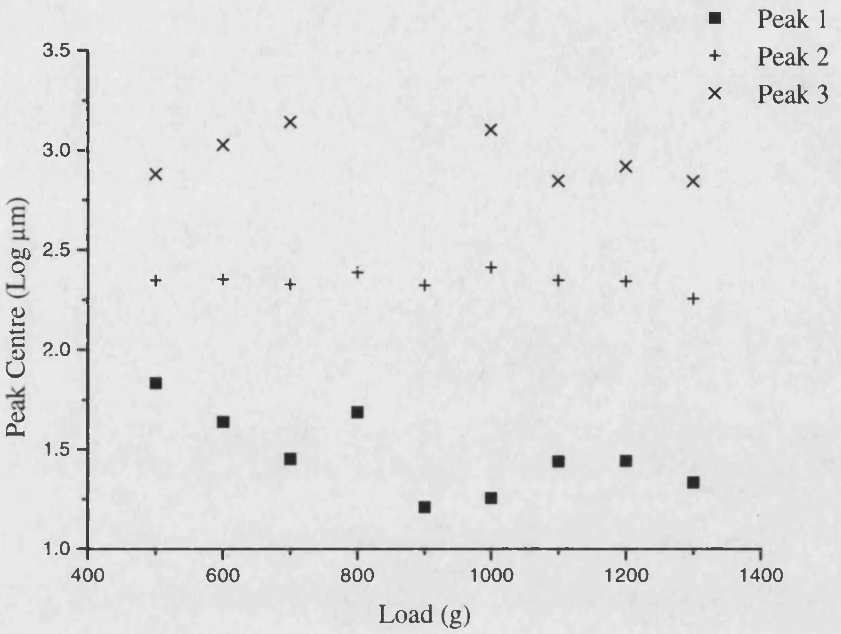

Figure 11-5 : The effect of tool load on the median particle size of unoxidised IM1-24 graphite debris for each peak, at a constant rotational speed of 50 rpm.

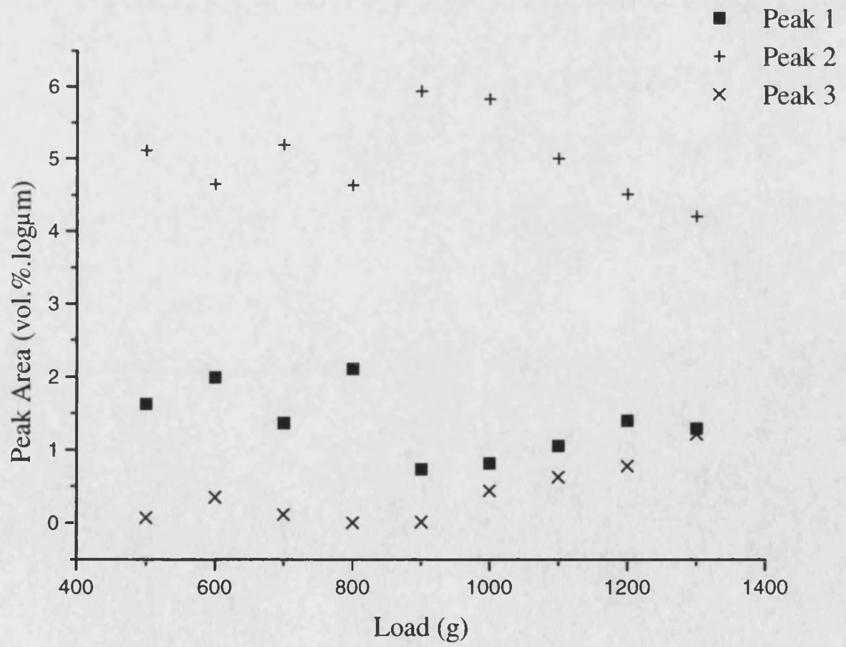

Figure 11-6 : The effect of tool load on the peak area for unoxidised IM1-24 graphite debris produced at a constant rotational speed of 50 rpm.

11.1.3 The effect of oxidation

The particle size distribution was measured for debris produced during the friability tests from samples oxidised to a range of weight losses. The size distributions for oxidised IM1-24 graphite with two different weight losses shown in Figure 11-7, exhibit a marked difference. The distribution for the sample with a low level of oxidation is very similar to distributions shown earlier, but, as the oxidation is increased, the third peak becomes very prominent. Figure 11-8. Shows that with increasing oxidation peak 1 changes very little, but there is a steady decline in the area of peak 2 accompanied by a steady increase in the area of peak 3. So, as the graphite is oxidised its propensity to produce debris in the larger size range is increased. It is also worth noting that generally the median particle size for each peak does not change greatly (see Figure 11-9) upon oxidation.

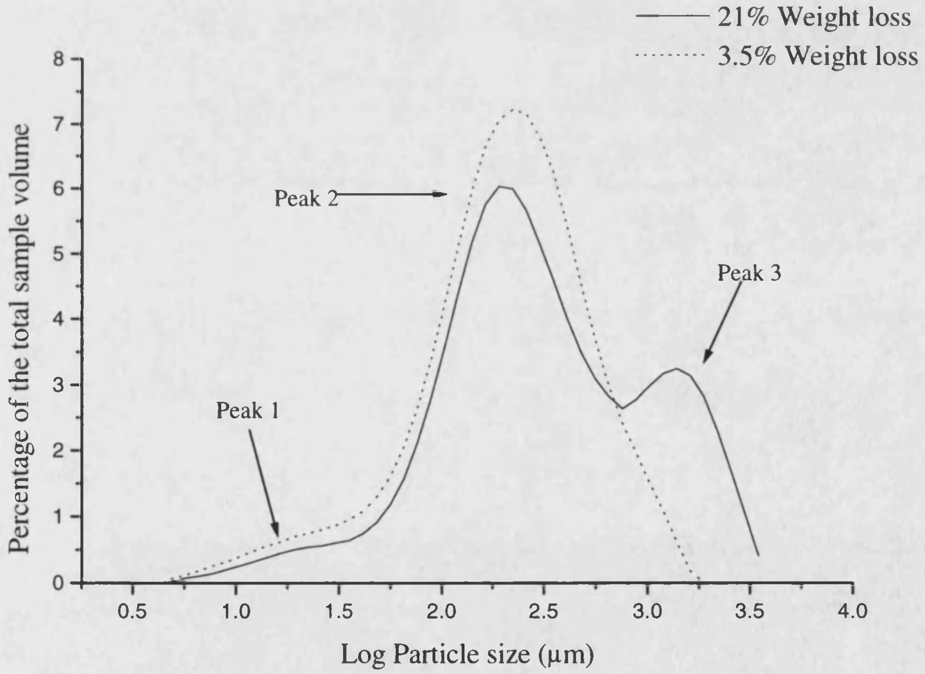

Figure 11-7 : Particle size distributions for debris from samples with different degrees of oxidation, tested at 50rpm with a 500g tool load.

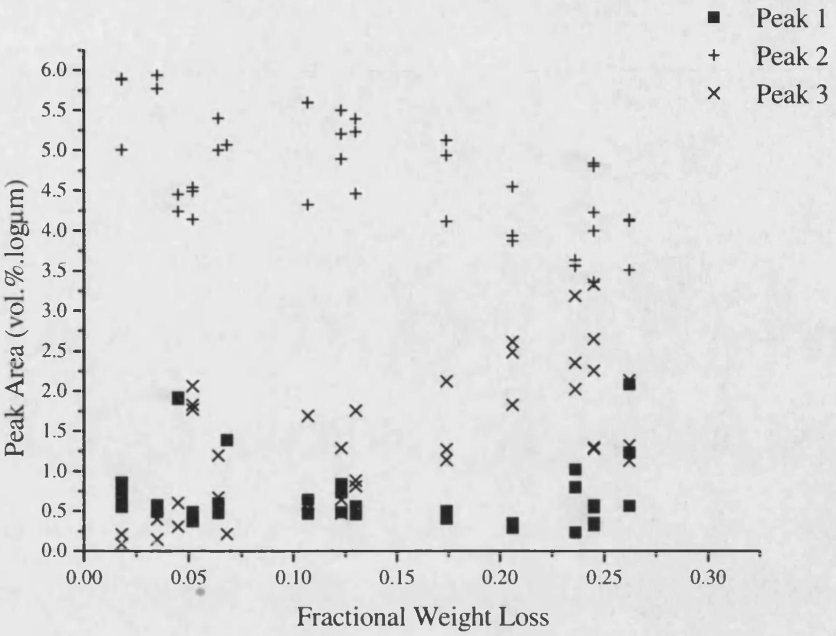

Figure 11-8 : The effect of oxidation of IM1-24 graphite on peak area for debris produced using a 500g tool load and a rotational speed of 50 rpm.

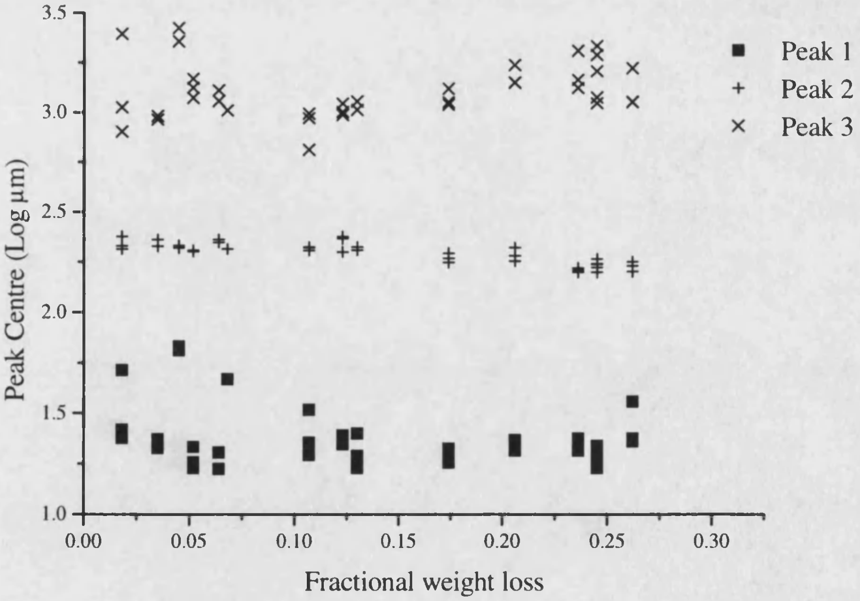

Figure 11-9 : The effect of oxidation of IM1-24 graphite on the median particle size of each peak, for debris produced using a 500g tool load and a rotational speed of 50 rpm.

11.2 Optical Microscopy

11.2.1 Debris from unoxidised IM1-24

For the unoxidised graphite a sample produced using a high load (1200g) was selected as reasonable quantities of the three different size ranges were visible in the particle size distributions. The debris was then separated into three size ranges, <75μm, 75-1000μm and >1000μm by careful sieving. These size ranges roughly correspond to the peaks in the particle size distributions. The sieved samples were then mounted in epoxy resin allowing sectioning and polishing to be carried out before viewing under an optical microscope. Figure 11-10 shows the very fine debris associated with peak 1 of the distribution, which appears to consist exclusively of binder phase. This is not surprising since the filler particles are unlikely to be broken down to this size range.

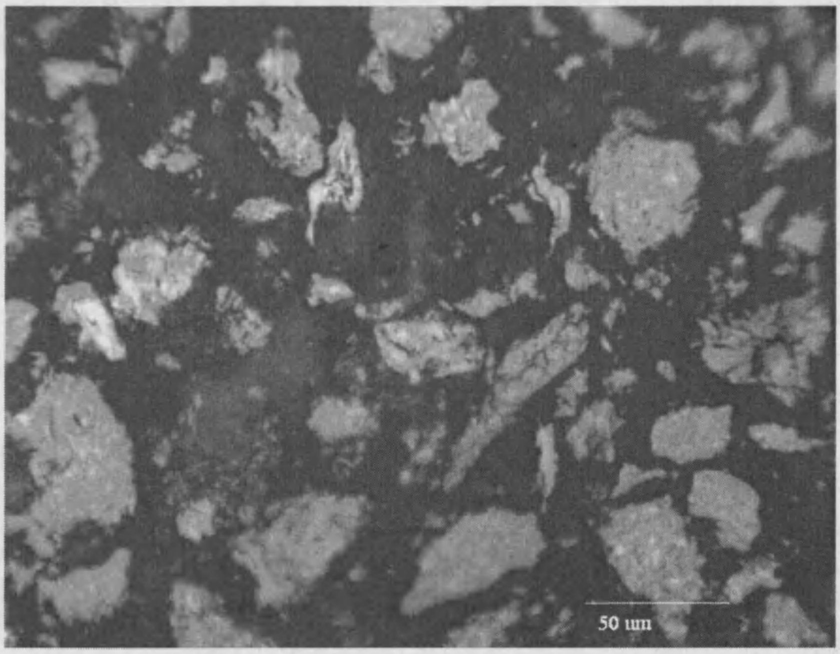

Figure 11-10 : Cross section of sub 75μm debris from unoxidised IM1-24 graphite.

The intermediate size range corresponding to peak 2 in the distribution is made up of larger pieces of fractured binder phase and some fractured filler particles marked as A and B respectively in Figure 11-11.

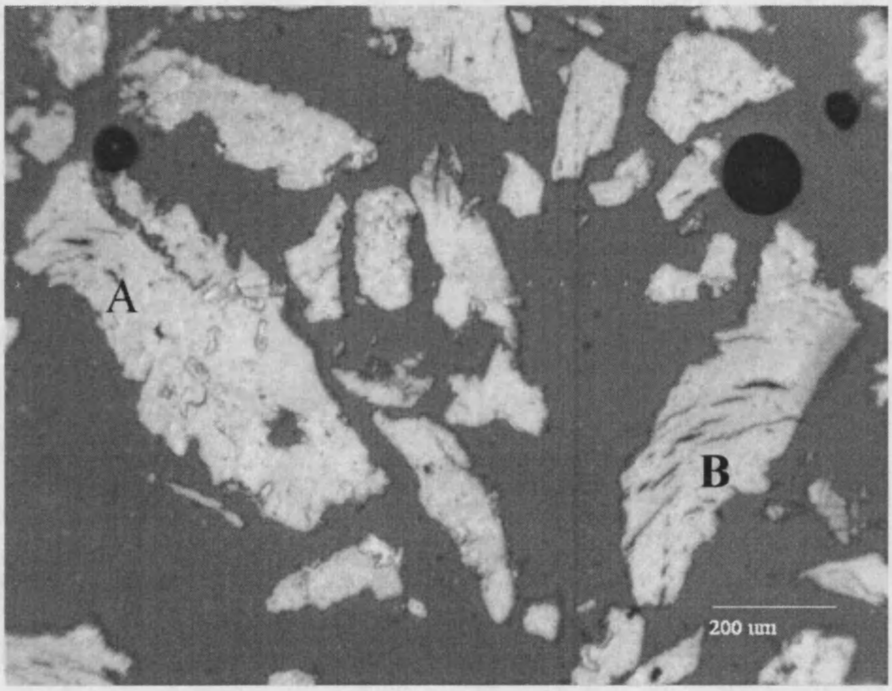

Figure 11-11 : Cross section showing intermediate sized debris from unoxidised IM1-24 graphite. A indicates a binder phase fragment and B indicates a Gilsocarbon filler particle fragment.

Lastly, when very large debris is examined whole filler particles are evident often still surrounded with binder (see Figure 11-12). In some cases groups of filler particles still bonded together are seen, although they are not always whole. So broadly speaking microstructural features in the debris can be assigned the particular peaks in the particle size distribution. It seems likely that the change in the nature of the debris is due to the increased depth of cut produced by a greater load being applied, which means there is a higher probability of removing whole filler particles.

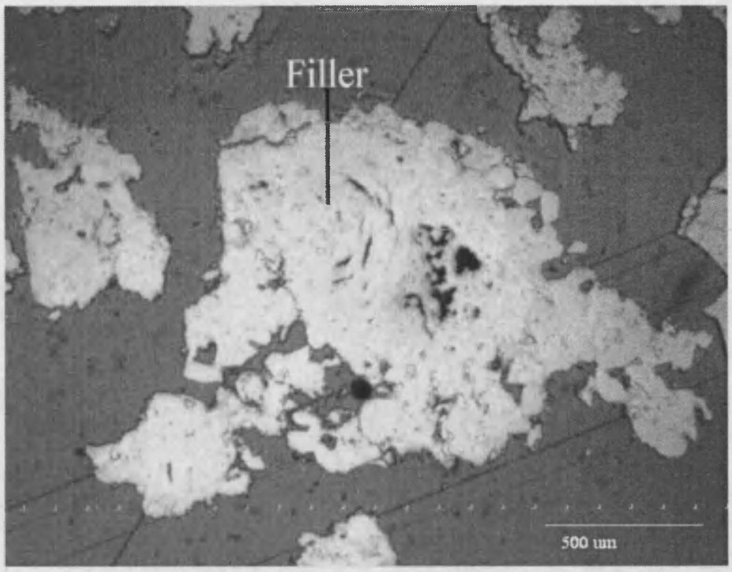

Figure 11-12 : Cross section of very large debris from unoxidised IM1-24 graphite showing filler particles with binder phase attached.

11.2.2 Debris from oxidised IM1-24 graphite

The particle size distribution showed an increase in the amount of large scale debris as the degree of oxidation is increased (Figure 11-8). If a fairly high weight loss sample is taken and the large scale debris is separated out in the same manner as before, the microstructure of the debris can be examined. The particles observed are generally larger than those recorded for the unoxidised IM1-24 graphite, even if high tool loads are used. Generally each particle is made up of several filler particles still surrounded with some binder phase (see Figure 11-13). These findings seem to support the suggestion made by Burchell *et al* [42] that the binder phase is preferentially attacked during oxidation in CO_2, allowing easy crack propagation and thus increasing the likelihood of relatively large particles being removed. The other size ranges show the same features evident in the unoxidised debris, with some microstructural evidence of oxidation.

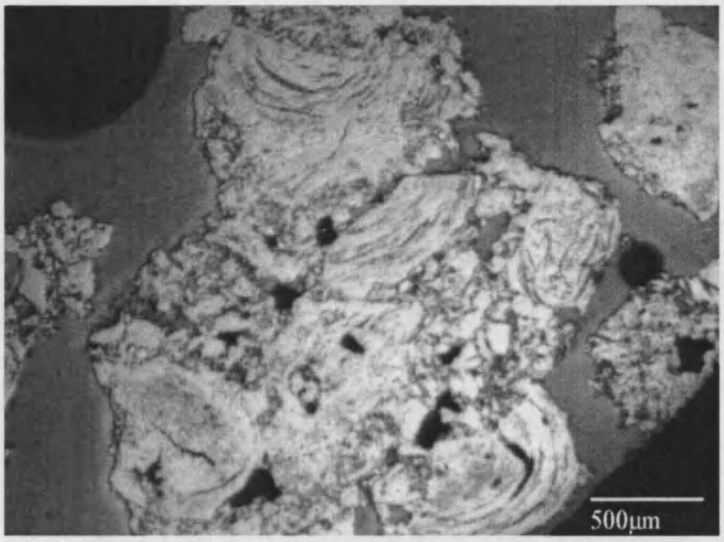

Figure 11-13 : Cross section of oxidised IM1-24 debris (approximately 20% weight loss) showing several filler particle fragments bound together with binder phase.

11.3 Summary

Generally the debris produced during the friability tests has a particle size distribution that can be deconvoluted into three peaks. The rate of rotation has little or no effect on the size distribution of the debris which is expected as a number of researchers [43, 122, 123] have shown there to be no effect of strain rate on the measured mechanical properties of graphite. There is the possibility that at high loads larger sized debris is produced, simply because of the substantial increase in the depth of cut being made during each revolution. However, this is by no means certain owing to the scatter in the results.

The fundamental changes to the microstructure of IM1-24 caused by thermal oxidation produce consistent changes in the particle size distributions recorded. As more porosity is introduced one would certainly expect a larger quantity of debris to be produced over a set sliding distance, which is indeed the case (see Chapter 10). However as the degree of oxidation is increased the production of larger size debris becomes progressively more dominant. This is most likely due to the preferential attack of the binder phase effectively weakening interfaces between filler and binder.

It is likely that the three peaks can be attributed to particular microstructural processes. The evidence suggests that peak 1 is due to the fracture of the binder phase into very small fragments. While the process controlling the production of debris corresponding to peak 2 is likely to be the fracture of the Gilsocarbon particles. The large scale debris corresponding to peak 3 is likely to be produced by crack propagation between large porosity.

12. Main Conclusions

1. A novel blunt indentation technique capable of testing small samples trepanned from a reactor core has been developed. For the first time, this allows the investigation of the effect of highly concentrated contact stresses on nuclear graphites. Loading to failure allows the change in strength of the graphite during service to be monitored. It was found that it is possible to obtain quantitative information on the degree of damage produced by analysis of hysteresis loops.

2. The sample thickness has been shown to affect both the failure load and displacement, as well as the mode of fracture. Above a critical size (~8mm thick), the failure load and displacement become independent of sample thickness, and fracture is initiated by the Hertzian stresses fracturing the sample in two pieces. However, samples of smaller thickness fracture into three roughly equal pieces, which is very likely due to biaxial bending.

3. For the first time, a comprehensive study of blunt indentation damage in polycrystalline graphites has been carried out, demonstrating the effects of both microstructural scale and porosity on the damage mode. Extremely fine textured graphite fractures in a Hertzian manner producing a classical Hertzian cone crack above a critical load. As the microstructural scale is increased, shear deformation becomes increasingly prominent until there is no evidence of Hertzian cracking, although catastrophic failure is still initiated by tensile stresses at the surface. The effect of porosity is more complex since it is inseparably linked with the microstructural scale. However, when graphites of similar microstructural scale with differing quantities of porosity were investigated the porosity was found to have a marked effect on the degree of damage.

4. The reduction in blunt indentation strength of IM1-24 graphite with increasing thermal oxidation is less severe than previously found with more conventional mechanical tests, and is closer to the reduction produced by radiolytic oxidation. A

change in the fracture mode occurs at high levels of oxidation (>40% weight loss), when the sphere begins to crush through the sample giving rise to much greater permanent deformation and a progressive failure. This coincides with the decrease in the measured elastic recovery to a very low level. Therefore, although the indentation depth at failure does not change significantly, the observed indentation depth is substantially larger if the load is removed before failure occurs.

5. A dynamic friability test relevant to reactor processes has been developed and used to investigate the effects of oxidation. Torque measurements were found to be of limited use for elucidating fracture processes, as the trace produced is inherently noisy. Monitoring the wear rate proved both more useful and more convenient.

6. The average size of the wear debris produced does not change significantly with oxidation, but the proportion of large debris present increases noticeably as the level of burn off is increased. This change in the debris has been attributed to the effect of oxidation on the microstructure of IM1-24 graphite.

7. As the degree of oxidation is increased the wear rate increases markedly. In conjunction with this the value of hardness calculated from an adapted form of the Archard relationship decreases in a similar manner to the blunt indentation strength measured in earlier experiments. This raises the possibility of using the simple blunt indentation test to predict the wear characteristics of the graphite. However, it is shown that the scatter of results does not allow an accurate prediction of wear rate from blunt indentation strength for oxidised IM1-24 graphite.

13. Suggestions for Further Work

The effect of sample geometry on the fracture morphology and stress could be investigated further using finite element analysis. Hertzian mechanics have been demonstrated to be inadequate for predicting the stresses beneath a blunt indenter in IM1-24 graphite. This is likely to be because Hertzian mechanics are designed for a purely elastic system and IM1-24 graphite is far from elastic. Non linear analysis is possible using finite element analysis which can account for porosity. Ultimately, such analysis could lead to a materials model incorporating a fracture criterion. This may allow not only the calculation of accurate uniaxial strengths from a blunt indentation test, but could also be used for predictions of stresses in more complex loading geometries.

Biaxial flexure tests of IM1-24 using a ball on a ring geometry could be used to investigate the effect of sample thickness further. The tests could help to determine the effects of thickness on fracture morphology, and whether biaxial stresses would give you the fracture morphology observed.

A detailed fracture mechanics study on the different graphites tested could potentially improve the understanding of how microstructure effects the damage evolution beneath a blunt indenter.

It would be useful to study how the severity of the exponential decrease in strength and modulus is effected by a density gradient within the sample. It would also possible to determine if measured exponential decrease in strength is effected by the test geometry.

14. Nomenclature

F = friability Index

ΔW = change in mass

W_0 = initial mass

PE = potential energy

g = acceleration due to gravity

D = diameter

σ_{crush} = crushing strength

K = diametric crushing force

H = height

ΔV = volume change

ρ = bulk density

e = fractional porosity

ρ_0 = density of as received graphite

ρ_{ox} = density of oxidised graphite

ρ_c = crystal density

σ_f = fracture strength

σ_0 = fracture stress of as received graphite

n = power law constant

A = constant (empirical)

b = exponential constant (empirical)

γ_s = surface energy

E = Youngs modulus

c = crack length

γ_p = energy for plastic deformation at the crack tip

G_c = critical strain energy release rate

σ = stress

K_c = critical stress intensity factor
a = radius of contact circle
P = load
R = sphere radius
P_0 = maximum Hertzian pressure
σ_m = maximum Hertzian tensile stress
P_{av} = average Hertzian pressure
v = Poisson's ratio
G = shear modulus
σ_B = blunt indentation fracture strength
δ = indentation depth
A = contact area
r = radial distance
z = z-axis distance
t = sample thickness
s = radius of the support circle
u = radius of the region of uniform loading
d = diameter of the disk
ΔK = cyclic stress intensity
x = fractional weight loss
R_1 = initial sample radius
R_2 = final sample radius
N = number of revolutions
Q = Volume of material removed per unit sliding distance
L = tool load
h = hardness
M = constant
C = constant
N_P = Number of particles

15. References

1. M.W. Davies, Proceedings of IAEA specialist meeting, *Graphite Moderator Lifecycle behaviour*, p47, (1995).

2. E.W. Carpenter and D.J. Norfolk, *Nuclear Energy*, **23**, p83, (1984).

3. C.O. Nwajagu and I.C.I. Okafor, *Applied Clay Science*, **4**, p211, (1989).

4. ASTM Standards, *Standard Test Method for Tumbling Friability of Pre-formed Block-type Thermal Insulation*, ASTM C 421-88, (1989).

5. British Standards, *Analysis and Testing of Coal and Coke*, BS 1016 Section 108.2, (1992).

6. J.A.H. De Jong, *Powder Technology*, **65**, p293, (1991).

7. British Standards, *Mechanical Properties of Desiccants*, BS 3482 : Part 11, (1991).

8. W.C. Duncan-Hewitt and D.J.W. Grant, *Powder Technology*, **52**, p17, (1987).

9. M.M. Bindal, S.K. Singhal, R.K.Nayar, R. Chopra and A. Dhar, *Journal of Materials Science letters*, **6**, p1045, (1987).

10. K.F. Philips and G.M. Halley, *The Friability of Radiolytically Oxidised Graphite*, The English Electric Company, Internal Report No. W/AT 1627, (1966).

11. B. Rand, *High Performance Carbon Materials*, conference proceedings of Hipermat 89, (1989).

12. H. Marsh and C. Cornford, *Petroleum Derived Carbons*, proceedings of an American Chemical Society symposium, Chapter 20, (1976).

13. J. Dubois, C. Agache and J.L. White, *Metallography*, **3**, p337, (1970).

14. S. Ragan and H. Marsh, *Journal of Materials Science*, **18**, p3161, (1983).

15. R.E. Nightingale, *Nuclear Graphite*, Academic Press Inc., (1962).

16. Blackman, *Modern Aspects of Graphite Technology*, Academic Press, (1970).

17. W. Chard, M. Conway and D. Niesz, *Petroleum Derived Carbons*, proceedings of an American Chemical Society symposium, Chapter 14 , (1975).

18. N. Ichinose, *Introduction to Fine Ceramics*, John Wiley & Sons Ltd, (1987).

19. A.M. Neville and J.J. Brooks, *Concrete Technology*, Longman Scientific and Technical, (1987).

20. H.H. Losty and J.S. Orchard, *Proceedings of the fifth Carbon Conference*, p519, (1962).

21. J.M. Illston, *Construction Materials their Nature and Behaviour*, Chapman & Hall, (1994).

22. G.M. Jenkins, *British Journal of Applied Physics*, **13**, p30, (1962).

23. E.J. Seldin, *Carbon*, **4**, p177, (1966).

24. O.D. Slagle, *Journal of the American Ceramic Society*, **50**, p495, (1967).

25. W.N. Reynolds, *Philosophical Magazine*, **11**, p357, (1964).

26. S. Amelinckx and J. Delavignette, *Philosophical Magazine*, **5**, p533, (1960).

27. B.T. Kelly, *Philosophical Magazine*, **9**, p721, (1964).

28. B.T. Kelly, *Physics of Graphite*, Applied Science Publishers, London, (1981).

29. P.E. Hart, *Carbon*, **10**, p233, (1972).

30. O.D. Slagle, *Carbon*, **7**, p337, (1969).

31. I. Ioka and S. Yoda, *Carbon*, **28**, p159, (1990).

32. J.F. Andrew and S. Sato, *Carbon*, **1**, p225, (1964).

33. I.B. Mason and R.H. Knibbs, *Carbon*, **5**, p493, (1967).

34. T. Maruyama, M. Eto, and T. Oku, *Carbon*, **25**, p723, (1987).

35. G. Neighbour, *private communication*, (Feb. 1997).

36. B. McEnaney, *Fundamental Issues in Control of Carbon Gasification Reactivity*, edited by J. Lahaye and P. Ehrburger, Kluwer Academic Publishers, (1991).

37. S. Ergan, *Journal of Physical Chemistry*, **60**, p480, (1956).

38. J.V. Best, W.J. Stephen and A.J. Wickham, *Progress in Nuclear Energy*, 16, p127, (1985).

39. P.C. Minshall, I.A. Sadler and A.J. Wickham, proceedings of IAEA specialists meeting, *Graphite Moderator Lifecycle behaviour*, p181, (1995).

40. N. Murdie, I.A.S. Edwards and H. Marsh, extended abstracts of *Carbon 82*, p350, (1982).

41. J.V. Best and W.J. Stephen, extended abstracts of *Carbon 82*, p341, (1982).

42. T.D. Burchell, I.M. Pickup, B. McEnaney and R.G. Cooke, *Carbon*, **24**, p545, (1986).

43. T.D. Burchell, *PhD thesis*, University of Bath, (1986).

44. J.A. Board and R.L. Squires, proceedings of the *Second Conference on Industrial Carbon and Graphite*, Society of Chemical Industries, p35, (1966).

45. C. Rounthwaite, G.A. Lyons and R.A. Snowdon, Proceedings of the *Second Conference on Industrial Carbon and Graphite*, Society of Chemical Industries, p299, (1965).

46. S. Yoda, M. Eto and T. Oku, *Carbon*, **23**, p33, (1985).

47. R.H. Knibbs and K.B. Morris, proceedings of the *Third Conference on Industrial Carbon and Graphite*, Society of Chemical Industries, p297, (1971).

48. P.A. Thrower and J.C. Bognet, *13th Biennial American Carbon Conference*, American Carbon Society, p265, (1977).

49. B.T. Kelly, P.A.V. Johnson, P. Schofield, J.E. Brocklehurst and M. Birch, *Carbon*, **21**, p441, (1983).

50. J.L. Wood, R.C. Bradt and P.L. Walker Jr., *14th Biennial Conference on Carbon*, p332, (1979).

51. J.L. Wood, R.C. Bradt and P.L. Walker Jr., *Carbon*, **18**, p179, (1980).

52. I. Pickup, *PhD Thesis*, University of Bath, (1984).

53. E. Ryshkewitch, *Journal American Ceramic Society*, **36**, p65, (1953).

54. W. Duckworth, *Journal American Ceramic Society*, **36**, p68, (1953).

55. F.P Knudsen, *Journal American Ceramic Society*, **42**, p376, (1959).

56. J.D. Buch, proceedings of the *16th Carbon Conference*, p400, (1983).

57. J.E. Brocklehurst, *Chemistry and Physics of Carbon*, **13**, p145, (1977).

58. Griffith, *Philosophical Transactions of the Royal Society*, **221**, 163, (1920). Cited by Neighbour, *PhD thesis*, University of Bath, (1993).

59. Orowan, Welding Research Supplement., **34**, 157, (1955). Cited by Neighbour, PhD thesis, University of Bath, (1993).

60. Irwin, *Handbook der Physik*, Springer-Verlag, Berlin, **6**, 551, (1958).

61. Ashby and Jones, *Engineering Materials*, Pergamon Press, (1993).

62. Knott, *Fundamentals of Fracture Mechanics*, Butterworths, (1973).

63. M.Rodig, G.Kleist and H.Nickel, proceedings of the *14th Biennial Conference on Carbon*, p336, (1979).

64. J.L.Wood, R.C.Bradt and P.L.Walker, proceedings of the *14th Biennial Conference on Carbon*, p330, (1979).

65. T.D Burchell, M.O. Tucker and B. McEnaney, *Materials for Nuclear Reactor Core Applications*, BNES, London, p95, (1987).

66. B. McEnaney and T.D. Burchell, private communication, (1994).

67. I.M. Pickup, B. McEnaney and R.G. Cooke, extended abstracts *Carbon 82*, p320, (1982).

68. A.P.G. Rose and M.O. Tucker, *Journal of Nuclear Materials*, **110**, p186, (1982).

69. T.D.Burchell, B.McEnaney, A.P.G.Rose and M.O.Tucker, proceedings of the *Biennial Conference on Carbon*, p346, (1985).

70. M.O. Tucker, A.P.G. Rose and T.D. Burchell, *Carbon*, **24**, p581, (1986).

71. M.O. Tucker and N. McLachlan, Journal of Physics D: Applied Physics , **26**, p893, (1993).

72. T.D. Burchell, *Carbon*, **34**, p297, (1996).

73. B.T. Kelly, *Carbon*, **20**, p3, (1981).

74. R. Taylor, R.G. Brown, K. Gilchrist, E. Hall, A.T. Hodds, B.T. Kelly and F. Morris, *Carbon*, **5**, p519, (1967).

75. M. Birch and D.J. Bacon, *Carbon*, **21**, p491, (1983).

76. B.T. Kelly, *Irradiation Damage and Radiolytic Oxidation in Nuclear Reactor Graphites*, AEA Technology internal report, (1992).

77. K.L.Johnson, *Contact mechanics*, Cambridge University Press, (1985).

78. W.B.Morton and L.J.Close, *Philosophical Magazine*, **43** ,p320, (1922).

79. A.Sackfield and D.A.Hills, *Journal of Strain Analysis*, **18**, p101, (1983).

80. K.Zeng, K.Breder and D.J.Rowcliffe, *Acta Metallurgica et Materiaia*, **40**, p2595, (1992).

81. M.T.Hanson and T.Johnson, *Journal of Tribology*, **115**, p327, (1993).

82. G.M.Hamilton, *Proceedings of the Institution of Mechanical Engineers*, **197C**, p53, (1983).

83. E.H.Yoffe, *Philosophical Magazine A*, **50**, p813, (1984).

84. I.N.Sneddon, *International Journal of Engineering Science*, **3**, p47, (1965).

85. Bunzai, *Bulletin of JSME*, **2**, p244, (1959).

86. R.W. Lewis, D.V. Tran and W.K. Sze, *Stress and Vibration Analysis*, edited by J.E. Mottersheard, Pergamon Press, (1989).

87. H.Matzke, *Key Engineering Materials*, **56**, p365, (1991).

88. M.T.Laugier, *Ceramics International*, **15**, p323, (1989).

89. S.J.Burns and K.Y.Chia, *Journal of the American Ceramics Society*, **78**, p2321, (1995).

90. P.D.Warren, D.A.Hills and S.G.Roberts, Journal of Materials Research, **9**, p3194, (1994).

91. F.C. Roesler, *Proceedings of the Physics Society*, London, **B69**, p981, (1956).

92. B.R. Lawn, *Fracture of Brittle Solids*, Cambridge University Press, (1993).

93. F. Auerbach, Ann. Phys. Chem., **43**, p61, (1891). Cited by F.B. Langitan and B.R. Lawn, Journal of Applied Physics, **40**, p4009, (1969).

94. F.B. Langitan and B.R. Lawn, Journal of Applied Physics, **40**, p4009, (1969).

95. H.L.Oh, I.Finnie, *Journal of Mechanics and Physics of Solids*, **15**, p401, (1967).

96. F.C.Roesler, *Proceedings Physics Society*, London, **B 69**, p55, (1956).

97. F.C.Frank and B.R.Lawn, *Proceedings of the Royal Society London*, **A299**, p291, (1967).

98. B.R.Lawn, *Journal of Applied Physics*, **39**, p4828, (1968).

99. K.L.Johnson, J.J.O'Connor, and A.C.Woodward, *Proceedings of the Royal Society London*, **A334**, p95, (1973).

100. P.D.Warren and D.A.Hills, *Journal of Materials Science*, **29**, p2860, (1994).

101. F. Guiberteau, N.P. Padture, and B.R. Lawn, *Journal of the American Ceramic Society*, **77**, p1825, (1994).

102. H. XU, L. Nitin, P. Padture, and B.R. Lawn, *Journal of Materials Science*, **30**, p869, (1995).

103. H. Cai, M. Stevens Kalceff, and B.R. Lawn, *Journal of Materials Research*, **9**, p762, (1994).

104. F. Guiberteau, N. Padture, H. Cai, and B.R. Lawn, *Philosophical magazine A*, **68**, p1003, (1993).

105. H.Cai, M. Stevens Kalceff, B, Hooks, and B.R. Lawn, *Journal of Materials Research*, **9**, p2654, (1994).

106. B.R. Lawn, N.Padture, F.Guiberteau and H. Cai, *Acta Metallurgica et Materialia*, **42**, p1683, (1994).

107. R. Mouginot, *Journal of the American Ceramic Society*, **71**, p658, (1988).

108. Nuclear Electric Ltd., *Internal report CSDMC/P 28*, (1991).

109. G. Neighbour, *PhD Thesis*, University of Bath, (1993).

110. A. Kauffmann, *Final year project*, University of Leeds, (1991).

111. G. de With and H.H.Wagemans, *Journal of the American Ceramic Society*, **72**, p1538, (1989).

112. D.K. Shetty, A.R. Rosenfield, P. McGuire, G.K. Bansal, and W.H. Duckworth, *Ceramic Bulletin*, **59**, p1193, (1980).

113. H.M. Westergaard, *Public Roads*, **7**, p25, (1926). Cited by G. de With and H.H.Wagemans, *Journal of the American Ceramic Society*, **72**, p1538, (1989).

114. J.A. Brysdon, *Plastic Materials* 5th edition, Butterworths, (1989)

115. Gareth Neighbour, *Private communication*, (1996).

116. J.C. Anderson, K.D. Lever, R.D. Rawlings and J.M. Alexander, *Materials Science* 4th edition, Chapman and Hall, (1990).

117. J.S. Field and M.V. Swain, *Carbon*, **34**, p1357, (1996).

118. Y. Aoki, *PhD thesis*, University of Bath, (1993).

119. A. Papoulis, *Signal Analysis*, McGraw-Hill, (1977).

120. I.M. Hutchings, *Tribology - Friction and wear of engineering materials*, Edward Arnold, (1992).

121. Y. He, L. Winnubst, A.J. Burggraaf, H. Verweij, P.G. van der Varst, and B. de With, *Journal of the American Ceramic Society*, **80**, p377, (1997).

122. M. Birch and J.E. Brocklehurst, *Carbon*, **21**, p497, (1983).

123. M. Futakawa, K. Kikuchi, Y, Muto and H. Shibata, *Journal of the European Ceramic Society*, **11**, (1993).